



Swansea University
Prifysgol Abertawe



Swansea University E-Theses

Modelling Damage, Fragmentation and Progressive Collapse of Structures Using Gaussian Springs Based Applied Element Method

Abdul Latif, Mai

How to cite:

Abdul Latif, Mai (2018) *Modelling Damage, Fragmentation and Progressive Collapse of Structures Using Gaussian Springs Based Applied Element Method*. Doctoral thesis, Swansea University.
<http://cronfa.swan.ac.uk/Record/cronfa48975>

Use policy:

This item is brought to you by Swansea University. Any person downloading material is agreeing to abide by the terms of the repository licence: copies of full text items may be used or reproduced in any format or medium, without prior permission for personal research or study, educational or non-commercial purposes only. The copyright for any work remains with the original author unless otherwise specified. The full-text must not be sold in any format or medium without the formal permission of the copyright holder. Permission for multiple reproductions should be obtained from the original author.

Authors are personally responsible for adhering to copyright and publisher restrictions when uploading content to the repository.

Please link to the metadata record in the Swansea University repository, Cronfa (link given in the citation reference above.)

<http://www.swansea.ac.uk/library/researchsupport/ris-support/>



Swansea University
Prifysgol Abertawe

**Modelling Damage, Fragmentation and
Progressive Collapse of Structures using
a Gaussian Springs based Applied
Element Method**

by

Mai Abdul Latif

Submitted to the College of Engineering,
Zienkiewicz Centre for Computational Engineering,
in fulfilment of the requirements for the Degree of

Doctor of Philosophy

at

Swansea University

Adviser: Professor Yuntian Feng

September 2018

Abstract

Modelling the progressive collapse of structures is necessary for planning controlled demolitions, studying the effect of natural disasters on structures, and determining the weakest locations of a structure for further reinforcement and enhancement. Computational mechanics served an important contribution to modelling the progressive collapse of structures, since it is very expensive to model collapse in an experimental evaluation for large scales.

Existing developments of computational methods for the scope of collapse of structures are extensively reviewed first. It is concluded that the Applied Element Method (AEM) is one of the simplest schemes for modelling the progressive collapse with sufficient accuracy. The AEM is represented as pairs of rigid elements connected by shear and normal springs, along the edges of the elements. The material properties are represented in the stiffness of the springs. The stresses and deflection between elements are based on the deflection of the springs.

The deflection and internal stresses of several structural beams are assessed using the conventional AEM and it is evident that the computational efficiency of the method is inadequate since a sizable amount of elements and springs per element is required to achieve a specific level of accuracy. Hence, a modification to the AEM is necessary to reduce the computational cost of the method. This thesis is focused on the development of the AEM for linear and nonlinear material behaviour, the development of a damage material model for representing damage and fragmentation, and an application of collapse of structures subject to earthquake and extreme wind loading.

The AEM is enhanced using the Gaussian quadrature to find the exact location of springs. Using a Gaussian distribution it is concluded that only 2 springs per element are required for elastic elements, while a total of 6 springs are required for elasto-plastic elements. In conjunction with the Gaussian springs modification, a further modification is implemented that utilises an adaptive technique for selecting the number of springs per element based on elasticity and elasto-plasticity of the springs. In nonlinear material analysis the Newton-Raphson integration scheme is adapted.

To model damage in materials a softening material behaviour is employed. The developed softening algorithm is a return mapping method that is based on the predictor-corrector hardening plasticity algorithm. To represent the failure of a spring in the AEM, the stiffness of the spring is set to zero. This results in a singular global stiffness matrix that can not be solved directly. Using a dynamic model for the analysis eliminates the need of inverting the stiffness matrix, so the explicit Central Difference Method is used for linear and nonlinear dynamic analysis.

The findings in this thesis are (1) the conventional AEM is modified by chang-

ing the distribution of the springs using the Gaussian quadrature allowing for exact calculation of optimal spring locations (2) only 2 and 6 linear and nonlinear springs are needed, respectively between a pair of elements, reducing the overall computational cost of the structure and increasing the accuracy (3) an adaptive transition springs technique is implemented and allowed for an overall reduced computational cost (4) a softening return mapping algorithm is developed for representing material damage (5) a time integrating technique is required when element separation occurs to avoid a singular matrix (6) application of the Gaussian AEM is performed on 2D frames subject to earthquake loads and extreme wind loads.

نبذة مختصرة

نمذجة الإنهيار التدريجي للمنشآت هو أمر ضروري لتخطيط عمليات الهدم الممنهجة، ودراسة تأثير الكوارث الطبيعية على هذه المنشآت، بالإضافة الى تحديد نقاط الضعف في البنية الإنشائية للمباني من أجل تحسينها و تدعيمها. لقد ساهمت الميكانيكا الحاسوبية بدور فعال في هذه العملية، حيث ساهمت في تخفيض التكلفة العالية لنمذجة الإنهيار في نطاق تجريبي ملموس. يتم أولاً في هذه الرسالة التطرق بتمعن لما شهدته الطرق الحسابية من تطورات في هذا المجال. و عليه، تم إستنتاج أن أسلوب العنصر التطبيقي (AEM) هو أحد أبسط الأساليب لنمذجة الإنهيار التدريجي بدقة كافية. يمثل (AEM) كأزواج من العناصر الصلبة المتصلة من خلال زنبركات قاصة و عمودية على إمتداد حواف العناصر. فيتم تحديد خصائص المواد من خلال صلابة الزنبرك، كما يعتمد تحديد الإجهاد والانحرافات بين العناصر على مقدار إنحراف الزنبرك.

تقييم إنحراف وعوامل الإجهاد الداخلية للعوارض الهيكلية تم بإستخدام (AEM) التقليدي. كان من الواضح أن الفعالية الحسابية للطريقة غير كافية، حيث أن العملية تتطلب عدد كبيراً من العناصر والزنبركات المرتبطة بكل عنصر لتحقيق مستوى كافي من الدقة. وبالتالي، يتطلب (AEM) تعديلاً لتقليل تكلفة هذه الطريقة الحسابية. تم التركيز في هذه الرسالة على تطوير (AEM) لتبسيط السلوك الخطي واللا خطي للمواد، و كذلك على تطوير نموذج مادي لتمثيل الضرر والتجزؤ، بالإضافة إلى تقديم تطبيق إنهيار الهياكل المعرضة للزلازل والرياح الشديدة. تم تحسين عمل (AEM) عن طريق إستخدام تربيع "جاوس" لتحديد موقع الزنبرك بدقة. وبإستخدام توزيع "جاوس"، تبين أن هناك حاجة لزنبركان فقط لكل عنصر خطي، ولستة زنبركات فقط لكل عنصر لاخطي. بالإقتران مع تعديل زنبركات "جاوس"، تم تنفيذ تعديل آخر يتضمن إستخدام تقنية تكيفية لإختيار عدد الزنبركات في كل عنصر على أساس المرونة والمرونة البلاستيكية للزنبركات. في التحليل الغير خطي للمواد، تم إستخدام مخطط تكامل نيوتن-رافيسون.

نمذجة الضرر (التلف) في المواد تم إستخدام سلوك مادة التليين. خوارزمية التليين المطورة في هذا المشروع هي طريقة تطبيق معاد تعتمد على خوارزمية التصلب متنبئ-مصحح. لتمثيل اخفاق الزنبرك في (AEM) نفترض أن صلابة الزنبرك تساوي صفر. هذا يؤدي الى الحصول على مصفوفة صلابة شاملة منفردة لا يمكن حلها مباشرة. استخدام نموذج ديناميكي للتحليل يلغي الحاجة إلى عكس مصفوفة الصلابة، و بذلك تُستخدم "طريقة الفرق المركزية" الصريحة للتحليل الديناميكي الخطي واللاخطي. نتائج هذه الرسالة هي:

1. تعديل (AEM) التقليدي عن طريق تغيير توزيع الزنبركات باستخدام تربيع "جاوس" مما يسمح بالحساب الدقيق للأماكن المثالية للزنبركات.
2. الحاجة فقط لزنبركان أو ستة زنبركات خطية ولا خطية على التوالي، بين زوج من العناصر، مما يخفض من التكلفة الحسابية الكلية للهيك و يرفع من الدقة.
3. تنفيذ تقنية الزنبركات الانتقالية التكيفية، مما أدى الى خفض التكلفة الحسابية بشكل عام.
4. تطوير خوارزمية طريقة تطبيق معاد لتليين لتمثيل الضرر.
5. الحاجة لإستخدام تقنية الكاملة الوقتية في حالة إنفصال عنصر لتجنب نشوء مصفوفة منفردة.
6. تم تنفيذ تطبيق (AEM) "جاوس" على إطارات ثنائية الأبعاد خاضعة لأحمال الزلازل وأعباء الرياح الشديدة.

Declaration

This work has not previously been accepted in substance for any degree and is not being concurrently submitted in candidature for any degree.

Signed(candidate)

Date

STATEMENT 1

This thesis is the result of my own investigations, except where otherwise stated. When correction services have been used, the extent and nature of the correction is clearly marked in a footnote(s). Other sources are acknowledged by footnotes giving explicit references. A bibliography is appended.

Signed(candidate)

Date

STATEMENT 2

I hereby give consent for my thesis, if accepted, to be available for photocopying and for inter-library loan, and for the title and summary to be made available to outside organisations.

Signed(candidate)

Date

Acknowledgements

First and foremost, I would like to express my sincerest gratitude to my supervisor, Professor Yuntian Feng, for his continuous support, his motivation, his patience and immense knowledge. He helped me realise my true potential and gave me the support I needed, especially at the moments when I doubted myself. I truly consider myself privileged for having the opportunity of working under his supervision. I could not have asked for a better mentor.

The friendships I made in the last four years will last a life time. First I have to thank, German Martinez-Ayuso and Nidhal Jemaia. You have been like family to me. I am Forever grateful for all the memories we made along the way. I thank you for the good laughs, the coffee breaks, the Crepe Vine breakfasts, and for your comfort during the stressful times. To the friends and colleagues of Swansea; Chen, Emilio, Sanjay, Anna, Katerina, Mariela, Kostis, Dimitris, Despoina, Christina, Leandro, Guillem, Mireia, Kensley, Serena, Quang, Alex L. , Alex J. and Leen. A special thanks to Siba Ewaiwi, for our phone calls over the years. My friends abroad that made it feel like I never left home, Hoda Anvar and Alia Qirreh. I feel lucky to have shared this experience with all of you and I could not have ended it sanely without you.

I would also like to thank my brother, Mohammed Nadher Abdul Latif, for being my flatmate, for sharing this experience with me, for being my best friend, and for being my home away from home. I will cherish these years we spent together, and the lifetime bond we have built.

Finally, my biggest thanks goes to my parents and sisters, Sara and Ola. I cannot begin to imagine the amount of stress I put you through in this journey. Thank you for always being there for me, for believing in me, for teaching me to dream big and for pushing me to become a better person every day.

Dedication

To my beloved parents, Mohammed Nadher and Randa Ibrahim.

إلى والدي الغاليين، محمد ناصر عبد اللطيف و رنده إبراهيم

لن تكفي الكلمات للتعبير عن شكري وإمتناني لكما. إن هذا الانجاز الذي تفخرون به لم يكن ممكنا من دون دعمكم وتوجيهكم المستمر لي خلال هذه السنوات، إيمانكم وثقتكم بقدرتي على تحقيق هذا، وحبكم اللامنتهي كانوا مفتاح نجاحي للوصول إلى هذه اللحظة. أهدي نجاحي لكم مع أنه بقليل أمام سعيكم الدؤوب وجهودكم من أجل تكليل مسيرتي التعليمية بنجاح.

بفضلكم أنا أقف فخورة بهذا الإنجاز. شكراً

عَنْ كَثِيرِ بْنِ قَيْسٍ عَنِ رَسُولِ اللَّهِ صَلَّى اللَّهُ عَلَيْهِ وَسَلَّمَ يَقُولُ:

" مَنْ سَلَكَ طَرِيقًا يَطْلُبُ فِيهِ عِلْمًا سَلَكَ اللَّهُ بِهِ طَرِيقًا مِنْ طُرُقِ الْجَنَّةِ وَإِنَّ الْمَلَائِكَةَ لَتَتَّعِبُ أَعْنَاقَهَا رِضًا بِطَالِبِ الْعِلْمِ بِمَا يَصْنَعُ ، وَإِنَّ الْعَالِمَ لَيَسْتَعْفِرُ لَهُ مَنْ فِي السَّمَوَاتِ ، وَمَنْ فِي الْأَرْضِ ، وَالْحَيَاتَانِ فِي جَوْفِ الْمَاءِ ، وَإِنَّ فَضْلَ الْعَالِمِ عَلَى الْعَابِدِ ، كَفَضْلِ الْقَمَرِ لَيْلَةَ الْبَدْرِ عَلَى سَائِرِ الْكَوَاكِبِ ، وَإِنَّ الْعُلَمَاءَ وَرَثَةُ الْأَنْبِيَاءِ ، وَإِنَّ الْأَنْبِيَاءَ لَمْ يُورَثُوا دِرْهَمًا وَلَا دِينَارًا ، وَإِنَّمَا وَرَثُوا الْعِلْمَ ، فَمَنْ أَخَذَهُ أَخَذَ بِحِطِّهِ وَافِرٍ "

Contents

Abstract	i
Arabic abstract	ii
Acknowledgements	vi
Acronyms	xxv
I State of the Art of Progressive Collapse Modelling	1
1 Background	3
1.1 Motivation	3
1.2 Introduction to Progressive Collapse	5
1.2.1 Types of Progressive Collapse	6
1.2.2 Analysis Procedure Possibilities	7
1.3 Scope of the thesis	10
1.4 Outline of the thesis	10
2 Literature Review	13
2.1 The Finite Element Method	13
2.2 Discrete Element Method	17
2.2.1 The Combined Finite Discrete Element Method (FDEM)	19
2.2.2 Modified Distinct Element Method	20
2.2.3 Extended Distinct Element Method	22
2.3 Rigid Bodies Spring Models	24
2.4 Shifted Integration Technique	25
2.4.1 Adaptive Shifted Integration Technique	26
2.4.2 ASI-Gauss Technique	26
2.5 Applied Element Method	29
2.5.1 Progressive Collapse of RC structures using ELS	30
2.5.2 Improved Applied Element Method	31
2.5.3 Voronoi Applied Element Method	33
2.6 Summary of Methods and Conclusion	34
3 Numerical Methods Approaches	37
3.1 Mechanics of Continuous Bodies	37
3.1.1 External and Internal Virtual Work	38
3.2 Energy Principle Equations	41

3.2.1	The Principle of Virtual Displacements	41
3.2.2	The Principle of Minimum Potential Energy	42
3.3	Finite Element Method	43
3.3.1	Isoparametric mapping	44
3.3.2	Jacobian of the Mapping	46
3.3.3	Differential Volume and Area	49
3.3.4	Numerical Integration	50
3.4	Discrete Model for Continuum	51
3.5	Lattice Model for RC using EDEM	54
3.6	Rigid Bodies Spring Models	57
3.6.1	Formulation of Beam Element	57
3.6.2	Plane strain elements	58
3.7	Shifted Integration Technique Formulation	60
3.7.1	Adaptively Shifted Integration Technique	61
3.7.2	ASI-Gauss Technique	62

II Formulation of Linear and Nonlinear Gaussian Based AEM 65

4	Applied Element Method Formulation 67
4.1	AEM Formulation for 2-D element 67
4.2	AEM Meshing and Element distribution 70
4.2.1	Structures with multiple materials 71
4.3	Effect of Number of Springs and Elements 72
4.3.1	Effect of Number of Springs Between Elements 73
4.3.2	Effect of Element Size 74
4.4	Large Displacement Analysis using AEM 74
4.5	Modifications in AEM 77
4.5.1	Improved Applied Element Method 77
4.5.2	Voronoi AEM 78
4.6	Conclusion 79
5	Gaussian based AEM Formulation 81
5.1	AEM for Linear Elastic Cases 82
5.2	Linear Elastic Case Studies: AEM vs. FEM 84
5.2.1	Cantilever Beam 84
5.2.2	Fixed End Beam 88
5.2.3	Simply Supported Beam 90
5.3	Gaussian Springs based AEM 92
5.3.1	Gaussian Springs Implementation in AEM 93
5.3.2	Comparison of equal springs with Gaussian springs 94
5.4	Conclusion 97
6	Gaussian AEM in Elasto-plasticity 99
6.1	Overview 99
6.2	Definitions 102
6.3	Elasto-plastic Constitutive Equations Derivation 103
6.4	Strain Hardening 106

6.5	Incremental 1D rate independent plasticity	108
6.5.1	Elastic step (Predictor Step)	109
6.5.2	Plastic step (Corrector Step)	110
6.5.3	Return Mapping	110
6.6	Application of AEM to elasto-plasticity	113
6.6.1	Newton Raphson Method	113
6.7	Gaussian AEM in Hardening Elasto-plasticity	116
6.7.1	Cantilever beam	117
6.8	Adaptive Gaussian Springs	123
6.8.1	Transition Point Locator	125
6.8.2	Examples	126
6.9	Conclusion	130

III Formulation of Damage, Fracture and Progressive Collapse in Gaussian Based AEM & Applications 133

7	Material Damage Model & Dynamic Analysis	135
7.1	Softening Material Behaviour	135
7.1.1	Return-Mapping Algorithm verification	141
7.1.2	Failed Elements	142
7.2	Introduction to Dynamic Analysis	145
7.2.1	Equation of Motion for MDOF Systems	145
7.2.2	Equations of Motion for Linear Systems	145
7.2.3	Natural Vibration Frequency and Modes Calculation	147
7.3	Time-stepping Methods for linear systems	150
7.3.1	The Central Difference Method	150
7.3.2	The Newmark- β Method	153
7.3.3	Numerical Methods Classifications	156
7.4	Time-stepping methods for Nonlinear Systems	157
7.4.1	Nonlinear Newmark- β Method	157
7.4.2	Nonlinear Central Difference Method	159
7.4.3	Summary of Methods	160
7.5	Dynamic Formulation and Application in AEM	161
7.5.1	Determination of Mass Matrix	161
7.5.2	Determination of Damping Matrix	162
7.5.3	Implementing dynamics and nonlinearity in MATLAB code	163
7.6	Dynamic Analysis for Verification	164
7.6.1	Free Vibration	164
7.7	Analysis Results	167
7.8	Conclusion	170
8	Structures subject to Earthquake loads	173
8.1	Introduction	173
8.1.1	How do earthquakes occur?	174
8.1.2	Seismic Scales	175
8.1.3	Structural Damage	175
8.2	Earthquake Implementation in AEM	178
8.2.1	Earthquake Data	179

8.2.2	Frame Implementation	180
8.3	Applications	180
8.3.1	1x1 Frame	180
8.3.2	3x8 Frame	185
8.3.3	Multi-storey frame	187
8.3.4	2x8 Frame	188
8.3.5	High rise frame - 15 floors	189
8.4	Conclusion	190
9	Structures Subject to Extreme Wind Loads	191
9.1	Collapse of Structures due to Wind loads	191
9.2	Using CFD for turbulent wind analysis	195
9.2.1	Solution Model	196
9.2.2	CFD Model	198
9.2.3	40 m/s 3 second gust wind	201
9.2.4	70 m/s 3 second gust wind	203
9.3	Loads from surrounding structures	206
9.4	Conclusion	210
IV	Conclusions	211
10	Concluding Remarks	213
10.1	Conclusions	213
10.1.1	Linear and Nonlinear Gaussian AEM	214
10.1.2	Modelling Damage Fragmentation and Progressive Collapse in AEM	216
10.2	Concluding Remarks	217
10.3	Recommendations for further research	218
V	References	219

List of Figures

1.1	Death rates from natural disasters [1]	4
1.2	Direct causes of death [2]	4
1.3	Relationship between structural damage among deceased cases [2]	4
1.4	Pancake-type Collapse [8]	6
1.5	Zipper-type Collapse [8]	7
1.6	Domino-type Collapse [8]	7
2.1	Element Separation Algorithms [14]	14
2.2	Comparison of collapse mechanism using the Element Erosion algorithm, and the Node-Split Algorithm [14]	16
2.3	Nine storey building evolution of collapse kinematics - using Node-Split algorithm [14]	16
2.4	Space frame discretisation using DEM [16]	17
2.5	Dome initial configuration and dimensions. Point B represents the location of the applied load [16]	18
2.6	Final configuration of Dome after load [16]	18
2.7	Collapse of structures with increasing α using DEM [18]	19
2.8	Fracture process [37]	20
2.9	Fracture of a rigid-frame concrete structure under horizontal impulsive loading [38]	21
2.10	Fracture of masonry concrete wall with a frame subject to sinusoidal horizontal loading	22
2.11	Whole collapse of RC column using Lattice EDEM [41]	23
2.12	Collapse of Wooden House [48]	25

2.13	Collapse of steel framed structure due to impact of aircraft using the ASI-Gauss technique for analysis [50]	28
2.14	Seismic Collapse of Frame using the ASI-Gauss Technique [52] . .	29
2.15	2D Frame analysis [55]	30
2.16	2D Frame analysis while considering debris collision [55]	30
2.17	3D Frame analysis [55]	31
2.18	Comparison of Real Demolition vs ELS [57]	32
2.19	IAEM frame collapse [58]	33
2.20	Comparison of crack pattern of beam [59]	34
3.1	Virtual Work Done [61]	40
3.2	Interpolation of a one-variable function	43
3.3	1D finite element e with shape functions	44
3.4	Quadrilateral in different planes	44
3.5	Infinitesimal quadrilateral element	49
3.6	Discrete element method models based on rigid disc elements [64]	52
3.7	Seven-disc model	54
3.8	Concrete Lattice Model [41]	55
3.9	Beam Bending Element [43]	57
3.10	Plane strain element in RBSM [43]	59
3.11	Timoshenko beam element compared to RBSM element [50] . . .	61
3.12	ASI element compared to ASI-Gauss [50]	63
4.1	2D AEM Elements [6]	68
4.2	2D AEM Elements degrees-of-freedom [65]	69
4.3	Mesh distribution for structural beam	70
4.4	Connectivity between adjacent elements	71
4.5	Frame meshing in AEM	71
4.6	Representation of a cantilever concrete and steel reinforcement springs	72
4.7	Effect of Element Size [6]	74
4.8	Large Displacement of Simply supported beam [66]	76
4.9	Element Assembly in VAEM [59]	78

5.1	Noded cantilever beam diagram	83
5.2	Local Orientation	83
5.3	Cantilever Free Body Diagram	84
5.4	ANSYS Cantilever Deflection	86
5.5	MATLAB Cantilever Deflection	86
5.6	MATLAB Cantilever Deflection 10 elements in x-direction oppo- site load	86
5.7	MATLAB Cantilever Normal Stress	87
5.8	ANSYS stress distribution	87
5.9	AEM stress distribution	87
5.10	ANSYS shear stress distribution	88
5.11	AEM shear stress distribution	88
5.12	AEM Cantilever Deflection 30 elements in x, 5 elements in y . . .	89
5.13	AEM Cantilever Deflection Load Positive Direction	89
5.14	ANSYS Fixed End Beam Deflection	90
5.15	AEM Fixed End Beam Deflection	90
5.16	Normal stress for FEB from ANSYS	91
5.17	Normal stress for FEB from AEM	91
5.18	AEM Different loading direction for FEB	91
5.19	AEM Deflection Simply Supported Beam	92
5.20	AEM Normal stress Simply Supported Beam	92
5.21	Comparison of Gaussian and Equal Springs Tributary Area for 3 and 5 springs	94
5.22	Beam with 10 elements	95
5.23	Fixed End Beam with 10 elements	96
6.1	Uniaxial Tension Test [68]	100
6.2	Return mapping scheme (a) with hardening (b) no hardening [68]	111
6.3	Return Mapping with hardening	112
6.4	Newton Raphson iteration - graphical representation [68]	116
6.5	Cantilever beam elements	118
6.6	Load displacement diagram at free end	118
6.7	Beam deflection through loading-unloading-loading	119

LIST OF FIGURES

6.8	Number of iterations required at every load step	120
6.9	Newton Raphson convergence	120
6.10	Convergence at different load steps for tolerance 10^{-5}	121
6.11	Normal stress for cantilever beam	122
6.12	Shear stress for cantilever beam	122
6.13	Adaptive Elastic Springs	123
6.14	Adaptive Elasto-plastic Springs	123
6.15	Representation of a cantilever with initial of 10 springs	124
6.16	Representation of a cantilever beam with all elastic springs	124
6.17	Representation of a cantilever beam using adaptive AEM springs	125
6.18	Transition Point locator	125
6.19	Cantilever beam with 10 elements	127
6.20	Deflection of cantilever beam with adaptive springs	127
6.21	Normal stress of cantilever beam with adaptive springs	127
6.22	Spring sets that are elasto-plastic	128
6.23	Springs distribution between elements	128
6.24	Normal stress distribution at every cross-section	128
6.25	Converge Rate of Newton Raphson	128
6.26	Deflection of FEB with adaptive springs	129
6.27	Normal stress distribution for Fixed End Beam	129
6.28	Stress with adaptive springs for FEB	130
6.29	New springs distribution for FEB	130
6.30	New stress distribution for FEB	130
7.1	Strain Softening Material Behaviour	136
7.2	Trial stress predictor calculation	139
7.3	Demonstrating the trial function	139
7.4	Representation of $\Delta\lambda$	140
7.5	Plastic strain	140
7.6	Trial stress calculation	141
7.7	f_{n+1}^{trial} calculation	141
7.8	$\Delta\lambda$ and ϵ^p calculation	142
7.9	Predictor-corrector Softening model	143

7.10	Predictor-corrector Softening model	144
7.11	(a) Two story shear frame (b) Forces acting on frame [81]	145
7.12	Modal Shapes for Cantilever Beam	149
7.13	Modal Shapes for a Fixed Ends Beam	150
7.14	Free vibration of undamped system [81]	165
7.15	Free vibration of point at which load is applied	165
7.16	Free vibration of damped system [81]	166
7.17	Displacement, velocity and acceleration of damped cantilever sys- tem at free end	166
7.18	displacement, velocity and acceleration at free end	167
7.19	Beam Deflection of cantilever beam at different time steps	168
7.20	Displacement, velocity and acceleration of free free end of can- tilever beam for undamped system	168
7.21	Force-displacement diagram for sin load	169
7.22	Displacement, velocity and acceleration at free end for cantilever beam with sin load	169
7.23	Large displacement for tall frame with no collapse	170
8.1	Focus, epicentre and seismic waves demonstration [99]	174
8.2	Seismogram of Sumatra, Indonesia 2004 earthquake [101]	175
8.3	El Centro 1940 time history acceleration graph	179
8.4	Kobe, Japan 1995 time history acceleration graph	180
8.5	Frame with point load	181
8.6	Acceleration, velocity and displacement vs. time at midspan be- fore failure occurs	181
8.7	Displacement, velocity and acceleration after failure at midspan .	182
8.8	Factored frame deflection in first 0.1 second under earthquake Kobe load	183
8.9	Progressive collapse of 1x1 frame with earthquake Kobe loading and loading applied at midspan	184
8.10	Progressive collapse of 3x8 frame with earthquake loading and loading applied at midspan	185

LIST OF FIGURES

8.11	Progressive collapse of 3x8 frame with earthquake loading and loading applied at midspan (continued)	186
8.12	Analysis of multi-storey steel frame subject to El Centro Earthquake	187
8.13	Time history of a high rise frame undergoing seismic loading and point load at in positive x-direction at first floor	188
8.14	Time history of a high rise frame undergoing seismic loading and point load at in positive x-direction at first floor	189
9.1	Devastating natural disasters. Red: Earthquake, Tsunami, Volcanic eruption. Blue: Flood. Green: wind-storm. Yellow: other events. [112]	192
9.2	Damage to soccer stadium in Korea due to Typhoon Rusa, 2002 [113]	194
9.3	Damage to wind energy facilities in Miyakojima island due to Typhoon Maemi, 2003 [114]	194
9.4	Broken windows in residential building in Korea, due to Typhoon Maemi [113]	194
9.5	Collapse of building under construction undergoing intense winds [115]	195
9.6	Flow chart for procedure	196
9.7	Configuration of the simulation for flow past a single building [116]	197
9.8	Comparison of results from FLUENT and from the wind tunnel test [116]	198
9.9	Boundary conditions	199
9.10	Mesh for flow around structure	200
9.11	Vorticity, velocity, dynamic pressure and turbulence kinetic energy for flow past building with 40 m/s wind speed	201
9.12	Residuals for turbulent flow	202
9.13	Forces on each wall in x and y directions due to 40 m/s wind speed	202
9.14	Displacement, velocity and acceleration of a single point of the frame due to the wind load of 40 m/s	203
9.15	Frame displacement factored by 10^3 for 3 sec gust 40 m/s wind speed	204

9.16	Forces on left and right wall due to 70 m/s wind speed	204
9.17	Contours due to the 70 m/s wind speed, 3 second gust	205
9.18	Collapse of frame subject to 70 m/s wind speed	205
9.19	Geometry model for three adjacent buildings	206
9.20	Mesh for three adjacent buildings	207
9.21	Forces on all the walls for the third building with 3 second gust wind 40m/s	207
9.22	Vorticity, velocity, turbulence and dynamic pressure contours of three adjacent buildings with 40 m/s wind speed	208
9.23	Displacement velocity and acceleration for the third building at 40 m/s 3 second gust	208
9.24	Frame deflection subject to 40 m/s wind; effect of neighbouring buildings	209

List of Tables

2.1	Comparison AEM vs IAEM steel beam	32
2.2	Summary of Advantages and disadvantages of Methods	35
2.3	Summary of methods formulation basis	36
5.1	Beam Properties	84
5.2	Small Displacement comparison	86
5.3	FEB deflection Comparison	90
5.4	3 springs coordinates and weighting factor	94
5.5	3 springs w_i and x_i for cross-section 5m	94
5.6	5 springs coordinates and weighting factor	94
5.7	5 springs coordinates and weighting factor	94
5.8	Deflection at free end comparison	95
5.9	y-deflection of beam at every node - 2 springs	96
5.10	y-deflection of beam at every node - 50 springs	96
5.11	y-deflection of beam at every node - 2 and 50 Gaussian springs	96
5.12	y-deflection of FEB at every node - 2 springs	96
5.13	y-deflection of FEB at every node - 50 springs	97
6.1	Residual at each iteration	120
6.2	Residual at each iteration	128
7.1	Summary of advantages and disadvantages	161
8.1	Some of the Deadliest Earthquakes [97]	174
8.2	Methods of measuring earthquakes [102]	176
8.3	Mercalli scale & Richter scale [102]	177
8.4	Section Properties	181

LIST OF TABLES

9.1	Wind induced phenomena [113]	193
9.2	Maximum Average force applied on each wall of the frame	203

Acronyms

AEM	Applied Element Method
FEM	Finite Element Method
DEM	Discrete Element Method
EDEM	Extended Distinct Element Method
MDEM	Modified Distinct Element Method
RBSM	Rigid Bodies Spring Models
IAEM	Improved Applied Element Method
VAEM	Voronoi Applied Element Method
ASI	Adaptively Shifted Integration Technique
ELS	Extreme Loading Software
ACI	American Concrete Institute
RC	Reinforced concrete
DOF	Degrees of freedom
MDOF	Multiple degrees of freedom
CPU	Central Processing Unit
CFD	Computational Fluid Dynamics
CDM	Central Difference Method
NR	Newton Raphson
RANS	Reynolds averaged Navier-Stokes models
LES	Large Eddy Simulations
DL	Dead load
LL	Live load

Nomenclature

E	Young's Modulus of Elasticity
G	Shear Modulus of Elasticity
I	Second moment of inertia
K	Stiffness matrix
K_n	Normal stiffness of spring in AEM
K_n^i	Normal stiffness of spring in Improved AEM
K_s	Shear stiffness of spring in AEM
K_s^i	Shear stiffness of spring in Improved AEM
$\Delta\lambda$	Consistency parameter - in hardening and softening materials
$\Delta\mathbf{u}$	Incremental displacement vector
$\Delta\ddot{\mathbf{u}}$	Incremental acceleration vector
$\Delta\dot{\mathbf{u}}$	Incremental velocity vector
$\Delta\mathbf{f}$	Incremental force vector
Ω	Material body
Π	Potential Energy
α	Isotropic internal hardening - equivalent plastic strain
δW	Virtual work
δW_E	External virtual work
δW_I	Internal virtual work
δu	Virtual displacement
\mathbf{J}	Jacobian Matrix
\mathbf{R}_G	Residual force vector due to geometrical changes
\mathbf{R}_m	Residual force vector due to cracking or incompatibility between spring strains and stresses

ν	Poisson's ratio
ρ	Density of considered material
a	Element width in AEM
b_{n1}	Distance between centre of element to spring location in AEM
d	Length of spring tributary area in AEM
ds	Surface element
dv	Volume element
n_g	N number of integration points in Gauss integration rule
t	Element thickness in AEM
t_{av}	Average thickness of element

Part I

State of the Art of Progressive Collapse Modelling

Chapter 1

Background

1.1 Motivation

"Earthquakes dont kill people, buildings do"

During earthquakes, hurricanes, tornadoes or even tsunamis, structures undergo several types of structural damage that can cause total collapse in structures, and more importantly, danger to human life. Modelling the progressive collapse of structures is necessary for understanding the weakest locations of structures for further reinforcement and enhancement. Figure 1.1 shows the death toll since the 1900's to the late 2010's due to natural disasters. From the figure it is evident that the most deaths were due to extreme weather and earthquakes, with a death toll of 210,000 and 350,000 respectively.

Figure 1.2 presents the distribution of the causes of death after the Great Hanshin-Awaji Earthquake occurred in 1995 [2]. The most common cause of death during this earthquake was suffocation.

The extensive study on the deaths from the Great Hanshin-Awaji Earthquake also showed that most deaths were caused by structural damage [2]. The study also showed that most people died in structures that were made of wood, rather than reinforced structures. Figure 1.3 shows the relationship of the human casualties with the structural damage and type [2]. The majority of the deaths occurred due to completely collapsed structures or severely damaged buildings, except for those that died due to burning wood buildings.

1.1. MOTIVATION

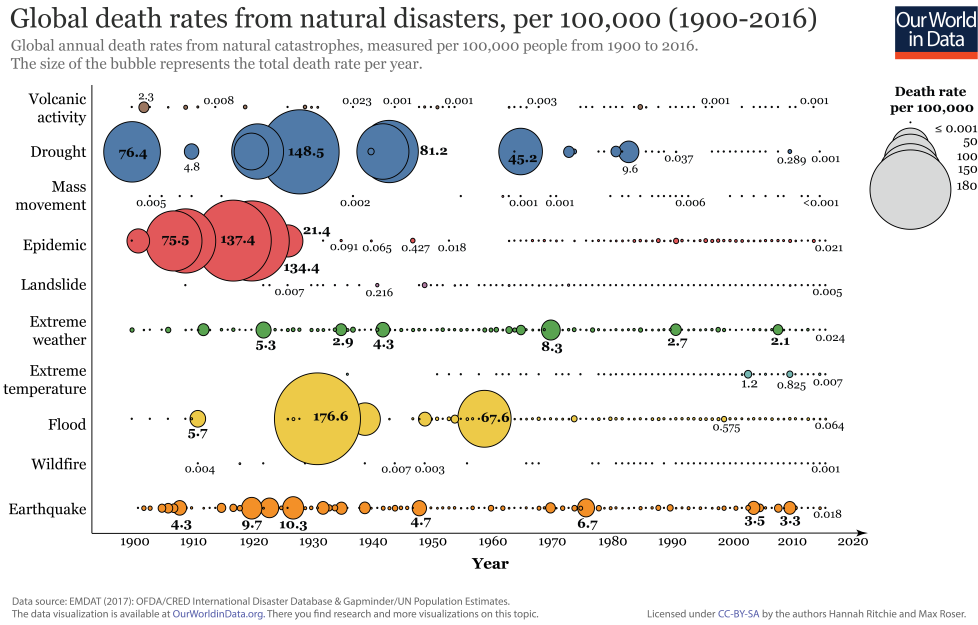


Figure 1.1: Death rates from natural disasters [1]

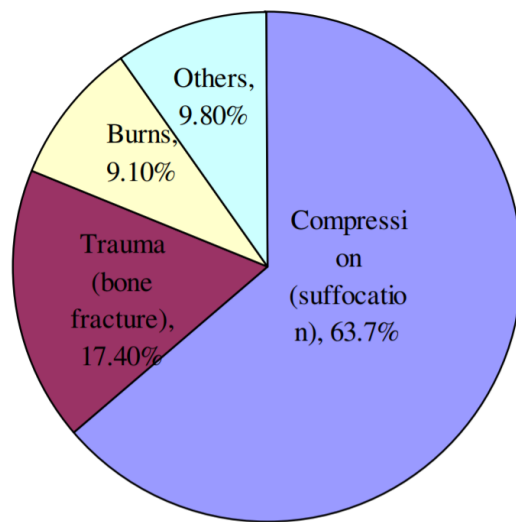


Figure 1.2: Direct causes of death [2]

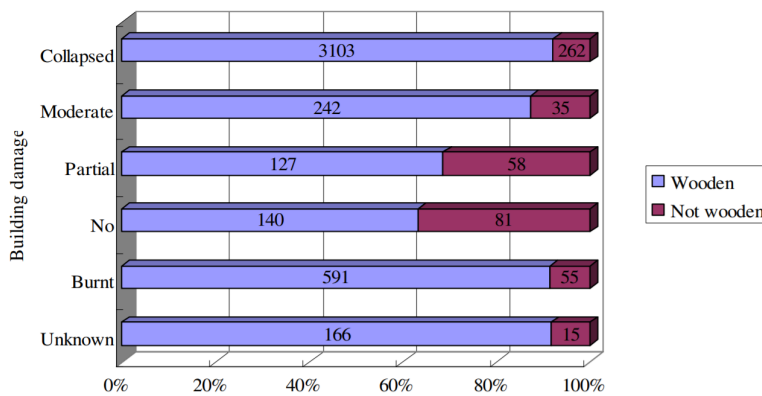


Figure 1.3: Relationship between structural damage among deceased cases [2]

1.2 Introduction to Progressive Collapse

Current structural design codes possess enough collapse resistance under conventional loads. However, since structural failure is the biggest cause of death when natural disasters strike, structural engineers face a responsibility of modelling structural collapse and damage, to further aid in reinforcing buildings at their weakest points, when the structures undergo such extreme loading. The phenomena of progressive collapse has become a topic of major interest, and can be defined as follows [3];

"A progressive collapse is characterized by the loss of load-carrying capacity of a relatively small portion of a structure due to an abnormal load which, in turn, triggers a cascade of failure affecting a major portion of the structure"

In other words, once a small structural element fails, it causes a chain reaction of other structural elements to fail. Understanding the collapse state of a building can allow a higher margin of safety in design [4]. Sometimes local failures can be unavoidable if subject to very rare abnormal loading, however, understanding how to control the expansion of the failure, from local to global state that can ensure an overall stability of a structure is the important aspect.

Testing the structural collapse of buildings using experiments can be quite demanding since they require a lot of time, cost, and resources. This is why numerical methods are significant in analysing such large scale problems.

Collapse analysis requires modelling a structure from a continuous body, to a discrete one [5]. The numerical model should be able to accurately model the structure's elasto-plastic deformation and energy dissipation before collapse, as well as the rigid body movement and impact of the structural members [5].

There are several methods that can be used to analyse the behaviour of structural collapse. Currently, the available numerical models for modelling collapse are classified into two categories; continuum method (such as the Finite Element Method), and discrete element method (such as Rigid Body and Spring Model (RBSM) or the Extended Distinct Element Method (EDEM)) [6]. Nonlinear

dynamic analysis has been widely modelled using the finite element method for analysis of progressive collapse of structures; however, difficulties in the analysis were found at the presence of excessively deformed elements with cracking or crushing, as well as having a high computational cost, and difficulties in choosing the appropriate material models for analysis [6].

1.2.1 Types of Progressive Collapse

Different structures are susceptible to different types of collapse and are described by a disproportion between a trigger and resulting in the collapse of a major part or the whole structure. The different types of collapse are explained in this section [7].

1. Pancake-type collapse

The mechanism of this collapse entails an initial failure or vertical load bearing elements that result in a separation of structural components and their fall in the vertical rigid body motion. The gravitational potential energy is transformed to kinetic energy. The failure progresses in the vertical direction, and impact forces are generated. The gravitational potential energy that occurs during the fall exceeds the strain energy in the structure. Once the energy is reintroduced in the structure in an impact manner, large internal forces are generated [7]. The pancake-type collapse is better demonstrated in Figure 1.4 [8].

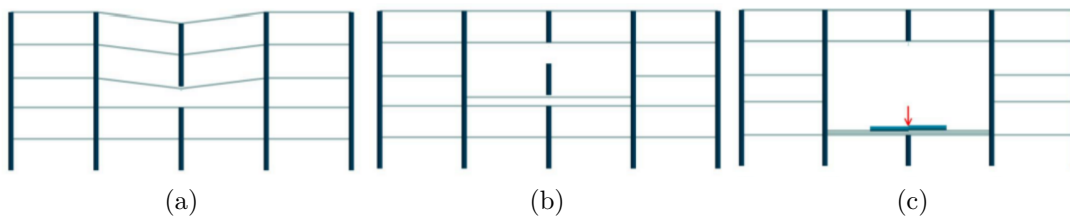


Figure 1.4: Pancake-type Collapse [8]

2. Zipper-type collapse

The mechanism of a zipper-type collapse entails an initial failure of one or few load bearing elements, continued by a redistribution of the forces on the elements remaining in the structure. There is a dynamic response of the

structure to the impulsive dynamic loading due to the suddenness of the initial failure. The failure progression is in the direction transverse to the principal forces in the failing elements. The zipper-type collapse mechanism is shown in Figure 1.5 [8].

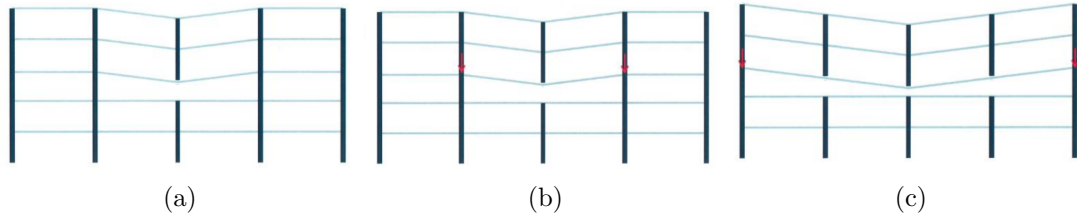


Figure 1.5: Zipper-type Collapse [8]

3. **Domino-type collapse** The mechanism behind a domino type collapse starts with one initial overturning of one element, that cause it to fall in an angular rigid body motion. There is then a lateral impact of the upper edge of the overturning element on the adjacent element, causing a chain reaction of the adjacent element overturning and causing an impact on its adjacent element. The mechanism is better represented in Figure 1.6 [8].

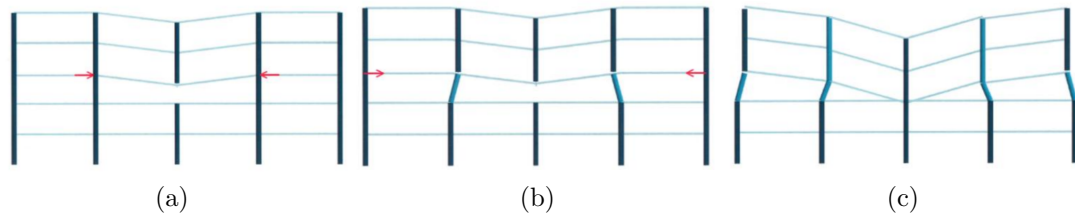


Figure 1.6: Domino-type Collapse [8]

4. **Mixed-type collapse**

The mixed type collapse includes a combination of different collapse mechanisms mentioned, as it is not necessary that only one of the mechanisms are encountered in actual collapse of structures.

1.2.2 Analysis Procedure Possibilities

There are several analytical methods of analysis to simulate the behaviour of structures after damage is initiated. It is important to note that the loss of

bearing elements is modelled as a sudden dynamic removal. The most common analysis methods are [9];

1. Linear Elastic Static Analysis
2. Nonlinear Static Analysis
3. Linear Elastic Time History Analysis
4. Nonlinear Time History Analysis

The linear elastic method is considered the simplest of all the methods and the removal of structural elements is performed statically. The method is considered relatively simple, with fast calculations. However, it does not consider dynamic effects and does not consider material nonlinear behaviour. Therefore, large or complex structures may not be evaluated with realistic results, instead it is limited to simple structures with predictable behaviour. Modelling the progressive collapse of a structure subject to a dynamic loading, such as an earthquake, will not be possible.

The nonlinear static analysis is commonly used to analyse a building undergoing a lateral load, and is known as a "push-over analysis". The applied load increases incrementally until the maximum load or displacement is reached, while undergoing nonlinear behaviour in structural members. It was found that the advantage of using this method is allowing nonlinear material behavior. However, the disadvantages outweigh the advantages since the method does not consider dynamic effects, it is expensive in terms of time, and is considered quite complex.

The linear elastic time history analysis is based on real-time removal of the major load bearing structural elements that result in real-time linear elastic motions, and can be referred to as a time history analysis. This method incorporates dynamic amplification factors, inertia and damping forces, in other words it includes dynamic behaviour. Disadvantages of the method are induced from the inability to consider material nonlinearity, time consuming, requires additional procedures for including time stepping and internal forces. The method is therefore limited to structures that may undergo large plastic deformations.

Finally, the nonlinear time history analysis provides the most realistic results from all approaches since it considers dynamic behaviour of structure, and material nonlinearity. Having those features allows larger deformations, energy

dissipation, material yielding, cracking and failure. However, is time demanding, complex and incorrect assumptions can lead to extremely incorrect and invalid results [9]. Of all the analytical approaches it is clear that the nonlinear time history analysis is the most applicable in analysing the progressive collapse of structures.

The design approaches developed and expanded belong to one of the following categories; Performance based methods - Direct design, and Prescriptive methods - Indirect design method.

The direct design methods consider potential dangers to a structure by attempting to suitably protect the structure from the adverse affects. This approach is implemented when a threat can be identified or quantified, such as vehicle impacts, high winds, earthquakes or even flooding. In order to generate such an analysis, information about the possible forces is required, and on which elements the forces are applied [7]. There are two approaches to implement this method (a) the Alternate Path Method or (b) the Specific Local Resistance Method [10]. The alternate path method allows local failure to occur; however redistributes the forces to find an alternate load path where the damage may be absorbed to avoid a major collapse. Whereas, the local resistance method, pursues to provide tolerable strength to resist an event [9].

The indirect design approaches are performed by removing structural elements and performing the analysis of the behaviour of the structure. For instance one approach is having a sudden loss of a column and the remaining structure is assessed. It should be noted that loss of a structural element can be a quite drastic assumption, leading to an over-design since the remainder of elements will be larger to compensate the loss. Also, every structural configuration must be considered and this cannot give a general solution [10].

The next chapter is a literature review of the numerical methods that include nonlinear behaviour of structures for progressive collapse, along with their applications.

1.3 Scope of the thesis

The scope of this thesis is to improve a progressive collapse model of structures for better accuracy and efficiency, and model material damage behaviour to analyse structures subject to earthquakes and extreme wind loads. With reference to this underlying objective, this work proposes a modification to the Applied Element Method based on using the Gaussian Quadrature for improving efficiency. The AEM is coded in MATLAB. The AEM will be analysed for both linear and nonlinear material models. This thesis will cover structures in 2D only.

1.4 Outline of the thesis

The chapters in the thesis are organised as follows.

- *Chapter 2* is a literature review of implementation of numerical methods that have been developed for modelling the progressive collapse of structures, as well as their advantages and disadvantages.
- *Chapter 3* demonstrates the numerical formulations to the methods that were presented in Chapter 2. The purpose is to display the logic in the evolution of the numerical models as well as their relationships to one another, and their limitations in implementation.
- *Chapter 4* is an overview of the formulation of the Applied Element method (AEM), as well as the developments to the method over the last two decades.
- *Chapter 5* displays an implementation of the AEM to elastic material behaviour, with a novel modification to the springs distribution using the gaussian quadrature, called the Gaussian-AEM. Examples in how the modification improves the size of the model and accuracy are presented.
- *Chapter 6* the Gaussian-AEM is implemented to nonlinear material behaviour by implementing isotropic hardening.

- **Chapter 7** the damage of materials is modelled through a softening return-mapping algorithm. A time integrating scheme is implemented to solve problems related to fracture and damage.
- **Chapter 8** the progressive collapse of structures due to earthquakes is presented for different multi-storey 2D framed structures.
- **Chapter 9** the progressive collapse of structures due to extreme wind loads is presented, with an analysis of the 3 second wind gusts using CFD models.
- **Chapter 10** is a conclusion of the work done in the thesis as well as future recommendations.

Chapter 2

Literature Review

Computational models for structural analysis have been developed for almost a century. There are several methods to model continuum behaviour and discrete element behaviour. This chapter entails the different computational methods that have been developed with applicability to the progressive collapse of structures field.

2.1 The Finite Element Method

The finite element method (FEM) originated as early as in the 1940's. It is based on continuum material equations and has been widely applied to engineering problems including the structural analysis of large-scale structures [11]. However, some limitations in FEM arise with nonlinear and discontinuous problems [11]. Different techniques developed in the FEM for implementing dynamic behaviours with nonlinearities and discontinuities are mentioned in this section.

The finite element method typically assumes that the structures remain continuous. In some cases the collapse mechanism is represented by plastic hinges. Among other numerical methods for analysing the dynamic behaviour of continuum are: the finite difference method, the finite volume method and the boundary element method. However, these methods cannot simulate the entire failure process because additional considerations are involved where damage or fracture appears. There are some developed elasto-plastic material models for reinforced concrete FEM analysis [12, 13], but their complexity lead to large computational

costs for calculation.

A study done by Michaloudis et al. in 2010 [14] was performed to model the structural failure of controlled demolition buildings using the finite element program LS-DYNA. The problems anticipated in modelling the collapse were due to high nonlinearities, multiple contact possibilities and the necessity for discretisation with continuum elements, which results in models with a very large number of elements. The discretisation on the LS-DYNA program was performed using 8-node solid finite elements, and a stabilisation technique developed by Belytschko-Bindeman was required. Other problems evolved from the material model. The material model did not allow detailed modification for simulating the behaviour of reinforced concrete. The explosion is modelled by removing key elements in the structure. Two different numerical models were studied: element erosion algorithm and the node-split algorithm, presented in Figure 2.1.

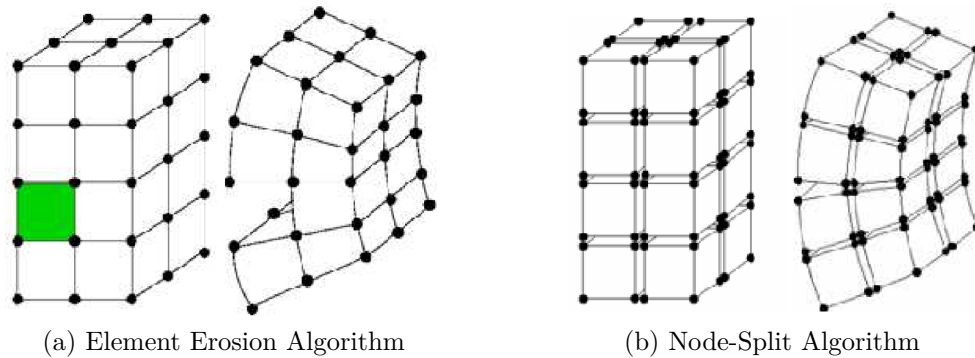


Figure 2.1: Element Separation Algorithms [14]

The element erosion algorithm is based on removing elements that have failed. It was noted that a ‘fairly fine mesh’ was required in order to capture the failure zone. This model did not allow a detailed modification to simulate the behaviour of reinforced concrete. It also deleted elements that exceed the plastic strain, resulting in a limitation in its usability, since the deletion of elements during the simulation resulted in inconsistent computations in terms of volume, mass and energy. Also, contact conditions between structural elements could not be described since contact surfaces were deleted due to the material failure. It was concluded that the results were not very useful since a very large part of the building was being deleted.

However, the results were different using the node-split algorithm. The method

is based on that the nodes are tied (constrained) together until a failure criteria is met. Figure 2.1b shows the split behaviour when the failure criteria at a node is met. The node is split into two separate nodes and the analysis proceeds. With this method no elements are deleted, so the simulation of the structure remains consistent in terms of energy, mass and volume. Also, all contact between elements is considered. Moreover, the kinematics of the failure procedure are not affected by any kind of artificial erosion, and the contact procedures during demolition were sufficiently taken into account. Each element consists of 8 nodes, shown in Figure 2.1b. So no node belongs to more than one element at the same time, which leads to an increase in the total simulation time, and an increase in the time to construct the model, as well as an increase in the number of equations in the problem, in comparison to the element erosion algorithm.

Figure 2.2 shows a comparison analysis of the collapse kinematics and the final rest position. The figures on the left are based on the element erosion behaviour, and on the right are based on the node-split algorithm. It was concluded that both approaches provided similar behaviour of the collapse kinematics at the initial stage of the collapse and also in the whole evolution. The structures showed similar rest position, because the failure occurred mostly at the connections.

Another example of the collapse is presented in Figure 2.3, where a nine storey building undergoes two phases of blasts. Firstly, two rows of columns are removed from the fifth floor, and after 1.5 seconds two rows of columns from the second and ground floor are destroyed. The node-split algorithm is selected for the analysis, since the element erosion model will remove a very large part of the structure from the system. The results showed a realistic description of the collapse kinematics and an appropriate final rest position of the structure.

This study showed the complexities of trying to use the FEM for modelling structural collapse, even though it included several modifications to the original method. Although the method was able to present realistic final resting position of the structure as well as providing information on the possible collapse kinematics, it does not seem to be concentrating on the details of the analysis neither the accuracy. It is evident that the finite element method alone may not be the most efficient method to solve large displacement problems that include elements

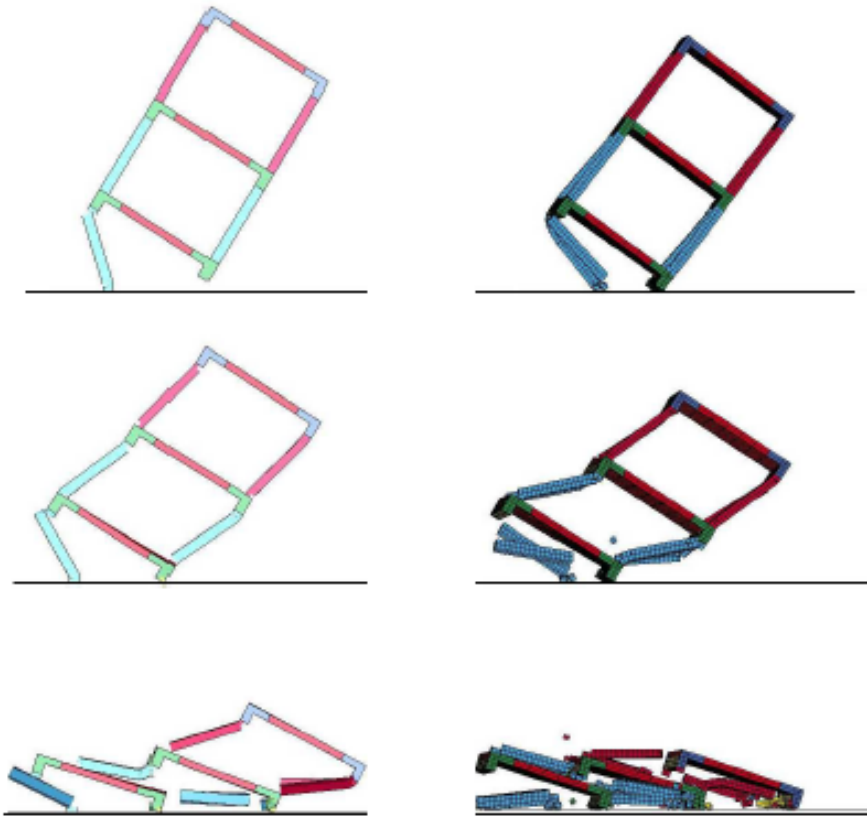


Figure 2.2: Comparison of collapse mechanism using the Element Erosion algorithm, and the Node-Split Algorithm [14]

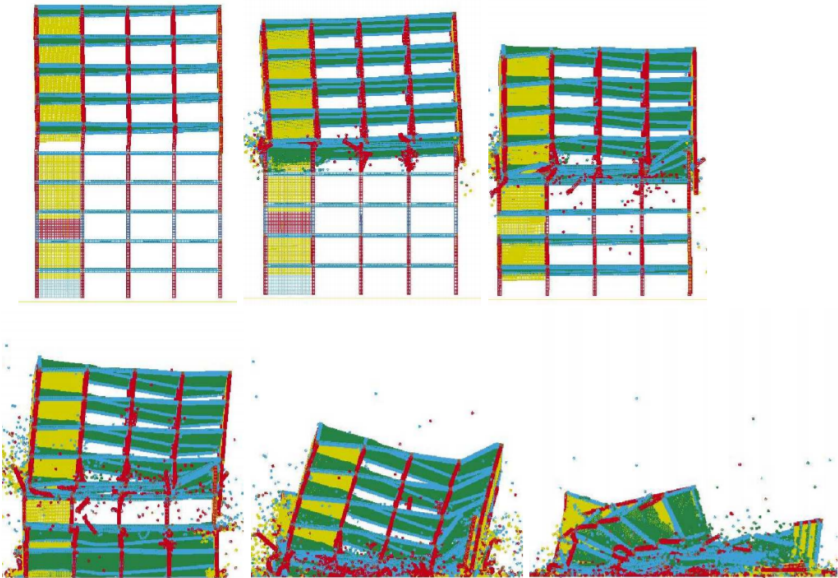


Figure 2.3: Nine storey building evolution of collapse kinematics - using Node-Split algorithm [14]

separation. For this reason different approaches were exploited, and are discussed in further detail in the following sections.

2.2 Discrete Element Method

The Discrete Element Method (DEM), also known as the distinct element method, was developed by Cundall [15], and is used to analyse non-continuum media such as rocks and granular materials. The significance of the method arises in its governing equations where no continuum condition is required, which allows it to be applicable in structural collapse. The DEM was proven very useful in geotechnical engineering since it is very effective in modelling behaviour analysis of discrete media. There have not been many applications of using the discrete method alone for progressive collapse analysis, however. The advantages of the DEM can be significant when coupled with the FEM. The coupled FEM-DEM analysis is presented in Section 2.2.1. Modifications to the DEM for better applicability in progressive collapse problems are presented in the sections 2.2.2 and 2.2.3.

Large displacement using DEM

Qi and Ye applied the DEM to nonlinear dynamic analysis of space frame structures [16]. A frame was divided into rigid spherical elements connected by spring systems between the elements to represent the discretisation using the DEM, and is shown in Figure 2.4. Using this discretisation procedure a dome under an im-

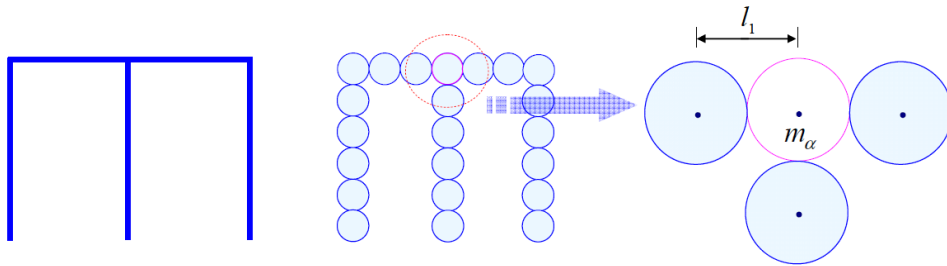


Figure 2.4: Space frame discretisation using DEM [16]

pact load was analysed. The dome geometry is shown in Figure 2.5. The dome is made of 169 nodes, and 462 members. The load is applied at point B shown in Figure 2.5. 3,355 particles were used for the DEM simulations. The deflection

of the dome is presented in Figure 2.6. The analysis was compared to a solution from ANSYS, however no converged solution was obtained due to the large displacements the dome had undergone. Although the results were not demonstrated for progressive collapse, they showed that the DEM is applicable for use in large displacement analysis for continuum problems, and are well applied for nonlinear dynamic analysis of frame structures.

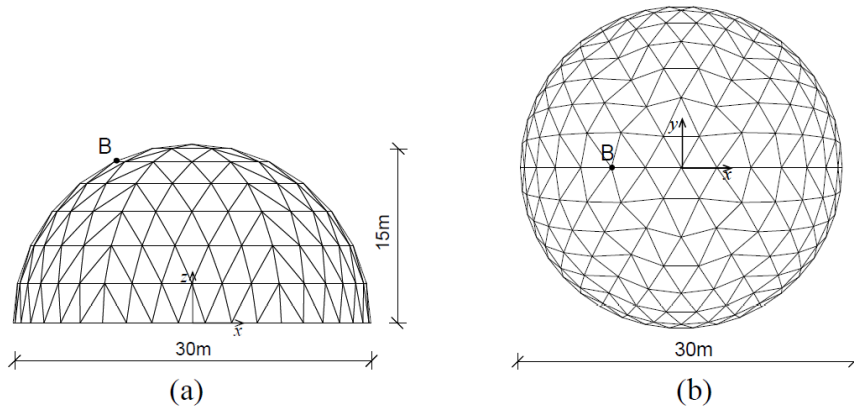


Figure 2.5: Dome initial configuration and dimensions. Point B represents the location of the applied load [16]

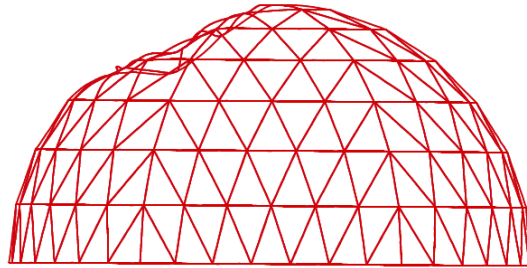


Figure 2.6: Final configuration of Dome after load [16]

Collapse using DEM

Masoero et al. showed the analysis of 3D framed structures that were subject to the removal of one column using the DEM [17]. Their analysis demonstrated that the DEM is a suitable approach for modelling the progressive collapse of structures since the mechanical response and the inter-particle contacts were captured within a robust and efficient simulation scheme [17]. They highlighted that there was a need for a fine mesh to reduce the discretisation errors of the volume representations and discrete local fracture. Also, small time increments were needed

for the contact of stiff elements. The small time increments were due to decreases in α , a uniform dimensionless geometry parameter. A large α signifies a larger element cross-sections which therefore led to stiffer and stronger structures. Figure 2.7 demonstrates the progressive collapse of the framed structures with increasing α over time. The time increments were in the order of $10^{-5} - 10^{-6}$, and the simulation needed to run for a range of at least 2 – 8 real time seconds of collapse, resulting in a very high computational cost.

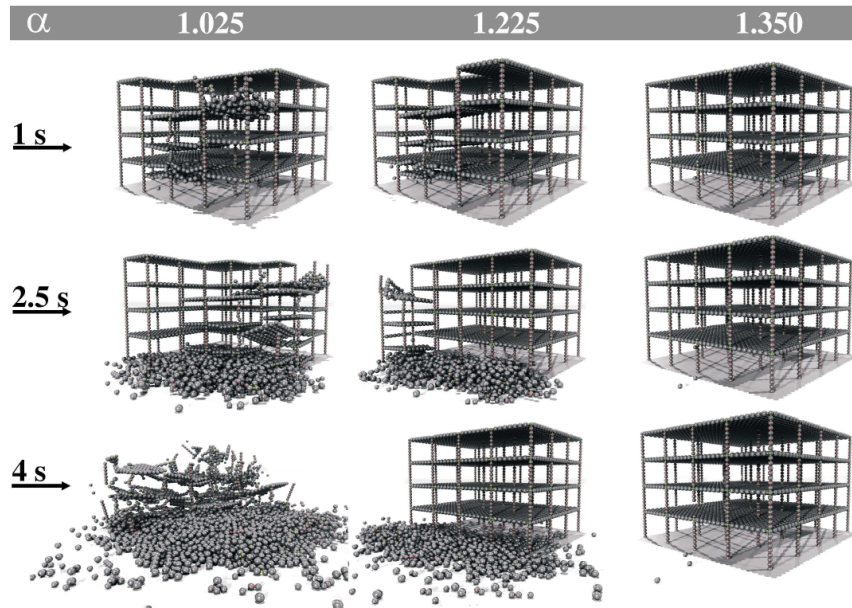


Figure 2.7: Collapse of structures with increasing α using DEM [18]

2.2.1 The Combined Finite Discrete Element Method (FDEM)

Munjiza, Owen, and Bicanic introduced a combined finite-discrete element method for modelling failing, fracture and fragmenting solids in 1990 [19]. The method is based on an incorporation of contact detection and contact interaction aspects of the discrete element method [20]- [22] into the finite element method. The contact interaction requires an accurate representation of the geometry of the contacting domains. This is achieved through discretised contact solutions. The discretisation of the contact and the deformation is assumed to coincide with the finite element discretisation in order to avoid having two separate discretisations [23]-[28]. The discretised contact solutions are used for both contact detection

and contact interaction [28] - [31]. The combined fem-dem has been implemented in many applications and enables simulation of initiation and propagation of a large number of cracks in both 2D and 3D solids [32] -[37].

In [37], a finite strain-finite displacement shell model was developed and incorporated to the combined FEM-DEM. A thin glass shell was analysed using the combined finite-discrete element method, shown in Figure 2.8. The shell has a 50 mm radius, and 1 mm thickness, and is subject to an impact of a 50g impactor at a speed of 5 m/s. The radial cracks are clearly captured. The large blocks of the shell move while the small fragments are being pushed by the impactor. The method is suitable for analysis of progressive fracture and fragmentation of shell structures with large number of cracks.

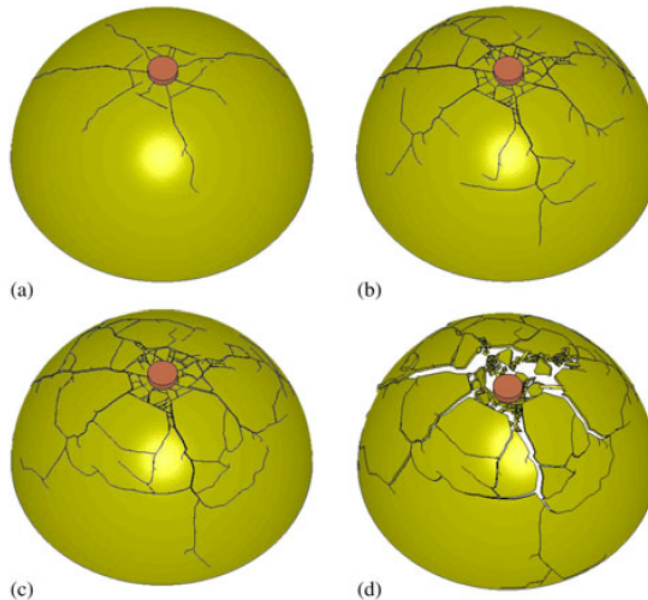


Figure 2.8: Fracture process [37]

2.2.2 Modified Distinct Element Method

Meguro and Hakuno extended the distinct element method to account for fracture of concrete structures [38], calling it the Modified Distinct Element Method (MDEM). The method has been applied to problems of concrete fracture, which could not be solved by the conventional DEM [38]. In MDEM, the concrete gravel and mortar are represented as circular particle elements and nonlinear springs referred as pore-springs. The model can therefore include continuity because of the

pore-spring. The model gradually becomes plastic as the pore-springs are fractured. The MDEM automatically conveys the nonlinearity of the medium. While the pore-springs are unyielding, the medium behaves as a continuum. Once the pore-springs are destroyed then the model starts to behave as a discrete body. Therefore, MDEM can follow the total fracture process, including the discontinuous medium [38]. The MDEM was used to simulate the dynamic fracture behaviour of concrete structures. Figure 2.9 shows the analysis of a frame that is subject to a horizontal impulsive load. The three diagrams in the first row of the figure show the normal compressive force distributions. The left diagram on the top row shows the particle distribution in the initial state. While the diagrams in the bottom row are the mortar spring distributions [38].

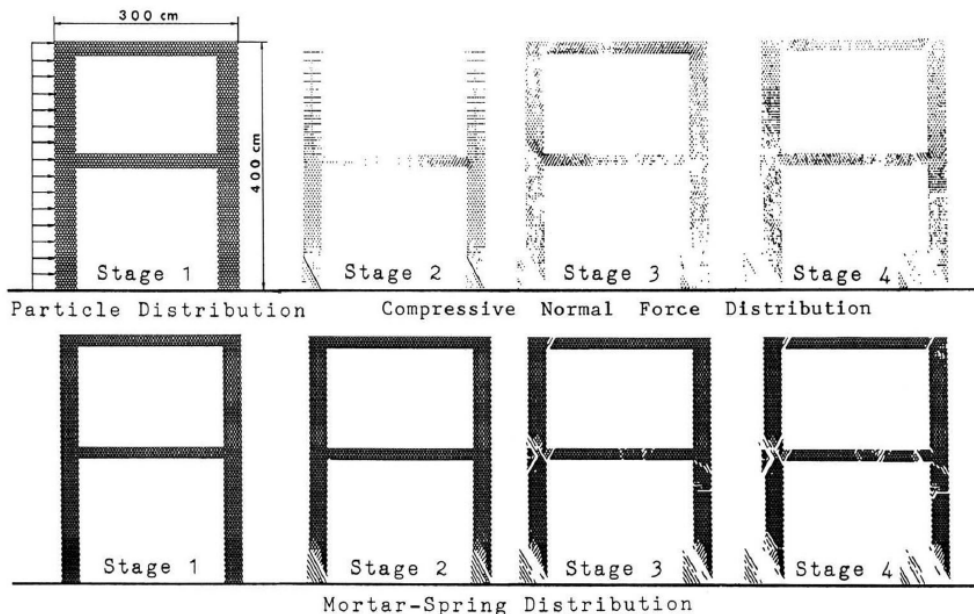


Figure 2.9: Fracture of a rigid-frame concrete structure under horizontal impulsive loading [38]

Figure 2.10 shows the fracture mechanism of the masonry concrete wall subject to horizontal sinusoidal loading. As presented, the fracture occurs within the wall. Cracks appear at stage between the column and the bottom wall. The findings of using the method on different structures with different dynamic loadings showed good agreement with laboratory tests performed on specimens in the past as well as comparison with actual seismic damage that was observed from past earthquakes [38].

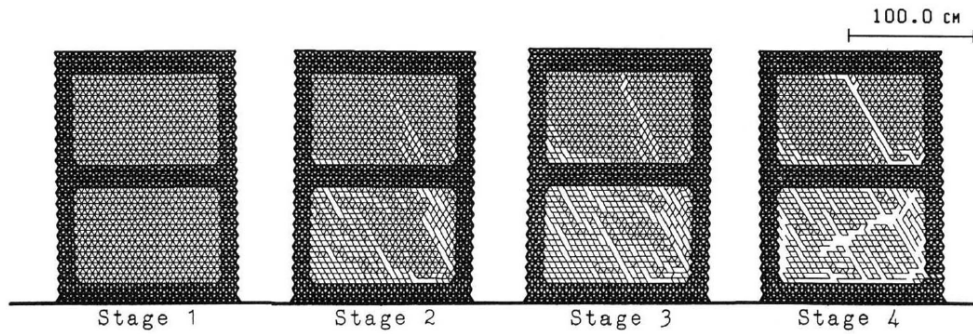


Figure 2.10: Fracture of masonry concrete wall with a frame subject to sinusoidal horizontal loading

2.2.3 Extended Distinct Element Method

Another modification to the original DEM is presented in this section done by Hakuno and Meguro [39][40], and is called the Extended Distinct Element Method (EDEM). The EDEM was developed where pore springs between rigid bodies could deal with continuous media. However the results from the papers explained that the EDEM requires a large calculation time because it involves explicit numerical integration, which requires a very small time step. Therefore the method is computationally very expensive for application to structures [39][40].

Sun et al. proposed a lattice element model for collapse analysis of RC bridges subject to earthquakes by using the EDEM [41]. The lattice method was developed in Reference [42], and it was compared to the conventional FEM. It was found that the analysis required less nodes, and a shorter CPU time [41]. Sun et al. proposed a model similar to the lattice element model in Reference [42], but the difference is in the details of modelling. With the model, the entire process of a structural response to an earthquake, including partial failure and collapse of whole structures was successfully simulated with good accuracy and CPU time [41].

The lattice model is composed of two parts, pre-fracture and post-fracture of the connecting springs. A concrete element consists of lumped masses connected to one another by truss elements (concrete springs), and the reinforcement bars are modelled as a discrete model, and an integrated model is used to describe the main steel bars. The constitutive relations of the springs are presented by one-dimensional material models. After spring fracture, the dynamic characteristics

are described by DEM. The fracture of the concrete and steel are determined by the ultimate strain of the material. A re-contact spring model is also proposed to simulate re-contact between the concrete masses after springs are fractures. The structure gradually changes from elastic to plastic and then to a discontinuous medium as the springs yield. Also, the effect of structural damping is mimicked by a viscous damper that is connected with a truss spring. The damping is assumed as a Rayleigh damping in proportion to the connected mass and spring stiffness. Experimental results of a RC cantilever column subjected to a static horizontal cyclic load was used to verify the lattice model developed, and only in the pre-collapse analysis. The results of this analysis showed acceptable results, for the pre-collapse stage. The use of EDEM with the lattice model allowed to analyse the process from elastic to collapse [41]. It was noted that the results were acceptable but further work is required to improve the accuracy of the simulations before collapse. Also, benchmark simulations must be compared with other existing models to further verify the method.

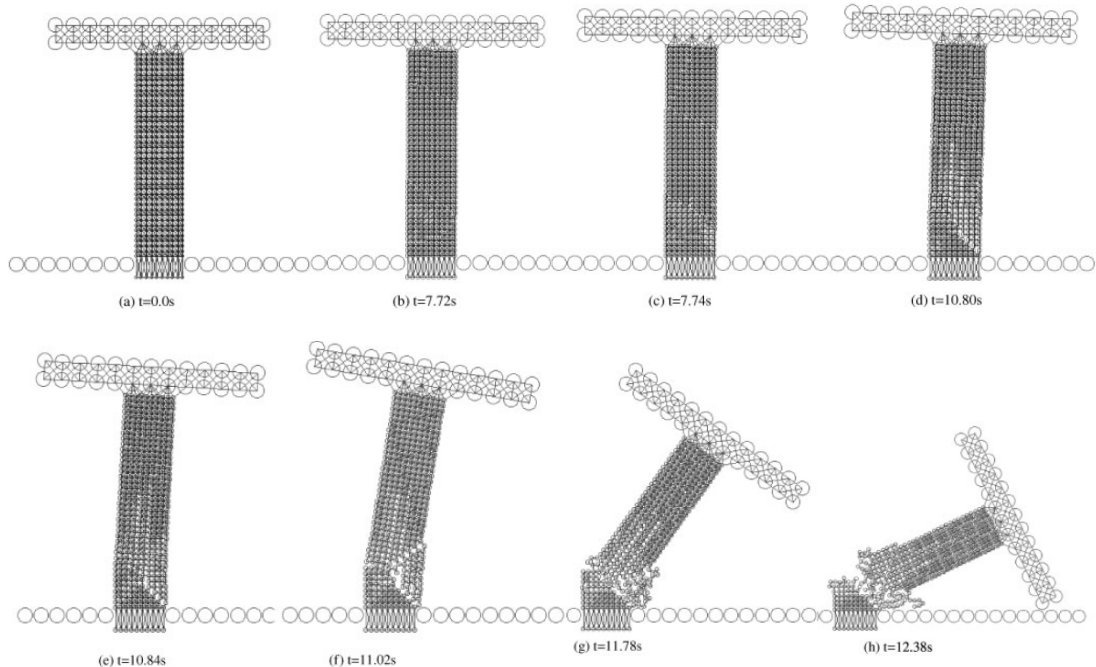


Figure 2.11: Whole collapse of RC column using Lattice EDEM [41]

2.3 Rigid Bodies Spring Models

The Rigid Bodies-Springs Model (RBSM) was developed by Kawai in 1977, as a method that can analyse structures undergoing cracking or sliding. RBSM are discrete models that are composed of rigid elements connected with two types of springs, one resisting dilatation, and the other resisting shearing. They are suitable for the plastic collapse analysis of structures using the concepts of plastic hinges, hinge lines and slip lines introduced by zero spring constraints after yielding [44]. The accuracy and convergence of the linear elastic solutions are not guaranteed [45]. The effects of the finite rotation of the blocks on the collapse load and mechanism were not taken into effect [46]. Accuracy and convergence of linear elastic solutions are not guaranteed because normal strains and stresses in the direction of inter-element boundaries are neglected, except in the case of one-dimensional elements [47].

A. Tingatinga, Kawakami, and M. Shrestha presented a study to model a three dimensional collapse simulation of wooden structures using the RBSM under an earthquake load. The approach of RBSM is to divide the structure into appropriate number of rigid elements connected by spring systems [48]. A nonlinear analysis was carried out by using nonlinear springs to model the large displacements [48].

A. Tingatinga, Kawakami, and M. Shrestha analysed the collapse of typical wooden houses in Japan that are subjected to a doubly amplified 1995 Kobe earthquake. The collapse of this structure is shown in Figure 2.12. A link system used to model the plastic hinges were able to simulate the local failure causing the total collapse of the house. Also, using this method, the weak points of the structure became easily identifiable and reinforcement plans were presented by the authors of this analysis [48].

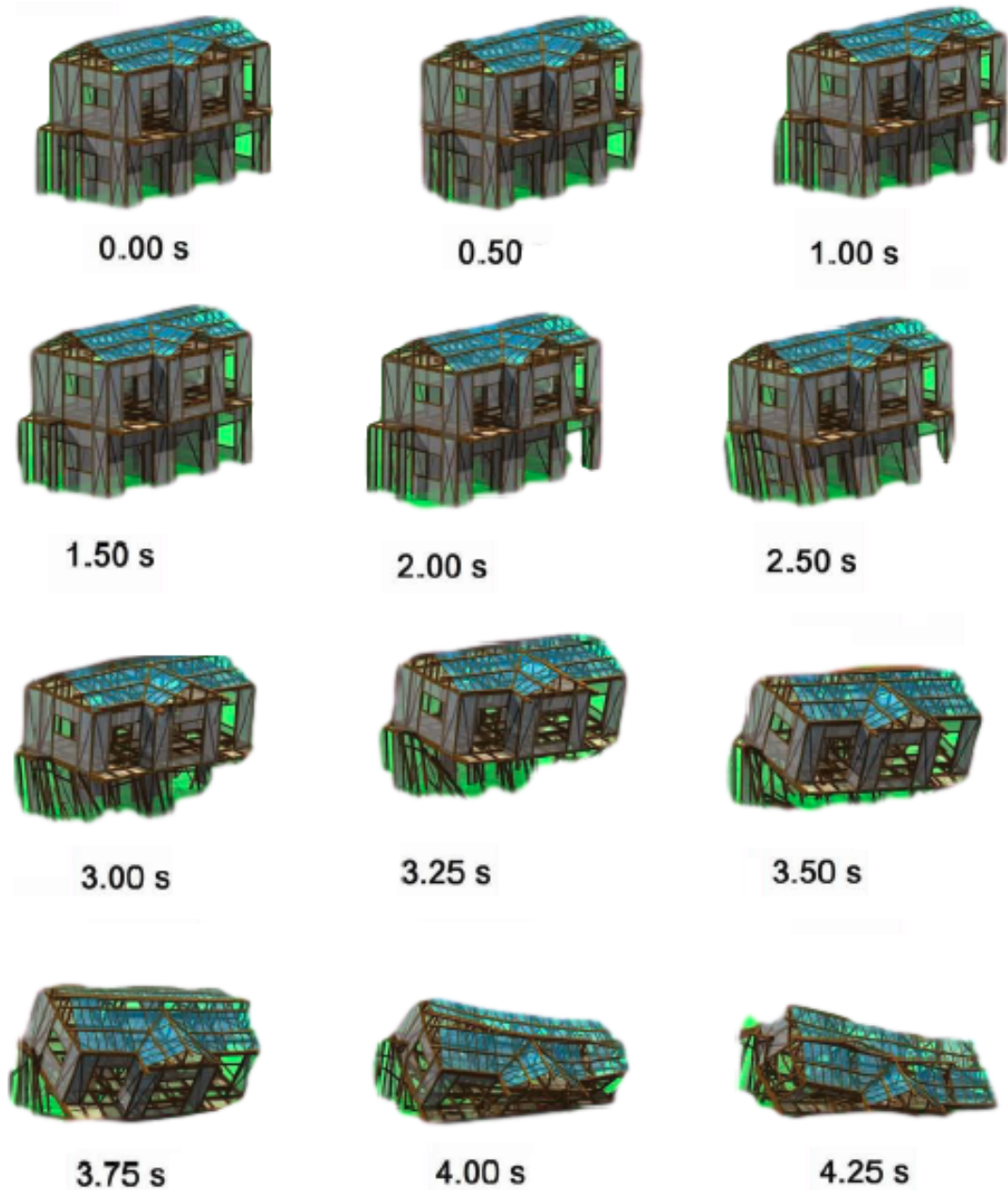


Figure 2.12: Collapse of Wooden House [48]

2.4 Shifted Integration Technique

Toi developed the shifted integration technique for modelling collapse of structures using the finite element method by using linear and cubic finite elements for beams and axisymmetric shells. The strain energy approximations were compared to the RBSM [47]. Toi was the first to find the relations between the locations of numerical integration points and the points with occurrences of plastic hinges.

The linear Timoshenko beam element and the cubic beam element, as well as the RBSM, can be used in plastic collapse analysis by using plastic hinges, where the occurrence of plastic hinges can be controlled by the shifting of locations of the numerical integration points. This shifting technique, defined as the 'shifted integration technique', was shown to be effective in the finite element collapse analysis of framed structure. The shifting formed plastic hinges at the exact locations where they were expected to form, such as at clamped ends, member joints and concentrated load points locations. There was a minor loss in the accuracy of displacement, but the accuracy of the solutions for plastic collapse load had improved. The equivalence conditions between the strain energy approximations of those finite elements and the physical models, the rigid-bodies-spring-models, in which the locations of stress evaluations and plastic hinge formulations are explicitly given, were considered [47].

2.4.1 Adaptive Shifted Integration Technique

Toi and Isobe implemented an adaptation procedure to improve the accuracy of the displacement solution [49]. The numerical integration points in an elastically deformed element are placed at the optimal points for linear analysis, which are the midpoint in the linear Timoshenko beam element, and Gaussian integration points in the cubic beam element. The shifted integration technique is applied immediately after the occurrence of a fully plastic section to form a plastic hinge exactly at that section. This procedure is called the Adaptively Shifted Integration Technique (ASI) [49]. It was found that this method gave accurate results in plastic collapse analysis with low number of elements. Since a low number of elements was attainable, the computational cost of a large-scale plastic collapse analysis is drastically lowered. It was noted that buckling and dynamic collapse problems were to be considered in future analysis.

2.4.2 ASI-Gauss Technique

Further research has been done by Lynn and Isobe to improve the ASI into a modified ASI-Gauss technique, where numerical integration points are placed in a way that the stresses and strains are calculated at the Gaussian integra-

tion points of the two element member. The results showed that the ASI-Gauss technique had higher accuracy than the ASI technique in the elastic range [11]. Lynn and Isobe performed an elasto-plastic analysis under static and dynamic loading, and it was confirmed that "nearly confirmed" solutions were obtained when the number of elements per member is two. Furthermore, due to the difficulty in determining the loads that result from impact in structures, applying the impact loads as nodal forces deems to falsely simulate impact[11]. The impact phenomenon was presented by means of contact between elements involved, using a contact algorithm.

Lynn and Isobe also applied the ASI-Gauss technique a dynamic analysis with high non-linearities and discontinuities, by considering the impact of an aircraft against a 10 storey steel framed structure. The structure was assumed to be made of steel, while the aircraft was made of duralumin. The 10 storied structure was assumed to be fixed at the lower ends. The aircraft had zero degree of inclination from the horizon, and an initial velocity was applied to it [11]. The collapse of the structure due to the impact is shown in Figure 2.13. The results showed a relatively low computational cost with reference to the scale of the problem. The authors mentioned that further study is required to clarify the effect of the size of the aircraft on the impact damage and to evaluate the structural damage caused by the tensile stresses of the columns [11]. The only difference between ASI and ASI-Gauss is in the initial location of the numerical integration point [50].

Katahira et al. implemented the ASI-Gauss technique into a nonlinear finite element code to develop an accurate seismic collapse simulator, including considering structural discontinuities [51]. A comparison of the conventional finite element scheme in which the numerical integration point of each element is fixed at the midpoint, the ASI technique and the ASI-Gauss technique was also presented. Analysis of a frame under seismic excitation was performed. The results showed that the conventional finite element scheme had a very slow convergence and only converges when a 64-element model is used. The ASI technique showed faster convergence results than the finite element scheme, but not with two element model since there is deficiency in accuracy in the elastic stage. The ASI-Gauss technique showed a very fast convergence, since the stress evaluation points are

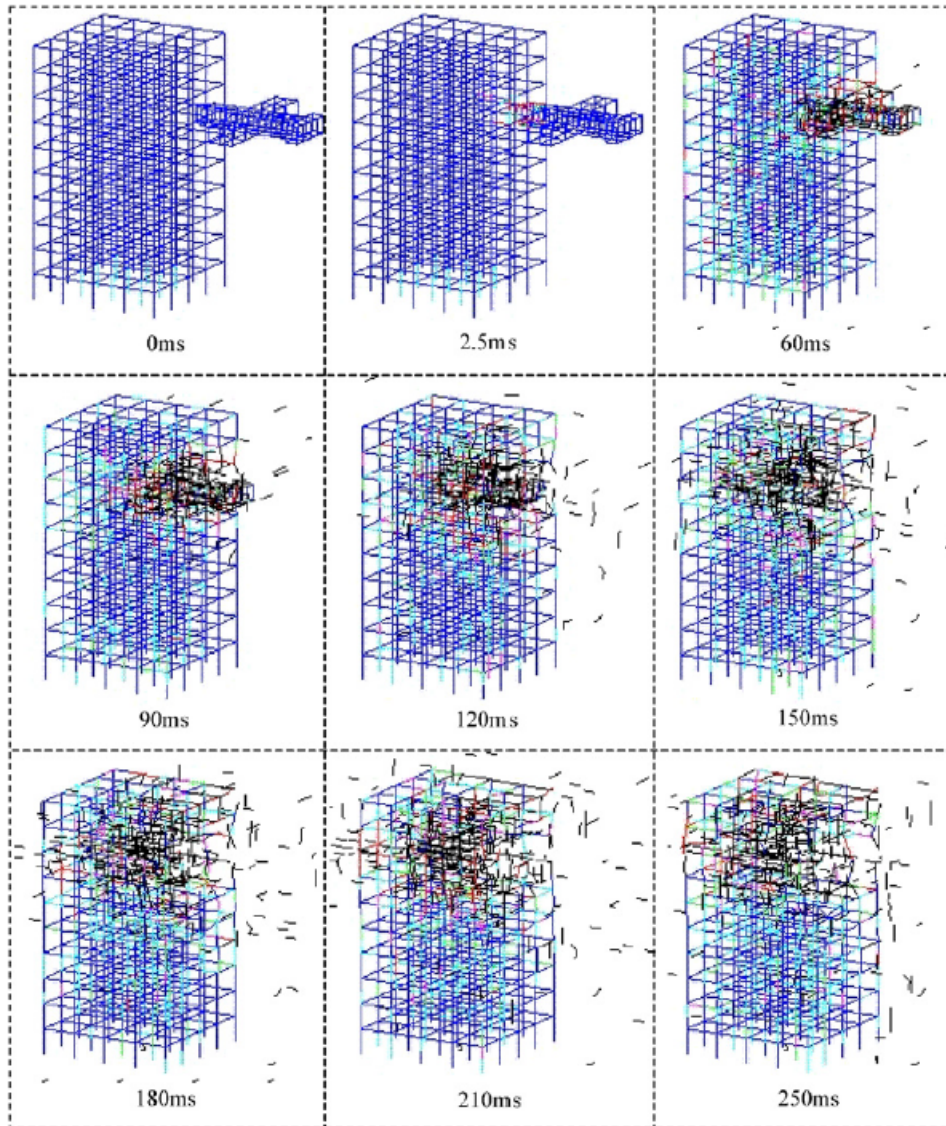


Figure 2.13: Collapse of steel framed structure due to impact of aircraft using the ASI-Gauss technique for analysis [50]

adaptively controlled in both the elastic and plastic ranges. Therefore, the ASI-Gauss technique gave realistic results in a short calculation time; however the damping matrices and the member properties such as local buckling were not considered [51].

Papadrakakis et al. performed a seismic collapse analysis on a 22 storey framed structure using a nonlinear finite element method with the ASI-Gauss technique [52]. The collapse of the frame is shown in Figure 2.14. The code that was used included contact between members. The results showed acceptable results for a numerical estimation of the seismic design of the large-scale framed structures. The authors noted that future work is needed to consider the damping matrices,

and more details in the material properties.

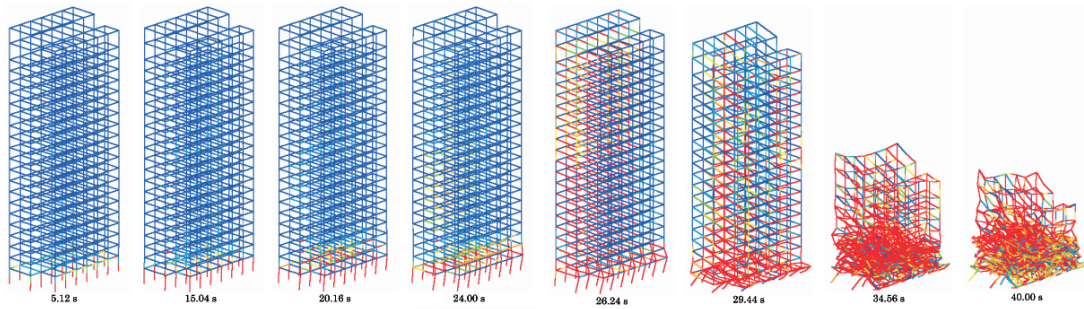


Figure 2.14: Seismic Collapse of Frame using the ASI-Gauss Technique [52]

2.5 Applied Element Method

The Applied Element Method (AEM), was developed by Meguro and Tagel-Din, and is based on combining FEM and DEM. In AEM the members are divided into rigid elements connected through the surface using shear and normal springs, that represent the stresses and strains within the structure. The AEM was developed to aid in the analysis of highly nonlinear behaviour of structures, such as crack initiation, crack propagation, separation of structural elements, rigid body motion of failed elements and total collapse of the structure [6]. Once the stresses in the springs exceed the ultimate yield value, the springs are disconnected and the discontinuous behaviour can be modelled. Several works have been done in this area to implement the collapse behaviour of structures. The Extreme Loading software was developed as a commercial software to analyse structures by using the AEM. The major advantages of the method come from the simplicity in the modelling analysis as well as the low CPU time. The AEM has been successful in modelling the collapse of structures under earthquake loading and blast loads, incorporating highly nonlinear behaviour, such as crack initiation, crack propagation [54].

There have been several modifications to the method as well as applications to progressive collapse of structures during the last 20 years. A commercial software was also developed using the AEM for design and modelling of structures. The commercial software is called the Extreme Loading Software (ELS). Several researchers have used the software to model structures under different loadings

such as blast loadings, earthquakes and impact, and found relatively good results. Some of the applications using ELS are shown below.

2.5.1 Progressive Collapse of RC structures using ELS

Helmy, Salem, and Mourad evaluated the resistance of RC structures designed, according to the American Concrete Institute 318-08 (ACI), to progressive collapse initiated by the loss of a primary vertical support [55]. ELS was used for the analysis of a 10-storey RC frame structure, with seven equal 6 metre bays in each direction. The cases of analysis were based on the General Services Administration Code specifications and were; removal of a corner column, removal of an edge column, removal of an internal column, removal of another internal column near the structure edge, removal of an edge shear wall, removal of an internal shear wall, and removal of an internal core corner. All the removals are to be taken from the ground floor.

The authors first analysed all the mentioned cases in 2D [55] . It was recommended that the consideration of debris collision should not be considered in 2D analysis since, it resulted in a 100 % chance that collapse of the structure would occur, as shown in Figures 2.15 and 2.16.

A 3D analysis was then performed by these authors for all the cases shown in Figure 2.17. All the cases showed partial collapse except for the internal shear wall and core corner cases. These cases did not include slabs. When the slabs were added no collapse took place. This research showed that modelling collapse cases using the ELS was an efficient way and code requirements were met.

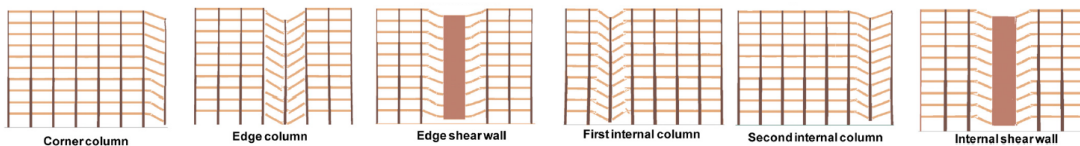


Figure 2.15: 2D Frame analysis [55]

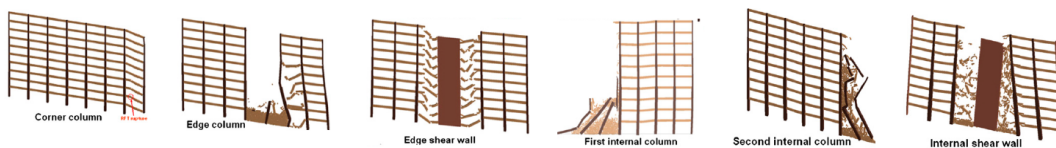


Figure 2.16: 2D Frame analysis while considering debris collision [55]

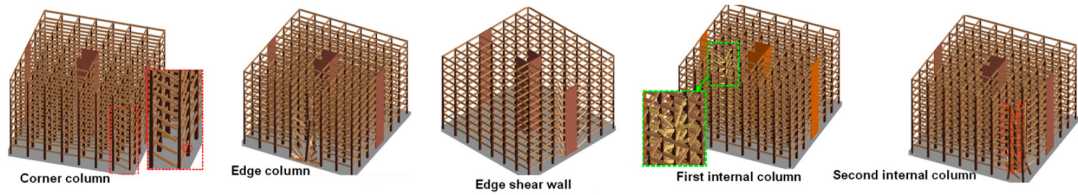


Figure 2.17: 3D Frame analysis [55]

Rahman, Elfouly, and Booth used the alternate path method to analyse a 5-story building for progressive collapse based on the criteria of the Department of Defence [56]. Two different wall sections were removed for the analysis. The ELS was used for the analysis for a 3D nonlinear dynamic analysis. The results showed that composite deck floor slabs were able to bridge over the removed wall sections. Re-distribution of gravity loads was achievable from the slabs to the adjacent wall components. The study provided an understanding of the composite deck floor-cold-formed steel stud bearing walls building system in resisting progressive collapse [56].

Lupoe and Bucur modelled the controlled demolition of a 6-storey reinforced concrete frame [57] using the ELS software. In order to demonstrate a demolition, several steps needed to take place. The sequence in which the elements destruction had to be presented, as well as the time of analysis and time step. Figure 2.18 displays images of the demolition of the building at different stages, compares to the ELS software generated results. The results show good accordance with the real collapse.

As well as using the AEM and its accompanying ELS for modelling structures, researchers have implemented modifications to the method in order to increase its usability and performance. Those modifications are explained in the following sections.

2.5.2 Improved Applied Element Method

AEM has shown high accuracy; however, it is hard to handle non-rectangular cross-sections. The Improved Applied Element Method [58], IAEM, is therefore introduced by Elkholy, Tagel-Din, and Meguro to handle steel materials such as I-beam cross-sections, and U-channels. This was done by using two extensions

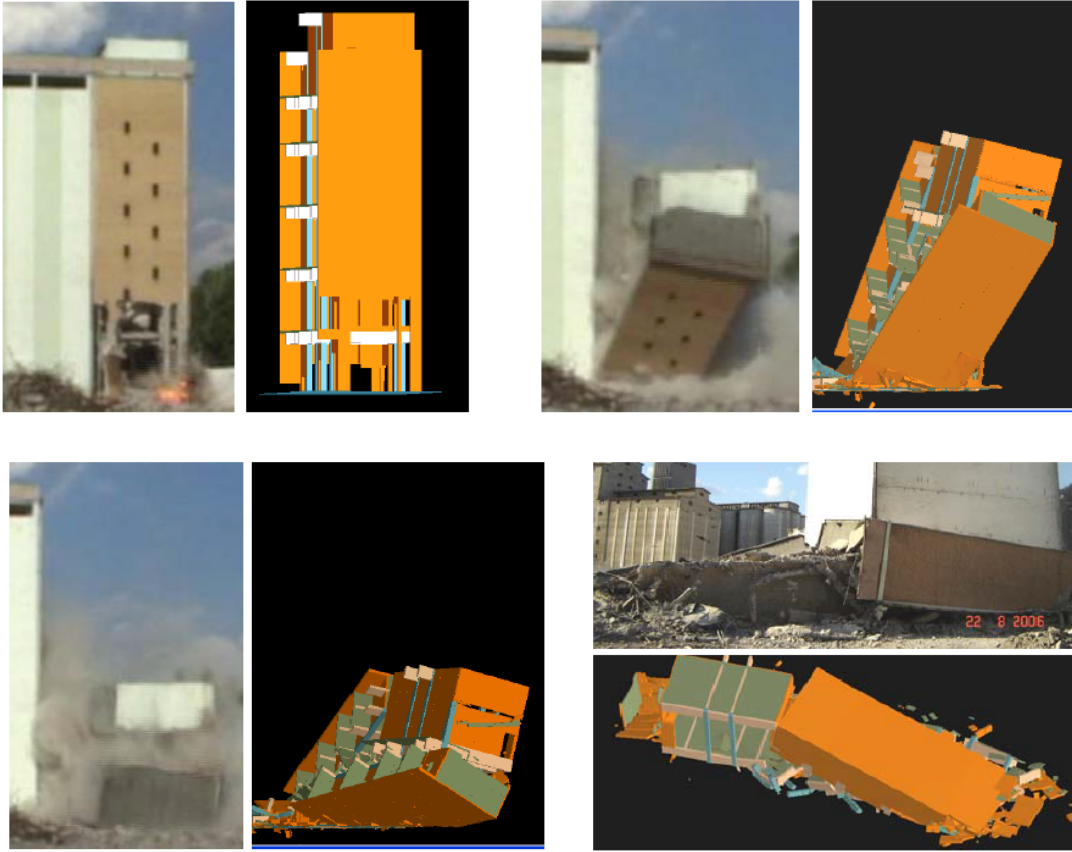


Figure 2.18: Comparison of Real Demolition vs ELS [57]

of the AEM: (1) improving the element type to follow any change in the non-rectangle cross-section thickness and (2) allowing different thickness to be used for calculating normal and shear stiffness [58].

A steel beam with an I cross-section was also analysed by the authors [58]. The results of both AEM and IAEM deflection results are shown in Table 2.1. The results showed that the number of elements required in IAEM is significantly lower than in AEM, as well as the DOF required, with a low change in error difference. This shows that the IAEM can get almost the same results as AEM but 120 times faster and with a model that is 355 times smaller. The error percentage is the difference with the solution obtained from AEM and IAEM compared to the analytical solution.

Table 2.1: Comparison AEM vs IAEM steel beam

	No. elements	No. DOF	CPU Time [sec]	Deflection [mm]	Error %
AEM	6040	17940	120.1	0.9003	+2.31
IAEM	17	45	> 1	0.8657	-1.59

A dynamic analysis of a 15 storey 2D frame was also performed. The columns are I-beams with the same cross-section. Using the IAEM, 870 elements were needed, while 543,750 elements were needed using conventional AEM. The results showed that the first 8 modes of vibration of the structure had less than 1.5% difference with the conventional AEM. This shows that almost the same results were obtained using a significantly different number of elements.

Finally, the collapse analysis of a 30 storey frame structure. The structure was subjected to a localized failure due to fire effect, modelled by changing the steel material properties for the members undergoing fire. Figure 2.19 displays the progressive collapse of the structure.

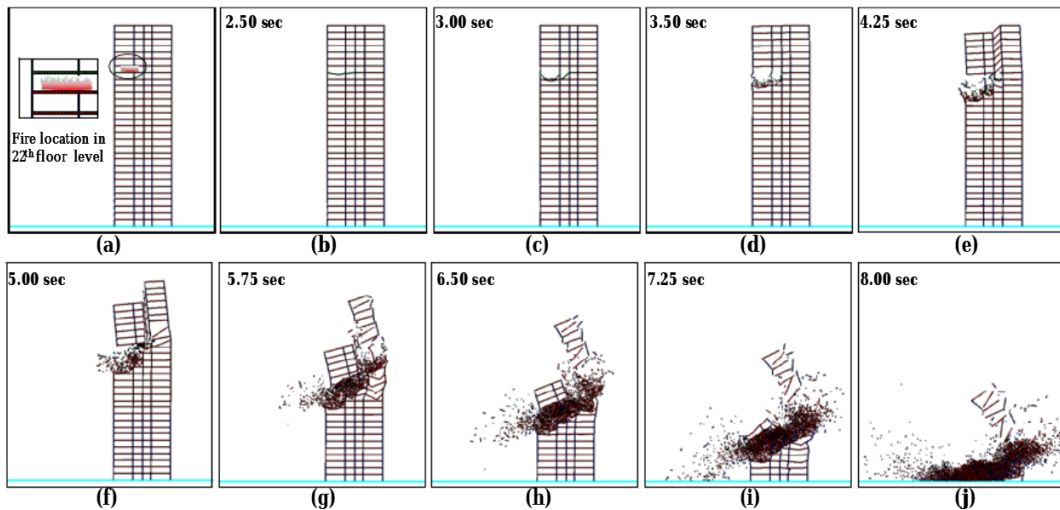


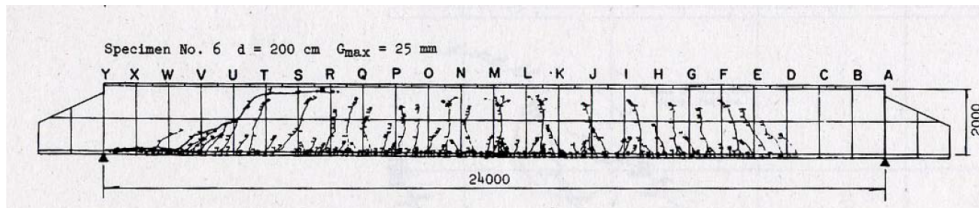
Figure 2.19: IAEM frame collapse [58]

2.5.3 Voronoi Applied Element Method

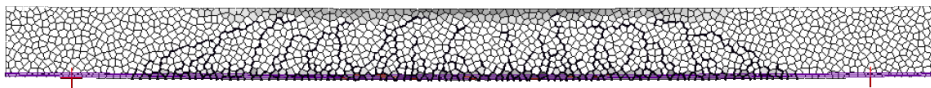
An AEM based on Voronoi shape was developed, where the elements are based on the Voronoi tessellation [59]. Representing the domain within the elements is done by associating the locations of the elements nodes in the physical domain, with the closest member(s) of the element nodal set with respect to Euclidean distance. Using the Voronoi Applied Element Method (VAEM), the element nodes can be placed in the physical domain without any constraint. This gives the advantage of being able to fit any domain shape without considerably reducing the element size in the original AEM. The advantages of the method were that the domain was easy to fit, the numerical Poisson's ratio is not required, varying the element

size is easy to implement and finally, the displacement solution is independent of element size. The formulation of the method is displayed in the next chapter.

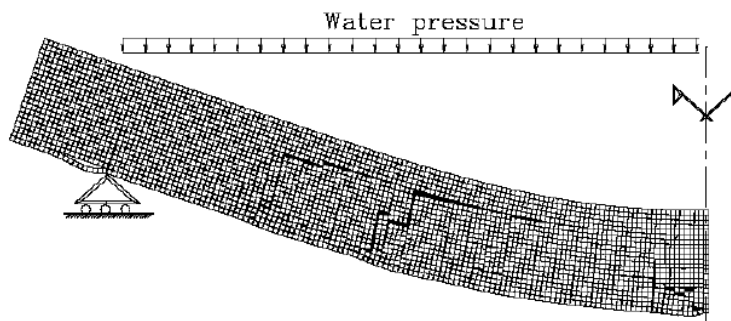
A simulation of a reinforced concrete beam was carried out by Worakanchana and Meguro [59]. Figure 2.20 shows the crack of the beam from the analysis using VAEM. By comparing the crack patterns from the VAEM, the AEM and the actual damage, it was observed that crack patterns from the VAEM were closer to the actual crack patterns rather than the AEM.



(a) Experimental crack pattern [59]



(b) VAEM crack pattern [59]



(c) AEM crack pattern [59]

Figure 2.20: Comparison of crack pattern of beam [59]

2.6 Summary of Methods and Conclusion

Different methods that have been used in modelling the progressive collapse of structures were presented in this chapter. The advantages and disadvantages of the methods mentioned are summarized in Table 2.2.

Table 2.2: Summary of Advantages and disadvantages of Methods

Method	Advantages	Disadvantages
FEM	Accurate in continuum phase	Cannot model element separation
DEM	Can model element separation	Not efficient in continuum
New DEM	Can model continuum behaviour	New method should be coupled with original method
FEM-DEM	Can model collapse of structures by using FEM for small displacements and DEM for large displacements	Complexity in coupled equations
MDEM	Can model continuous media - such as concrete	Explicit - requires large computational time
EDEM	Can model collapse of structures	Explicit - requires large computational time
RBSM	Can analyse structures undergoing cracking or sliding. Suitable for plastic collapse analysis using plastic hinges, hinges lines and slip lines	The accuracy and convergence of the linear elastic solutions are not guaranteed. The effects of rotation are not taken into account.
ASI-Gauss	Gives realistic results in short period of time	Damping matrices are not considered.
AEM	Can model collapse of structures. accurate in continuum and discontinuous phase	-

Table 2.3 shows what the formulations of the methods are based on. The FEM and DEM are considered to have been original formulations, and the remainder of the methods are formulated based on improvements or modifications to the methods. The RBSM, although based on the FEM was one of the first methods to use springs between elements to represent discrete behaviour.

From this review it is clear that there were three different approaches to modelling the collapse of structures behaviour. The first is by combining the finite element method and the discrete element method, where the finite element method was used for the continuum phase, and the discrete element method models in the discontinuous phase.

Another approach that was found in most of the presented solution models is the use of springs between elements. The rigid bodies spring model was one of the

Table 2.3: Summary of methods formulation basis

Method	Formulation
FEM	Original
Discrete element method	Original
FEM-DEM	Coupling between FEM and DEM
New Distinct Element method	Based on DEM
RBSM	Original Springs based method
EDEM	Based on RBSM and DEM
MDEM	Based on RBSM and DEM
ASI-Gauss	Based on FEM and use of plastic hinges
AEM	Based on RBSM

first methods to use springs between elements for analysis of collapse behaviour. The method is based on using springs between rigid elements. When the elements springs fail, the elements behave as discrete elements. The extended distinct element method used pore springs between rigid bodies. The disadvantage of the method is that it required large computational cost. A modification to the method was presented by implementing the lattice element model in the extended distinct element method. The method successfully modelled the collapse of reinforced concrete structures, but further verifications to the method were required. The modified distinct element method also used pore springs between elements to model the progressive collapse behaviour of structures. The applied element method can accurately model the behaviour of a structure from no loading to total failure, since the elements can be separated and act both as continuum when connected together with springs, and discrete when they separate.

The final approach, presented in the shifted integration technique, is based on finding the exact location of plastic hinges.

It is clear that the methods are related to one another and have been derived by creating different modifications that allowed the presence of different types of results. In the next chapter the formulation of the methods is presented.

Chapter 3

Numerical Methods Approaches

This chapter is a summary of the formulations of some methods mentioned in Chapter 2. The purpose is to demonstrate the evolution of the formulations, to have a full understanding of the method used for modelling the collapse of structures. Also, it is important to comprehend the difference between the computational algorithms of the methods for a clearer view on the advantages and disadvantages of each as well as their relationships to one another. The methods formulations presented in this chapter are the finite element method, the discrete model for continuum, the Lattice model using the Extended distinct element method, the rigid bodies spring models, and the shifted integration technique. The formulation of the Applied Element Method is presented in the next chapter.

3.1 Mechanics of Continuous Bodies

Before describing the numerical methods, a couple of principles must first be introduced. The mathematical models of structural problems are generated from differential equations that satisfy the whole domain. These equations are formulated from the three fundamental laws of mechanics; conservation of mass, conservation of linear momentum, and conservation of angular momentum [60]. For Lagrangian description of problems, the conservation of mass is satisfied and the conservation of angular momentum is symmetric, leaving the conservation of linear momentum to be the leading equation that must satisfy the force equilib-

rium. The principle of conservation of linear momentum can be derived either by using Newton's Second Law, or the principle of virtual displacements [61]. The use of Newton's laws required the isolation of a volume element of a structure with all its applied and reactive forces. The sum of the static and dynamic forces and moments acting on the element is then set to zero in order to retrieve the equations of motion. For a simple mechanical system, this approach may be viable since the free-body diagram can be set up, and it is a simple way to derive the governing equations. However, this approach is more inconvenient for more complicated systems, and the type of boundary conditions are not always clear [61]. The energy principle is one of the simplest theories that can formulate a structural problem, since, if the structural system is in equilibrium, then it has potential energy [60]. In the energy approach the total work done in the volume element due to the actual forces moving through the virtual displacements that are consistent with the geometric constraints are set to zero to obtain the equations of motion [61]. The energy approach produces both the equations of motions and the force boundary conditions, as well as the form of the variables related to the boundary conditions. The energy expressions are also effective in obtaining approximate solutions by direct variational methods, such as the finite element method [61].

3.1.1 External and Internal Virtual Work

The work done by a force that acts on a material point and moves through a displacement, is defined by the projection of the force in the direction of the displacement times the magnitude of the displacement [61]. The work done through virtual displacements is called virtual work. The virtual work done by actual forces F in a body Ω is given by Equation 3.1.

$$\delta W = \int_{\Omega} F \cdot \delta u dv \quad (3.1)$$

where dv is the volume element in the material body Ω [61], δu is the virtual displacement. The virtual work done by virtual forces moving through the actual

displacement u is;

$$\delta W^* = \int_{\Omega} \delta F \cdot \delta u dv \quad (3.2)$$

The virtual work done by externally applied forces moving through their respective virtual displacements is called the *external virtual work* denoted by δW_E . Similarly, the virtual work done by internal forces moving through the virtual displacements is called *internal virtual work*, denoted by δW_I .

External Virtual Work

The external virtual work due to virtual displacements δu in a body Ω subjected to body forces f per unit volume and surface tractions T per unit area of the boundary Γ_{Ω} is given by 3.3.

$$\delta W_E = - \left(\int_{\Omega} f \cdot \delta u dv + \int_{\Gamma_{\Omega}} T \cdot \delta u ds \right) \quad (3.3)$$

where ds denotes the surface element. The first integral extends over the volume of the body, while the second integral extends over the surface of the body. The negative sign indicates that the work is performed on the body. The external virtual work done due to virtual body forces is given by;

$$\delta W_E^* = - \left(\int_{\Omega} \delta f \cdot u dv + \int_{\Gamma_u} \delta_t \cdot u ds \right) \quad (3.4)$$

Internal Virtual Work

Internal stresses are experienced in bodies when they deform due to forces applied. The movement of the particles in the body can be represented in terms of strains [61]. The internal virtual work done due to the virtual displacement can be computed. Assuming an infinitesimal material element of volume $dv = dx_1 dx_2 dx_3$, experiencing small virtual strains $\delta \varepsilon_{ij}$, shown in Equation 3.5 due to the virtual displacements δu_i ; the work done by the force due to the actual stress σ_{11} , in

moving through the virtual displacement $\delta u_1 = \delta \varepsilon_{11} dx_1$ is shown in Equation 3.9.

$$\delta \varepsilon_{ij} = \frac{1}{2} \left(\frac{\partial \delta u_i}{\partial x_j} + \frac{\partial \delta u_j}{\partial x_i} \right) \quad (3.5)$$

$$(\sigma_{11} dx_2 dx_3)(\delta \varepsilon_{11} dx_1) = \sigma_{11} \delta \varepsilon_{11} dx_1 dx_2 dx_3 \quad (3.6)$$

The work done by the force due to stress σ_{12} in the shearing body from Figure 3.1 is

$$(\sigma_{12} dx_2 dx_3)(2\delta \varepsilon_{12} dx_1) = 2\sigma_{12} \delta \varepsilon_{12} dx_1 dx_2 dx_3 \quad (3.7)$$

Therefore the total virtual work done by the forces due to all the stresses is

$$(\sigma_{11} \delta \varepsilon_{11} + \sigma_{22} \delta \varepsilon_{22} + \sigma_{33} \delta \varepsilon_{33} + 2\sigma_{12} \delta \varepsilon_{12} + 2\sigma_{13} \delta \varepsilon_{13} + 2\sigma_{23} \delta \varepsilon_{23}) dx_1 dx_2 dx_3 = \sigma_{ij} \delta \varepsilon_{ij} dv \quad (3.8)$$

The total internal virtual work done δW_I is obtained by integrating Equation 3.8 over the volume of the body, giving

$$\delta W_I = \int_{\Omega} \sigma_{ij} \delta \varepsilon_{ij} dv = \int_{\Omega} \sigma : \delta \varepsilon dv \quad (3.9)$$

where “:” is the double dot product.

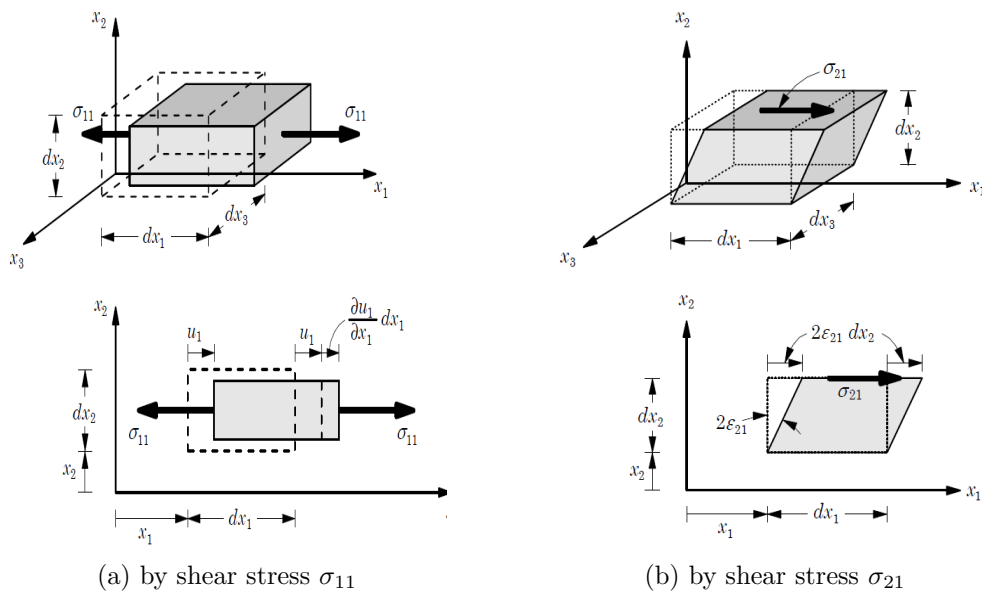


Figure 3.1: Virtual Work Done [61]

3.2 Energy Principle Equations

3.2.1 The Principle of Virtual Displacements

The virtual work due to virtual displacements is the work done by the actual forces required in moving particles of a body through virtual displacements. Considering a rigid body with applied forces F_1, F_2, \dots , and the points subject to those forces undergo virtual displacements $\delta u_1, \delta u_2, \dots$, respectively. The external virtual work done by the virtual displacements is given by Equation 3.10 [61].

$$\delta W_E = -[F_1 \cdot \delta u_1 + F_2 \cdot \delta u_2 + \dots + F_n \cdot \delta u_n] = -F_i \cdot \delta u_i \quad (3.10)$$

The internal virtual work done $\delta W_I = \delta U$ is zero because a rigid body does not undergo any strains. Thus,

$$\delta W_E = -F_i \cdot \delta u_i = -\left(\sum_{i=1}^n F_i\right) \cdot \delta u \quad \text{and} \quad \delta W_I = 0 \quad (3.11)$$

Now considering a body β in equilibrium under body forces \mathbf{f} and boundary forces \mathbf{T} , and the initial configuration of the body C^0 , with volume denoted by Ω . \mathbf{u} is the displacement vector corresponding to the equilibrium configuration of the body, and σ and ε are the stress and strain tensors respectively. In order to determine the equations that govern the equilibrium configuration \mathbf{C} , the body should experience a virtual displacement δu from the true configuration. The principle of virtual work can be stated as: *If a continuous body is in equilibrium, the virtual work of all actual forces in moving through a virtual displacement is zero*, given by Equation (3.12)

$$\delta W_I + \delta W_E = \delta W = 0 \quad (3.12)$$

The principle of virtual displacements for deformable body can be expressed as Equation (3.13)

$$\int_{\Omega} \sigma : \delta \varepsilon dv - \int_{\Omega} \rho f \cdot \delta u dv - \int_{\Gamma_{\sigma}} T \cdot \delta u ds = 0 \quad (3.13)$$

3.2.2 The Principle of Minimum Potential Energy

Consider a body in static equilibrium under an applied force. Due to the load, the structure experiences deformation, described by $u(x) = [u_1, u_2, u_3]^T$. The structure resists deformation by generating internal forces, where each internal force is proportional to the amount of deformation. If the internal force is smaller than the load, then the structure continues to deform to equilibrate the forces. The internal force generated during deformation may be considered as the energy stored in the structure. As the structure deforms, the internal force increases as well as the energy in the structure. The stored energy is referred to as the strain energy and is shown in Equation 3.14.

$$U(u) = \frac{1}{2} \iint_{\Omega} \sigma(u) : \varepsilon(u) d\Omega \quad (3.14)$$

where the components of the strain tensor are defined as;

$$\varepsilon_{ij}(u) = \frac{1}{2} \left(\frac{\delta u_i}{\delta x_j} + \frac{\delta u_j}{\delta x_i} \right) = \frac{1}{2} (u_{i,j} + u_{j,i}) \quad (3.15)$$

where $u_{i,j} = \delta u_i / \delta x_j$. The strain energy $U(u)$ is the energy required to produce the displacement u . Since $U(u)$ does not depend on the deformation path in elastic problems, it is a function of the displacement only. If the forces are applied to the structure, and the deformation is in the direction of the applied forces, then the work is done by those applied forces, and can be defined as

$$W(u) = \iint_{\Omega} u \cdot f d\Omega \quad (3.16)$$

If the applied force is conservative (the load is independent of deformation), then the work done is a negative value of the potential energy generated by the loads. And since the strain energy $U(u)$ is independent of the path, it is the potential energy that is stored in the structure. The potential energy is the difference between the strain energy and the work done, and is written as

$$\Pi(u) = U(u) - W(u) = \frac{1}{2} \iint_{\Omega} \sigma(u) : \varepsilon(u) d\Omega - \iint_{\Omega} u \cdot f d\Omega \quad (3.17)$$

3.3 Finite Element Method

Many problems are expressed in partial differential equations that cannot be solved with analytical methods. Thus, an approximation is required, and can be based on different types of discretisation. The discretisation methods approximate the differential equations with numerical model equations, which can be solved using numerical methods. Since the solution can have a complicated expression, the finite element can be used [62].

Figure 3.2 is used to interpolate the two nodes ξ_1 and ξ_2 . The element is the segment between the two nodes, and the values of the function are f_1 and f_2 . Approximating the function at an arbitrary point in the element gives

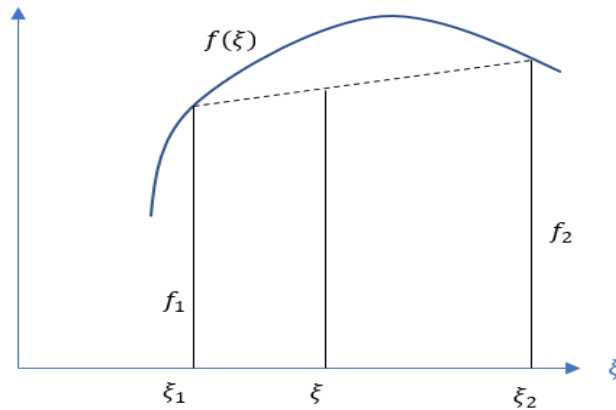


Figure 3.2: Interpolation of a one-variable function

$$f(\xi) = \frac{\xi_2 - \xi}{\xi_2 - \xi_1} f_1 + \frac{\xi - \xi_1}{\xi_2 - \xi_1} f_2 \quad (3.18)$$

The interpolation can be written in the form

$$f(\xi) = N_1(\xi) f_1 + N_2(\xi) f_2 \quad (3.19)$$

where N_1 and N_2 are functions of ξ and are known as the shape functions. The shape functions must satisfy the following conditions

$$N_1(\xi_1) = 1, \quad N_1(\xi_2) = 0 \quad (3.20)$$

$$N_2(\xi_1) = 0, \quad N_2(\xi_2) = 1 \quad (3.21)$$

The shape functions are shown in Figure 3.3.

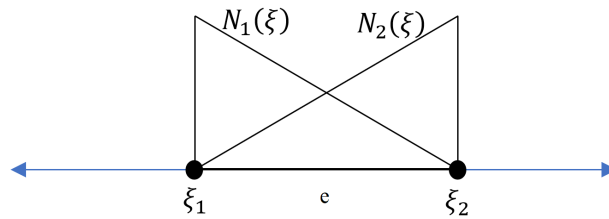


Figure 3.3: 1D finite element e with shape functions

3.3.1 Isoparametric mapping

A solid component in the (x, y) plane should be divided into finite elements. For the scope of this thesis quadrilateral elements are considered. First, a unit square on plane (ξ, η) must be mapped to a quadrilateral on plane (x, y) . The unit square is a reference element. It is necessary to use a reference element so that different shape functions are not needed to be built for different elements. Assume the four nodes of the quadrilateral are labelled as 1, 2, 3, 4 in the counter-clockwise direction. Thus on the (x, y) plane the four nodes have coordinates (x_1, y_1) , (x_2, y_2) , (x_3, y_3) , (x_4, y_4) . The quadrilateral in both planes is shown in Figure 3.4. Mapping a point in the (ξ, η) to a point in the (x, y) plane gives

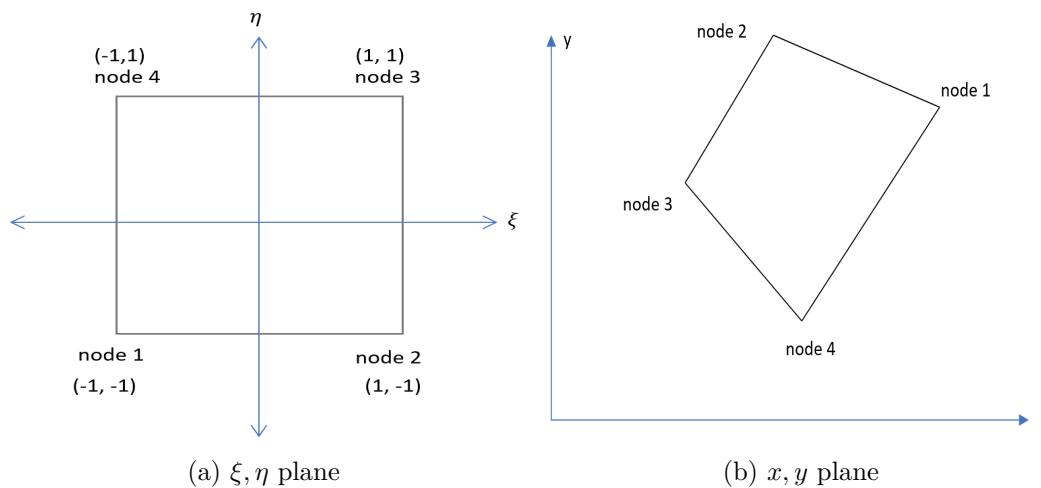


Figure 3.4: Quadrilateral in different planes

$$\begin{aligned}
 x &= N_1x_1 + N_2x_2 + N_3x_3 + N_4x_4 \\
 y &= N_1y_1 + N_2y_2 + N_3y_3 + N_4y_4
 \end{aligned}
 \tag{3.22}$$

Equation 3.22 can be written as

$$x(\xi) = \sum_{i=1}^n N_i(\xi)x_i \quad (3.23)$$

where n is the number of nodes in the element, for a linear quadrilateral $n = 4$. Now the shape functions must be determined. On the plane (ξ, η) , N_1 should be 1 at node 1 and zero at the other three nodes. The four shapes functions are

$$N_1 = \frac{1}{4}(1 - \xi)(1 - \eta) \quad (3.24)$$

$$N_2 = \frac{1}{4}(1 + \xi)(1 - \eta) \quad (3.25)$$

$$N_3 = \frac{1}{4}(1 + \xi)(1 + \eta) \quad (3.26)$$

$$N_4 = \frac{1}{4}(1 - \xi)(1 + \eta) \quad (3.27)$$

The mapping is called isoparametric mapping because the shape functions are used for interpolating geometry and displacements [60]. The displacements of the four nodes are presented in vector \mathbf{q}

$$\mathbf{q} = [u_1 \ v_1 \ u_2 \ v_2 \ u_3 \ v_3 \ u_4 \ v_4]^T \quad (3.28)$$

$$\mathbf{N} = \begin{bmatrix} N_1 & 0 & N_2 & 0 & N_3 & 0 & N_4 & 0 \\ 0 & N_1 & 0 & N_2 & 0 & N_3 & 0 & N_4 \end{bmatrix} \quad (3.29)$$

The displacement vector is

$$\mathbf{u} = \mathbf{N}\mathbf{q} \quad (3.30)$$

$$u(\xi) = \sum N_i(\xi)u_i \quad (3.31)$$

Representing the strain field in terms of the nodal displacements, $\boldsymbol{\varepsilon} = \mathbf{B}\mathbf{q}$, where \mathbf{B} is a matrix depending on (ξ, η) .

3.3.2 Jacobian of the Mapping

The displacement gradient on the (ξ, η) plane is

$$\begin{bmatrix} \frac{\partial u}{\partial \xi} \\ \frac{\partial u}{\partial \eta} \end{bmatrix} = \frac{1}{4} \begin{bmatrix} -(1-\eta) & (1-\eta) & (1+\eta) & -(1+\eta) \\ -(1-\xi) & (1-\xi) & (1+\xi) & -(1+\xi) \end{bmatrix} \begin{bmatrix} u_1 \\ u_2 \\ u_3 \\ u_4 \end{bmatrix} \quad (3.32)$$

Using the chain rule for converting the gradient on (ξ, η) to (x, y)

$$\begin{bmatrix} \frac{\partial u}{\partial \xi} \\ \frac{\partial u}{\partial \eta} \end{bmatrix} = \begin{bmatrix} \frac{\partial x}{\partial \xi} & \frac{\partial y}{\partial \xi} \\ \frac{\partial x}{\partial \eta} & \frac{\partial y}{\partial \eta} \end{bmatrix} \begin{bmatrix} \frac{\partial u}{\partial x} \\ \frac{\partial u}{\partial y} \end{bmatrix} \quad (3.33)$$

The two by two matrix is the Jacobian matrix \mathbf{J} of the map (ξ, η) to (x, y) . The elements of the Jacobian matrix are calculates as

$$J_{11} = \frac{\partial x}{\partial \xi} = \frac{1}{4}(1-\eta)(-x_1+x_2) + \frac{1}{4}(1+\eta)(x_3-x_4) \quad (3.34)$$

$$J_{12} = \frac{\partial y}{\partial \xi} = \frac{1}{4}(1-\eta)(-y_1+y_2) + \frac{1}{4}(1+\eta)(y_3-y_4) \quad (3.35)$$

$$J_{21} = \frac{\partial x}{\partial \eta} = \frac{1}{4}(1-\xi)(-x_1+x_4) + \frac{1}{4}(1+\xi)(-x_2+x_3) \quad (3.36)$$

$$J_{22} = \frac{\partial y}{\partial \eta} = \frac{1}{4}(1-\xi)(-y_1+y_4) + \frac{1}{4}(1+\xi)(-y_2+y_3) \quad (3.37)$$

Using Cramer's rule to find $\frac{\partial u}{\partial x}$ and $\frac{\partial u}{\partial y}$ from Equation 3.33, gives

$$\begin{bmatrix} \frac{\partial u}{\partial x} \\ \frac{\partial u}{\partial y} \end{bmatrix} = \frac{\begin{vmatrix} \frac{\partial u}{\partial \xi} & \frac{\partial y}{\partial \xi} \\ \frac{\partial u}{\partial \eta} & \frac{\partial y}{\partial \eta} \end{vmatrix}}{\begin{vmatrix} \frac{\partial x}{\partial \xi} & \frac{\partial y}{\partial \xi} \\ \frac{\partial x}{\partial \eta} & \frac{\partial y}{\partial \eta} \end{vmatrix}} = \frac{\begin{vmatrix} \frac{\partial u}{\partial \xi} & J_{12} \\ \frac{\partial u}{\partial \eta} & J_{22} \end{vmatrix}}{\begin{vmatrix} J_{11} & J_{12} \\ J_{21} & J_{22} \end{vmatrix}} = \frac{1}{\det \mathbf{J}} \begin{vmatrix} \frac{\partial u}{\partial \xi} & J_{12} \\ \frac{\partial u}{\partial \eta} & J_{22} \end{vmatrix} \quad (3.38)$$

$$\begin{bmatrix} \frac{\partial u}{\partial x} \\ \frac{\partial u}{\partial y} \end{bmatrix} = \frac{1}{\det \mathbf{J}} \left(J_{22} \frac{\partial u}{\partial \xi} - J_{12} \frac{\partial u}{\partial \eta} \right) \quad (3.39)$$

where $\frac{\partial u}{\partial \xi}$ and $\frac{\partial u}{\partial \eta}$ are known from Equation 3.32. Similar expressions can be formed for $\frac{\partial v}{\partial x}$ and $\frac{\partial v}{\partial y}$. The strain vector is

$$\boldsymbol{\varepsilon} = \left[\left(\frac{\partial u}{\partial x} \right), \left(\frac{\partial v}{\partial y} \right), \left(\frac{\partial u}{\partial y} + \frac{\partial v}{\partial x} \right) \right]^T \quad (3.40)$$

and since

$$\boldsymbol{\varepsilon} = \mathbf{B}\mathbf{q} \quad (3.41)$$

$$\delta\boldsymbol{\varepsilon} = \mathbf{B}\delta\mathbf{q} \quad (3.42)$$

The entries to the \mathbf{B} matrix are

$$B_{11} = \frac{1}{4\det\mathbf{J}} [-J_{22}(1 - \eta) + J_{12}(1 - \xi)] \quad (3.43)$$

Now the stress should be presented in terms of the nodal displacements. The in-plane stresses are $\boldsymbol{\sigma} = [\sigma_x, \sigma_y, \sigma_{xy}]^T$. The stress is related to the strain as

$$\boldsymbol{\sigma} = \mathbf{D}\boldsymbol{\varepsilon} \quad (3.44)$$

Under plane strain conditions, this can be explicitly be represented as

$$\begin{bmatrix} \sigma_x \\ \sigma_y \\ \sigma_{xy} \end{bmatrix} = \frac{E}{(1 + \nu)(1 - 2\nu)} \begin{bmatrix} 1 - \nu & \nu & 0 \\ \nu & 1 - \nu & 0 \\ 0 & 0 & 0.5 - \nu \end{bmatrix} \begin{bmatrix} \varepsilon_x \\ \varepsilon_y \\ \varepsilon_{xy} \end{bmatrix} \quad (3.45)$$

From Equation 3.41

$$\boldsymbol{\sigma} = \mathbf{D}\mathbf{B}\mathbf{q} \quad (3.46)$$

Recall the internal work done from Equation 3.9. Substituting the terms from Equation 3.42 and 3.46, results in the internal virtual work as

$$\partial W_I = \delta\mathbf{q}^T \mathbf{k}\mathbf{q} \quad (3.47)$$

where \mathbf{k} is an integral over the volume of the element and presented as

$$\mathbf{k} = \int_{\Omega} \mathbf{B}^T \mathbf{D} \mathbf{B} dV \quad (3.48)$$

Writing the internal virtual work in terms of the global degrees of freedom gives

$$\partial W_I = \delta \mathbf{Q}^T \mathbf{K} \quad (3.49)$$

Recall the external virtual work, from Equation 3.3

$$\partial W_E = \left(\int_{\Omega} f \cdot \delta u dv + \int_{\Gamma_{\Omega}} T \cdot \delta u ds \right)$$

and replacing the displacement variation $\delta u = N \delta q$

$$\delta W_E = \int_{\Omega} \delta u^T f dv + \int_{\Gamma_{\Omega}} \delta u^T T ds \quad (3.50)$$

$$\delta W_E = \int_{\Omega} N^T \delta q^T f dv + \int_{\Gamma_{\Omega}} N^T \delta q^T T ds \quad (3.51)$$

$$\delta W_E = \delta q^T \left(\int_{\Omega} N^T f dv + \int_{\Gamma_{\Omega}} N^T T ds \right) \quad (3.52)$$

where the first integral is over the volume body, and the second over the surface body where traction is prescribed. Let

$$F = \int_{\Omega} N^T f dv + \int_{\Gamma_{\Omega}} N^T T ds \quad (3.53)$$

then Equation 3.52 becomes

$$\delta W_E = \delta q^T F \quad (3.54)$$

The principle of virtual work requires that the $\partial W_E = \partial W_I$, so

$$\delta Q^T K Q = \delta Q^T F \quad (3.55)$$

$$K Q = F \quad (3.56)$$

Large displacement can be handled in the framework. Refer to [63] for complete large displacement formulations.

3.3.3 Differential Volume and Area

The differential volume dV is the differential area dA on the (x, y) plane multiplied by the thickness of the element h . The integration will be over each element, and then all elements will be summed. The integration will be carried out over the ξ, η plane. Consider a rectangular infinitesimal element in the (ξ, η) plane, defined by four points shown in Figure 3.5. The element maps to the (x, y) plane. The point (ξ, η) maps to a vector $\mathbf{x}(\xi, \eta)$ on the (x, y) plane.

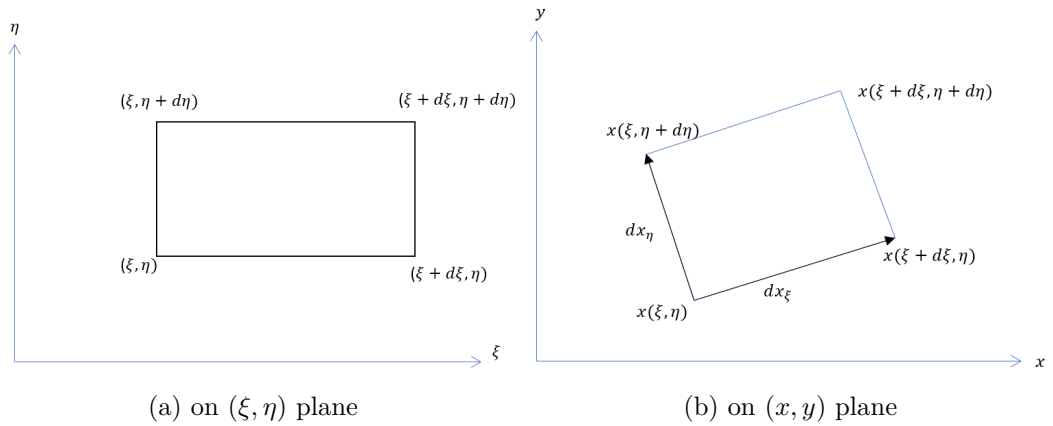


Figure 3.5: Infinitesimal quadrilateral element

The quadrilateral is made of the vectors

$$d_{\mathbf{x}\xi} = \mathbf{x}(\xi + d\xi, \eta) - \mathbf{x}(\xi, \eta) = \frac{\partial \mathbf{x}}{\partial \xi} d\xi \quad (3.57)$$

$$d_{\mathbf{x}\eta} = \mathbf{x}(\xi, \eta + d\eta) - \mathbf{x}(\xi, \eta) = \frac{\partial \mathbf{x}}{\partial \eta} d\eta \quad (3.58)$$

The area of the quadrilateral is the cross product of the two vectors

$$dA = |d_{\mathbf{x}\xi} \times d_{\mathbf{x}\eta}| \quad (3.59)$$

Calculating the cross product gives

$$d\mathbf{x}_\xi \times \mathbf{x}_\eta = \begin{vmatrix} \mathbf{i} & \mathbf{j} & \mathbf{k} \\ \frac{\partial x}{\partial \xi} d\xi & \frac{\partial y}{\partial \xi} d\xi & 0 \\ \frac{\partial x}{\partial \eta} d\eta & \frac{\partial y}{\partial \eta} d\eta & 0 \end{vmatrix} = \mathbf{k} \left(\frac{\partial x}{\partial \xi} \frac{\partial y}{\partial \eta} - \frac{\partial x}{\partial \eta} \frac{\partial y}{\partial \xi} \right) \quad (3.60)$$

Therefore, the area of the differential element is

$$dA = \det \mathbf{J} d\xi d\eta \quad (3.61)$$

The differential line length is

$$dL = |d\mathbf{x}_\eta| = \sqrt{\left(\frac{\partial x}{\partial \eta}\right)^2 + \left(\frac{\partial y}{\partial \eta}\right)^2} d\eta \quad (3.62)$$

The volume integral then becomes

$$\mathbf{k} = \int_{-1}^1 \int_{-1}^1 h \mathbf{B}^T \mathbf{D} \mathbf{B} \det \mathbf{J} d\xi d\eta \quad (3.63)$$

$$\mathbf{f}_b = \int_{-1}^1 \int_{-1}^1 h \mathbf{N}^T \mathbf{b} \det \mathbf{J} d\xi d\eta \quad (3.64)$$

$$\mathbf{f}_t = dL \int_{-1}^1 h \mathbf{N}^T t d\eta \quad (3.65)$$

where h is the thickness of the element.

3.3.4 Numerical Integration

The finite element formulation requires solving Equations 3.63-3.65 over the domain for the construction of the element stiffness matrix and force vector [60]. Most integrals cannot be evaluated explicitly. It is usually faster to integrate them numerically rather than analytically [60]. Among numerical integration methods, the Gauss integration rule is most commonly used for its simplicity and extreme accuracy [60]. The Gauss integration method integrates polynomials with the order of $2n_p - 1$ exactly, with n_p is the number of integration points.

Since the integration is carried out in the reference configuration $\xi \in [-1, +1]$,

then all the values must be transformed to the following configuration

$$\int_X g(X)dX = \int_{-1}^{+1} g(\xi) \frac{dX}{d\xi} d\xi = \int_{-1}^{+1} g(\xi)J(\xi)d\xi \quad (3.66)$$

where $g(\xi)$ is the function that should be integrated, and J is the Jacobian of the transformation configuration, calculated in Equations 3.34-3.37. The integration is done numerically since the product $g(\xi)J(\xi)$ is in general not a polynomial. Therefore it is approximated by the sum

$$\int_{-1}^{+1} g(\xi)J(\xi)d\xi \approx \sum_{p=1}^{n_p} g(\xi_p)J(\xi_p)W_p \quad (3.67)$$

where W_p are the weighting factors and ξ_p denote the coordinates of the evaluation points.

3.4 Discrete Model for Continuum

The following method is the modification that was implemented to the original discrete element method. The modification allows to model structures accurately in continuum and in discrete behaviour. The modification to the method is based on connective links between destroyed elements change to contact links of the traditional DEM and the element arrangement patterns remain the same. The DEM model for continuum dynamics problems was presented by [64] based on the principle of minimum potential energy. The method used a seven-disc model as well as an extension to a nine-disc model. The seven-disc model derivation is presented in this section.

Consider an elastic plate that is divided into rigid disc elements, connected by normal and tangential springs. Two potential compact arrangement patterns are possible; type A and type B. Type A is a seven-disc model, while type B is a nine-disc model. The model is presented in Figure 3.6.

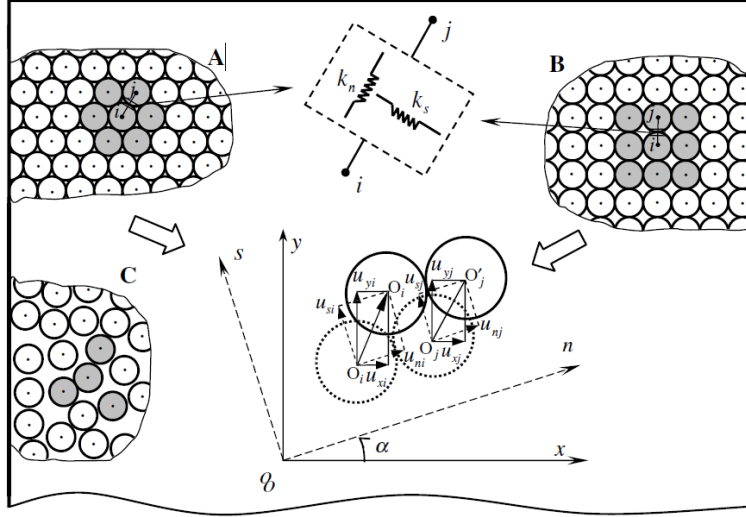


Figure 3.6: Discrete element method models based on rigid disc elements [64]

The total potential energy for the disc-spring system is

$$\begin{aligned} \Pi = \sum_i^N (U_i V_i) + \sum_i^N (u_{xi} \rho \ddot{u}_{xi} V_i + u_{yi} \rho \ddot{u}_{yi} V_i) - \sum_i^N (u_{xi} f_{xi} V_i + u_{yi} f_{yi} V_i) \\ - \sum_i^N (u_{xi} \bar{T}_{xi} S_i + u_{yi} \bar{T}_{yi} S_i) \end{aligned} \quad (3.68)$$

where U_i is the average strain energy around disc i , V_i is the volume of the disc, ρ is the mass density, S_i is the boundary area of the external force on the disc, u_{xi} and u_{yi} are the displacements, \ddot{u}_{xi} and \ddot{u}_{yi} are the accelerations in the horizontal and vertical directions, respectively. f_{xi} , f_{yi} and \bar{T}_{xi} , \bar{T}_{yi} are the components of the body force and surface force in the horizontal and vertical directions, respectively.

The deformation of the body is presented through the deformation of the springs. For a disc i that connects with p discs, the average strain energy around disc i is

$$U_i = \frac{1}{V_i} \sum_j^p \frac{1}{2} \left[\frac{1}{2} k_{nij} (u_{nj} - u_{ni})^2 + \frac{1}{2} k_{sij} (u_{sj} - u_{si})^2 \right] \quad (3.69)$$

where k_{nij} and k_{sij} are the normal and tangential spring constants between discs i and j . Assuming the rotation angle between the x-axes and the normal direction

of the spring as α , $l = \cos \alpha$ and $m = \sin \alpha$, then

$$u_n = u_x l + u_y m, \quad u_s = u_y l - u_x m \quad (3.70)$$

Substituting Equation 3.70 in 3.69 gives

$$U_i = \frac{1}{4V_i} \sum_j^p k_{nij} [l_{ij}(u_{xj} - u_{xi}) + m_{ij}(u_{yj} - u_{yi})]^2 + \frac{1}{4V_i} \sum_j^p k_{sij} [l_{ij}(u_{yj} - u_{yi}) - m_{ij}(u_{xj} - u_{xi})]^2 \quad (3.71)$$

Substituting Equation 3.71 into the total potential energy Equation 3.68, and according to variational calculus $\partial\Pi/\partial u_{xi} = 0$, $\partial\Pi/\partial u_{yi} = 0$, \ddot{u}_{xi} and \ddot{u}_{yi} are given by

$$\ddot{u}_{xi} = \frac{1}{\rho V_i} (f_{xi} V_i + \bar{T}_{xi} S_i + \sum_j^p k_{nij} [l_{ij}^2 (u_{xj} - u_{xi}) + l_{ij} m_{ij} (u_{yj} - u_{yi})] + \sum_j^p k_{sij} [m_{ij}^2 (u_{xj} - u_{xi}) - l_{ij} m_{ij} (u_{yj} - u_{yi})]) \quad (3.72)$$

$$\ddot{u}_{yi} = \frac{1}{\rho V_i} (f_{yi} V_i + \bar{T}_{yi} S_i + \sum_j^p k_{nij} [l_{ij} m_{ij} (u_{xj} - u_{xi}) + m_{ij}^2 (u_{yj} - u_{yi})] + \sum_j^p k_{sij} [-l_{ij} m_{ij} (u_{xj} - u_{xi}) + l_{ij}^2 (u_{yj} - u_{yi})]) \quad (3.73)$$

At moment t , \ddot{u}_{xi} and \ddot{u}_{yi} are obtained from Equations 3.72 and 3.73. At moment $t + \Delta t$

$$[\dot{u}_{xi}]_{t+\Delta t} = [\dot{u}_{xi}]_t + [\ddot{u}_{xi}]_t \Delta t \quad (3.74)$$

$$[\dot{u}_{yi}]_{t+\Delta t} = [\dot{u}_{yi}]_t + [\ddot{u}_{yi}]_t \Delta t \quad (3.75)$$

$$[u_{xi}]_{t+\Delta t} = [u_{xi}]_t + [\dot{u}_{xi}]_t \Delta t \quad (3.76)$$

$$[u_{yi}]_{t+\Delta t} = [u_{yi}]_t + [\dot{u}_{yi}]_t \Delta t \quad (3.77)$$

where Δt is a time increment.

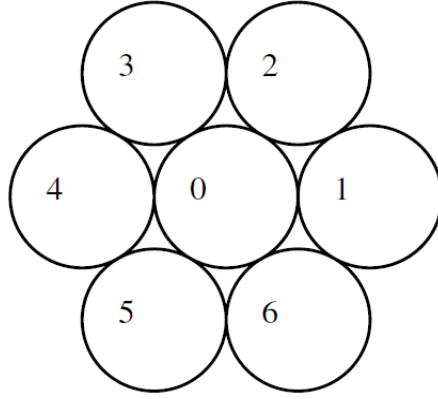


Figure 3.7: Seven-disc model

Seven-disc model

The seven-disc model is presented in Figure 3.7.

$$A = r^2(2k_{n1} + \frac{1}{8}k_{n2} + \frac{1}{8}k_{n3}), \quad B = r^2(\frac{9}{8}k_{n2} + \frac{9}{8}k_{n3}), \quad (3.78)$$

$$C_1 = r^2(\frac{3}{8}k_{n2} + \frac{3}{8}k_{n3}), \quad C_2 = r^2(\frac{3}{8}k_{s2} + \frac{3}{8}k_{s3}), \quad (3.79)$$

$$D = r^2(2k_{s1} + \frac{1}{2}k_{s2} + \frac{1}{2}k_{s3}), \quad E = r^2(\frac{\sqrt{3}}{8}k_{n2} - \frac{\sqrt{3}}{8}k_{n3}) \quad (3.80)$$

$$F = r^2(\frac{3\sqrt{3}}{8}k_{n2} - \frac{3\sqrt{3}}{8}k_{n3}), \quad G = r^2(-\frac{\sqrt{3}}{4}k_{s2} + \frac{\sqrt{3}}{4}k_{s3}) \quad (3.81)$$

where $\delta = V/(2\sqrt{3}r^2)$ is the disc thickness. For orthotropic $c_{16} = 0$ and $c_{26} = 0$ [64].

3.5 Lattice Model for RC using EDEM

The lattice model is composed of two parts; before fracture, and after fracture. A concrete element is modelled as a lattice model consisting of two lumped-masses connected by axial truss elements as shown in Figure 3.8. The constitutive model of a concrete truss element is therefore described by a uni-axial tensile/compressive law.

The dynamic characteristics of the model after spring fracture are described by DEM. Re-contact of the fracture materials is also considered. The lumped-

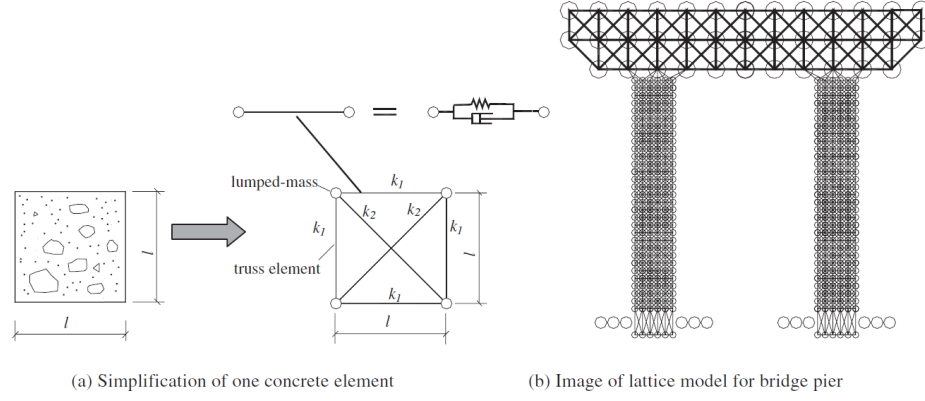


Figure 3.8: Concrete Lattice Model [41]

mass cannot be treated as an abstract point in this case, rather as a planar circular solid with a some radius after fracture of all connected springs [41]. Each two-dimensional square element is modelled as a lattice model cell composed of four lumped masses and six uni-axial concrete truss members. Every concrete truss member consists of a concrete spring and damper. The initial stiffness of the horizontal and vertical truss is k_1 , and the two diagonal trusses is k_2 . Under a unit compressive load the vertical and horizontal deformations of the concrete element are shown in Equations 3.82 and 3.83.

$$\delta_1^C = \frac{2l}{EA} = \frac{2l}{Etl} = \frac{2}{Et} \quad (3.82)$$

$$\delta_2^C = v\delta_1 = \frac{2v}{Et} \quad (3.83)$$

where E is the elastic modulus, and v is the Poisson's ratio of concrete, t , A and l are the thickness, the sectional area and the length of the element. The deformations of the lattice model are;

$$\delta_1^L = \frac{2(2k_1 + k_2)}{2k_1(k_1 + k_2)} \quad (3.84)$$

$$\delta_2^L = \frac{k}{2k_1(k_1 + k_2)} \quad (3.85)$$

Equating the deformations of the two systems gives;

$$\delta_1^C = \delta_1^L, \quad \delta_2^C = \delta_2^L \quad (3.86)$$

k_1 and k_2 are;

$$k_1 = \frac{1}{2(1+v)}Et \quad (3.87)$$

$$k_2 = \frac{v}{1-v^2}Et \quad (3.88)$$

Under a unit shear load, the shear deformations for the systems are;

$$\delta_3^C = \frac{2}{GA/L} = \frac{2}{Gt} = \frac{1+v}{Et} \quad (3.89)$$

$$\delta_3^L = \frac{2}{k_2} \quad (3.90)$$

Equating 3.89 and 3.90, gives;

$$k_2 = \frac{Et}{2(1+v)} \quad (3.91)$$

It must be noted that Equations 3.88 and 3.91 are satisfied simultaneously when $v = 1/3$. For concrete, this value increases the limit of 0.1 – 0.2. Therefore, Equation 3.88 should be used for a beam-like member, where the deformation is primarily a results of flexural strain. Equation 3.91 should be used for wall-like members in which the deformation is mainly due to the shear strain [41].

For modelling the steel bars in the concrete, the stiffness of the springs are shown in Equation 3.92. The steel bars are treated as lumped masses connected to one another by an axial spring.

$$k_s = \frac{E_s A_s}{l_s} \quad (3.92)$$

where, E_s is the elastic modulus of the steel, A_s is the cross-sectional area of the steel bar, and l_s is the displacement between two adjacent nodes. The nodes of the steel bar and the concrete are independent of one another. The model can simulate local failure, and local buckling of the bar, and stripping of the concrete cover. The springs for bonding and sliding between steel and concrete are also considered.

3.6 Rigid Bodies Spring Models

The Rigid Bodies Spring Models (RBSM), has several different formulations for different element types. For the scope of this project, the beam element and the plane strain elements are the most relevant, and are shown in the following sections.

3.6.1 Formulation of Beam Element

Consider the deformation of two rigid bars that are connected by one rotational spring in the middle, shown in Figure 3.9. At locations A,B, and C, the bars have a displacement of u_{i-1} , u_i and u_{i+1} , and a force applied of X_{i-1} , X_i and X_{i+1} , respectively. The strain energy of the bar is shown in Equation 3.93. where, k_b

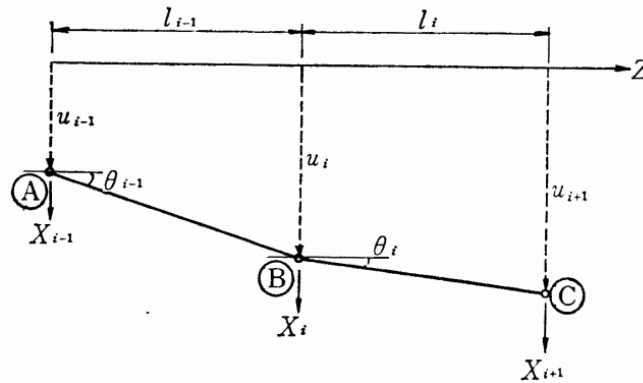


Figure 3.9: Beam Bending Element [43]

is the spring constant. Then it is written in terms of the displacements u_{i-1} , u_i and u_{i+1} , Equation 3.94

$$V(\theta_{i-1}, \theta_i) = \frac{k_b}{2} (\theta_i - \theta_{i-1})^2 \quad (3.93)$$

$$V(u_{i-1}, u_i, u_{i+1}) = \frac{k_b}{2} \left[\left(\frac{u_{i+1} - u_i}{l_i} \right) - \left(\frac{u_i - u_{i-1}}{l_{i-1}} \right) \right]^2 \quad (3.94)$$

The stiffness matrix can then be resolved by applying Castigliano's theorem on Equation 3.94, which leads to the stiffness matrix shown in Equation 3.101. The

partial derivatives of the energy are as follows

$$\frac{\partial V}{\partial u_{i-1}} = k \left(\frac{1}{l_{i-1}} \right) \left(\frac{u_{i+1} - u_i}{l_i} + \frac{-u_i + u_{i-1}}{l_{i-1}} \right) \quad (3.95)$$

$$\frac{\partial V}{\partial u_i} = k \left(\frac{-1}{l_i} - \frac{1}{l_{i-1}} \right) \left(\frac{u_{i+1} - u_i}{l_i} + \frac{-u_i + u_{i-1}}{l_{i-1}} \right) \quad (3.96)$$

$$\frac{\partial V}{\partial u_{i+1}} = k \left(\frac{1}{l_i} \right) \left(\frac{u_{i+1} - u_i}{l_i} + \frac{-u_i + u_{i-1}}{l_{i-1}} \right) \quad (3.97)$$

Rewriting the equations in terms of u_{i-1} , u_i and u_{i+1} , gives Equations 3.98 - 3.100

:

$$X_{i-1} = k \left[\left(\frac{1}{l_{i-1}^2} \right) u_{i-1} - \left(\frac{1}{l_i l_{i-1}} + \frac{1}{l_{i-1}^2} \right) u_i + \left(\frac{1}{l_{i-1}^2} \right) u_{i+1} \right] \quad (3.98)$$

$$X_i = k \left[- \left(\frac{1}{l_i l_{i-1}} + \frac{1}{l_{i-1}^2} \right) u_{i-1} + \left(\frac{1}{l_i} + \frac{1}{l_{i-1}} \right)^2 u_i + \left(\frac{-1}{l_i} - \frac{1}{l_{i-1}} \right) u_{i+1} \right] \quad (3.99)$$

$$X_{i+1} = k \left[\left(\frac{1}{l_i l_{i-1}} \right) u_{i-1} - \left(\frac{1}{l_i l_{i-1}} + \frac{1}{l_i^2} \right) u_i + \left(\frac{1}{l_i^2} \right) u_{i+1} \right] \quad (3.100)$$

Rewriting Equations 3.98 - 3.100 in matrix format, gives the stiffness matrix in Equation 3.101.

$$\begin{pmatrix} X_{i-1} \\ X_i \\ X_{i+1} \end{pmatrix} = k_b \begin{bmatrix} \frac{1}{l_{i-1}^2} & & \\ \frac{-1}{l_{i-1}} \left(\frac{1}{l_i} + \frac{1}{l_{i-1}} \right) & \left(\frac{1}{l_i} + \frac{1}{l_{i-1}} \right)^2 & \\ \frac{-1}{l_{i-1} l_i} & \frac{-1}{l_{i-1}} \left(\frac{1}{l_i} + \frac{1}{l_{i-1}} \right) & \frac{1}{l_i^2} \end{bmatrix} \begin{matrix} sym \\ \\ \\ \end{matrix} \begin{pmatrix} u_{i-1} \\ u_i \\ u_{i+1} \end{pmatrix} \quad (3.101)$$

3.6.2 Plane strain elements

Considering the beam bending model in plane strain, where two rigid triangular plates are connected by three different types of springs at the middle of the boundary edges, shown in Figure 3.10. Points 1 and 2 are the centroids of $\triangle ABC$ and $\triangle ACD$. $\triangle ABC$ and $\triangle ACD$ are connected at the middle of \overline{AC} by three types of springs k_d , k_s and k_r . The centroid displacements of the plate are denoted by (u_1, v_1, θ_1) and (u_2, v_2, θ_2) .

The potential energy of the two elements is given in Equation 3.102:

$$V = \frac{1}{2} k_s (u_1 + u_2)^2 + \frac{1}{2} k_d (v_1 + v_2)^2 \quad (3.102)$$

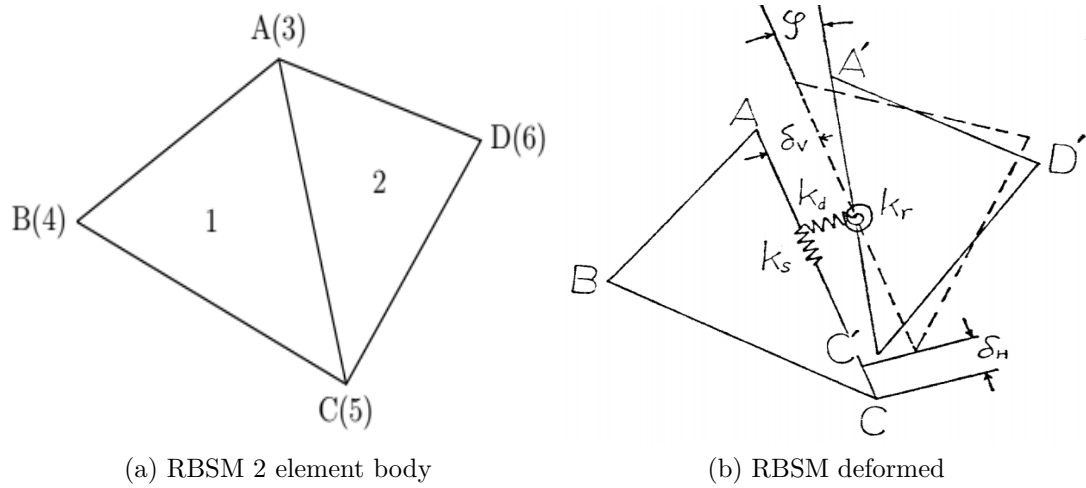


Figure 3.10: Plane strain element in RBSM [43]

Applying Castigliano's theorem gives;

$$\frac{\partial V}{\partial u_1} = k_s(u_1 + u_2), \quad \frac{\partial V}{\partial u_2} = k_s(u_1 + u_2) \quad (3.103)$$

$$\frac{\partial V}{\partial v_1} = k_d(v_1 + v_2), \quad \frac{\partial V}{\partial v_2} = k_d(v_1 + v_2) \quad (3.104)$$

Writing the equations in matrix format gives:

$$\begin{bmatrix} k_s & 0 & k_s & 0 \\ 0 & k_d & 0 & k_d \\ k_s & 0 & k_s & 0 \\ 0 & k_d & 0 & k_d \end{bmatrix} \begin{pmatrix} u_1 \\ v_1 \\ u_2 \\ v_2 \end{pmatrix} \quad (3.105)$$

Considering that the angle of rotation is shown in Figure 3.10 and is γ , and given that a transformation matrix is given by $\begin{bmatrix} \cos\theta & \sin\theta \\ -\sin\theta & \cos\theta \end{bmatrix}$. Since $\theta = 90 - \gamma$, then the transformation matrix will be $\begin{bmatrix} \sin\gamma & \cos\gamma \\ -\cos\gamma & \sin\gamma \end{bmatrix}$. For simplicity $\sin(\gamma)$ and $\cos(\gamma)$ will be denoted by s and c respectively. Transforming the stiffness matrix using $T'K$, Equation 3.106:

and collapse, the Timoshenko beam element with one integration point is more suitable, because fracture cannot be considered by a single Bernoulli-Euler beam element [50].

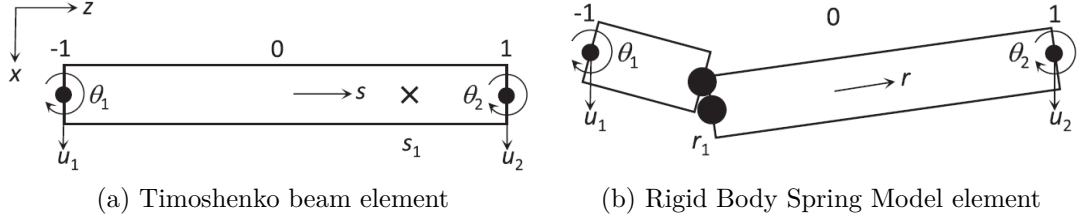


Figure 3.11: Timoshenko beam element compared to RBSM element [50]

3.7.1 Adaptively Shifted Integration Technique

The location of the numerical integration point during the elastic stage is the midpoint of the element. When a fully plastic section occurs, the numerical integration point is shifted to the location at where the plastic hinge would occur. Figure 3.11 is a linear Timoshenko beam element and its equivalence to the RBSM. The location of the numerical integration point and stress evaluation point is shown in Equation 3.110 [47].

$$s_1 = -r_1 \quad (3.110)$$

When the entire region is elastic, $s = s_1 = 0$ and $r = r_1 = 0$, since the integration point is at midpoint. The stiffness matrix for the element is as follows;

$$[K_E] = l[B(0)]^T[D_e(0)][B(0)] \quad (3.111)$$

The strain vector $\{\Delta\}_n \varepsilon(0)$ and the force increment vector $\{\Delta\}_n \sigma(0)$ at $r = r_1 = 0$ are;

$$\{\Delta_n \varepsilon(0)\} = [B(0)]\{\Delta_n u\} \quad (3.112)$$

$$\{\Delta_n \sigma(0)\} = [D_e(0)]\{\Delta_n \varepsilon(0)\} \quad (3.113)$$

The forces calculated in Equation 3.113 are at the midpoint of the element. The bending moments along the elastic deformed element are;

$$\Delta_n M_x(s) = \Delta_n M_x(0) - \Delta_n V_y(0) \frac{l_s}{2} \quad (3.114)$$

$$\Delta_n M_y(s) = \Delta_n M_y(0) - \Delta_n V_x(0) \frac{l_s}{2} \quad (3.115)$$

Once a plastic section has fully formed, the integration points are shifted to $s = s_1 = -r_1$. The elemental stiffness matrix, the generalized strain and the force increment vectors are as follows;

$$[K_E] = l[B(s_1)]^T [D_p(r_1)] [B(s_1)] \quad (3.116)$$

$$\{\Delta_n \varepsilon(r_1)\} = [B(s_1)] \{\Delta_n u\} \quad (3.117)$$

$$\{\Delta_n \sigma(r_1)\} = [D_p(r_1)] \{\Delta_n \varepsilon(r_1)\} \quad (3.118)$$

where $[D_p(r)]$ is the force-strain matrix for plastic deformation. This matrix can be expressed as;

$$[D_p(r_1)] = [D_e(r_1)] - \frac{[D_e(r_1)] \{\partial f / \partial \sigma\} [\partial f / \partial \sigma] [D_e(r_1)]}{H' + [\partial f / \partial \sigma] [D_e(r_1)] \{\partial f / \partial \sigma\}} \quad (3.119)$$

where, H' is the strain hardening coefficient and f is the plastic potential expressed as;

$$f = f_y(\sigma(r_1)) - 1 = 0 \quad (3.120)$$

3.7.2 ASI-Gauss Technique

In both the ASI and ASI-Gauss techniques, the numerical integration point is shifted adaptively if a full plastic section is developed to express a plastic hinge. When the plastic hinge is unloaded the numerical integration point is shifted back to its initial locations. The initial location of the integration point in the ASI is the midpoint of the beam element, and is considered optimal when the entire element is elastic. Bending deformations are inaccurate because the displacement functions of the element are defined by linear functions. An efficient way to solve

the discrepancy is using the ASI-Gauss technique where the numerical integration points of a member coincide with the Gaussian integration points of the member, shown in Figure 3.12. The locations are optimal for two-point integration in Gaussian quadrature and the accuracy of the deformation defined by a cubic function is guaranteed. The relation between the locations of the numerical inte-

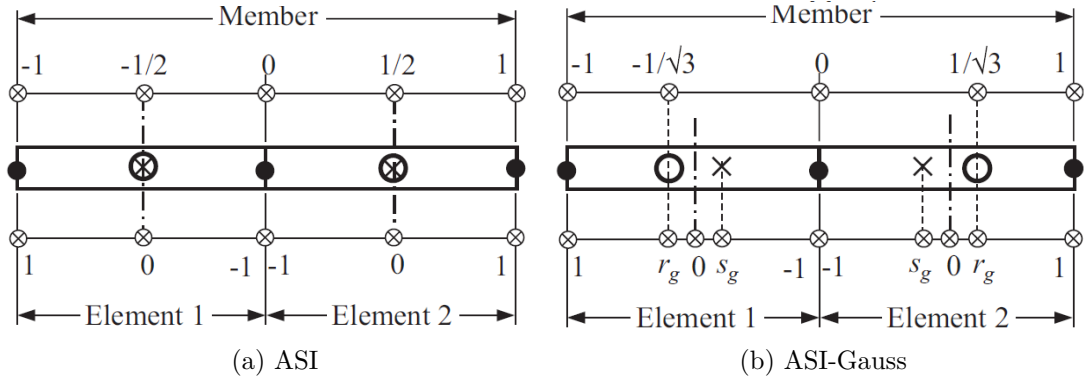


Figure 3.12: ASI element compared to ASI-Gauss [50]

gration point and the stress evaluation point is the same as Equation 3.110 [47]. The numerical integration points of the elements in the ASI-Gauss technique are placed at $s = s_1 = s_g$ when the element is entirely elastic. The initial locations of the numerical integration points in the ASI-Gauss technique is $s_g = 1 - (2/\sqrt{3})$, and the stress evaluation points is $r_g = -s_g = -1 + (2/\sqrt{3})$. Therefore, the elemental stiffness matrix, the strain and the force increment vectors in the ASI-Gauss technique are shown in Equations 3.121-3.123.

$$[K_E] = l[B(s_g)]^T [D_e(r_g)] [B(s_1g)] \quad (3.121)$$

$$\{\Delta_n \varepsilon(r_g)\} = [B(s_g)] \{\Delta_n u\} \quad (3.122)$$

$$\{\Delta_n \sigma(r_e)\} = [D_e(r_g)] \{\Delta_n \varepsilon(r_g)\} \quad (3.123)$$

The bending moments are;

$$\Delta_n M_x(s) = \Delta_n M_x(s_g) - \Delta_n V_y(s_g) \frac{l}{2}(s + s_g) \quad (3.124)$$

$$\Delta_n M_y(s) = \Delta_n M_y(s_g) - \Delta_n V_x(s_g) \frac{l}{2}(s + s_g) \quad (3.125)$$

The yield condition by the plastic flow theory is;

$$f = \left(\frac{M_x}{M_{xo}}\right)^2 + \left(\frac{M_y}{M_{yo}}\right)^2 + \left(\frac{N}{N_0}\right)^2 - 1 = f_y - 1 = 0 \quad (3.126)$$

where f_y is the yield function, and M_x, M_y and N are the bending moments around the x-axis, y-axis and axial force respectively. The remainder of the equations are the same as the ASI technique. By adaptively shifting the numerical integration point of an element, a precise location of a plastic hinge is found and highly accurate elasto-plastic solutions can be obtained with a very small number of elements [50].

Part II

Formulation of Linear and Nonlinear Gaussian Based AEM

Chapter 4

Applied Element Method Formulation

To model the progressive collapse of structures the continuum and discrete element behaviour must be considered to capture all stages of collapse. In Chapters 2 and 3, different methods were presented along with their formulations to present the brief progression of methods used for modelling the progressive collapse. Out of all the methods that were presented, the Applied Element Method stood out, since it is based on combining the FEM and DEM in some sense. Since the AEM was developed to aid in the analysis of highly nonlinear behaviour of structures, it is selected as the appropriate model to analyse the progressive collapse of structures.

In this chapter a complete formulation of the AEM is presented along with modifications to the method that have been presented in the previous decades for use in different applications.

4.1 AEM Formulation for 2-D element

The AEM was developed in year 2000 by Meguro and Tagel-Din [6]. The elements in AEM are rigid bodies that are connected with sets of normal and shear springs along the edges of the elements. The springs represent the two connecting elements in that region. The material properties are specified through the spring stiffness. For a 2-D element, three degrees-of-freedom are considered per element:

deflection in x , deflection in y and rotation [6].

Consider a linear spring that is subjected to axial forces at both ends of the spring, f_1 and f_2 . The displacement at each end of the spring is represented as u_1 and u_2 . Assuming the spring is in equilibrium then the sum of the forces should be zero. So, $f_1 + f_2 = 0$, or $f_1 = -f_2$. By using the spring constant k , the force displacement relationship of each spring from Hooke's law gives, $k(u_1 - u_2) = f_1$ and $k(u_2 - u_1) = f_2$. Rewriting these equations in matrix form gives

$$\begin{bmatrix} k & -k \\ -k & k \end{bmatrix} \begin{Bmatrix} u_1 \\ u_2 \end{Bmatrix} = \begin{Bmatrix} f_1 \\ f_2 \end{Bmatrix} \quad (4.1)$$

The equivalent spring constant for a linear spring when considered as an axial member with cross-sectional area A and length l is shown in Equation 4.2.

$$k = \frac{EA}{l} \quad (4.2)$$

The stiffness matrix for a pair of elements is a 6×6 matrix shown in Equation 4.3. The upper left quadrant of the matrix is displayed in Equation 4.4 [6]. Each spring location in an element is represented by a pair of normal and shear springs, with stiffness displayed in Equation 4.5. The elements distribution is displayed in Figure 4.1, and the details in elements are presented in Figure 4.2.

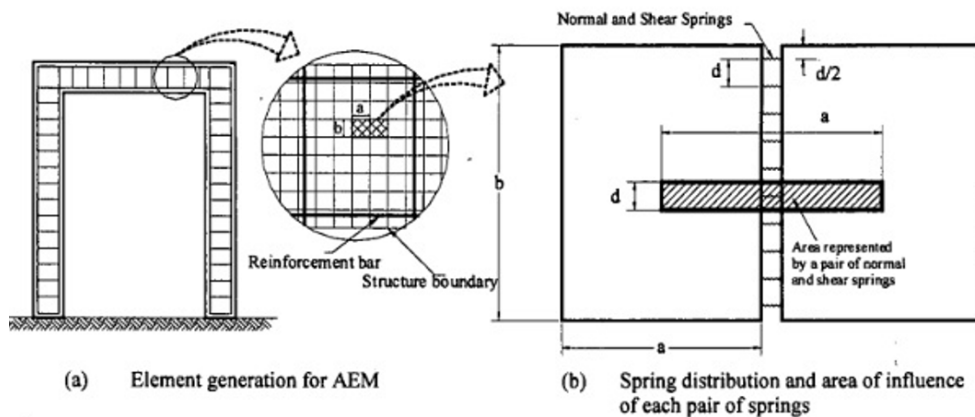


Figure 4.1: 2D AEM Elements [6]

$$K = \begin{bmatrix} k_{11} & k_{12} \\ k_{21} & k_{22} \end{bmatrix} \quad (4.3)$$

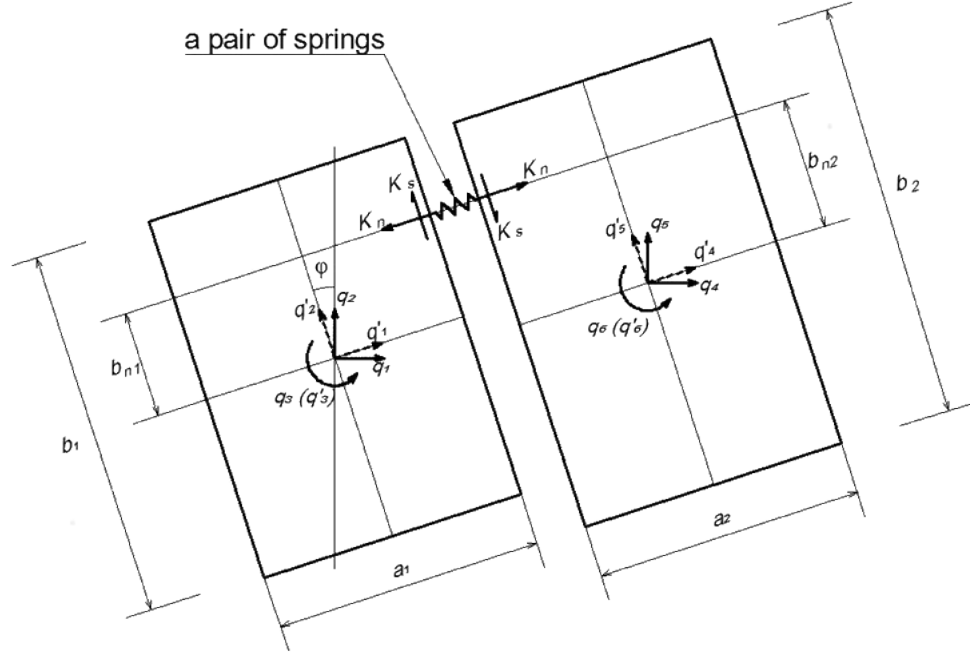


Figure 4.2: 2D AEM Elements degrees-of-freedom [65]

where k_{11} is

$$k_{11} = \begin{bmatrix} K_{n1} & 0 & -K_{n1}b_{n1} \\ 0 & K_{s1} & K_{s1}\frac{a}{2} \\ -K_{n1}b_{n1} & K_{s1}\frac{a}{2} & (K_{n1}b_{n1}) + (K_{s1}\frac{a}{4}) \end{bmatrix} \quad (4.4)$$

where K_n and K_s are

$$K_n = \frac{Edt}{a}; \quad K_s = \frac{GdT}{a} \quad (4.5)$$

where E is the Young's Modulus of elasticity of the material; G is the shear modulus of elasticity of the material; b_{n1} is the distance between the centre of the element and the spring location, that can be positive, negative or zero; d is the length from the tributary area each spring covers; a is the width from the tributary area each spring covers (also the width of the element if the elements are the same size, since the width of the element is also the width from centre to centre of two adjacent elements); and t is the thickness of the element. K is the stiffness matrix in the local system, represented by q in Figure 4.2. The local to global transformation matrix L , Equation 4.6 is used to calculate the stiffness

matrix in the global system.

$$L = \begin{bmatrix} c & s & 0 & 0 & 0 & 0 \\ -s & c & 0 & 0 & 0 & 0 \\ 0 & 0 & 1 & 0 & 0 & 0 \\ 0 & 0 & 0 & c & s & 0 \\ 0 & 0 & 0 & -s & c & 0 \\ 0 & 0 & 0 & 0 & 0 & 1 \end{bmatrix} \quad (4.6)$$

where $c = \cos(\varphi)$ and $s = \sin(\varphi)$. φ is shown in Figure 4.2, and is the angle between the local q axis, and the global y axis. The transformation of the local K matrix to the global K^{global} matrix for one element is shown in Equation 4.7.

$$K^{global} = L^T K L \quad (4.7)$$

4.2 AEM Meshing and Element distribution

MATLAB is used to mesh beam structural elements. Consider a cantilever beam displayed in Figure 4.3. As mentioned previously the AEM elements are rectangular, so distributing elements is straightforward in rectangular and square shaped structures. Figure 4.3 shows the mesh distribution for different number of elements.

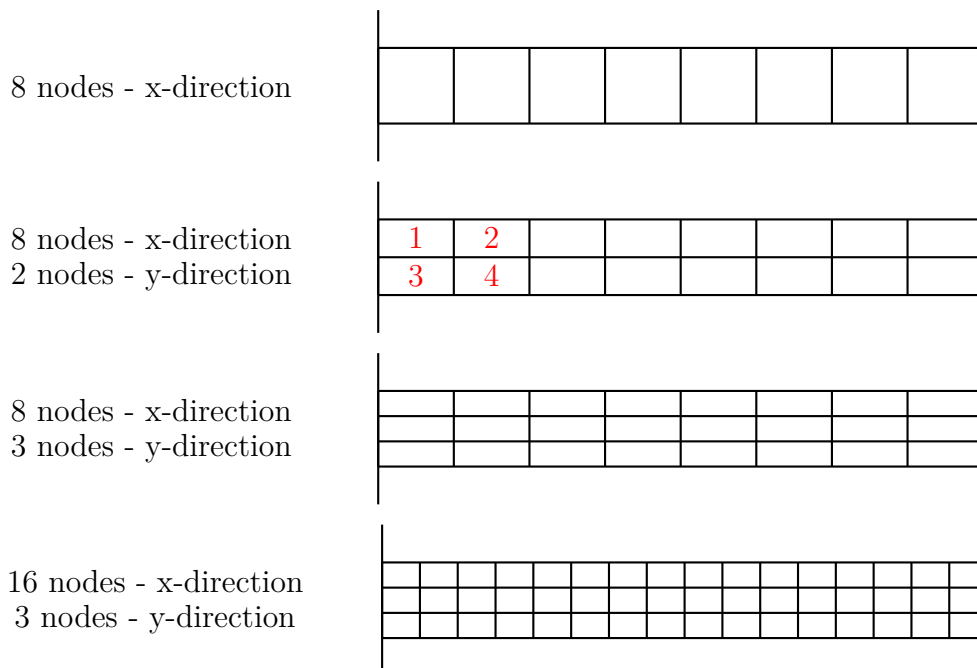


Figure 4.3: Mesh distribution for structural beam

In the second mesh for the beam configuration, with 8 elements in the x-direction and 2 in the y-direction, the connectivity of springs between elements 1,2,3 and 4 are presented in Figure 4.4c, where all edges are connected by springs. Figure 4.4a displays the connectivity between elements 1 and 2, and Figure 4.4b shows the connectivity between elements 1 and 3. For a structural frame shown in Figure

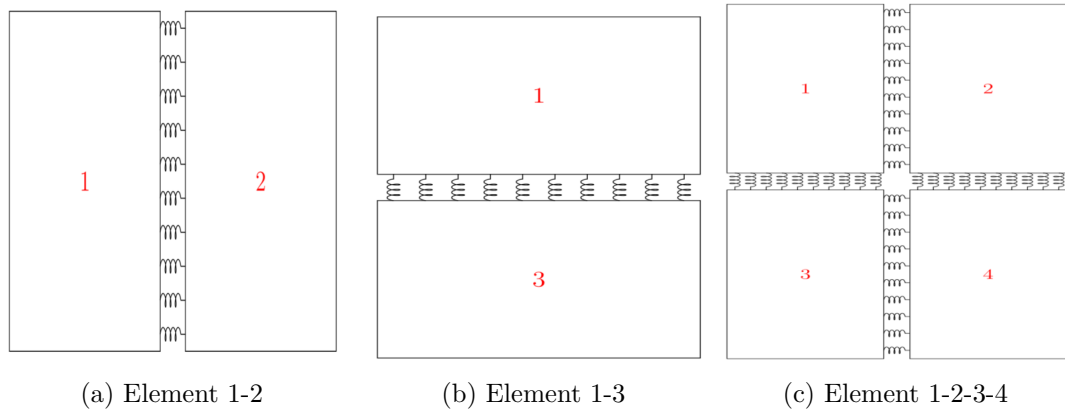


Figure 4.4: Connectivity between adjacent elements

4.5 the general meshing is shown, where the elements are connected by springs through the faces of the elements.

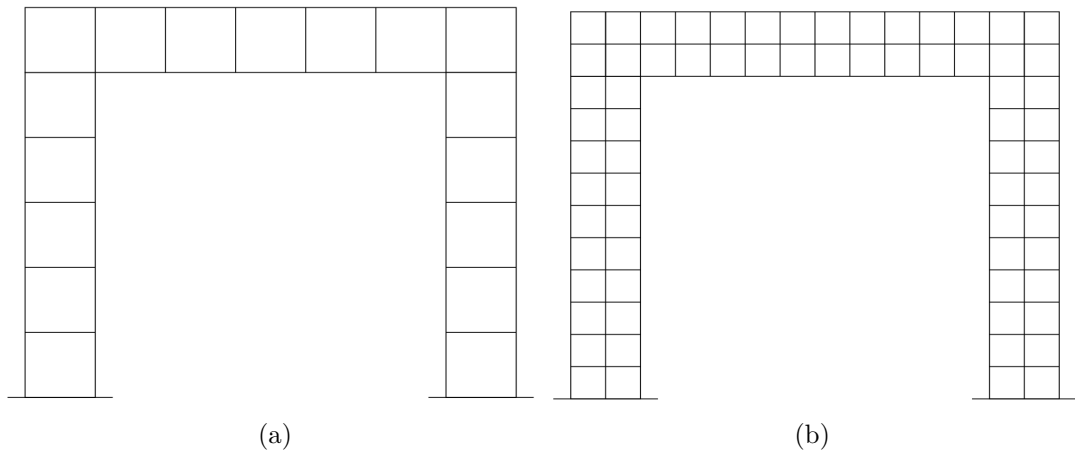


Figure 4.5: Frame meshing in AEM

4.2.1 Structures with multiple materials

One of the advantages of using springs between elements is that different material properties can be easily represented in different springs. For example, consider

modelling a reinforced concrete beam. The springs that are depicting the concrete behaviour will have the modulus of elasticity of concrete, while the springs modelling the reinforcement will have the steel modulus of elasticity. Figure 4.6 displays an example of a beam with both concrete springs (represented in black) and reinforcing steel springs (represented in red). The highlighted red area depicts the location of the steel reinforcement, since that is the tributary area of all springs. Implementing this in the MATLAB code is done by defining which spring from the element has the reinforcement properties, and the analysis will be carried on. An example of this is displayed below.

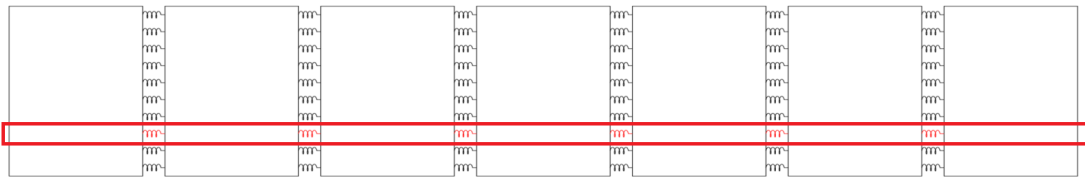


Figure 4.6: Representation of a cantilever concrete and steel reinforcement springs

In order to analyse a structural beam in the AEM code, the following input information is required:

- **Material properties**
- **Beam geometry:** span, width of cross-section, thickness of beam.
- **AEM properties:** Number of elements in the x-direction, number of elements in the y-direction, local dimensions of element (a and b), number of springs.
- **Connectivity table:** node 1, node 2, element orientation.

4.3 Effect of Number of Springs and Elements

Using different numbers of elements and springs when modelling structural elements will lead to different accuracy in results. This section provides the effect of the number of springs and number of elements in a system, and how increasing the accuracy of an analysis is achieved by changing these two variables.

4.3.1 Effect of Number of Springs Between Elements

Firstly, the number of springs between elements is considered. In elastic analysis the number of springs may not seem as crucial as in nonlinear analysis, since increasing the number of springs between elements leads to better analysis of crack propagation. It is assumed that "2n" evenly-spaced springs are connecting two elements together, where each spring represents the distance of "d=b/2n" [6]. For translational degrees of freedom, number of connecting springs does not affect the element stiffness, since decreasing the number of springs increases the area represented by each spring, in the translational degrees-of-freedom case [6]. Theoretical rotational stiffness K_r , calculated from normal springs, is given in Equation 4.8 [6].

$$K_r = \int_{y=-b/2}^{y=b/2} \frac{Et}{b} \times b_{n1} \times b_{n1} \times db_{n1} = \frac{Et}{3b} \times 2\left(\frac{b}{2}\right)^3 = \frac{Etb^2}{12} \quad (4.8)$$

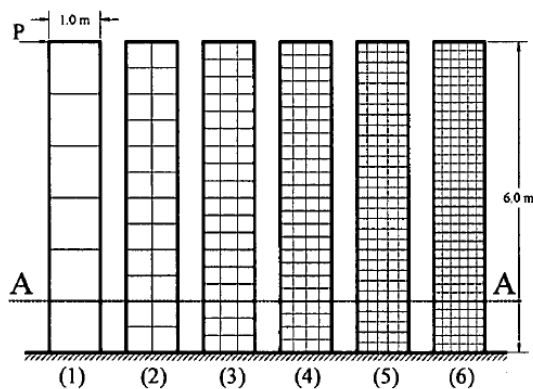
The element rotational stiffness is obtained by summing up all the rotational stiffness calculates for each spring separately. Therefore, the total rotational stiffness is given in Equation 4.9. From Equation 4.8 substitute $b = b/2n$, since b will now represent each spring separately. Therefore $\frac{Etb^2}{12}$ will be $\frac{Etb^2}{4n^3}$ and is multiplied by the number of springs.

$$K_r = \frac{Etb^2}{4n^3} \sum_{i=1}^n (i - 0.5)^2 \quad (4.9)$$

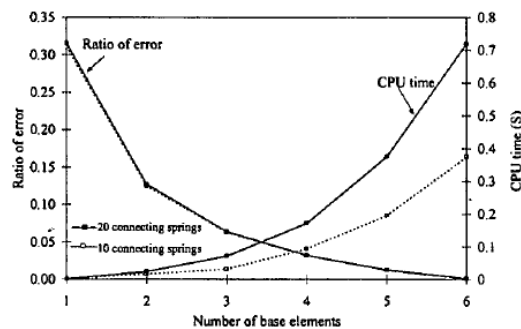
where i is the spring number. The calculated rotational stiffness is a function of the number of connecting springs. From Reference [6], it was found that the rotational stiffness is smaller than the theoretical value by 25%, and the error reduced to less than 1% when the number of connecting springs is larger than 10. If the element size is relatively large in comparison to the structure size then the rotational stiffness affects the accuracy. However if the element size is small then the rotational stiffness cannot affect the system because the rotation between elements becomes small [6].

4.3.2 Effect of Element Size

The element size in the model is an important factor in the accuracy of results [6]. Large elements increase the structure stiffness and thus the failure load of the structure. A series of simulations were carried out of a laterally loaded cantilever to show the element size effect. Two analyses were performed using 10 and 20 springs respectively [6]. Figure 4.7a displays the cantilever with different numbers of base elements. Figure 4.7b shows the percentage error and CPU time for each cantilever with 10 and 20 springs. The results show that there is an increase of the CPU time as the number of elements increases, which is expected. Moreover, the ratio of error decreases as the number of elements increases. Using 10 springs resulted in half the CPU time of using 20 springs, but both spring cases resulted in the same ratio of error [6]. It is concluded that using a large number of elements with a relatively low number of connecting springs leads to a high accuracy with acceptable CPU time. Therefore, in order to increase the accuracy of an analysis, it is recommended to increase the number of elements rather than increasing the number of springs [6].



(a) Cantilever beams with different number of base elements



(b) CPU time and error difference

Figure 4.7: Effect of Element Size [6]

4.4 Large Displacement Analysis using AEM

The numerical procedure for simulating large displacement is shown below [66]. The modification to the displacement calculation equation is shown in Equation

4.10.

$$K\Delta\mathbf{u} = \Delta\mathbf{f} + \mathbf{R}_m + \mathbf{R}_G \quad (4.10)$$

where K is the linearised stiffness matrix; $\Delta\mathbf{u}$ is the incremental displacement vector; $\Delta\mathbf{f}$ is the incremental load vector; \mathbf{R}_m is the residual force vector due to cracking or incompatibility between spring strains and stresses; and \mathbf{R}_G is the residual force vector due to the geometrical changes in the structure during loading. The limitations of the method are as follows: (1) complete symmetry of the structure and loading must be avoided in buckling analysis; (2) small displacement theory is assumed during each increment, therefore small increments of load and displacements should be assumed; and (3) the apparent structure stiffness decreases after buckling.

Box. 4.4.1: Large displacement analysis procedure in AEM

1. Assume that \mathbf{R}_m and \mathbf{R}_G are null and solve Equation 4.10 to get $\Delta\mathbf{u}$.
2. Modify the structural geometry according to the calculated incremental displacements.
3. Modify the direction of the spring force vectors according to the new element configuration. The geometrical changes generate incompatibility between the applied forces and internal stresses.
4. Verify whether cracking occurred and calculate \mathbf{R}_m . In elastic analysis $\mathbf{R}_m = 0$.
5. Calculate the element force vector, F_m , by summing the forces of the springs around each element.
6. Calculate the geometrical residuals around each element with Equation 4.11.

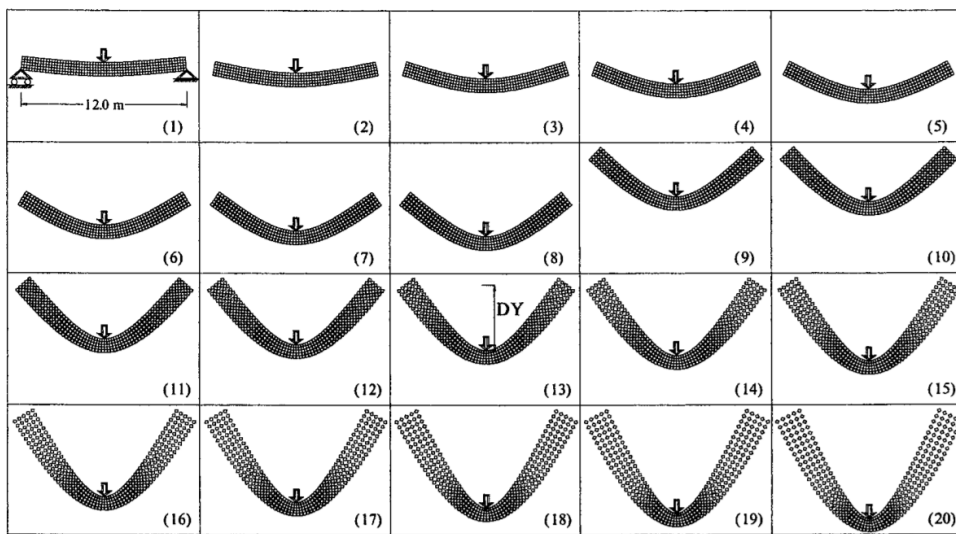
$$\mathbf{R}_G = \mathbf{f} - \mathbf{F}_m \quad (4.11)$$

7. Small deformations are assumed during each increment.
8. Calculate the stiffness matrix for the structure with the new configuration considering stiffness changes due to cracking or yielding.
9. Repeat the entire process.

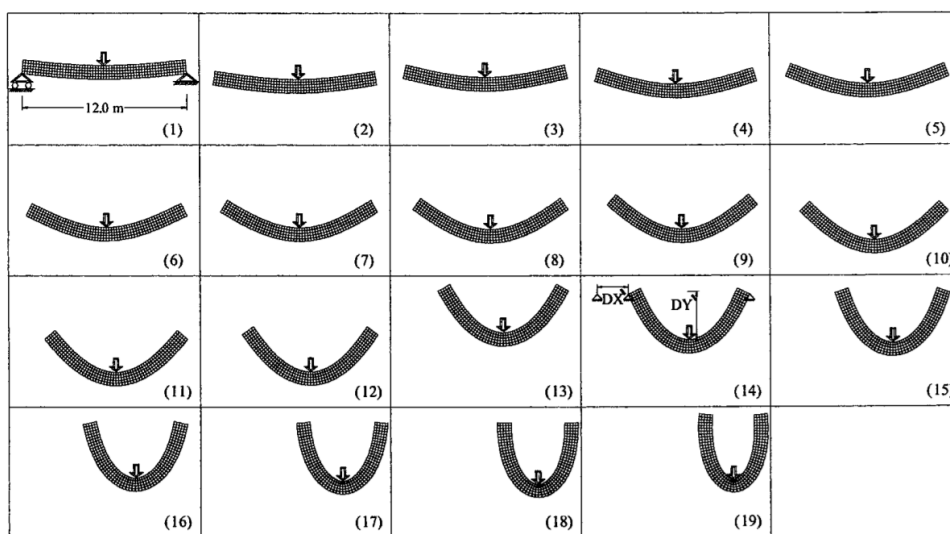
A simply supported beam was analysed to test the accuracy of the modifi-

4.4. LARGE DISPLACEMENT ANALYSIS USING AEM

cation for large displacement [66]. The beam has a span of $12m$, square cross section of $1m$, and simply supported (pinned on one side and roller on the other), with a point load at the midspan. The Young's modulus is 210 MPa . Figure 4.8a displays the deflection of the beam without accounting for the modifications for the large displacement analysis, while Figure 4.8b is the beam deflection with large displacement modification considered. In the case of small displacement analysis, the volume of the beam increases when the analysis approaches very large deformations, and the roller does not move, which is unrealistic. By using the large displacement theory, the more realistic results were found.



(a) Without large displacement modifications



(b) With large displacement modifications

Figure 4.8: Large Displacement of Simply supported beam [66]

4.5 Modifications in AEM

As mentioned in the previous chapter, some modifications have been done to the original AEM to improve the methods applicability. The modifications are the Improved Applied Element Method in 2003, and the Voronoi Applied Element method, 2008.

4.5.1 Improved Applied Element Method

The Improved Applied Element Method can accurately simulate the shear stiffness without using a large number of springs [58]. The normal and shear stiffness for each spring is shown in Equation 4.12.

$$K_N^i = \frac{E dt_N^i}{a} \quad K_S^i = \frac{G dt_s^i}{a} \quad (4.12)$$

where t_N^i and t_s^i are the thickness represented by spring i for normal and shear cases respectively. The differences in the values of t for each spring are due to the change of effective area for both normal and shear directions. This modification allows modelling different flanged steel sections, like I-beam, Box and Channel cross-sections. There were also modifications in the dynamic properties. Recalling that the general dynamic equation of motion governing the response of structure in small displacement is shown in Equation 4.13.

$$[M]\{\Delta\ddot{\mathbf{u}}\} + [C]\{\Delta\dot{\mathbf{u}}\} + [K]\{\Delta\mathbf{u}\} = \Delta\mathbf{f}(t) - [M]\Delta\{\ddot{\mathbf{u}}_{\mathbf{G}}\} \quad (4.13)$$

where $[M]$ is the mass matrix; $[C]$ is the damping matrix and $[K]$ is the non-linear stiffness matrix; $\Delta\mathbf{f}(t)$ is the incremental applied load vector; $\{\Delta\ddot{\mathbf{u}}\}$, $\{\Delta\dot{\mathbf{u}}\}$, $\{\Delta\mathbf{u}\}$ and $\{\Delta\ddot{\mathbf{u}}_{\mathbf{G}}\}$ are the incremental acceleration, velocity, displacement and gravity acceleration vectors, respectively. The mass matrix and the polar moment of inertia of each element are lumped at the element centroid. Equation 4.14 represents the value of lumped mass in each degree of freedom direction assuming

elements having square shape [58].

$$\begin{bmatrix} M1 \\ M2 \\ M3 \end{bmatrix} = \begin{bmatrix} D^2 \cdot \rho \cdot t_{av} \\ D^2 \cdot \rho \cdot t_{av} \\ \frac{D^4 \cdot \rho}{nsp} \cdot \sum_{i=1}^{i=nsp} \left(\frac{t_i^x}{12} + \frac{t_i^y}{12} \right) \end{bmatrix} \quad (4.14)$$

where D is the element size; t_{av} is the average thickness of the element; ρ is the density of the material. $[M1]$ and $[M2]$ correspond to the element mass, and $[M3]$ is the element polar moment of inertia about the centre of gravity.

4.5.2 Voronoi AEM

The Voronoi AEM (VAEM) was presented by Worakanchana and Meguro to eliminate the disadvantages of using square shaped elements from the conventional AEM [59]. The element formulation of the VAEM is shown in Figure 4.9, and is based on the Voronoi tessellation [67]. Considering a two-particle assembly, each

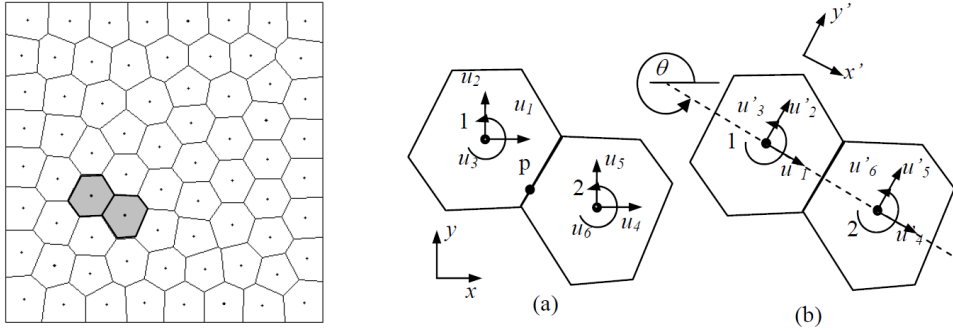


Figure 4.9: Element Assembly in VAEM [59]

rigid particle has two translational and a rotational degree of freedom defined at the particle centroid. For small rotations, the motion of any two points (x, y) of a rigid body can be defined as in Equation 4.16

$$u_1 = u_{c1} - u_3(y - y_{c1}); u_2 = u_{c2} + u_3(x - x_{c1}) \quad (4.15)$$

$$u_4 = u_{c4} - u_6(y - y_{c2}); u_5 = u_{c5} + u_6(x - x_{c2}) \quad (4.16)$$

where $u_1, u_2, u_3, u_4, u_5, u_6$, are translational displacements and rotation angles of elements 1 and 3 in the global coordinate system. The subscript c specifies the value at the particle centroid. The relative displacement vector of spring

deformation in the global coordinate system at point p can be defined as Equation 4.17

$$\{\delta_g\} = \overrightarrow{p'p''} = \begin{Bmatrix} \delta_x \\ \delta_y \end{Bmatrix} = \begin{Bmatrix} u_4 - u_1 \\ u_5 - u_2 \end{Bmatrix} \quad (4.17)$$

Substituting Equation 4.16 in 4.17 and rotating the displacement to the local coordinates parallel to the element surface, the relationship between the spring deformation in the local coordinates and particle displacement in the global coordinates is obtained, shown in Equation 4.18

$$\{\delta_t\} = [R][B]\{u\} \quad (4.18)$$

where $\{\delta_t\}^T = [\delta_n, \delta_t]$ in which δ_n and δ_t are the normal and shear deformation of a spring respectively, and $[R]$ is the rotational matrix

$$[B] = \begin{bmatrix} -1 & 0 & (y - y_{c1}) & 1 & 0 & -(y - y_{c2}) \\ 0 & -1 & -(x - x_{c1}) & 0 & 1 & (x - x_{c2}) \end{bmatrix} \quad (4.19)$$

and $\{u\}^T = [u_1, u_2, u_3, u_4, u_5, u_6]$.

4.6 Conclusion

The complete formulation of the Applied Element Method was presented in this chapter, along with modifications to the method. The AEM showed to have some advantages in modelling structural behaviour. Some of the advantages include the ease of modelling structures with multiple materials, such as reinforced concrete, since the material properties are represented in the springs. The AEM was examined for small displacements, large displacements, and modification to element shape and the stiffness for improvements of the method, which are summarised as follows.

An analysis run by Meguro and Tagel-Din was presented to show the effect of the number of elements and the number of springs in a structure and how they affect computational cost and accuracy. The study highlighted very important

factors that must be considered. It was mentioned that the number of springs did not affect the element stiffness, when only considering the translational degrees-of-freedom. Problems must arise when bending is considered. It was concluded that at least 10 springs were needed per element in order to reduce the rotational stiffness error. So it was suggested to use 10 springs per element and use smaller sized elements as errors arise in the rotational stiffness.

The AEM was also examined for validation of large displacement analysis. Residual force vectors are needed to be considered in this analysis. Some limitations were presented which were, symmetry of structure must be avoided in buckling analysis. Small increments of load must be assumed since the small displacement theory is implemented. Moreover, the stiffness of the structure decreases after buckling.

Different modifications in the last decades have been made to the original AEM. One of the modifications presented is the Improved Applied Element Method. The major advantage is its capability of accurately analysing shear stiffness without requiring a large number of springs. The modification is implemented by having different values of t thickness for each spring. The modification allows modelling different cross-sectional elements such as I-beams, box and channel sections.

Another modification to the AEM is the change in the shape of the elements. Rather than using square elements, the element formulation is based on the Voronoi tessellation. The advantage of using Voronoi elements is that meshing of structures is not limited to square shaped elements.

From this chapter it is concluded that there is a need for optimization of the number of springs required to successfully model beam bending accurately without requiring a large number of springs or elements. An optimization solution to this problem will be presented in the following chapter using Gaussian quadrature for spring distribution.

Chapter 5

Gaussian based AEM

Formulation

In this chapter structural elements in linear elastic cases using the AEM are presented. In the scope of this research, the AEM is programmed using MATLAB.

As mentioned in the previous chapter, the number of springs required in the system is quite large for linear problems in the case that rotational stiffness needs to be considered. A number of at least 10 springs were required with the limitation that the element size is also relatively small. Solving linear elastic problems should be simple enough to use larger number of elements and less number of springs to optimise the computational cost. An optimisation solution is presented in this chapter by modifying the AEM springs distribution using the Gaussian quadrature.

This chapter entails two parts. First the AEM with equally distributed springs is modelled using MATLAB. The conventional AEM is compared with the FEM which is analysed on ANSYS Workbench. The two methods will be compared for validation purposes. The second part of this chapter addresses the problem of using many springs per element. An optimisation modification to the AEM is presented: a new distribution for the springs based on the Gaussian quadrature in section 5.3.

5.1 AEM for Linear Elastic Cases

As previously mentioned, the AEM is coded on MATLAB. The algorithm for a linear elastic beam analysis is split into the pre-processing, processing and post-processing stage. In the preprocessing stage, user defined input is required: determining the geometrical and material properties of the beam, the load applied and its location, as well as the boundary conditions. Given the span and the number of elements required, the meshing of the beam can be done using the *meshgrid* function on MATLAB, where the element centres are obtained, along with the vertices of the elements. The connectivities between elements are then obtained based on finding elements with shared vertices. The springs locations are then determined based on the number of springs between elements, and if elements are connected in all directions. The processing stage then commences. There are two loops in the code: the first loop goes through every pair of connected elements, while the second one loops through every pair of springs to calculate the stresses and strains in each spring.

Consider the cantilever beam shown in Figure 5.1 as an example. The code will loop through every pair of elements; 1-2, 2-3, 3-4, 1-9, 2-10, 9-10, etc. In each element loop, there is a loop to pass through all the springs between each pair of elements. For the simplicity and reduction of redundancy in analysis, every pair of elements is analysed locally and then transformed back to the global matrix. The elements are transformed to the local coordinates which have the orientation shown in Figure 5.2 and then the loop through every spring is done. The stiffness matrix for each spring is obtained and added to the global stiffness matrix. For example, the global element 1-9 is transformed from the local coordinates to global coordinates, as shown in Figure 5.2. The computational algorithm for analysing beam deflection in the elastic stage is shown in Box 5.1.

Box. 5.1.1: Applied Element method linear algorithm

1. Input: Geometric and material properties, boundary conditions, load application and method properties (number of elements, springs, etc.)
2. Calculate global springs locations
3. Loop through every pair of connected elements
 - (a) obtain nodes, dof's and coordinates of springs
 - (b) transform global coordinates to local
 - i. Loop through every spring
 - ii. Calculate stiffness matrix
 - (c) Assemble in Global stiffness matrix
4. Calculate displacement

$$u = [K]^{-1}(f_{ext}) \tag{5.1}$$

5. Calculate stress and strain from obtained deflection

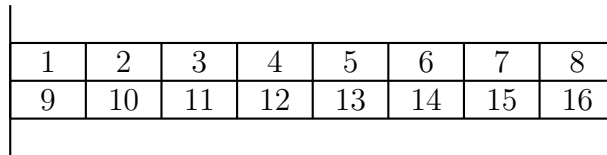


Figure 5.1: Noded cantilever beam diagram

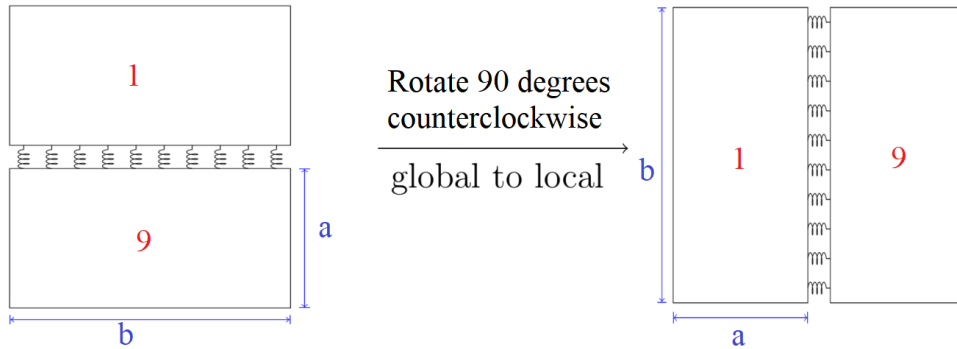


Figure 5.2: Local Orientation

The computational method is efficient and can successfully obtain the displacement between elements. If the load is applied in one time step, and no further time steps are considered or load increments implemented, then the beam is analysed by calculating the stiffness of each spring and implementing the stiffness in the local stiffness matrix, that is eventually assembled in the global stiffness matrix. When the stiffness matrix of the whole system is obtained, the deflection

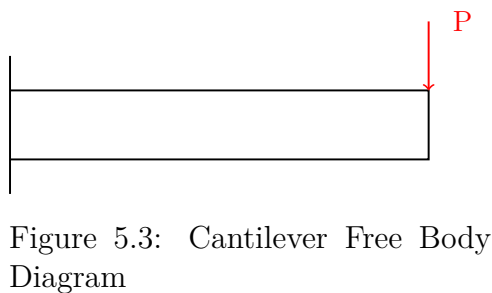
can be calculated along with corresponding stresses and strains in the system due to the applied load.

5.2 Linear Elastic Case Studies: AEM vs. FEM

This section entails the verification of the AEM code written and compared to FEM and analytical solutions, in order to quantify the accuracy of the method. In this section, simple structural elements will be analysed using AEM and compared to the finite element method using ANSYS. Analysis will be done to also find the optimal number of elements and springs needed in AEM to acquire a good level of convergence. The load in these examples is applied in one time step. No load increments are presented.

5.2.1 Cantilever Beam

Assume a cantilever beam, fixed at one end and free at the other, with a point load applied at the free end, as displayed in Figure 8.5. The material properties of the beam are shown in Table 5.1, which are of steel. The load applied is very small to allow only small deformations and elastic material behaviour. The beam will initially be analysed using the same number of elements, in both AEM and in FEM. Then a comparison of the number of elements to springs using AEM will be displayed.



Modulus of Elasticity E	200,000	[MPa]
Shear Modulus of Elasticity G	76,923	[MPa]
Yield Stress	250	[MPa]
Beam span	1	[m]
cross-section width	0.15	[m]
cross-section thickness	0.15	[m]
Applied Load	1000	[N]

Table 5.1: Beam Properties

Analytical Solution

For a cantilever beam, with a point load at the free end, the rotation, deflection at any point and the maximum deflection, are shown in Equations 5.2 - 5.4.

$$\theta = \frac{Pl^2}{2EI} \quad (5.2)$$

$$y = \frac{Px^2}{6EI}(3l - x) \quad (5.3)$$

$$\delta_{max} = \frac{Pl^3}{3EI} \quad (5.4)$$

where l is the beam length; P is the applied load, x is the point on the beam at which the deflection is to be calculated; E is the Modulus of Elasticity, and I is the moment of inertia. For an applied load of 1 kN applied at the free end, the deflection at the free end is

$$\delta_{max} = \frac{1000 \times 1^3}{3 * 210 \times 10^9 * 4.2187 \times 10^{-05}} = 3.76 \times 10^{-5}[m] \quad (5.5)$$

This deflection will be used for comparison with the solutions obtained from AEM and FEM.

Computational Solutions

The FEM solution is obtained using ANSYS. The beam deflection and normal stresses are compared. Assuming a beam with an initial number of 10 elements in the x-direction and 1 element in the y-direction, the beam deflection from ANSYS is shown in Figure 5.4, and from the MATLAB code using AEM in Figure 5.5. As seen from the figures, the distribution of the deflection is the same. The reason the FEM results appear with a higher deflection is due to the factor that the deflection is multiplied by to extenuate the deflection for better visibility.

The analytical solution for deflection at the free end of the the cantilever compared with FEM and AEM is shown in Table 5.2. The results of both the FEM and AEM showed good accordance in comparison to the analytical solution.

Figure 5.6 is the analysis of the cantilever beam from the example in Figure



Figure 5.4: ANSYS Cantilever Deflection

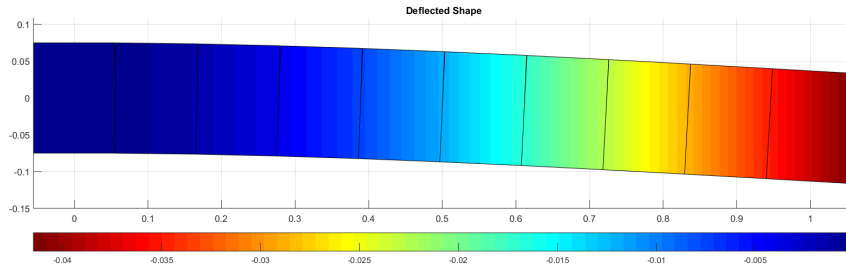


Figure 5.5: MATLAB Cantilever Deflection

Table 5.2: Small Displacement comparison

	FEM [m]	AEM [m]	Analytical [m]
Deflection	3.82×10^{-5}	3.88×10^{-5}	3.78×10^{-5}

5.5, with the load applied in the positive direction. The purpose is to validate that the deflection is the same in the opposite direction. This shows that the elements are reacting to the load in the correct way.

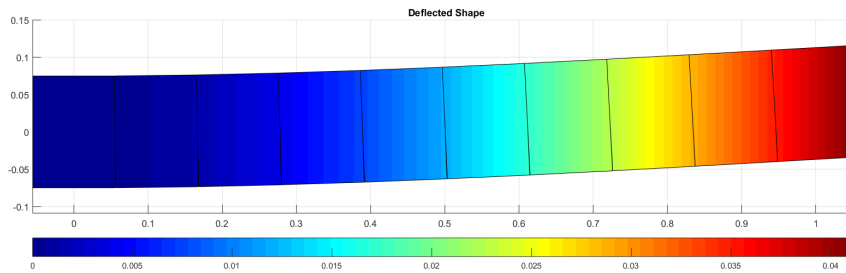


Figure 5.6: MATLAB Cantilever Deflection 10 elements in x-direction opposite load

Normal Stress

The stresses of the springs are calculated after the deflection is obtained. Figure 5.7 is the stress at each spring, for every cross section between elements. The

stresses show that the behaviour of all elements are in the linear elastic region. It can be seen that the stress distribution at each cross-section is exactly symmetric, and at the neutral axis, the stress is zero.

Figure 5.8 is the normal stress distribution across the beam from ANSYS, and Figure 5.9 displays the results from the AEM MATLAB code. A visual comparison of the figures shows that the results are almost exact. The absolute value of the normal stress is shown in the figures (this is why the red appears in both the top and bottom fibres at the sections closest to the fixed support). The maximum stress is 1.6×10^6 for both the FEM and the AEM.

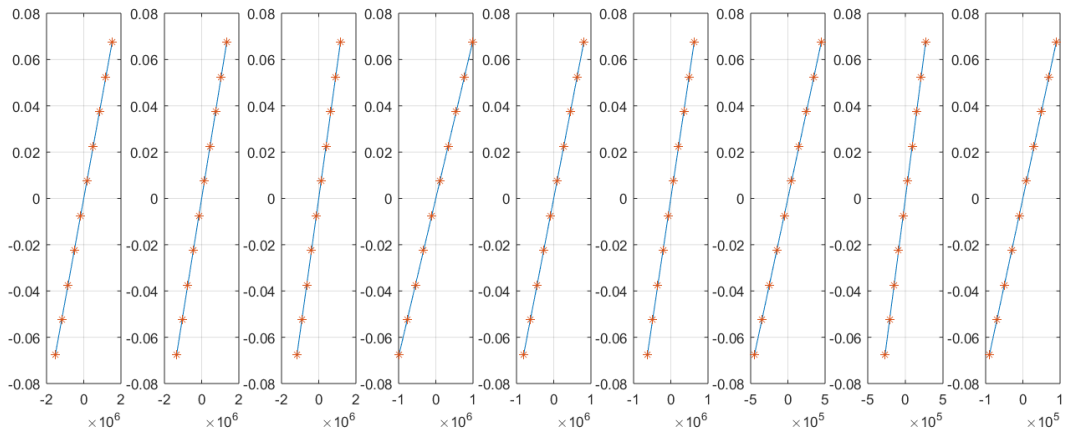


Figure 5.7: MATLAB Cantilever Normal Stress

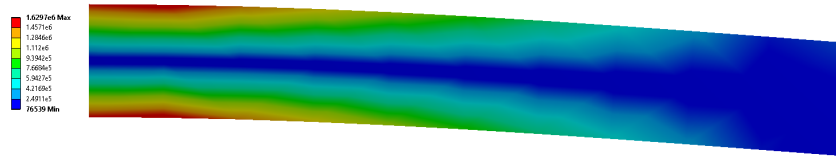


Figure 5.8: ANSYS stress distribution

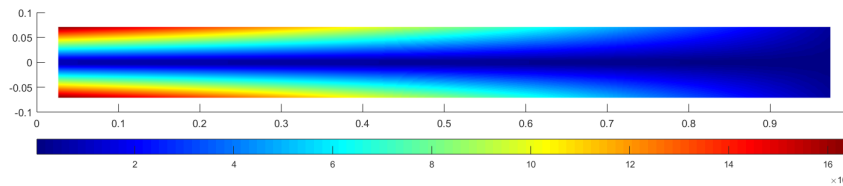


Figure 5.9: AEM stress distribution

Shear Stress

The maximum shear stress from the ANSYS was 4.8×10^4 , while it was 4.445×10^4 from the AEM. The shear stress is constant across the element. Figure 5.10 is

the shear stress using FEM, and Figure 5.11 is the shear stress from the AEM analysis. The results are quite similar as the stress is almost constant throughout the whole beam, except for the ends where the load is applied.

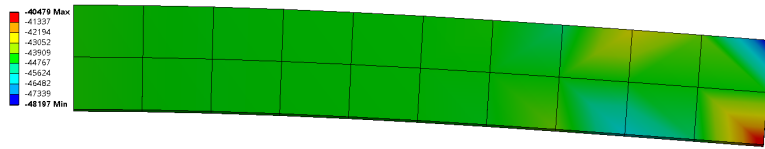


Figure 5.10: ANSYS shear stress distribution

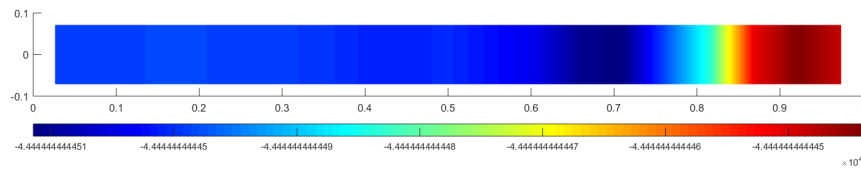


Figure 5.11: AEM shear stress distribution

Validation of Multilayer Mesh

A multilayer mesh is used to analyse the same cantilever beam as the previous sections. Recall that an element connected in all four edges will need have four contributions to the stiffness matrix. The purpose of this example is to ensure that the elements are transformed from the local to global coordinates correctly, and that adding the extra elements in the y-direction does not cause any errors. Figure 5.12 displays the deflection of the beam with the load applied in the negative y-direction. The deflection is compared to the FEM analysis and similar results were obtained. Figure 5.13 shows the deflection of the beam with the load applied in the positive y-direction. The deflection is exactly the same for the positive and negative load. This is a good indication that the system can successfully model elements that are presented in any direction.

5.2.2 Fixed End Beam

Similar to the cantilever beam analysis, a fixed end beam is analysed. The fixed end beam is fixed at both ends. A point load is applied at the midspan. The

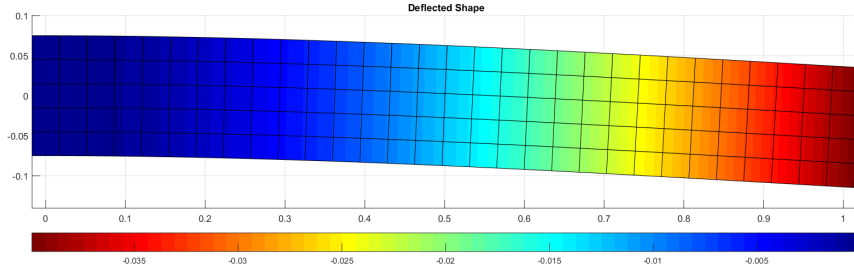


Figure 5.12: AEM Cantilever Deflection 30 elements in x, 5 elements in y

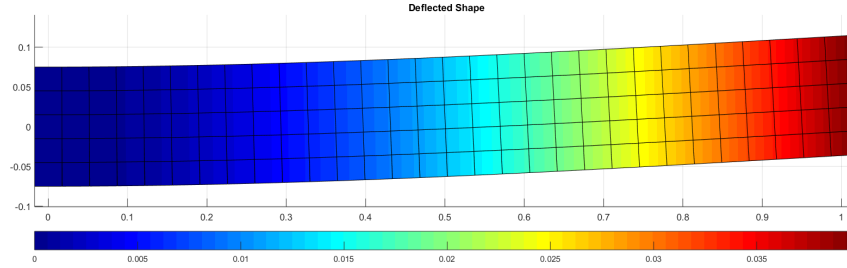


Figure 5.13: AEM Cantilever Deflection Load Positive Direction

beam properties are the same as the properties shown in Figure 5.1.

Analytical Solution

The deflection at the location of the applied load is shown in Equation 5.6.

$$\delta_{max} = \frac{Pl^3}{192EI} \quad (5.6)$$

For an applied load of $1kN$ the deflection at the location of the load is

$$\delta_{max} = \frac{1000 * 1^3}{192 * 210 * 10^9 * 4.2187 * 10^{-05}} = 5.88 * 10^{-07}[m] \quad (5.7)$$

This deflection will be used for comparison with the solutions obtained from AEM and FEM.

Computational Solution

The deflection of the fixed end beam from MATLAB is shown in Figure 5.15, where the results are scaled up to show the deflection of the beam since the displacement is very small. The beam deflection from the FEM analysis is shown

in Figure 5.14. The results in Table 5.3 show that both the FEM and AEM have similar results. However there is a difference with the analytical result. The number of elements in both the FEM and AEM analysis were exactly the same: 10 elements along the x-direction and 2 elements along the y-direction.

Table 5.3: FEB deflection Comparison

	FEM	AEM	Analytical
Deflection	7.04×10^{-7}	7.8×10^{-7}	5.88×10^{-07}



Figure 5.14: ANSYS Fixed End Beam Deflection

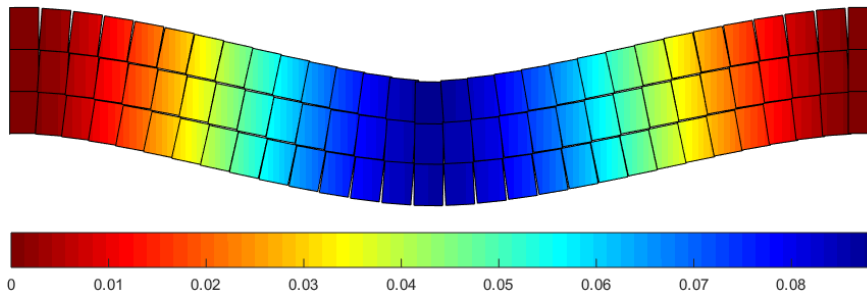


Figure 5.15: AEM Fixed End Beam Deflection

Figure 5.17 is the normal stress along the beam cross-section from the AEM in MATLAB, and Figure 5.16 displays the stress from ANSYS. The maximum stress from the AEM was $1.95 \times 10^5 [Pa]$ and from ANSYS was $1.81 \times 10^5 [Pa]$.

Figures 5.18a and 5.18b display the deflection of the beam with more elements in the y-direction. The results were exactly the same in both cases of applied loads in opposite directions.

5.2.3 Simply Supported Beam

A simply supported beam is also analysed. The boundary conditions consist of a constrained x degree-of-freedom on one side, and the x and y degrees-of-freedom on the other side.

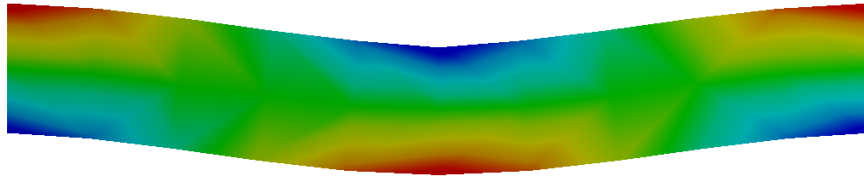


Figure 5.16: Normal stress for FEB from ANSYS

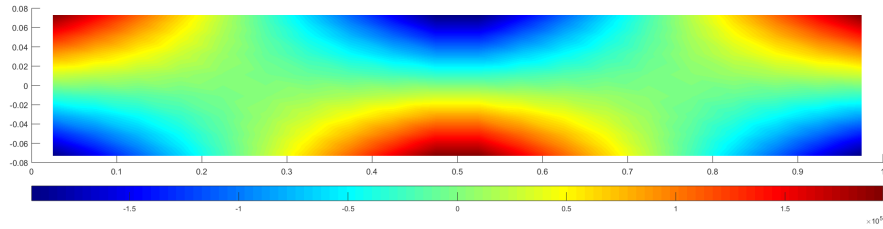
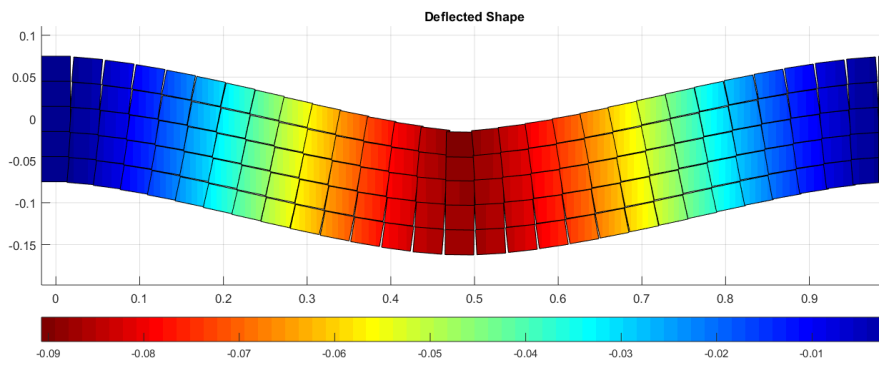
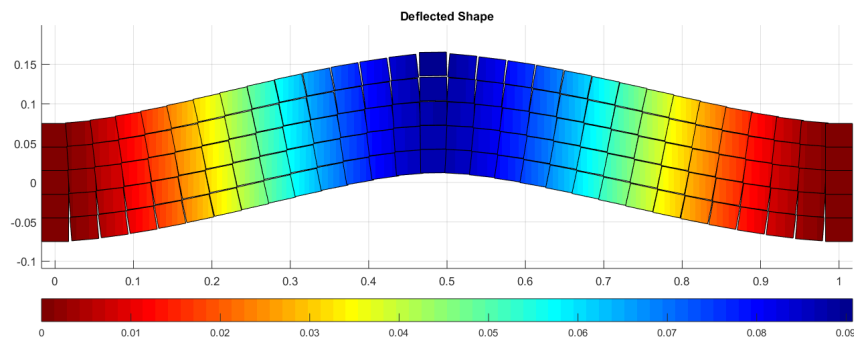


Figure 5.17: Normal stress for FEB from AEM



(a) Negative load



(b) Positive load

Figure 5.18: AEM Different loading direction for FEB

Analytical Solution

The analytical solution for the deflection of a simply supported beam with a point load at the midspan is

$$\delta_{max} = \frac{PL^3}{48EI} \quad (5.8)$$

In this case, for a point load of 1 kN, the deflection at the midspan is

$$\delta_{max} = \frac{1000 * 1^3}{48 * 210 * 10^9 * 4.2187 * 10^{-5}} = 2.35 * 10^{-6} [m] \quad (5.9)$$

Computational Solution

Figure 5.19 is the y-deflection of the beam scaled up by a factor of 10^3 , and Figure 5.20 is the absolute value of the normal stress of the beam.

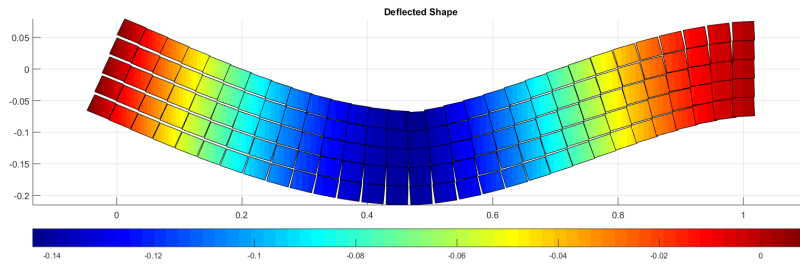


Figure 5.19: AEM Deflection Simply Supported Beam

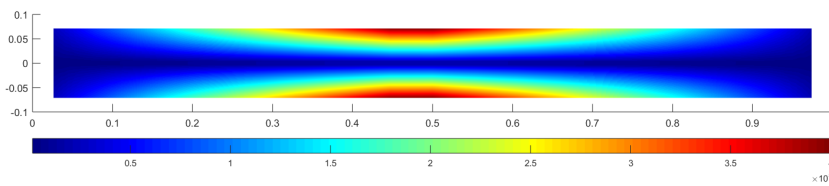


Figure 5.20: AEM Normal stress Simply Supported Beam

5.3 Gaussian Springs based AEM

For a beam, the exact second moment of inertia is needed for the stress calculation, and using the Gaussian quadrature rule with $n = 2$ points will integrate a polynomial of order $2n - 1 = 3$ exactly. Since the moment of inertia is of order

2, 2 points were sufficient. However, 50 equally spaced springs were required to obtain the same results.

Gaussian quadrature is used for finite element applications because it has fewer function evaluations for given orders. The weights and evaluation points are determined so that the integration rule is exact to as high an order as possible. Gaussian quadrature of order N for the standard interval $[-1, 1]$, is given by

$$\int_{-1}^1 g(\xi) d(\xi) = \sum_{i=1}^N w_i g(\xi_i) \quad (5.10)$$

where ξ_i and w_i are the Gaussian quadrature points and weights. A Gaussian quadrature using N points can provide the exact integral if $g(\xi)$ is a polynomial of the degree $2N - 1$ or less. The Gaussian quadrature for the general integral $I=[a,b]$ is given by

$$\int_a^b f(x) dx = \frac{b-a}{2} \int_{-1}^1 f\left(\frac{b-a}{2}x + \frac{b+a}{2}\right) dx = \frac{b-a}{2} \sum_{i=1}^n W_i f(x_i) \quad (5.11)$$

5.3.1 Gaussian Springs Implementation in AEM

The Gaussian Quadrature is implemented to a pair of 2-D AEM elements to determine the Gaussian weights and coordinates using the number of springs. The location of the springs is determined by considering w as the width of the tributary area of each spring ($'d'$ in AEM Equation 4.5), and x as the spring location from Equation 5.11.

Figure 5.21a and Figure 5.21b show the comparison of the tributary area when the distribution of the springs is equal (left), and springs are distributed using the Gaussian quadrature (on the right).

Table 5.4 shows the Gaussian and Equal spring location, x_i , and weighting factor, w_i , of each spring i for 3 springs, and Table 5.6 is the distribution for 5 springs. x_{ie} is the spring location for an equal spring, and x_{ig} is for a Gaussian spring. Similarly for w_{ie} and w_{ig} .

Assuming the width of the section is 5, then x_i and w_i are multiplied by $5/2 = 2.5$. The multiplication is presented in Tables 5.5 and 5.7 for 3 and 5 springs, respectively. Looking at row $2.5w_{ie}$ and $2.5w_{ig}$, a clear distinction of the

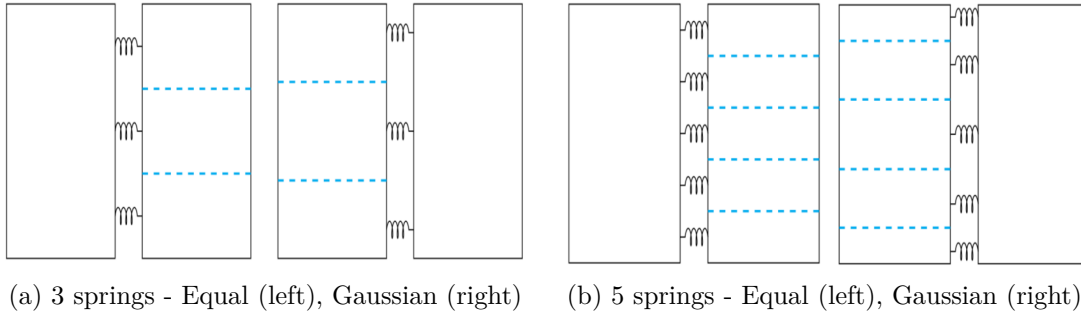


Figure 5.21: Comparison of Gaussian and Equal Springs Tributary Area for 3 and 5 springs

weight of each spring is shown. For instance for the 3 springs, the middle spring (point 2), has a weighted factor of 1.67 in the equal distribution rather than 2.2 in the Gaussian distribution.

Table 5.4: 3 springs coordinates and weighting factor

Point	x_{ie}	w_{ie}	x_{ig}	w_{ig}
1	-0.667	0.67	-0.775	0.556
2	0	0.67	0	0.889
3	0.667	0.67	0.775	0.556

Table 5.5: 3 springs w_i and x_i for cross-section 5m

Point	$2.5x_{ie}$	$2.5w_{ie}$	$2.5x_{ig}$	$2.5w_{ig}$
1	-1.668	1.67	-1.937	1.389
2	0	1.67	0	2.222
3	1.668	1.67	1.937	1.389

Table 5.6: 5 springs coordinates and weighting factor

Point	$2.5x_{ie}$	$2.5w_{ie}$	$2.5x_{ig}$	$2.5w_{ig}$
1	-2	1	-1.359	0.355
2	-1	1	-0.808	0.718
3	0	1	0	0.853
4	1	1	0.808	0.718
5	2	1	1.359	0.355

Table 5.7: 5 springs coordinates and weighting factor

Point	x_{ie}	w_{ie}	x_{ig}	w_{ig}
1	-0.8	0.4	-0.906	0.237
2	-0.4	0.4	-0.538	0.479
3	0	0.4	0	0.569
4	0.4	0.4	0.538	0.479
5	0.8	0.4	0.906	0.237

5.3.2 Comparison of equal springs with Gaussian springs

A comparison of equal and Gaussian springs will be shown to prevail the impact the distribution of the springs can have on the accuracy of the solution. As before, a cantilever beam and a fixed end beam analysis will be done, with a small linear-elastic load.

Cantilever Beam

Consider a cantilever beam with the similar properties shown from Table 5.1, and a point load applied at the free end. The only difference in the MATLAB code occurs in the spring distribution definition. For a load of 1kN, a comparison of the beam deflection is shown in Table 5.8, for an equal number of 10 elements along the x-direction, and varying springs. The results show that using the Gaussian springs distribution with just 2 springs gives almost the same deflection that was calculated with 50 equally distributed springs. The error percentage presented is the difference in the deflection at the free between the result obtained from the equal springs distribution and the Gaussian springs distribution. Therefore, a beam with 10 elements, requires a total of $10 \times 2 = 20$ Gaussian springs, or $10 \times 50 = 500$ equal springs.

Table 5.8: Deflection at free end comparison

No. springs	2	5	10	15	30	50
Equal	0.4215	0.3295	0.3196	0.3179	0.3168	0.3165
Gaussian	0.3164	0.3164	0.3164	0.3164	0.3164	0.3164
Difference	24.9%	4.0 %	1.0 %	0.5 %	0.1 %	0.0 %

Table 5.9 displays the y-deflection at each node of the beam using 2 equally-distributed springs, and 2 Gaussian springs. The y-deflection in the first element is not shown since it is fixed to zero as a boundary condition. The results show that the percentage difference in the deflection is quite different for every element, almost 25%. Table 5.10 displays the y-deflection at each node, with 50 springs per element. It can be seen that the beam deflection is almost exactly the same at every node.

It is also important to compare the data of the deflection of the elements using 2 Gaussian springs and 50 Gaussian springs, displayed in Table 5.11. It is clear that the results are exactly the same. This verifies that using Gaussian springs is much more efficient than using equally distributed springs, since the deflection of all the elements along the beam is the same.

1	2	3	4	5	6	7	8	9	10
---	---	---	---	---	---	---	---	---	----

Figure 5.22: Beam with 10 elements

Table 5.9: y-deflection of beam at every node - 2 springs

Element	2	4	5	6	8	10
Equal	-0.0075	-0.0624	-0.1063	-0.1589	-0.2831	-0.4213
Gaussian	-0.0057	-0.0469	-0.0799	-0.1193	-0.2126	-0.3162
Difference	24.0%	24.8%	24.8%	24.9%	24.9%	24.9%

Table 5.10: y-deflection of beam at every node - 50 springs

Element	2	4	5	6	8	10
Equal	-0.0057	-0.0469	-0.0799	-0.1194	-0.2127	-0.3164
Gaussian	-0.0057	-0.0469	-0.0799	-0.1193	-0.2126	-0.3162
Difference	0	0	0	-0.08%	-0.05%	-0.06 %

Table 5.11: y-deflection of beam at every node - 2 and 50 Gaussian springs

Element	2	4	5	6	8	10
2 springs	-0.0057	-0.0469	-0.0799	-0.1193	-0.2126	-0.3162
50 springs	-0.0057	-0.0469	-0.0799	-0.1193	-0.2126	-0.3162
Difference	0	0	0	0	0	0

Fixed End Beam

An analysis similar to that of the cantilever beam will be done for a fixed end beam. Tables 5.12 and 5.13, display the deflection in the y-direction of every element in the beam for elements with 2 springs and 50 springs respectively. The results show that the use of Gaussian springs is much more efficient than equally distributed springs. Elements 1 and 10 have a boundary condition of fixed displacement of 0, so they are not shown in the tables.

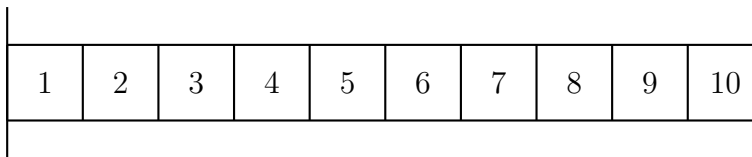


Figure 5.23: Fixed End Beam with 10 elements

Table 5.12: y-deflection of FEB at every node - 2 springs

Element	2	4	5	6	8	9
Equal	-0.0449	-0.279	-0.375	-0.395	-0.182	-0.055
Gaussian	-0.0341	-0.211	-0.283	-0.299	-0.139	-0.042
Difference	31.67 %	32.54 %	32.54 %	32.37 %	32.29 %	31.73 %

Table 5.13: y-deflection of FEB at every node - 50 springs

Element	2	4	5	6	8	9
Equal	-0.034	-0.211	-0.283	-0.299	-0.137	-0.0417
Gaussian	-0.034	-0.211	-0.283	-0.299 -0.239	-0.137	-0.0416
Difference	0	0	0.035 %	0.033 %	0.073 %	0.240 %

Therefore, it can be concluded that using a Gaussian distribution for the springs, rather than an equal spring distribution, can have a significant effect on the number of springs needed to acquire a rapid convergence in terms of solution accuracy, with a significantly low number of springs.

5.4 Conclusion

This chapter entailed an analysis difference between the FEM and the AEM, where the AEM was modelled using MATLAB. Analysis of different structural beams (a cantilever beam, a fixed ends beam and a simply supported beam), were performed to prove the validity and accuracy of the method. The maximum deflection of each beam was compared to its respective analytical solution as well as the solution from the finite element analysis, using ANSYS. The shear and normal stresses were also compared. The results showed that the applied element method is a good tool for modelling structural members in the elastic range, and the developed code is valid for future modifications in the method.

A modification to the method was presented in this chapter, since the conventional AEM required a large number of springs and elements in linear elastic solution states. The distribution of the springs by using the Gaussian quadrature, referring to the springs as Gaussian springs, is developed. Instead of using equally distributed springs along element edges, the springs are distributed based on the Gaussian quadrature. The Gaussian springs showed an advantage in the number of springs required to accurately model an elastic behaviour of a structural element.

A cantilever beam with 10 elements and a load of 1 KN applied at the free end was analysed using ANSYS for FEM results, the conventional AEM (with equally spaced springs), and the Gaussian AEM. The findings of the solutions were remarkable. It was found that a total of 50 equally spaced springs were needed to

obtain the same result as obtained from 2 Gaussian springs when compared to the FEM analysis. A comparison analysis was performed for the cantilever beam deflection of each element with 2 Gaussian springs and 50 Gaussian springs, and it the results showed that the deflection at each element was exactly the same regardless of the number of springs. The comparison analysis was also performed for a fixed ends beam, and the results were just as remarkable. The comparison was performed for analysis between FEM, conventional AEM and Gaussian AEM. When 50 equal springs were used, there was a small discrepancy of 0.03%.

In other words, for the same beam and same number of elements, the conventional AEM required a total of 500 springs, while only 20 springs were required using the Gaussian distribution. This substantially decreases the CPU time required to model the structural element, which in larger scale models will have a much larger effect.

Since the Gaussian springs showed to be much more efficient for modelling structural elements in the elastic region, the model will be extended for analysis of materials subject to elasto-plasticity, in the next chapter.

Chapter 6

Gaussian AEM in Elasto-plasticity

The goal of this research is to model the collapse behaviour of structures. Therefore materials are expected to undergo elasticity, elasto-plasticity, full plasticity, fracture and collapse. To model the complete behaviour from an initial state of no loading until total collapse, all the stages must be considered.

This chapter is an introduction to constitutive models and their applications for material behaviour in elasto-plasticity. A constitutive model is implemented to the MATLAB code, and analysis results are shown for different structural members where comparisons of deflections and stresses are performed. The Gaussian AEM, which was developed in the previous chapter, is implemented for hardening elasto-plasticity and a modification is presented to implement adaptive springs that are based on the yield criteria. The efficiency of the modification is also presented.

6.1 Overview

The theory of plasticity is based on solids that sustain permanent deformations when completely unloaded, after being subjected to a loading. This theory is regarded as one of the most successful phenomenological constitutive models of solid materials [68].

Consider a uniaxial tension experiment with a metallic bar in order to il-

illustrate features of the phenomenological behaviour of materials. The uniaxial tension tests produce stress-strain curves, as shown in Figure 6.1. The axial stress, σ , is plotted against the axial strain, ϵ , where the bar is subjected to an increase in axial stress from zero to a prescribed values, σ_0 . The bar is then unloaded, and subsequently loaded to a higher stress level, σ_1 , and produces the corresponding stress-strain curve. In the initial line segment O_0Y_0 , the bar is regarded as linear elastic. Loading and unloading before reaching Y_0 , the bar will remain linearly elastic. After Y_0 the slope changes and the bar is in plastic range where it will undergo permanent plastic deformation. At point Z_0 (for instance), if the bar is unloaded it will follow the same linear elastic behaviour as from O_0Y_0 . The new permanent shape is observed from the unstressed state O_1 , instead of O_0 .

The vital phenomenological properties from the uniaxial test are as follows [68]: (1) an elastic domain exists, (2) plastic yielding takes place if the material is loaded further than the yield stress, and (3) the evolution of the plastic strain is also observed, known as hardening (in Figure 6.1 Y_0 and Y_1 are observed to have different yielding stresses). These material behaviours are observed in metals, concrete, soils, rocks and others [68]. This nonlinear material behaviour will be tested in the developed MATLAB code in the following sections.

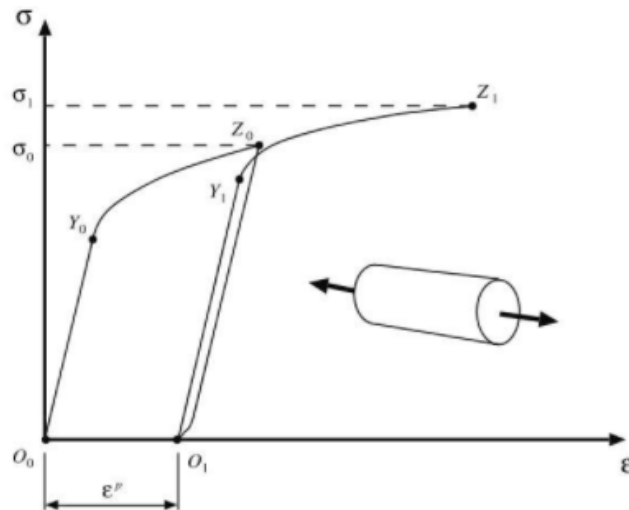


Figure 6.1: Uniaxial Tension Test [68]

In order to represent this material behaviour, mathematical theory of plasticity must be used to demonstrate continuum constitutive models that are capable

of describing the phenomenological behaviour of materials, quantitatively and qualitatively, with sufficient accuracy. Characterising material behaviour from the initial stages of loading until final stages of failure, or modelling material behaviour with instabilities require complex models of the material behaviour which are obtained through constitutive modelling.

Different engineering materials require different constitutive models due to the difference in the physical mechanisms of the material degradation at the macroscopic level. However, materials show similar mechanical behaviour, such as: elasticity, yielding, plastic strain, strain induced anisotropy, damage by monotonic loading and crack growth. Therefore, models may be developed to display the common behaviour of materials, using continuum mechanics without requiring the complex physical micro structures of the materials, and these models are the constitutive models. In other words, constitutive models are the mathematical simplification of the complex physical behaviour. The mathematical structure of a model depends on the material and the purpose (loading conditions). Different purposes may include [69]:

1. Structural analysis under working load: Linear elasticity
2. Analysis of damped vibrations: Viscoelasticity
3. Calculation of limit load: Rigid perfect plasticity
4. Accurate calculation of permanent deformation after monotonic and cyclic loading: Hardening elasto-plasticity
5. Analysis of stationary creep and relaxation: Perfect (non-hardening) elasto-viscoplasticity
6. Prediction of lifetime in high-cycle-fatigue: Damage coupled to elastic deformations
7. Prediction of lifetime in low-cycle-fatigue: Damage coupled to plastic deformations
8. Prediction of lifetime in creep and creep-fatigue: Damage coupled to viscoplastic deformations
9. Prediction of stability of a pre-existing crack: Linear elasticity (from which singular stress fields are derived for sharp cracks)
10. Prediction of strain localization in shear bands and incipient material fail-

ure: Softening plasticity or damage coupled to plastic deformation

In the scope of this thesis, the linear elasticity, perfect plasticity, hardening elasto-plasticity and softening plasticity are demonstrated.

6.2 Definitions

In this section, a brief description of how a constitutive model typically works, and the conditions that must be satisfied are explained. The following section entails detailed constitutive equations and derivations. The terminology used in modelling plasticity is presented here and is based on terminology from [70].

Elastic strain, ε^e , is any strain that occurs before exceeding the yield stress. The plastic strain, ε^p , is the permanent strain that remains after unloading. The total strain is the sum of the elastic strain and plastic strain. When plastic strain is taking place, then it follows that plastic flow is taking place. Internal hardening variables are used when hardening takes place, because when hardening occurs the yield stress changes. The internal variables keep track of the plastic strain. The isotropic internal hardening variable, α , is the equivalent plastic strain [71].

A yield condition is used to determine when yielding occurs, denoted by f . The yield condition usually includes the current stress minus the initial yield stress added to a function of α , which describes the type of hardening. When plastic strain occurs, α is updated. The yield condition f is then calculated, and results in either a positive or negative value.

If a positive result is obtained from the yield condition, then the stress is currently greater than the yield stress, which means that the elastic and plastic strains are increasing. However, $f > 0$ is not permitted, and the amount of plastic flow and hardening such that the condition $f = 0$ is satisfied must be calculated.

For this, a consistency parameter λ is introduced to determine the level of plastic flow and hardening required to achieve the condition $f = 0$. The process of elastic or elasto-plastic loading and unloading requires a mathematical description, which led to the use of the Kuhn-Tucker conditions that are used to develop the mathematical algorithms to model the plastic flow [71].

The Kuhn-Tucker conditions are: $\lambda \geq 0$, $f(\sigma) \leq 0$ and $\lambda f(\sigma) = 0$. Plastic-

ity algorithms are often used to model nonlinear material behaviour which are incremental in nature. As the load increment increases, the stresses, strains and displacements also increase. The initial displacement is assumed to be in the elastic region, and the resulting new stress is defined as a trial stress. The trial stress is placed in the yield function f , and the algorithm is applied. The algorithm "corrects" the trial stress to a new stress if it is not elastic. Assuming the current values of the internal variable α is α_n , then during the load increment α may increase by $\Delta\alpha$ and, $\alpha_{n+1} = \alpha_n + \Delta\alpha$. For this reason, for a rate independent material, the load increment is like a time increment.

Another important issue to consider is that the tangent modulus is equivalent to the elasto-plastic modulus, which is not true in higher dimensions. This causes difficulty in solving the consistency parameter and this issue can be overlooked by using the Newton-Raphson method. To obtain a second order convergence, the derivative of the stress to the total strain must be taken. The algorithmic tangent modulus is defined as $C_{n+1}^k = \frac{\partial\sigma_{n+1}^k}{\partial\varepsilon_{n+1}^k}$. The way that plastic strain evolves in plasticity algorithms is referred to as the flow rule, which takes the form of $\dot{\varepsilon}^p = \lambda \frac{df}{d\sigma} = \lambda \text{sign}(\sigma)$. The isotropic hardening law takes the form of $\dot{\alpha} = \Delta\alpha = \lambda$ [71].

The definitions have now been explained as well as the logic behind the constitutive equations in plasticity. The following section is a derivation of the equations used and implementation of the computational algorithm.

6.3 Elasto-plastic Constitutive Equations Derivation

Deformations of elasto-plastic solids at small strains are characterized by the additive split of the total strain

$$\varepsilon = \varepsilon^e + \varepsilon^p \tag{6.1}$$

where ε is the total strain, ε_e is the elastic reversible strain, and ε_p is the plastic permanent strain. Hence, the elastic strain can be defined as

$$\varepsilon^e = \varepsilon - \varepsilon^p \quad (6.2)$$

The stress σ is governed by the elastic constitutive equation (when $f < 0$), and is calculated as

$$\sigma = E\varepsilon^e = E(\varepsilon - \varepsilon^p) \quad (6.3)$$

The phenomenological properties that were described in section 6.1 must be satisfied in the constitutive equations [68].

The stress cannot be greater in absolute value than σ_Y . Therefore, the stresses cannot exceed the closed interval $[-\sigma_Y, \sigma_Y]$ where σ_Y is the yield stress. This condition is formally expressed as

$$\mathbb{E}_\sigma = \sigma \in \mathbb{R} | f(\sigma) := |\sigma| - \sigma_Y \leq 0 \quad (6.4)$$

where σ_y is the yield stress and f is the yield function. If $|\sigma|$ is less than the flow stress, no change in ε^p occurs, so

$$\dot{\varepsilon}^p = 0, \quad \text{if } f(\sigma) < 0 \quad (6.5)$$

Plastic strain occurs when the yield criterion is satisfied; $f(\sigma) := |\sigma| - \sigma_Y = 0$. Introducing a parameter $\dot{\lambda} \geq 0$ as $\dot{\lambda} = |\dot{\varepsilon}^p|$, the plastic slip can be expressed as

$$\dot{\varepsilon}^p = \dot{\lambda}, \quad \text{if } \sigma = \sigma_Y \quad (6.6)$$

$$\dot{\varepsilon}^p = -\dot{\lambda}, \quad \text{if } \sigma = -\sigma_Y \quad (6.7)$$

This may be written as Equation 6.8, and is known as the flow rule.

$$\dot{\varepsilon}^p = \dot{\lambda} \text{sign}(\sigma) \quad (6.8)$$

The sign function is defined as

$$\text{sign}(\sigma) = \begin{cases} +1 & \text{if } \sigma > 0 \\ -1 & \text{if } \sigma < 0 \end{cases} \quad (6.9)$$

The boundary of the elastic range is called the yield surface, and is defined as

$$\partial\mathbb{E}_\sigma = \{\sigma \in \mathbb{R} | f(\sigma) := |\sigma| - \sigma_Y = 0\} \quad (6.10)$$

From the above discussion it follows that σ must be valid ($\sigma \in \mathbb{E}$) and $\dot{\lambda}$ must be non-negative [72, 73]

$$\dot{\lambda} \geq 0, f(\sigma) \leq 0 \quad (6.11)$$

Also if

$$f(\sigma) < 0 \Rightarrow \dot{\lambda} = 0, \quad (6.12)$$

$$\dot{\lambda} > 0 \Rightarrow f(\sigma) = 0, \quad (6.13)$$

which implies

$$\dot{\lambda} f(\sigma) = 0 \quad (6.14)$$

Conditions 6.11 and 6.13 are the Kuhn-Tucker conditions. Now consider a Taylor expansion of the function

$$\hat{f}(t + \Delta t) = \hat{f}(t) + \dot{\hat{f}}(t)\Delta t + (O)(\Delta t) \quad (6.15)$$

where $\dot{\hat{f}}(t) = \frac{\partial}{\partial t}\hat{f}(t)$ and $(O)(\Delta t)$ represents the Taylor series terms that tend to zero faster than Δt . Since the assumption $\hat{f}(t) = 0$, it has $\dot{\hat{f}}(t) \leq 0$. Therefore

$$\dot{\hat{f}} < 0 \Rightarrow \dot{\lambda} = 0 \quad (6.16)$$

$$\dot{\lambda} > 0 \Rightarrow \dot{\hat{f}} = 0 \quad (6.17)$$

which implies that

$$\dot{\lambda} \dot{f}(\sigma) = 0 \quad (6.18)$$

The 1-D model for rate independent perfect elasto-plasticity [72] is shown as follows in Box 6.3.

Box. 6.3.1: 1-D Model for rate independent perfect elasto-plasticity

1. Additive strain split: $\varepsilon = \varepsilon^e + \varepsilon^p$ [eq.6.1]
2. Elastic constitutive law: $\sigma = E\varepsilon^e$ [eq.6.3]
3. Yield criterion: $f(\sigma) := |\sigma| - \sigma_Y \leq 0$ [eq.6.4]
4. Flow rule: $\dot{\varepsilon}^p = \dot{\lambda} \text{sign}(\sigma)$ [eq.6.8]
5. Kuhn-Tucker (loading/unloading) conditions: $\dot{\lambda} \geq 0, f(\sigma) \leq 0, \dot{\lambda} f(\sigma) = 0$ [eq.6.11, 6.13]
6. Consistency condition $\dot{\lambda} \dot{f}(\sigma) = 0$, Equation 6.14

6.4 Strain Hardening

Strain hardening occurs when a solid is plastically deformed, then unloaded, and then re-loaded so as to induce further plastic flow. It will be found that its resistance to plastic flow would have increased; its yield point/elastic limit increases. For a finite element material model, there are two ways for modelling the strain hardening:

1. Isotropic Hardening: plastically deform a solid, then unload it, then reload it again. It will be found that the yield stress/elastic limit would have increased in comparison to the first cycle. In other words, if something was loaded in tension past its yield point, then unloaded, and then loaded in compression, it will not yield in compression until it reaches the level past yield achieved when loading in tension.
2. Kinematic Hardening: correctly model cyclic behaviour and the Bauschinger effect, since the material softens in compression.

In the scope of this research, only the isotropic hardening is considered.

Isotropic Hardening

The mathematical representation for the yield criterion in isotropic hardening is:

$$f(\sigma, \alpha) = |\sigma| - [\sigma_Y + H\alpha] \leq 0 \quad (6.19)$$

where α is a hardening parameter (internal variable) that describes the evolution of the elastic domain, and $\alpha > 0$. There are several ways to represent α . The most widely used approach represents strain and work hardening respectively as

$$\dot{\alpha} = |\dot{\varepsilon}^p|, \text{ and } \dot{\alpha} = \sigma |\dot{\varepsilon}^p| \quad (6.20)$$

The 1-D Model for rate independent isotropic hardening elasto-plasticity is presented in Box 6.4.

Box. 6.4.1: 1-D Model for rate independent isotropic hardening elasto-plasticity

1. Additive strain split: $\varepsilon = \varepsilon^e + \varepsilon^p$ [eq.6.1]
2. Elastic constitutive law: $\sigma = E\varepsilon^e$ [eq.6.3]
3. Yield criterion: $f(\sigma, \alpha) = |\sigma| - [\sigma_Y + H\alpha] \leq 0$ [eq.6.19]
4. Flow rule and hardening Law: $\dot{\varepsilon}^p = \dot{\lambda} \text{sign}[\sigma]$, $\dot{\alpha} = |\dot{\varepsilon}^p|$ [eq.6.8,6.20]
5. Kuhn-Tucker loading/unloading conditions: $\dot{\lambda} \geq 0$, $f(\sigma, \alpha) \leq 0$, $\dot{\lambda} f(\sigma, \alpha) = 0$ [eq.6.11, 6.13]
6. Consistency condition, Equation 6.14

Tangent Elasto-plastic Modulus

The tangent modulus $\hat{C} = d\sigma/d\varepsilon$ is obtained by explicitly solving for the parameter $\dot{\lambda}$. The consistency condition is used for this purpose.

$$\dot{f}(\sigma, \alpha) = \frac{\partial f(\sigma, \alpha)}{\partial \sigma} \dot{\sigma} + \frac{\partial f(\sigma, \alpha)}{\partial \alpha} \dot{\alpha} \quad (6.21)$$

taking the partial derivative with respect to σ and α gives

$$\frac{\partial f(\sigma, \alpha)}{\partial \sigma} \dot{\sigma} = |\dot{\sigma}| = |E\dot{\varepsilon}^e| = |E(\dot{\varepsilon} - \dot{\varepsilon}^p)| = \text{sign}[\sigma] E(\dot{\varepsilon} - \dot{\varepsilon}^p) \quad (6.22)$$

$$\frac{\partial f(\sigma, \alpha)}{\partial \alpha} \dot{\alpha} = -H\dot{\alpha} \quad (6.23)$$

From Equation 6.21, the tangent elasto-plastic modulus is:

$$\dot{f}(\sigma, \alpha) = \text{sign}[\sigma] E(\dot{\varepsilon} - \dot{\varepsilon}^p) - H\dot{\alpha} = \text{sign}[\sigma] E(\dot{\varepsilon} - \dot{\varepsilon}^p) - H\dot{\varepsilon}^p \quad (6.24)$$

From Equation 6.20,

$$\begin{aligned} \dot{f}(\sigma, \alpha) &= \text{sign}[\sigma] E(\dot{\varepsilon} - \dot{\varepsilon}^p) - \dot{\varepsilon}^p H \\ &\rightarrow \text{sign}[\sigma] (E\dot{\varepsilon} - \dot{\varepsilon}^p (E + H)) \end{aligned} \quad (6.25)$$

By using the flow rule, Equation 6.8: $\dot{\lambda} = \dot{\varepsilon}^p \text{sign}[\sigma]$

$$\dot{f}(\sigma, \alpha) = \text{sign}[\sigma] E\dot{\varepsilon} - \dot{\lambda}(E + H) \quad (6.26)$$

By using the consistency condition that $\dot{f}(\sigma, \alpha) = 0$, then solving for $\dot{\lambda}$, gives

$$\dot{\lambda} = \frac{\text{sign}[\sigma] E}{E + H} \dot{\varepsilon} \quad (6.27)$$

Hence, the following rate form is obtained

$$\dot{\sigma} = \begin{cases} E\dot{\varepsilon} & \text{if } f < 0 \\ \frac{EH}{E+H} & \text{if } f = 0 \end{cases} \quad (6.28)$$

6.5 Incremental 1D rate independent plasticity

Assuming equal time steps Δt , the discrete time instances t_0, t_1, t_2, \dots are indicated by subscripts; generally denoted as equation 6.30, so the strain increment is

denoted as ε_{n+1} :

$$t_{n+1} = t_n + \Delta t \quad (6.29)$$

$$\varepsilon_{n+1} = \varepsilon_n + \Delta\varepsilon_n \quad (6.30)$$

The backward Euler method is used to transform the equations to incremental form at time instant t_{n+1} . The algebraic equations become [72];

1. Flow rule

$$\frac{\varepsilon_{n+1}^p - \varepsilon_n^p}{\Delta t} = \frac{\Delta\lambda}{\Delta t} \text{sign}(\sigma_{n+1}) \quad (6.31)$$

2. Isotropic Hardening Law

$$\frac{\alpha_{n+1} - \alpha_n}{\Delta t} = \frac{\Delta\lambda}{\Delta t} \quad (6.32)$$

3. Yield function

$$f(\sigma_{n+1}, \alpha_{n+1}) = |\sigma_{n+1}| - (\sigma_y + H\alpha_{n+1}) \quad (6.33)$$

4. Complementary conditions

$$\Delta\lambda \geq 0, \quad f_{n+1} \leq 0, \quad \Delta\lambda f_{n+1} = 0 \quad (6.34)$$

Since there are two inequalities that do not give a direct solution, operator splitting is applied to get rid of them: predictor and corrector.

6.5.1 Elastic step (Predictor Step)

The elastic trial step is first done by freezing the plastic flow: $\Delta\lambda = 0$. This state is admissible only when the incremental process is elastic.

$$\varepsilon_{n+1}^{p,trial} = \varepsilon_n^p \quad (6.35)$$

$$\sigma_{n+1}^{trial} = E(\varepsilon_{n+1} - \varepsilon_n^p) = E((\varepsilon_{n+1} - \varepsilon_n) + (\varepsilon_n - \varepsilon_n^p)) = \sigma_n + E\Delta\varepsilon_n \quad (6.36)$$

$$\alpha_{n+1}^{trial} = \alpha_n \quad (6.37)$$

$$f_{n+1}^{trial} = |\sigma_{n+1}^{trial}| - (\sigma_Y + H\alpha_n) \quad (6.38)$$

6.5.2 Plastic step (Corrector Step)

If $f_{n+1}^{trial} \leq 0$ the trial state is admissible. So, $\varepsilon_{n+1}^p = \varepsilon_n^p$, $\alpha_{n+1} = \alpha_n$ and $\sigma_{n+1} = \sigma_{n+1}^{trial}$. However if $f_{n+1}^{trial} > 0$ then the trial state is violating the complimentary condition that $f(\alpha, \sigma) < 0$ and $\Delta\lambda > 0$ is required. In other words if $f_{n+1}^{trial} \leq 0$ then this is an elastic step and $\Delta\lambda = 0$. If $f_{n+1}^{trial} > 0$, then this is a plastic step and $\Delta\lambda > 0$, and a return mapping algorithm can be implemented to accommodate for that.

6.5.3 Return Mapping

As mentioned earlier, the return mapping algorithm is implemented because the trial stress lies outside of the yield surface. The return mapping algorithm brings the stress that lies outside the plastically admissible domain back to the yield surface. Figure 6.2 is a visual representation of the return mapping scheme [68], where Figure 6.2a shows that the elastic predictor takes σ_n to σ_{n+1}^{trial} , and the plastic corrector will bring back σ_{n+1}^{trial} to σ_{n+1} the new (updated) yield surface (graphically shown as ϕ , otherwise presented in this thesis as f). In Figure 6.2b, the predictor-corrector is similar. However since there is no hardening (perfect plasticity), the plastic corrector will place σ_{n+1} at the initial yield surface. The first of this algorithm was presented by **Wilkins1984** in the "radial return method" [**Wilkins1984**].

An expression for σ_{n+1} in terms of σ_{n+1}^{trial} must be written

$$\sigma_{n+1} = E(\varepsilon_{n+1} - \varepsilon_{n+1}^p) \quad (6.39)$$

$$= E(\varepsilon_{n+1} - \varepsilon_n^p) - E(\varepsilon_{n+1}^p - \varepsilon_n^p) \quad (6.40)$$

$$= \sigma_{n+1}^{trial} - E\Delta\lambda sign(\sigma_{n+1}) \quad (6.41)$$

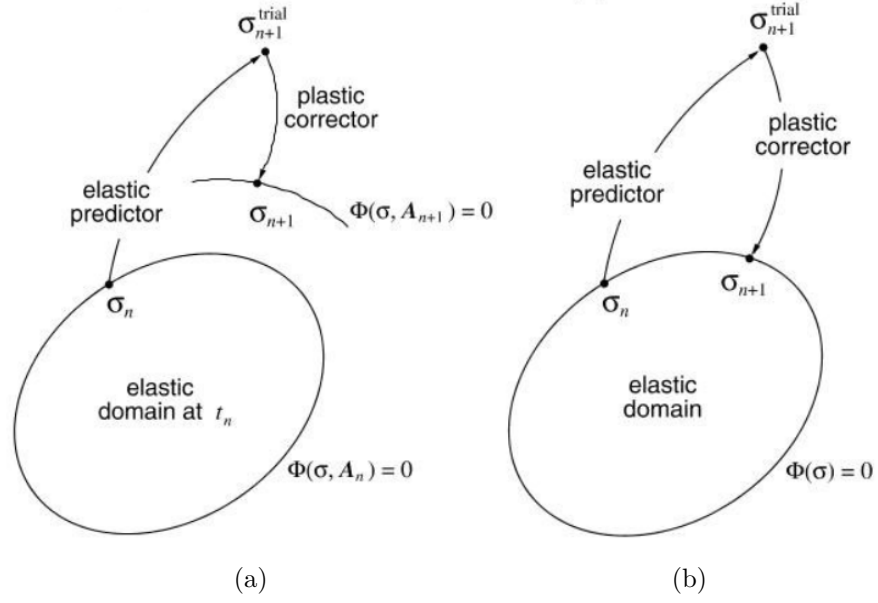


Figure 6.2: Return mapping scheme (a) with hardening (b) no hardening [68]

Applying this expression in incremental Equations 6.35 - 6.45 gives

$$\sigma_{n+1} = \sigma_{n+1}^{trial} - E\Delta\lambda \text{sign}(\sigma_{n+1}) \quad (6.42)$$

$$\varepsilon_{n+1}^p = \varepsilon_n^p + \Delta\lambda \text{sign}(\sigma_{n+1}) \quad (6.43)$$

$$\alpha_{n+1} = \alpha_n + \Delta\lambda \quad (6.44)$$

$$f_{n+1} = |\sigma_{n+1}^{trial}| - (\sigma_Y + H\alpha_{n+1}) = 0 \quad (6.45)$$

The sign of the stress is the sign of the trial stress [72]

$$\sigma_{n+1} = |\sigma_{n+1}| \text{sign}(\sigma_{n+1}) = |\sigma_{n+1}^{trial}| \text{sign}(\sigma_{n+1}^{trial}) - E\Delta\lambda \text{sign}(\sigma_{n+1}) \quad (6.46)$$

$$\Rightarrow (|\sigma_{n+1}| + \Delta\lambda E) \text{sign}(\sigma_{n+1}) = |\sigma_{n+1}^{trial}| \text{sign}(\sigma_{n+1}^{trial}) \quad (6.47)$$

$$\Rightarrow \text{sign}(\sigma_{n+1}) = \text{sign}(\sigma_{n+1}^{trial}) \quad (6.48)$$

$$\Rightarrow (|\sigma_{n+1}| + \Delta\lambda E) = |\sigma_{n+1}^{trial}| \quad (6.49)$$

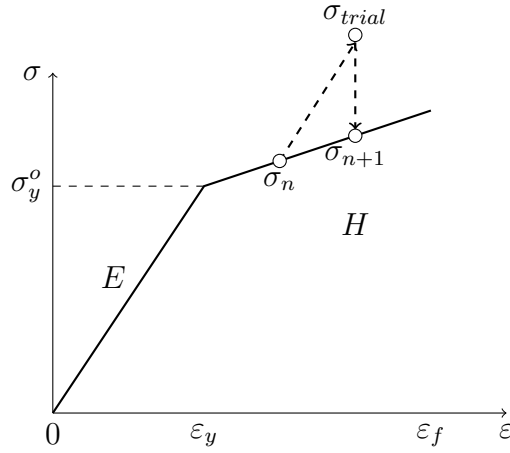


Figure 6.3: Return Mapping with hardening

Therefore [72]

$$f_{n+1} = |\sigma_{n+1}| - (\sigma_Y + H\alpha_{n+1}) \quad (6.50)$$

$$= |\sigma_{n+1}^{trial}| - \Delta\lambda - (\sigma_Y + H\alpha_{n+1}) \quad (6.51)$$

$$= |\sigma_{n+1}^{trial}| - \Delta\lambda - (\sigma_Y + H\alpha_n) - H(\alpha_{n+1} - \alpha_n) \quad (6.52)$$

$$= f_n^{trial} - \Delta\lambda(E + H) = 0 \quad (6.53)$$

$$\Rightarrow \Delta\lambda = \frac{F_{n+1}^{trial}}{E + H} \quad (6.54)$$

Hence [72]

$$\sigma_{n+1} = \sigma_{n+1}^{trial} - E\Delta\lambda \text{sign}(\sigma_{n+1}^{trial}) \quad (6.55)$$

$$\varepsilon_{n+1}^p = \varepsilon_n^p + \Delta\lambda \text{sign}(\sigma_{n+1}^{trial}) \quad (6.56)$$

$$\alpha_{n+1} = \alpha_n + \Delta\lambda \quad (6.57)$$

$$f_{n+1} = 0 \quad (6.58)$$

Another visual representation of the return mapping algorithm is shown in Figure 6.3 where from σ_n to σ_{trial} is the predictor step, and then σ_{trial} to σ_{n+1} is the corrector (plastic) step.

The return mapping algorithm is summarised in Box 6.5.3 [72].

Box. 6.5.1: Incremental 1D Return-mapping (predictor-corrector) plasticity

1. Evaluate elastic predictor:

$$\sigma_{n+1}^{trial} = \sigma_n + E\Delta\varepsilon_n \text{ [Eq. 6.36]}$$

2. Discrete version of Khun-Tucker conditions:

$$f_{n+1}^{trial} = |\sigma_{n+1}^{trial}| - \sigma_Y + H\alpha_n \text{ [eq.6.45]}$$

3. **If** $f_{n+1}^{trial} \leq 0 \rightarrow$ Elastic state

- (a) $(\bullet)_{n+1} = (\bullet)_{n+1}^{trial}$
- (b) Exit

Else \rightarrow Plastic corrector

- (a) $\Delta\lambda = \frac{F_{n+1}^{trial}}{E+H}$
- (b) $\sigma_{n+1} = \sigma_{n+1}^{trial} - E\Delta\lambda \text{sign}(\sigma_{n+1}) \text{ [Eq. 6.42]}$
- (c) $\varepsilon_{n+1}^p = \varepsilon_n^p + \Delta\lambda \text{sign}(\sigma_{n+1}) \text{ [Eq. 6.43]}$
- (d) $\alpha_{n+1} = \alpha_n + \Delta\lambda \text{ [Eq. 6.44]}$

4. Repeat steps

6.6 Application of AEM to elasto-plasticity

Equations [6.42 - 6.44] are generally nonlinear and must be solved using some iterative procedures [68]. The common iterative procedure used in solving the return mapping equations is the Newton-Raphson method. The motivation of using this method is due to its quadratic rate of convergence [68]. The method is explained in the following section.

6.6.1 Newton Raphson Method

As mentioned, the Newton Raphson method is an efficient nonlinear equation solution scheme with a quadratic convergence. For the infinitesimal incremental boundary value problem, given the internal variables α_n at time t_n such that

$$\int_{\Omega} [\hat{\sigma}(\alpha_n, \nabla^s u_{n+1}) : \nabla^s \eta - b_{n+1} \cdot \eta] dv - \int_{\partial\Omega_t} t_{n+1} \cdot \eta da = 0 \quad (6.59)$$

where b_{n+1} and t_{n+1} are the body force and the surface traction fields prescribed at time instant t_{n+1} . Equation 6.59 can be reduced after a standard finite element discretisation. Let u_{n+1} be the nodal displacement at time t_{n+1} , the incremental finite element equation becomes

$$r(u_{n+1}) \equiv f_{int}(u_{n+1}) - f_{n+1}^{ext} = 0 \quad (6.60)$$

where $f_{int}(u_{n+1})$ and f_{n+1}^{ext} are assembled from the element vectors in Equations 6.61 and 6.62. The nonlinearity in Equation 6.60 is from the incremental constitutive function that takes part in the definition of the element internal force vector [68].

$$f_{(e)}^{int} = \int_{\Omega^{(e)}} B^T \hat{\sigma}(\alpha_n, \varepsilon(u_{n+1})) dv \quad (6.61)$$

$$f_{(e)}^{ext} = \int_{\Omega^{(e)}} N^T b_{n+1} dv + \int_{\partial\Omega^{(e)}} N^T t_{n+1} da \quad (6.62)$$

The loading is described by the body force and the surface traction fields at an instant t_{n+1} by

$$b_{n+1} = \lambda_{n+1} \tilde{b} \quad (6.63)$$

$$t_{n+1} = \lambda_{n+1} \tilde{t} \quad (6.64)$$

where λ_{n+1} is the load factor at t_{n+1} and \tilde{b} and \tilde{t} are prescribed constant fields in time [68]. The global external force reduces to

$$f_{n+1}^{ext} = \lambda_{n+1} \bar{f}^{ext} \quad (6.65)$$

where \bar{f}^{ext} is computed only once at the beginning of the incremental procedure for the element vectors as [68]

$$\bar{f}_{(e)}^{ext} = \int_{\Omega^{(e)}} N^T \tilde{b} dv + \int_{\partial\Omega_t^{(e)}} N^T \tilde{t} da \quad (6.66)$$

The typical iteration of the Newton-Raphson scheme consists of solving the linear(ised) system of equations for $\delta u^{(k)}$ [68]

$$K_T \delta u^{(k)} = -r^{(k-1)} \quad (6.67)$$

where the the residual vector is

$$r^{(k-1)} \equiv f^{int}(u_{n+1}^{(k-1)}) - f_{n+1}^{ext} \quad (6.68)$$

and K_T is the global tangent stiffness matrix obtained from the applied element method. With the solution of $\delta u^{(k)}$, applying the Newton correction to the global displacement gives [68]

$$u_{n+1}^{(k)} = u_{n+1}^{(k-1)} + \delta u^{(k)} \quad (6.69)$$

and in terms of displacement increments [68]

$$u_{n+1}^{(k)} = u_n + \Delta u^{(k)} \quad (6.70)$$

where $\Delta u^{(k)}$ is the incremental displacement vector

$$\Delta u^{(k)} = \Delta u^{(k-1)} + \delta u^{(k)} \quad (6.71)$$

The Newton Raphson iterations are repeated until the following convergence criteria are satisfied

$$\frac{|r^{(i)}|}{f_{n+1}^{ext}} \leq \epsilon_{tol} \quad (6.72)$$

where ϵ_{tol} is a small specified value for equilibrium convergence tolerance. The schematic representation of the Newton-Raphson iteration procedure is shown in Figure 6.4.

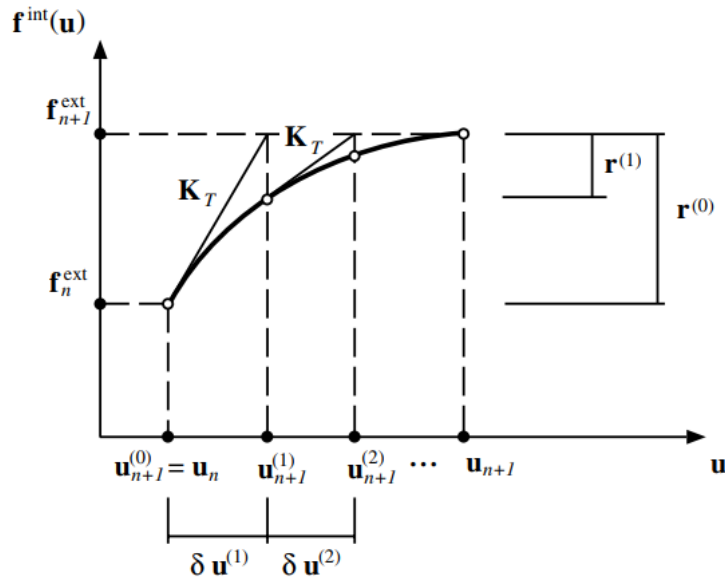


Figure 6.4: Newton Raphson iteration - graphical representation [68]

6.7 Gaussian AEM in Hardening Elasto-plasticity

The hardening elasto-plasticity is implemented into the Gaussian based AEM code. This section demonstrates different examples and implementations of behaviour of structures compared to FEM. For every load step, a Newton Raphson iteration begins where α and ε (the plastic parameters) are updated and carried to the next Newton Raphson iteration, and to the next load step. This is what ensures that during unloading, if the stress had exceeded the yield stress limit, the plasticity effect would remain. Different beams are presented below, with loading-unloading-loading type mechanism, in order to view the behaviour of the force-displacement diagram. For all the examples presented, a maximum of 20 Newton Raphson iterations is set as the limit in case the convergence criteria is not met. Moreover, the tolerance for the convergence criteria is 10^{-3} .

Comparison of Ansys results with Gaussian AEM with material nonlinearity was examined. The deflection from the ANSYS analysis at the free end of the beam was 0.0112m, and from Gaussian AEM was 0.0117m. The discrepancy is about 3mm. These results are considered accurate enough for using the Gaussian AEM. Therefore a detailed analysis of the cantilever beam using the Gaussian AEM is presented.

6.7.1 Cantilever beam

Considering a cantilever beam with load incrementally applied at the free end. The stresses and beam deflection are shown as follows.

Beam deflection

The beam has 30 elements shown in Figure 6.5, with 10 Gaussian distributed springs. The maximum applied load on the cantilever is 1000 kN, and a total of 60 load increments for loading, unloading and loading again. The load displacement diagram of the free end of the beam is shown in Figure 6.6. The figure shows good accordance with expected behaviour from Figure 6.1, since the stress increases linearly with the slope of the modulus of elasticity E , then after the stress yield limit, the slope changes with the value of the hardening. At unloading, the stress decreases with slope E . Loading again causes the stress to follow the linear path of E and continue to a new yield stress limit where the path continues with H . The stress which the load will exceed the elastic limit is shown in Equation 6.73.

$$\sigma = \frac{My}{I} \quad (6.73)$$

Since the maximum moment the beam encounters is at the fixed end with $M = Pl$, where P is the applied force at the cantilever beam, and l is the span of the beam. Substituting the moment in terms of the applied force P gives

$$P = \frac{\sigma I}{yl} \quad (6.74)$$

Therefore, for the given cantilever beam with span $1m$, cross section $b = h = 0.15$, and yield stress $\sigma_y = 250$ MPa, the calculated yield force is 136.2 kN. Applying a force greater than the yield force will result in exceeding the elastic limit, and plasticity will be obtained. The deflection of the beam at different load steps is displayed in Figure 6.7.

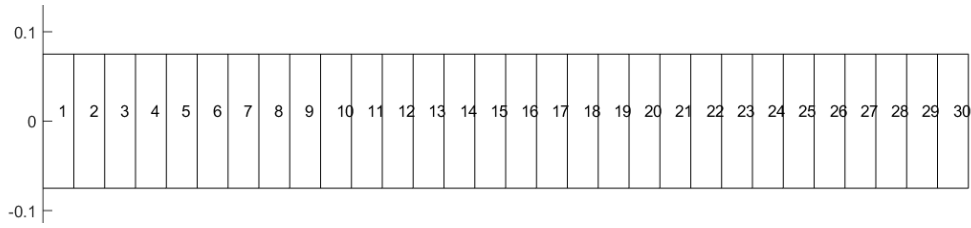


Figure 6.5: Cantilever beam elements

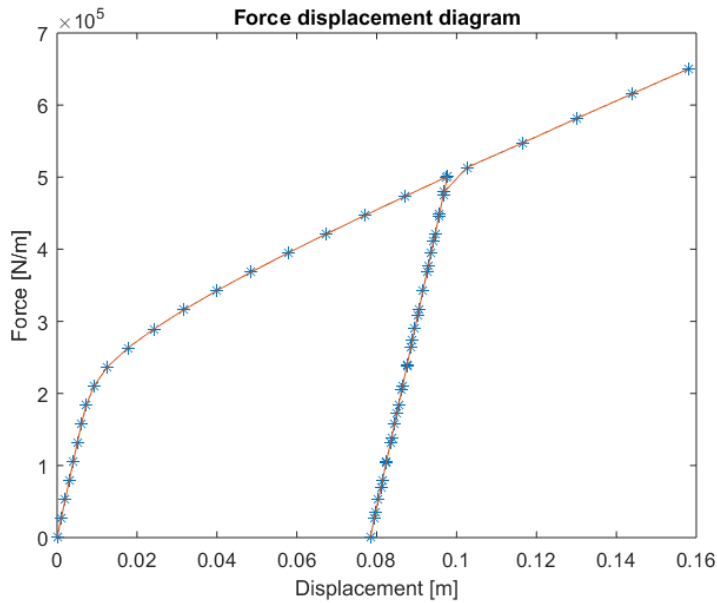


Figure 6.6: Load displacement diagram at free end

Newton Raphson convergence

Figure 6.8 shows the number of Newton Raphson iterations required at every load iteration. For cases of elasto-plasticity it can be seen that a maximum of four Newton Raphson iterations were required when a tolerance of 10^{-3} is used, shown in Figure 6.8a. Decreasing the tolerance to 10^{-5} resulted in more iterations, since the accuracy has improved. The number of iterations can be seen in Figure 6.8b. An important feature of using the Newton Raphson scheme is its quadratic convergence. Considering a point where the Newton Raphson iterations required is 5, the convergence plot is shown in Figure 6.9. The residual at every iteration is shown in Table 6.2.

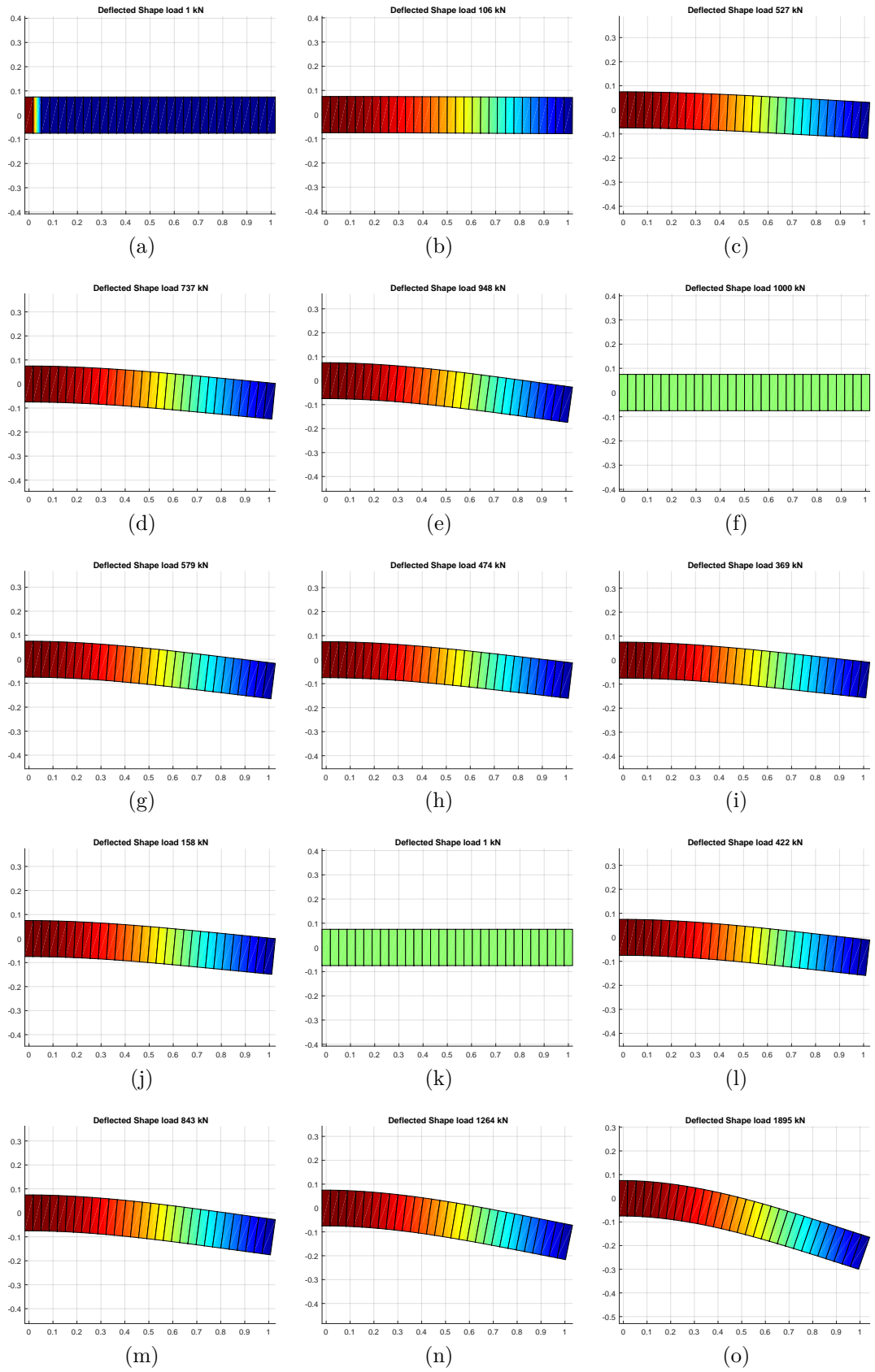


Figure 6.7: Beam deflection through loading-unloading-loading

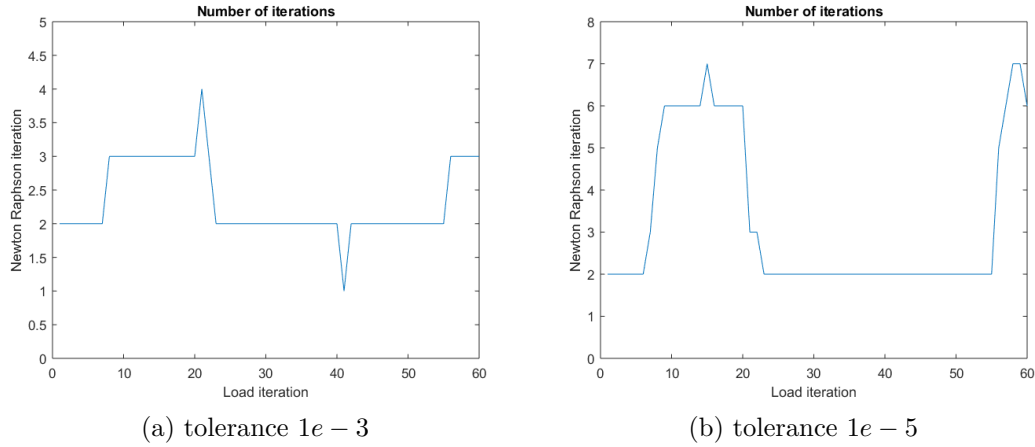


Figure 6.8: Number of iterations required at every load step

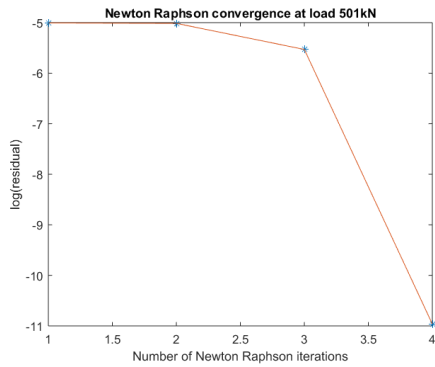


Figure 6.9: Newton Raphson convergence

Table 6.1: Residual at each iteration

Iteration	Residual	log(residual)
1	0.006697	-5.006
2	0.006640	-5.0145
3	0.003961	-5.5303
4	0.000017	-10.963

Normal and Shear Stresses

For the cantilever beam with an applied load of $10^7 N$, the normal stress is shown in Figure 6.11 and the shear stress of the beam is shown in Figure 6.12. From Figure 6.11, the stress at 10 cross sections is shown. It is clear that the last 2 cross sections were linear, and the rest display the elasto-plastic behaviour. Also, the values at the top and bottom fibres at each cross-section are the same. The stress at the neutral axis is zero for all cross-sections.

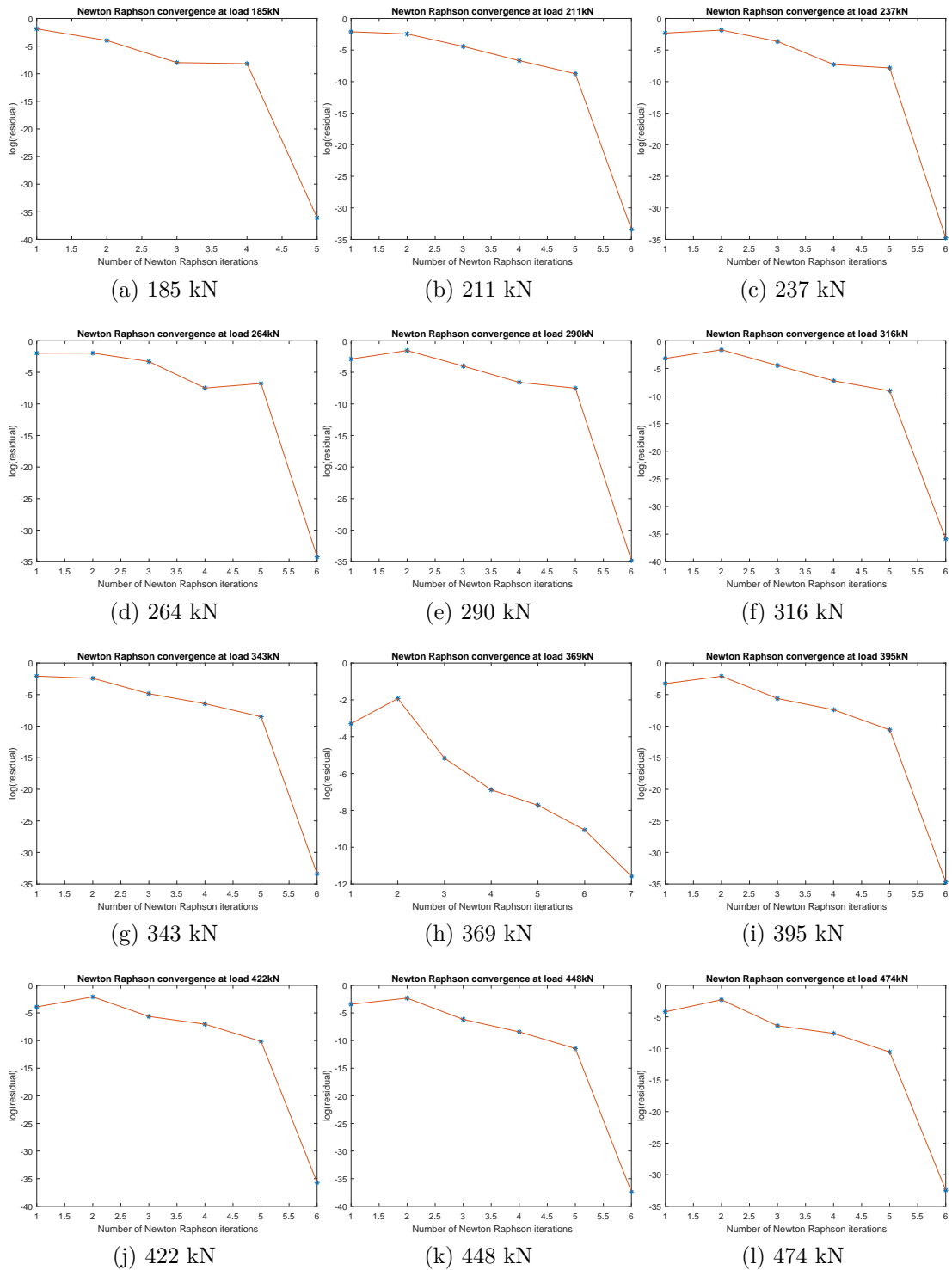


Figure 6.10: Convergence at different load steps for tolerance 10^{-5}

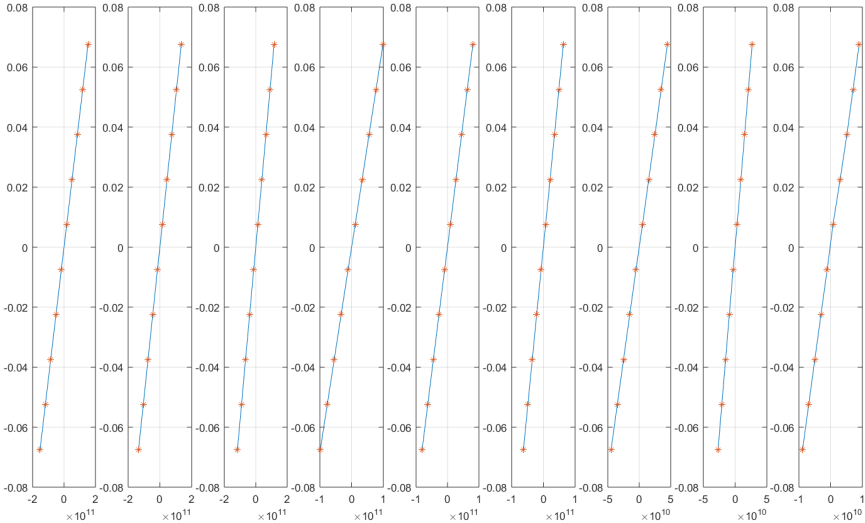


Figure 6.11: Normal stress for cantilever beam

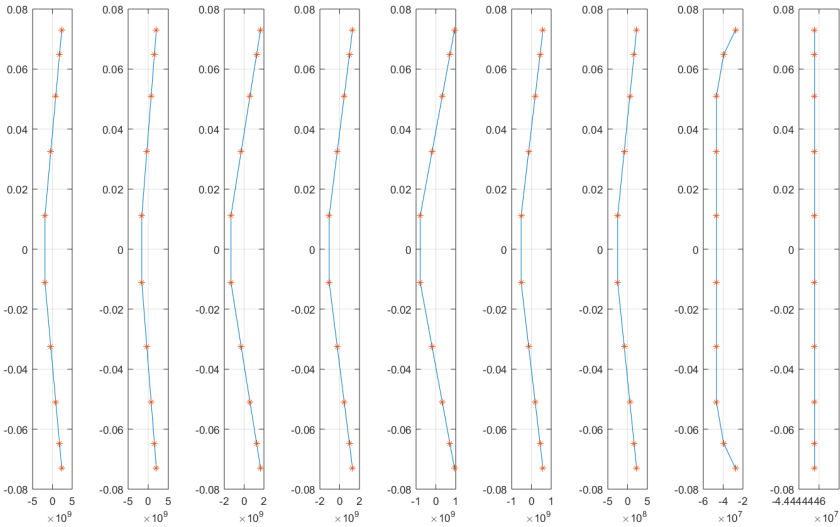


Figure 6.12: Shear stress for cantilever beam

6.8 Adaptive Gaussian Springs

Using the Gaussian quadrature for the springs distribution, and the plasticity algorithm for calculating the stresses in the springs, an adaptive method for springs distribution can be implemented. In each iteration, the stress in each spring is calculated and determined whether it is in the elastic or the plastic stage. If all springs between two elements are elastic, then the initial number of springs will be changed to only two springs between elements, since only two points are required to model the linear behaviour of the elastic region, displayed in Figure 6.13. Hence, assuming an initial number of 10 springs between a pair of elements, after the first Newton Raphson iteration, if all springs are deemed to be elastic, then the total number of springs per pair of elements is reduced from 10 springs to 2 springs.

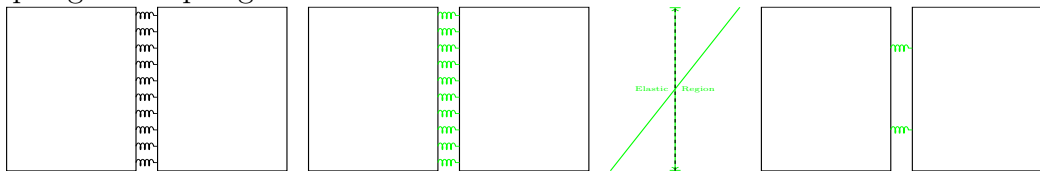


Figure 6.13: Adaptive Elastic Springs

However, if plasticity is observed in springs between a pair of elements, then the normal stress is split into 3 regions, plastic at the top and bottom, and elastic in the middle of the cross-section, as displayed in Figure 6.14. Since at least two springs are required for each region, then instead of having a total of 10 springs, 6 springs are required for elasto-plastic cases.

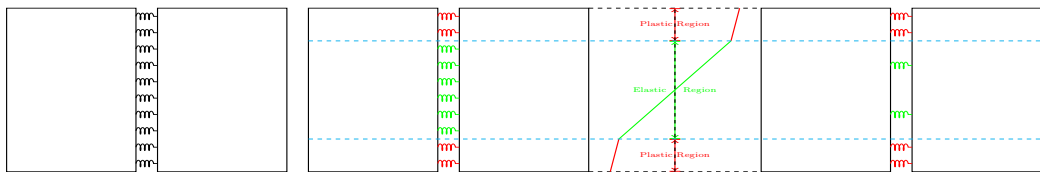


Figure 6.14: Adaptive Elasto-plastic Springs

An algorithm procedure for the beam deflection analysis would first entail an initial Newton Raphson iteration, where all spring stresses and strains are preallocated as zero. After the first iteration, the deflection vector is obtained and at the next iteration the stresses are recalculated. Depending on the yield criteria the springs are determined as belonging in the elastic or in the plastic region. Transition points at which exactly the change in regions occur are determined,

and then the new spring locations are distributed.

The beam is analysed for the first Newton Raphson iteration, and the stresses in the springs are calculated. Based on the springs elasticity - whether they were elastic or plastic, the new springs will be placed between calculated transition points. The transition points are the points calculated where the stress changes from the elastic to plastic region, and vice versa.

Considering a cantilever beam fixed on the left end as displayed in Figure 6.17, and loaded on the right end. The spring distribution is resolved from the adaptive Gaussian Springs based Applied Element Method proposed. Initially there are 10 springs between each element, after determining the plasticity conditions of the springs, the new springs will be allocated. Assuming a small load was applied where all the springs remain in the elastic region, then all the springs between elements will be reduced from 10 springs per pair of elements, to two springs. While in the case of an elasto-plastic condition, where the elements closest to the fixed end will have higher stresses than the elements closer to the free end, it is expected that some plasticity will appear. So the elements with plasticity will have a total of 6 springs, while elements that are totally elastic will have 2 springs per element. In a more global effect, consider a beam with 10 elements, 10 springs between each element, the initial number of springs in total is $10 \times 9 = 90$ springs. After reduction, and in the case that all elements are elastic, the total number of springs becomes $2 \times 9 = 18$ springs.

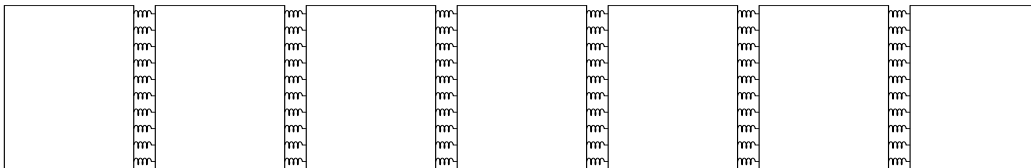


Figure 6.15: Representation of a cantilever with initial of 10 springs

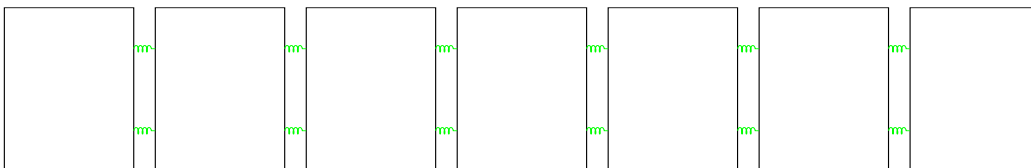


Figure 6.16: Representation of a cantilever beam with all elastic springs

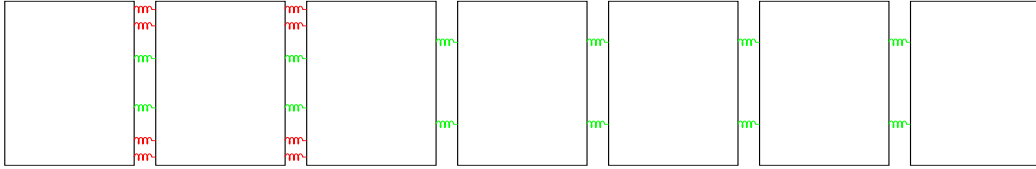


Figure 6.17: Representation of a cantilever beam using adaptive AEM springs

6.8.1 Transition Point Locator

There are two different approaches that were used to locate the transition point in a cross-section. The calculation of the transition point is based on determining between which two springs there was a difference in the elasticity of the spring. An initial guess of 10 springs is recommended so there are at least two springs in each region between where the transition point will occur. This is to ensure that there are two points to create a line, and an intersection point between these two lines is calculated. Consider the intersection of two lines L_1 defined by the points (x_1, y_1) and (x_2, y_2) , and line L_2 defined by points (x_3, y_3) and (x_4, y_4) , the intersection of the point P_x, P_y is defined using determinants, as displayed in Equation 6.75:

$$\begin{aligned}
 P_x &= \frac{(x_1y_2 - y_1x_2)(x_3 - x_4) - (x_1 - x_2)(x_3y_4 - y_3x_4)}{(x_1 - x_2)(y_3 - y_4) - (y_1 - y_2)(x_3 - x_4)} \\
 P_y &= \frac{(x_1y_2 - y_1x_2)(y_3 - y_4) - (y_1 - y_2)(x_3y_4 - y_3x_4)}{(x_1 - x_2)(y_3 - y_4) - (y_1 - y_2)(x_3 - x_4)}
 \end{aligned}
 \tag{6.75}$$

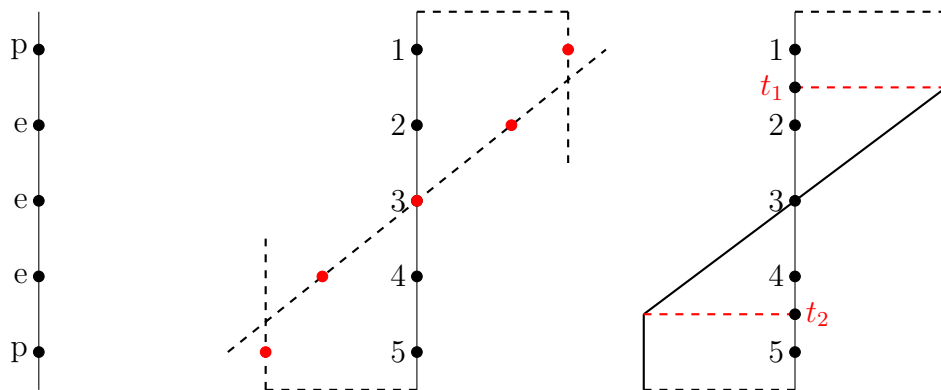


Figure 6.18: Transition Point locator

Figure 6.18 displays the process at which the transition point is located. Consider a cross-section between a pair of elements. The five points on the figure represent five springs between the cross-section. The first part of the figure shows

"p" which demonstrates plastic, and "e" represents elastic. This explains that the spring is plastic or elastic. The way that the transition point is located is based on the fact that the transition will occur between two points that have different plasticity. So between spring 1 and 2 there should be a transition point, and another transition between spring 4 and 5. The second part of the figure shows the red points, which is the stress of each spring. Connecting the location of the stresses to one another shows where the intersection between the two lines will occur, and so the location of the transition point. Since the coordinates of the stress at each spring is known, using equation 6.75 the transition springs can be calculated. From knowing the transition points now the section can be separated where the springs are Gaussian distributed within each region.

6.8.2 Examples

In this section, different structural beams subject to incremental loading will be analysed using the adaptive Gaussian springs technique. First, consider a cantilever beam, fixed at one end and load applied at the free end. As mentioned every pair of elements starts with an initial 10 springs, and after the plasticity is determined for that load step, the springs are redistributed. If the element is totally elastic, then only 2 springs are required, while if it is elasto-plastic, a total of 6 springs are required. The difference in the MATLAB code for the conventional springs and the adaptive springs is adding an extra requirement in the second iteration by checking the elasticity and redistributing the springs. For elasto-plastic cases usually five Newton Raphson iterations were required. Therefore, for an elasto-plastic case, the first iteration would have 10 springs, in the second iteration there is an evaluation of the springs and they are redistributed with 6 total springs, and finally from the third iteration on, the analysis continues for just 6 springs. This is presented in examples as follows.

Cantilever Beam

Considering a cantilever beam, an elastic analysis and an elasto-plastic analysis is performed. The cantilever beam with its deflected shape is shown in Figure 6.19. From the stress diagram, the first three spring sets were elasto-plastic, while the

remainder of the spring sets are totally elastic. The transition point location for the three spring sets is shown in Figure 6.22. The new springs distribution in every spring set is shown in Figure 6.23.



Figure 6.19: Cantilever beam with 10 elements

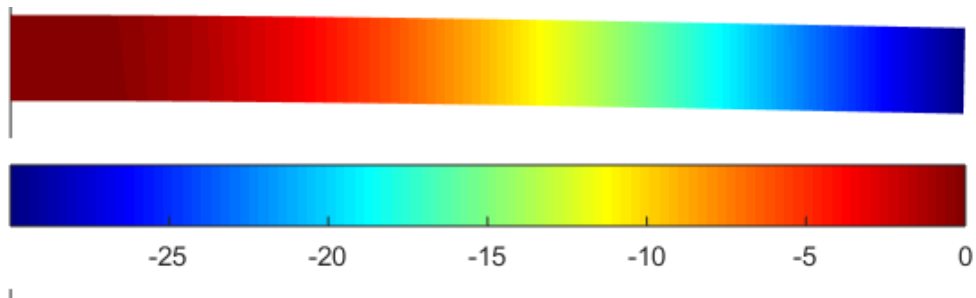


Figure 6.20: Deflection of cantilever beam with adaptive springs

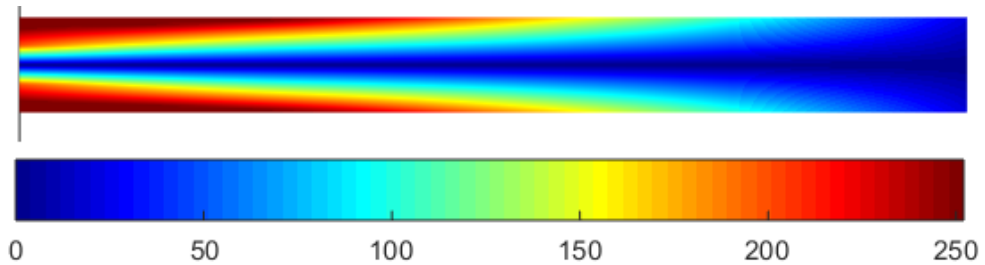


Figure 6.21: Normal stress of cantilever beam with adaptive springs

Figure 6.24 displays the stress distribution at every cross-section and the points are the spring locations. Figure 6.25 is the convergence rate of the Newton Raphson iteration for the beam with transition points. Also, it is worth mentioning that the transition points calculation did not change the convergence rate from the conventional springs, so with less springs accurate results were obtained. In the scheme of larger scale structures, the number of springs can be significantly reduced.

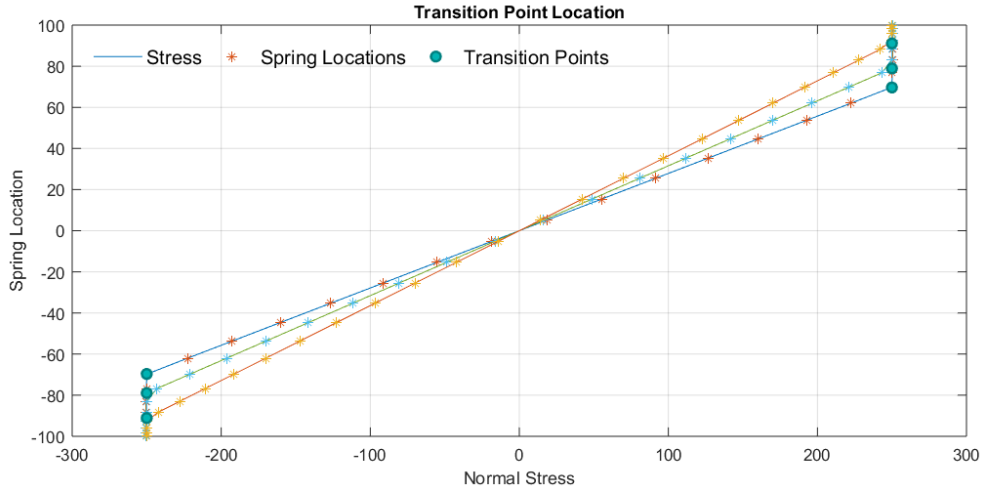


Figure 6.22: Spring sets that are elasto-plastic

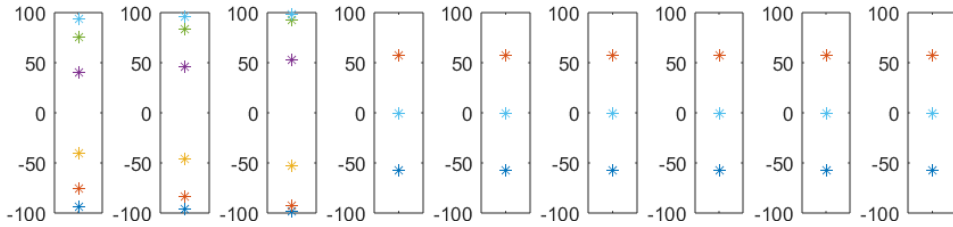


Figure 6.23: Springs distribution between elements

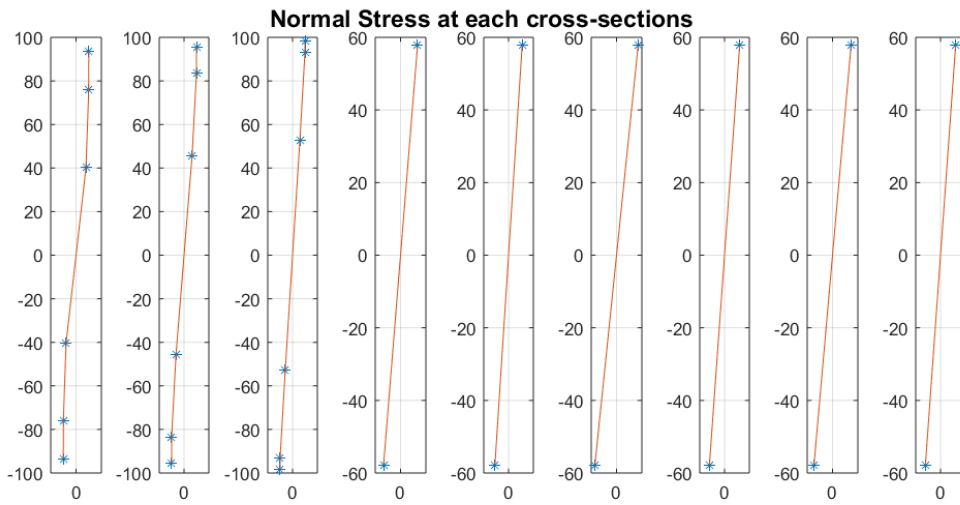


Figure 6.24: Normal stress distribution at every cross-section

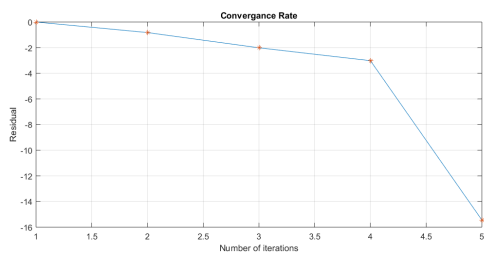


Figure 6.25: Converge Rate of Newton Raphson

Table 6.2: Residual at each iteration

Iteration	Residual
1	1
2	1.50×10^{-1}
3	9.75×10^{-3}
4	9.67×10^{-4}
5	3.64×10^{-16}

Fixed End Beam

Figure 6.28 shows the stress distribution at the elasto-plastic cross-sections. The deflection of the beam is shown in Figure 6.26. Figure 6.27 is the normal stress distribution for the fixed end beam. As can be seen, the maximum stresses occur at the ends of the beam and at the location of the applied load at the midspan. Therefore it is expected that elasto-plasticity occurs at the ends and midspan. This is correctly conveyed in Figure 6.29. The stress distribution with the springs displayed as points along the beam cross-sections are shown in Figure 6.30.

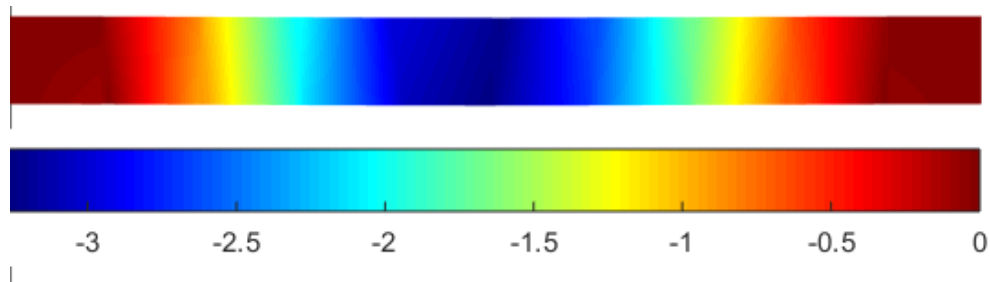


Figure 6.26: Deflection of FEB with adaptive springs

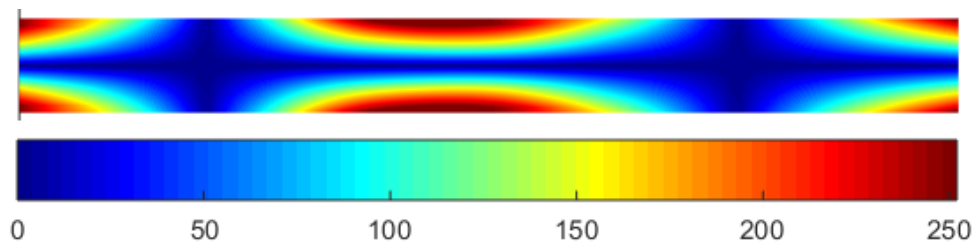


Figure 6.27: Normal stress distribution for Fixed End Beam

The results for the adaptive springs showed good accordance with the original AEM and in comparison to the Gaussian AEM. The convergence rate did not change. The main advantage of the method is that the number of springs is significantly reduced. For perfectly elastic cases, only 2 springs per element are needed, while for elasto-plastic cases 6 springs are needed.

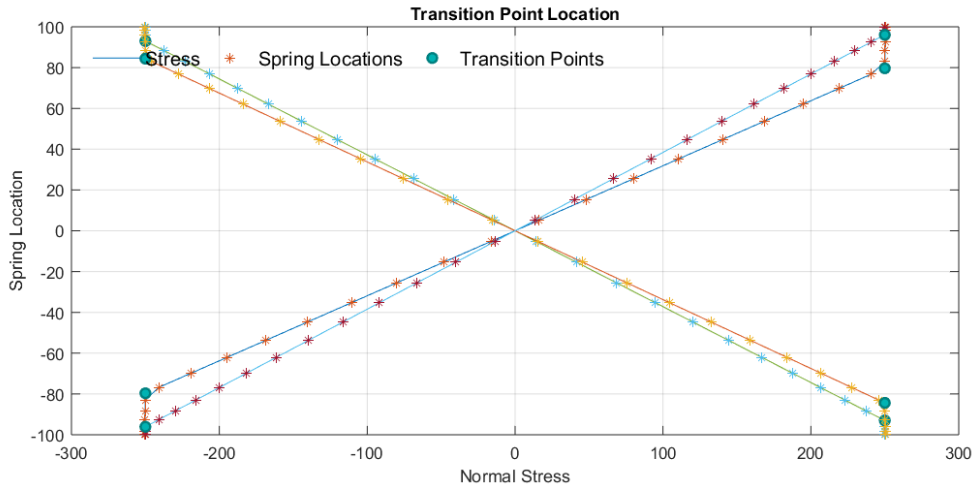


Figure 6.28: Stress with adaptive springs for FEB

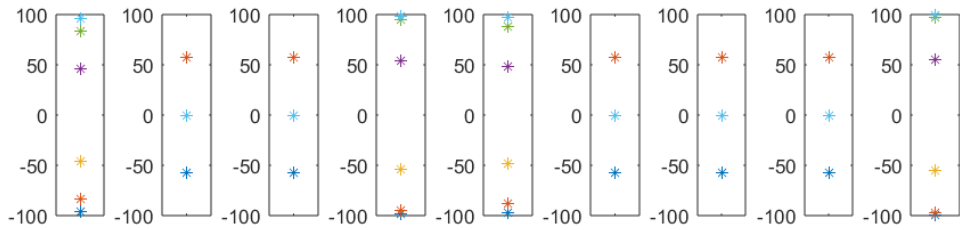


Figure 6.29: New springs distribution for FEB

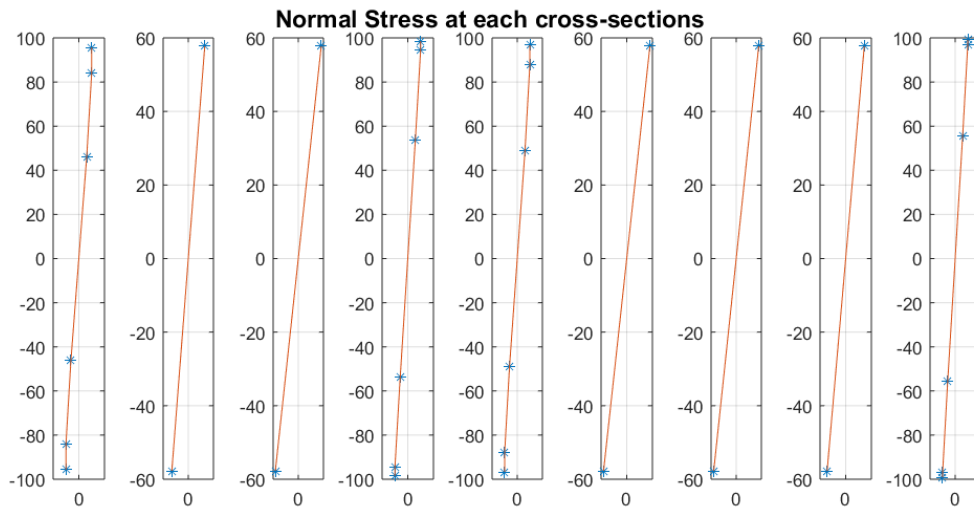


Figure 6.30: New stress distribution for FEB

6.9 Conclusion

The Applied Element Method has been modified for elasto-plastic problems by efficiently distributing springs using the Gaussian quadrature. The Hardening plasticity algorithm was used for representing the elasto-plastic material. The

Newton Raphson iteration scheme was implemented, and resulted in quadratic convergence. Moreover, an adaptive method was used to model the behaviour of the elements in elasto-plasticity, where a total of 6 springs is required for elasto-plastic elements, and 2 springs for elastic elements. This revelation allowed an accurate analysis of structural members while have a remarkably low number of springs per element.

The material damage behaviour is presented in the next chapter.

Part III

Formulation of Damage, Fracture and Progressive Collapse in Gaussian Based AEM & Applications

Chapter 7

Material Damage Model & Dynamic Analysis

In the previous chapters, the elastic and elasto-plastic material behaviour was successfully modelled for applications in AEM. The modelling of progressive collapse is an extension of these methods and is presented in this chapter. Modelling progressive collapse entails that the material must undergo damage and fracture first. One material behaviour that exhibits material damage is softening material behaviour. The following sections describe material softening and constitutive equations developed to model the collapse of structures.

7.1 Softening Material Behaviour

Strain softening is the deterioration of material strength with increasing strain [74]. This is usually found in damaged quasi brittle materials such as fibre reinforced composites and concrete [74]. Other materials include rocks, some soils, wood, sea ice, fibre-reinforced concretes, asphalt concretes, polymer concretes, ceramics and some metals [75]. Strain softening has been considered as inadmissible in continuum mechanics [75]- [79]. Hadamard [80] pointed out that the wave velocity becomes imaginary and the differential equation becomes elliptic if the tangent moduli matrix is not positive definite [75].

A major part of construction materials around the world include materials from the above listed. For this reason, there is an importance to modelling the

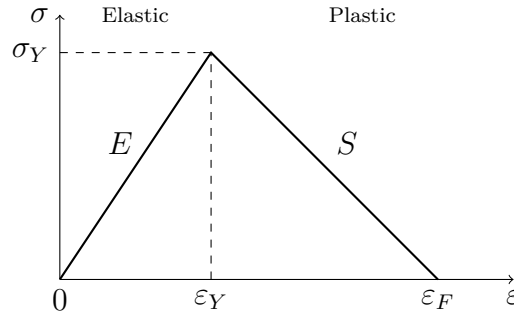


Figure 7.1: Strain Softening Material Behaviour

softening materials behaviour after materials exceed their elastic limit. In this section the return mapping algorithm for softening is developed. The strain softening behaviour is exhibited when failure occurs by progressive damage [75].

Return Mapping Algorithm for Softening Model

The stress-strain diagram of the softening materials is presented as a bilinear model, with the slope as a positive E in the elastic region, and a declining negative slope S that represents the strain-softening behaviour. Based on the constitutive model derived for hardening, similar principles are implemented to develop the softening behaviour. Figure 7.1 is a representation of the material model presented as a stress-strain diagram. In AEM each spring will have a unique stress-strain diagram. Once the strain exceeds the elastic yield limit ϵ_Y , it enters the plastic region and the slope is the negative S . Then when the strain exceeds the failed strain ϵ_F the material is considered to have been totally damaged in that region. Since each spring represents a tributary area of a section of an element, then a failed spring physically represents that that portion of the region has failed.

The return mapping algorithm is described as follows. First the strain is calculated from the beam deflection, and the strain increment is obtained. The trial stress is calculated based on using E , shown in Equation 7.1. Note that there are two different strain definitions in the equation: ϵ is the strain and ϵ^p is the plastic softening strain calculated in Equation 7.6. ϵ keeps track of the plastic strain. If the stress and strain do not exceed the yield limit state yet, then ϵ^p is zero because there is no plastic strain yet. So Equation 7.1 will be simply

$$\sigma_{n+1}^{trial} = E(\varepsilon_{n+1}).$$

$$\sigma_{n+1}^{trial} = E(\varepsilon_{n+1} - \epsilon_n^p) \quad (7.1)$$

Similar to the 1D hardening plasticity, a yield criterion is developed for the softening material behaviour. The yield condition is used to determine when yield occurs, and is denoted by f . The yield function results in either a positive or negative value. The yield function f is shown in Equation 7.2.

$$f_{n+1}^{trial} = |\sigma_{n+1}^{trial}| - (\sigma_Y^0 + S(\varepsilon_{n+1} - \varepsilon_Y^0)) \quad (7.2)$$

The yield function is examined to determine which region the spring is currently located: elastic, plastic or failed. If the strain is larger than the failed strain then the spring has failed. If the yield criteria is less than zero this means that the difference of the yield stress and the calculated softening stress is smaller than the current trial stress, so the location of the trial stress is before the yield stress meaning that it is still in the elastic region, and the plasticity parameter $\Delta\lambda = 0$. In the elastic region linear stiffness of a spring is calculated from Equation 7.3.

$$K_n = \frac{EA}{l}; \quad K_s = \frac{GA}{l} \quad (7.3)$$

Otherwise the spring is in the plastic region. The plasticity parameter $\Delta\lambda$ is calculated and is greater than zero, shown in Equation 7.4.

$$\Delta\lambda = \frac{f_{n+1}^{trial}}{E} \quad (7.4)$$

The new stress σ_{n+1} is then calculated (corrector-step) Equation 7.5, and the corresponding plastic strain ϵ_{n+1}^p .

$$\sigma_{n+1} = \sigma_Y^0 + S(\varepsilon_{n+1} - \varepsilon_Y) \quad (7.5)$$

$$\epsilon_{n+1}^p = \epsilon_n^p + \Delta\lambda \text{sign} [\sigma_{n+1}^{trial}] \quad (7.6)$$

The nonlinear stiffness of the springs are calculated in Equation 7.7.

$$\begin{aligned} K_n &= \frac{C_n A}{l}; C_n = \frac{EH}{E + H} \\ K_s &= \frac{C_s A}{l}; C_s = \frac{GH}{G + H} \end{aligned} \quad (7.7)$$

For a failed spring, the stiffness is set as zero.

The return mapping softening algorithm is presented in Box 7.1.

Box. 7.1.1: Return Mapping Softening algorithm

1. Loop for every element

- (a) Loop for every spring
- (b) Obtain new strain $\epsilon_{n+1} = \epsilon_n + \delta\epsilon_{n+1}$
- (c) Evaluate elastic predictor

$$\sigma_{n+1}^{trial} = E(\epsilon_{n+1} - \epsilon_{n+1}^p)$$

$$f_{n+1}^{trial} = |\sigma_{n+1}^{trial}| - (\sigma_Y + S(\epsilon_n - \epsilon_Y))$$

(d) Check yield criterion

$$if \begin{cases} \epsilon_n > \epsilon_f & \text{spring failed} \\ f_{n+1}^{trial} \leq 0 & \Delta\lambda = 0 \\ f_{n+1}^{trial} > 0 & \Delta\lambda > 0 \end{cases}$$

- (e) If spring failed set stiffness of spring to zero.
- (f) else Elastic step (if $f_{n+1}^{trial} \leq 0$). Calculate linear stiffness of springs.
- (g) Plastic step (if $f_{n+1}^{trial} > 0$)

$$\Delta\lambda = \frac{f_{n+1}^{trial}}{E}$$

$$\sigma_{n+1} = \sigma_Y^0 + S(\epsilon_{n+1} - \epsilon_Y)$$

$$\epsilon_{n+1}^p = \epsilon_n^p + \Delta\lambda \text{sign}[\sigma_{n+1}^{trial}]$$

Calculate nonlinear stiffness of springs.

- (h) Repeat from step for more springs within the same pair of elements
2. Assemble internal forces in global force vector, and stiffness in global stiffness matrix
3. Repeat for next pair of elements

Softening Return Mapping algorithm schematic representation

The return mapping algorithm is presented schematically for better explanation of the formulation.

1. Trial stress predictor

First consider that the strain ε_n has not exceeded the yield strain ε_y , but the next increment ε_{n+1} exceeds ε_y , as shown in Figure 7.2. Since there is no plastic strain, the corresponding σ_{n+1}^{trial} is calculated as $\sigma_{n+1}^{trial} = E\varepsilon_{n+1}$.

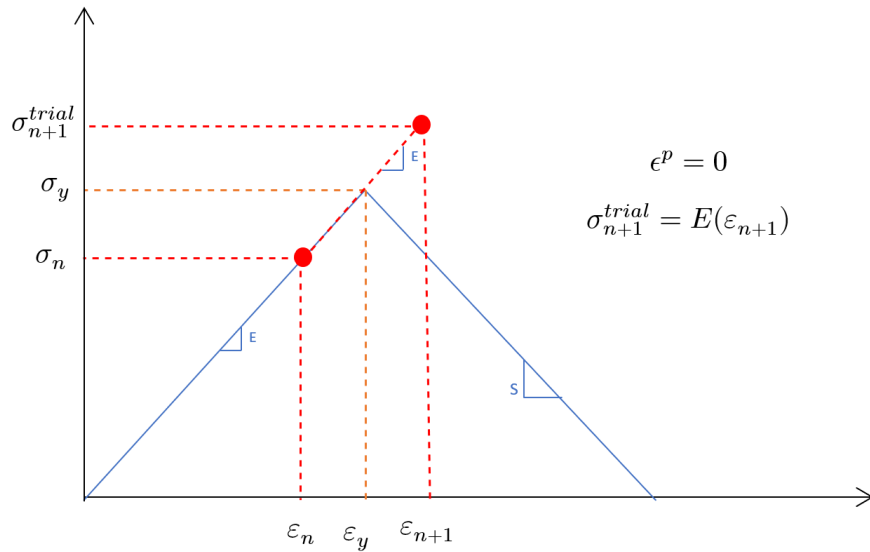


Figure 7.2: Trail stress predictor calculation

2. Calculate f_{n+1}

Now the yield function must be evaluated. Recall that S is negative, so the purple line presents $\sigma_Y + S(\varepsilon_{n+1} - \varepsilon_y)$ and is less than σ_Y because it is being subtracted. The yield function f_{n+1}^{trial} calculation is displayed in Figure 7.3.

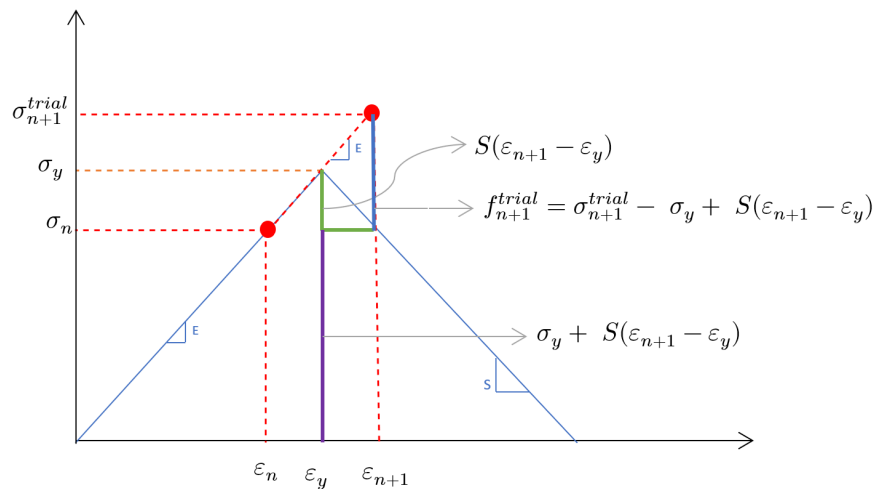


Figure 7.3: Demonstrating the trial function

3. Calculate $\Delta\lambda$

Since f_{n+1}^{trial} is now known, $\Delta\lambda$ is used to calculate the plastic strain ϵ^p just by using the elastic slope E . $\Delta\lambda$ is represented in Figure 7.4.

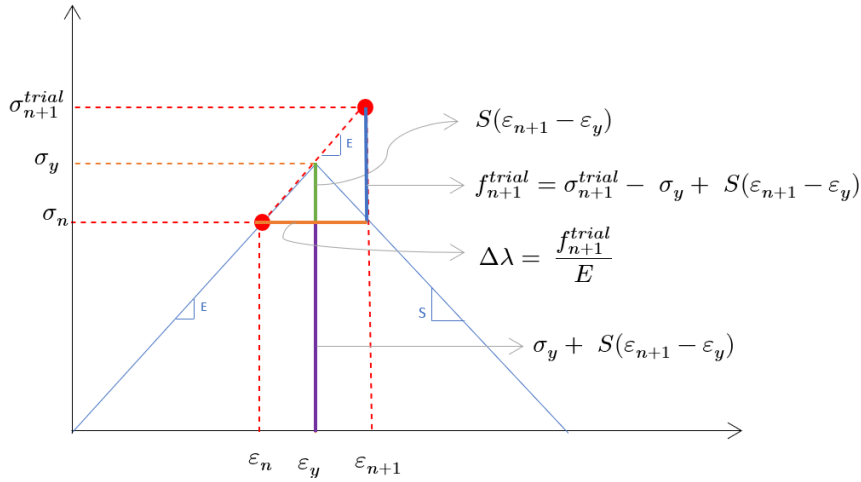


Figure 7.4: Representation of $\Delta\lambda$

4. Obtain the plastic strain ϵ^p .

The plastic strain is shown in Figure 7.5. Since there is no previous plastic strain because this is the first time step in which the strain has exceeded the yield strain, the plastic strain at this time step = $\Delta\lambda$.

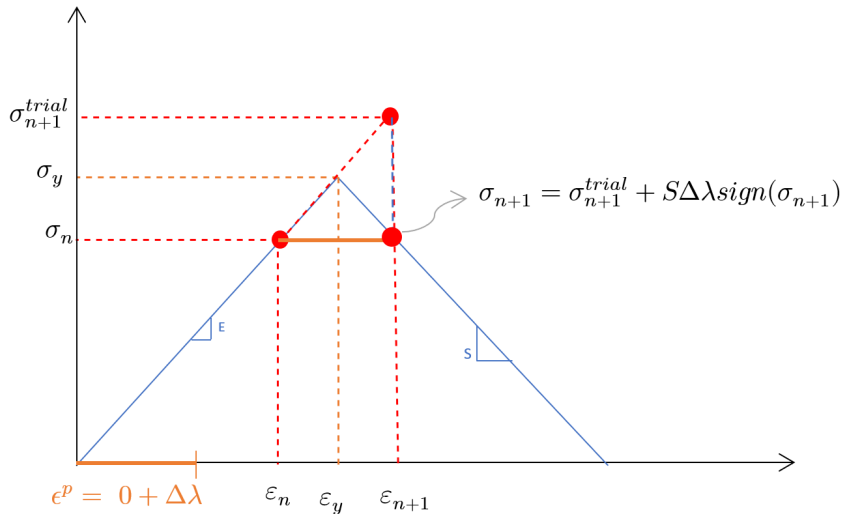


Figure 7.5: Plastic strain

5. Now that the strain and corrected stress is obtained the corresponding stiffness of the spring is obtained as well as the internal force.
6. Begin next time step and calculate the trial stress. Since there is a plastic strain, ϵ^p is included in the trial stress equation. $\epsilon_{n+1} - \epsilon^p$ is schematically represented in Figure 7.6, along the x-axis. The trial stress is then obtained using the Young's Modulus E .

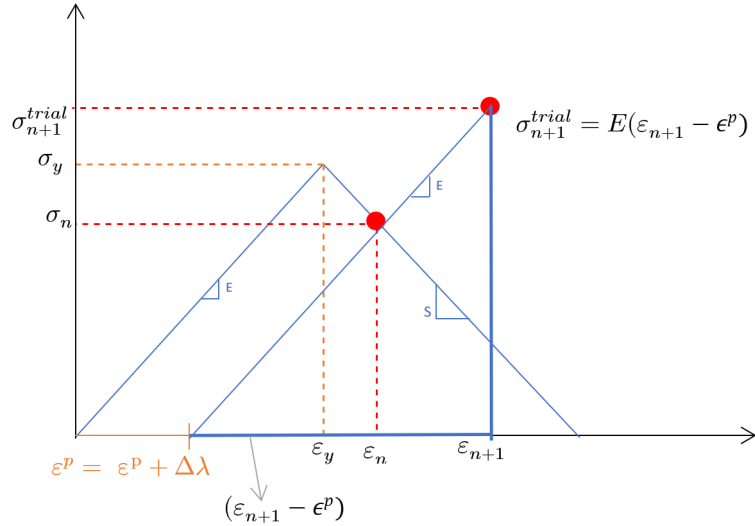
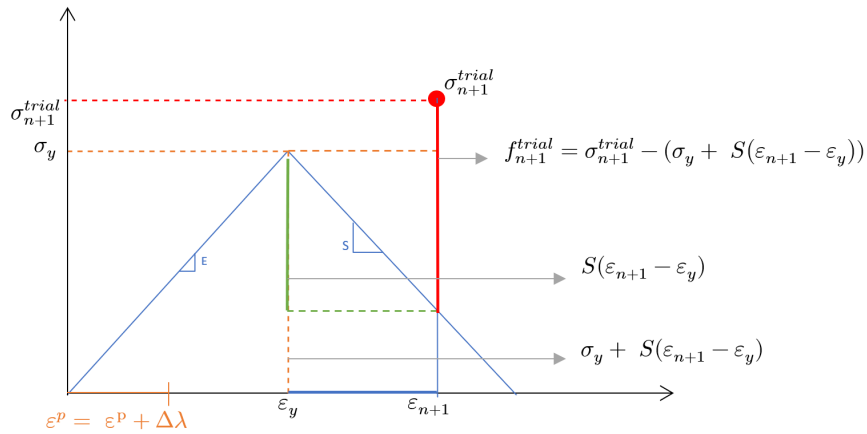


Figure 7.6: Trial stress calculation

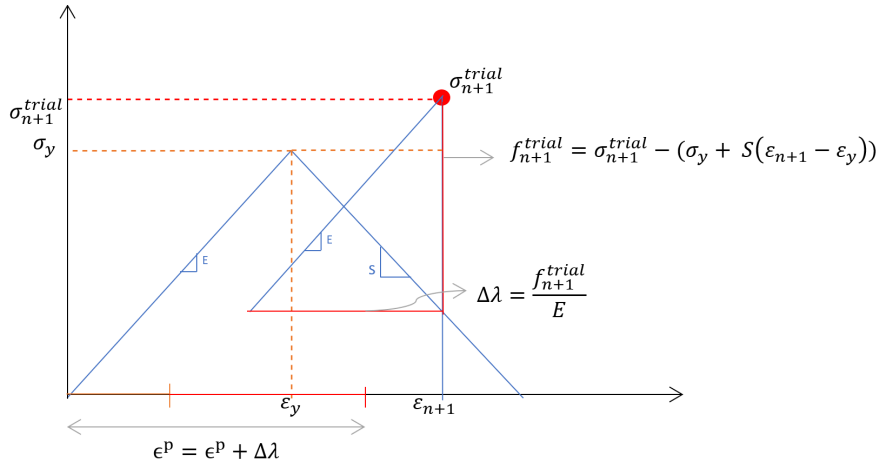
7. Similar to the previous time step f_{n+1}^{trial} is obtained, and shown in Figure 7.7.


 Figure 7.7: f_{n+1}^{trial} calculation

8. $\Delta\lambda$ and new ϵ^p can now be obtained, and is shown in Figure 7.8.

7.1.1 Return-Mapping Algorithm verification

In this section the verification of the Predictor-Corrector algorithm is presented and the Newton Raphson convergence is examined. Figures 7.9 and 7.10 show the return mapping for the predictor and corrector at different time steps. The green points describe the predictors, and the red points describe the correctors. From the first figures it is clear that when the spring is in the elastic stage it will follow the Young's Modulus E , and therefore the predictor takes the next stress


 Figure 7.8: $\Delta\lambda$ and ϵ^p calculation

time step to the correct location, and no correction is actually needed. Once the stress exceeds the elastic limit, the predictor predicts the stress along the elastic modulus, and later the algorithm corrects the stress to the correct location along the Softening modulus. Later the unloading stage is shown. Since the unloading occurs after the yield stage it follows a new path which is parallel to the modulus E , however, since there is permanent plastic strain, it will not go back to zero. Finally in the reloading stage, the predictor predicts along the new slope of E , and once it intersects with the softening slope, it starts to correct to the softening slope rather than E . The point of intersection is considered the new yield stress.

7.1.2 Failed Elements

Newton Raphson convergence cannot be obtained with softening damage materials due to the singularity of the stiffness matrix. The stress-strain diagram of the predictor corrector method shows a good behaviour of the strain softening, however there is no Newton Raphson convergence. Also the eigen values for the system are negative after the yield point is surpassed. For this reason a dynamic model must be used. After failure or crack occurs in the static analysis (element separation), the stiffness matrix becomes singular, causing inaccurate solutions since it cannot be invertible. Solving the problem in a dynamic case will eliminate this issue.

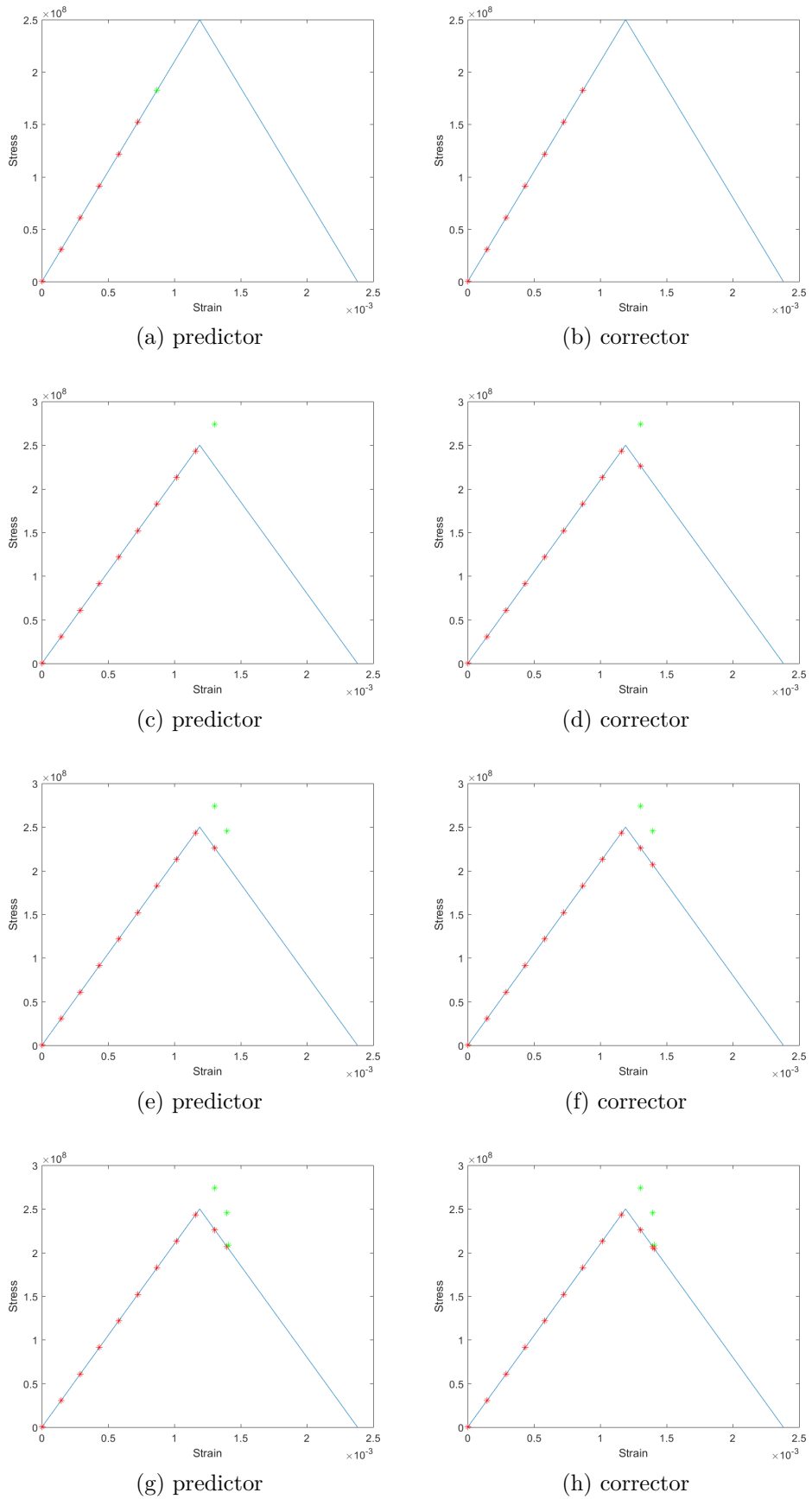
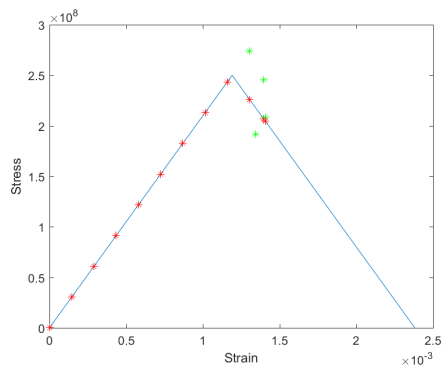
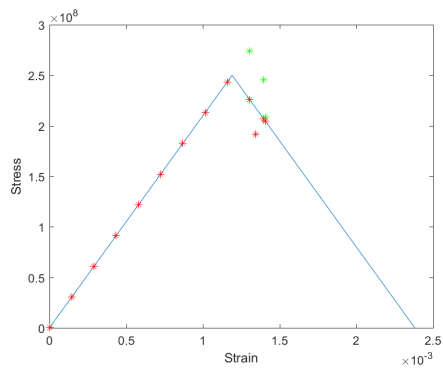


Figure 7.9: Predictor-corrector Softening model

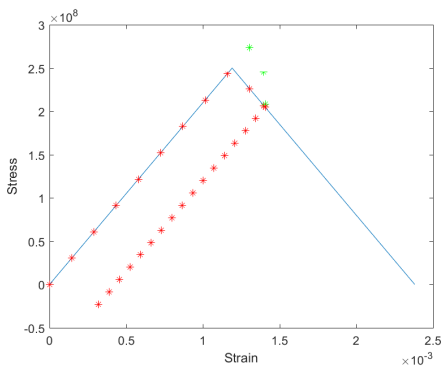
7.1. SOFTENING MATERIAL BEHAVIOUR



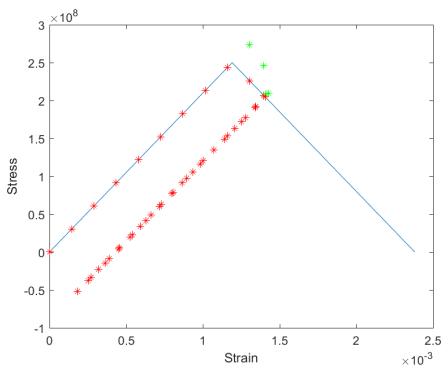
(a) predictor



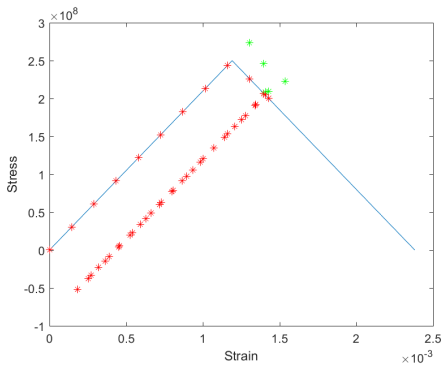
(b) corrector



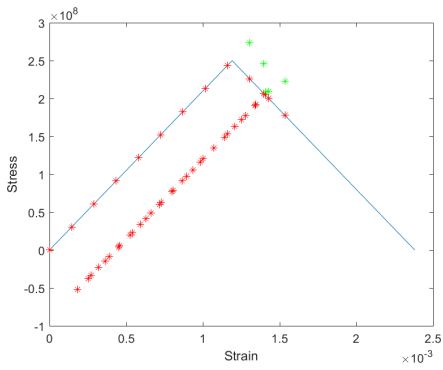
(c) predictor



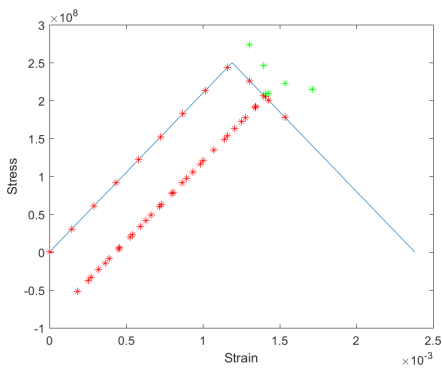
(d) corrector



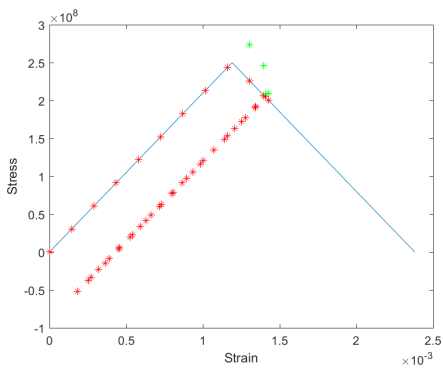
(e) predictor



(f) corrector



(g) predictor



(h) corrector

Figure 7.10: Predictor-corrector Softening model

7.2 Introduction to Dynamic Analysis

In this section, the formulation of the dynamic aspect in AEM is presented. A general formulation of the equation of motion for multiple degrees-of-freedom systems subject to external forces or earthquake ground motion is shown. Based on the presented formulations, the most applicable numerical time integrator for use in progressive collapse in AEM is selected. The equations for multiple degrees-of-freedom system (MDOF) are presented, since the scope of this thesis covers MDOF systems.

7.2.1 Equation of Motion for MDOF Systems

Consider the two story shear building shown in Figure 7.11a, with lumped mass at each floor level. The system has two degrees-of-freedom; lateral displacements u_1 and u_2 in the direction of the x-axis. The forces acting on the frame are in Figure 7.11b, where f_S is the resisting force, f_D is the damping force and $p(t)$ is the external applied force. The derivation of these forces is shown in the following section.

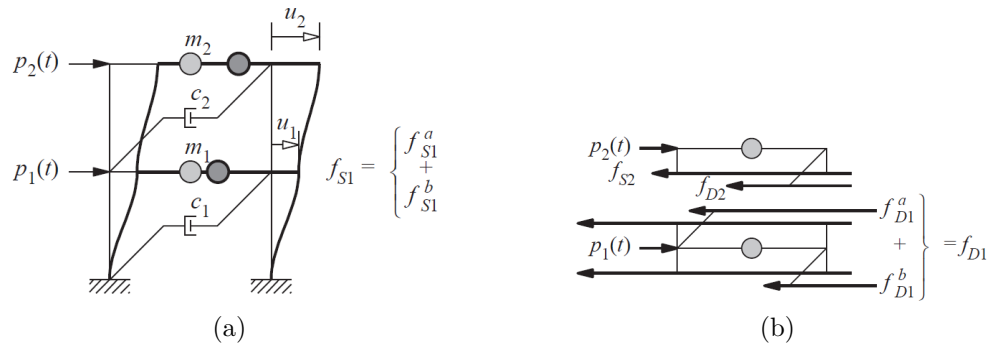


Figure 7.11: (a) Two story shear frame (b) Forces acting on frame [81]

7.2.2 Equations of Motion for Linear Systems

In a single degrees-of-freedom linear system the relationship between the lateral force and the deformation u is linear and shown in Equation 7.8.

$$f_s = ku \quad (7.8)$$

where k is the lateral stiffness of the system, f_s is the external force, and the internal force is equal and opposite to f_s [81]. The linear relationship implies that the loading and unloading curves are identical. For structures undergoing cyclic deformations, from earthquakes for instance, the initial loading curve is nonlinear at larger amplitudes of deformation, and the unloading and loading curves may differ from each other. This system is inelastic [81]. The resisting force is an implicit function of deformation

$$f_s = f_s(u) \quad (7.9)$$

Damping in structures is idealised since it is impossible to identify or mathematically represent the energy dissipation mechanisms in actual structures [81]. For simple degrees-of-freedom structures the damping is idealised by a linear viscous damper. The damping force is related to the velocity \dot{u} across the linear viscous damper by

$$f_D = c\dot{u} \quad (7.10)$$

where c is the viscous damping coefficient and \dot{u} is the velocity. Vibration experiments on actual structures provide the data for the damping coefficient. Therefore, the forces acting on a mass at an instance of time are the external force $p(t)$, the resisting force f_s and the damping resistance force f_D . The resultant force along the x-axis is $p - f_s - f_D$. The Newton's second law of motion gives

$$p - f_s - f_D = m\ddot{u} \quad (7.11)$$

which becomes

$$m\ddot{u} + c\dot{u} + ku = p(t) \quad (7.12)$$

Equation 7.12 can be extended for inelastic systems as

$$m\ddot{u} + c\dot{u} + f_s(u) = p(t) \quad (7.13)$$

The Newton's second law of motion for each mass is

$$p_j - f_{Sj} - f_{Dj} = m_j \ddot{u}_j \quad (7.14)$$

for $j = 1$ and 2 , Equation 7.14 can be written in matrix form

$$\begin{bmatrix} m_1 & 0 \\ 0 & m_2 \end{bmatrix} \begin{Bmatrix} \ddot{u}_1 \\ \ddot{u}_2 \end{Bmatrix} + \begin{Bmatrix} f_{D1} \\ f_{D2} \end{Bmatrix} + \begin{Bmatrix} f_{S1} \\ f_{S2} \end{Bmatrix} = \begin{Bmatrix} p_1(t) \\ p_2(t) \end{Bmatrix} \quad (7.15)$$

which can be written as

$$M\ddot{u} + f_D + f_S = p(t) \quad (7.16)$$

where M is the mass matrix. Since the elastic resisting force f_S is related to the displacement vector and stiffness matrix K , the force can be represented as Equation 7.17. Also, the damping resistance force and the velocity vector are related the damping matrix C , as shown in Equation 7.18.

$$f_S = Ku \quad (7.17)$$

$$f_D = C\dot{u} \quad (7.18)$$

The equation of motion can now be written as

$$M\ddot{u} + C\dot{u} + Ku = p(t) \quad (7.19)$$

For a general description of linear systems, with more than just two stories, the same approach is used. The degrees-of-freedom in the system will increase. The form of the equations of motion will remain the same as shown in Equation 7.19.

7.2.3 Natural Vibration Frequency and Modes Calculation

The solution to the eigenvalue problem presented in this section gives the natural frequencies and the modes of a structural system [81]. The free vibration of an undamped system of one of the vibration modes can be represented using

Equation 7.20.

$$u(t) = q_n(t)\phi_n \quad (7.20)$$

where the deflected shape ϕ_n does not vary with time. The time variation of the displacements is described by the simple harmonic function

$$q_n(t) = A_n \cos(\omega_n t) + B_n \sin(\omega_n t) \quad (7.21)$$

where A_n and B_n are constants determined from the initial conditions. Combining Equations 7.20 and 7.21 gives

$$u(t) = \phi_n(A_n \cos(\omega_n t) + B_n \sin(\omega_n t)) \quad (7.22)$$

Substituting in the undamped form Equation 7.19, \ddot{u} is required.

$$\dot{u}(t) = \phi_n \omega_n (-A_n \sin(\omega_n t) + B_n \cos(\omega_n t)) \quad (7.23)$$

$$\ddot{u}(t) = \phi_n \omega_n^2 (-A_n \cos(\omega_n t) - B_n \sin(\omega_n t)) \quad (7.24)$$

so

$$\ddot{u}(t) = -\phi_n \omega_n^2 q_n(t) \quad (7.25)$$

therefore, the undamped equation of motion can be rewritten as

$$-M(\phi_n \omega_n^2 q_n(t)) + K(q_n(t)\phi_n) = 0 \quad (7.26)$$

Equation 7.26 can be satisfied either if $q_n(t) = 0$, which is a trivial solution since it implies $u(t) = 0$ and there is no motion in the system, or

$$[K - \omega_n^2 M]\phi_n = 0 \quad (7.27)$$

The solution $\phi_n = 0$ is also a trivial solution suggesting that there is no motion. Therefore, Equation 7.28 must be satisfied and is known as the characteristic

equation.

$$\det[K - \omega_n^2 M] = 0 \tag{7.28}$$

When Equation 7.28 is expanded, a polynomial of order N in ω_n^2 is retrieved. The N roots, ω_n^2 , determine N natural frequencies of vibration, and are known as the eigenvalues, characteristic values or normal values [81]. Once the natural frequency is known, Equation 7.27 can be solved to obtain the vector, ϕ_n . For every ω_n there is a corresponding ϕ_n . ϕ_n vectors are known as the eigenvectors, natural modes of vibration, or natural mode shapes of vibration [81].

Natural vibration and modes for structural beams

In MATLAB, there exists a function $[V,D] = EIG(A,B)$ that produces a diagonal matrix D of generalized eigenvalues and a full matrix V whose columns are the corresponding eigenvectors. In this case A would be the stiffness matrix, and B would be the mass matrix. Assuming a cantilever beam where the mass matrix M and the stiffness matrix K are already known. The eigenvalues and vectors would be easily retrieved using the function, where as previously noted, the eigenvalues correspond to the natural frequency ω_n and the eigenvectors are the natural modes of vibration ϕ_n . The first six modal shapes of a cantilever beam using the function are shown in Figure 7.12, and for a fixed ends beam in Figure 7.13.

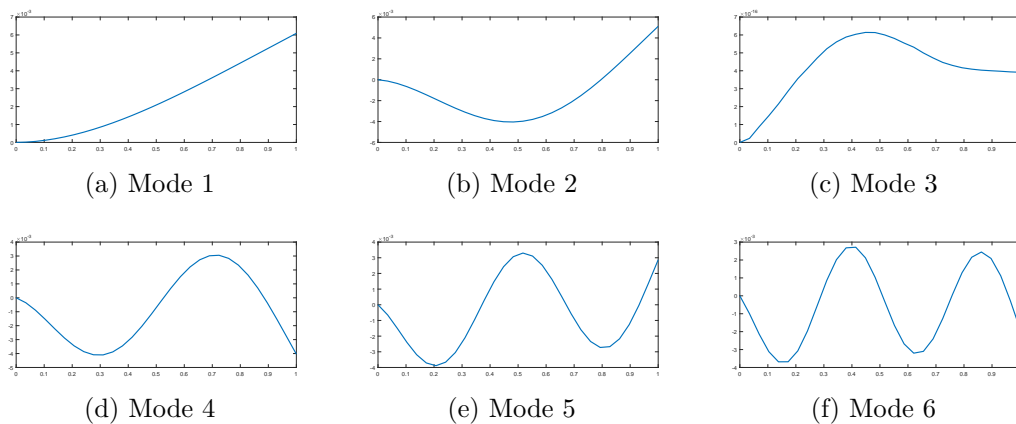


Figure 7.12: Modal Shapes for Cantilever Beam

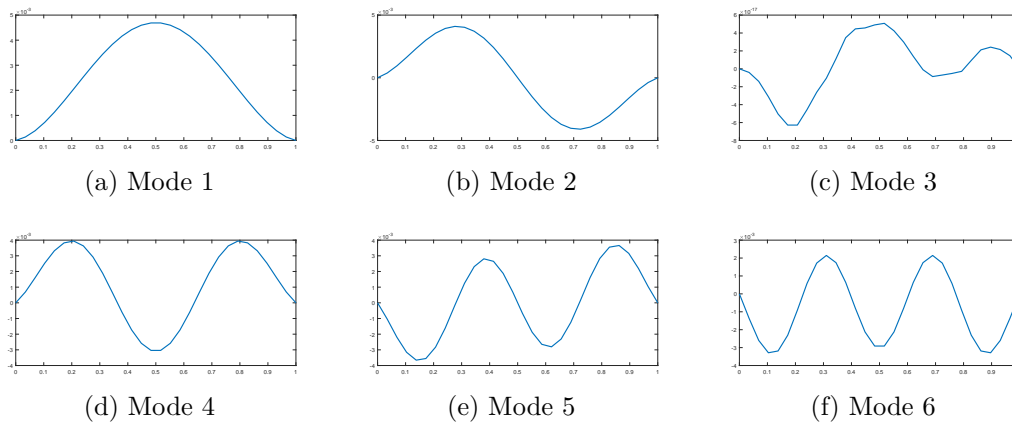


Figure 7.13: Modal Shapes for a Fixed Ends Beam

7.3 Time-stepping Methods for linear systems

There are several time integrating methods for solving the equations of motion. Some of the most common are the Newmark- β method (NBM), the Runge-Kutta method (RKM), the Central Difference method (CDM), and several more. For the scope of this project, the Newmark-Beta method, the Linear acceleration method and the Central Difference method are listed below. Three requirements are needed for selecting an appropriate numerical procedure: (1) convergence, (2) stability, and (3) accuracy [81].

7.3.1 The Central Difference Method

The CDM is based on a finite difference approximation of the time derivatives of displacement [81]. The expressions for velocity and acceleration are [81]

$$\dot{u}_i = \frac{u_{i+1} - u_{i-1}}{2\Delta t} \quad (7.29)$$

$$\ddot{u}_i = \frac{u_{i+1} - 2u_i + u_{i-1}}{(\Delta t)^2} \quad (7.30)$$

Substituting these expressions for velocity and acceleration into the equation of motion gives [81]

$$M \left[\frac{u_{i+1} - 2u_i + u_{i-1}}{(\Delta t)^2} \right] + C \left[\frac{u_{i+1} - u_{i-1}}{2\Delta t} \right] + K u_i = p_i \quad (7.31)$$

From time stepping, u_i and u_{i-1} are assumed known. Solving for u_{i+1} gives

$$\left[\frac{M}{(\Delta t)^2} + \frac{C}{2\Delta t} \right] u_{i+1} = - \left[\frac{M}{(\Delta t)^2} - \frac{C}{2\Delta t} \right] u_{i-1} + \left[\frac{2M}{(\Delta t)^2} - K \right] u_i + p_i \quad (7.32)$$

which may be written as

$$A_0 u_{i+1} = A_1 u_i + A_2 u_{i-1} + p_i \quad (7.33)$$

where

$$A_0 = \left[\frac{M}{(\Delta t)^2} + \frac{C}{2\Delta t} \right] \quad (7.34)$$

$$A_1 = \left[\frac{M}{(\Delta t)^2} - \frac{C}{2\Delta t} \right] \quad (7.35)$$

$$A_2 = - \left[\frac{2M}{(\Delta t)^2} + K \right] \quad (7.36)$$

The unknown u_{i+1} is given by

$$u_{i+1} = \frac{A_1 u_i + A_2 u_{i-1} + p_i}{A_0} \quad (7.37)$$

From Equation 7.30 it is evident that u_0 and u_{-1} are needed to determine u_1 .

The initial displacement u_0 is known. For $i = 0$

$$(\dot{u}_0) = \frac{u_1 - u_{-1}}{2\Delta t} \quad (7.38)$$

$$(\ddot{u}_0) = \frac{u_1 - 2u_0 + u_{-1}}{(\Delta t)^2} \quad (7.39)$$

solving for u_{-1} from Equation 7.38 and substituting in Equation 7.39,

$$u_{-1} = u_0 - \Delta t(\dot{u}_0) + \frac{(\Delta t)^2}{2} \ddot{u}_0 \quad (7.40)$$

The equations of motion at time $t=0$ shown in Equation 7.41 gives the acceleration in Equation 7.42,

$$M\ddot{u}_0 + C\dot{u}_0 + K u_0 = P_0 \quad (7.41)$$

$$\ddot{u}_0 = [M]^{-1}(P_0 - C\dot{u}_0 - K u_0) \quad (7.42)$$

Based on the equations shown, the solution in the central difference method is explicit.

Stability Condition

The stability condition for the CDM is

$$\frac{\Delta t}{T_n} < \frac{1}{\pi} \quad (7.43)$$

In CDM, a much smaller time step is required to approach good accuracy. Rather, $\frac{\Delta t}{T_n} < 0.1$ for definition of an adequate response, and $\Delta t = 0.01$ to 0.02 to represent ground acceleration accurately [81].

Computational Algorithm for Central Difference Method

The computational algorithm of the MDOF CDM is shown in Box 7.3.1. The mass and damping matrix of the system are first obtained. Then the CDM method starts where the initial acceleration, velocity and displacement are calculated. The Gaussian AEM algorithm begins where the stresses and strains of each spring is calculated using the return mapping softening model, and the internal forces at each degree-of-freedom is calculated. The next time step begins where the new internal force is presented in the equations of motion and the new acceleration, velocity and displacement are calculated.

Box. 7.3.1: Linear Central difference method

1. Initial Calculations
 - (a) Obtain Mass and Damping matrix of system
 - (b) $\ddot{u}_0 = [M]^{-1}(P_0 - C\dot{u}_0 - Ku_0)$ from [Eq. 7.42]
 - (c) Solve $u_{-1} = u_0 - \Delta t(\dot{u}_0) + \frac{(\Delta t)^2}{2}\ddot{u}_0$ from [Eq. 7.40]
 - (d) select appropriate Δt
2. Calculate for each time step, $i = 0, 1, 2, 3, \dots$
 - (a) update p_i to include the new internal force vector
 - (b) $u_{i+1} = \frac{A_1 u_i + A_2 u_{i-1} + p_i}{A_0}$ from [Eq. 7.37]
 - (c) $\dot{u}_i = \frac{u_{i+1} - u_{i-1}}{2\Delta t}$ and $\ddot{u}_i = \frac{u_{i+1} - 2u_i + u_{i-1}}{(\Delta t)^2}$ Eq. [7.30]
3. Repeat for the next time step. Replace i by $i + 1$

7.3.2 The Newmark- β Method

The finite difference approximations for the Newmark- β method developed by Newmark in 1959 are [82]

$$u_{i+1} = u_i + \Delta t \dot{u}_i + \frac{1}{2} \Delta t^2 \left[\left(1 - \frac{\beta}{2}\right) \ddot{u}_i + 2\beta \ddot{u}_{i+1} \right] \quad (7.44)$$

$$\dot{u}_{i+1} = \dot{u}_i + \Delta t \left[(1 - \gamma) \ddot{u}_i + \gamma \ddot{u}_{i+1} \right] \quad (7.45)$$

The parameters β and γ represent the variation of acceleration over a time step and determine the stability and accuracy of the method [81]. γ is typically $\frac{1}{2}$ and $\frac{1}{6} < \beta < \frac{1}{2}$. For linear systems, the equations of motion with iterations is

$$M\ddot{u}_{i+1} + C\dot{u}_{i+1} + Ku_{i+1} = p_{i+1} \quad (7.46)$$

Rewriting Equation 7.44 to represent \ddot{u}_{i+1} gives Equation 7.47. Substituting Equation 7.47 in 7.45 gives 7.48.

$$\ddot{u}_{i+1} = \frac{1}{\beta \Delta t^2} (u_{i+1} - u_i) - \frac{1}{\beta \Delta t} \dot{u}_i - \left(\frac{1}{2\beta} - 1 \right) \ddot{u}_i \quad (7.47)$$

$$\dot{u}_{i+1} = \frac{\gamma}{\beta \Delta t} (u_{i+1} - u_i) + \left(1 - \frac{\gamma}{\beta}\right) \dot{u}_i + \Delta t \left(1 - \frac{\gamma}{2\beta}\right) \ddot{u}_i \quad (7.48)$$

Regrouping and solving for u_{i+1} , by substituting Equations 7.47 and 7.48 into Equation 7.46 gives

$$\begin{aligned}
 & M \left(\frac{1}{\beta \Delta t^2} (u_{i+1} - u_i) - \frac{1}{\beta \Delta t} \dot{u}_i - \left(\frac{1}{2\beta} - 1 \right) \ddot{u}_i \right) + \\
 & C \left(\frac{\gamma}{\beta \Delta t} (u_{i+1} - u_i) + \left(1 - \frac{\gamma}{\beta} \right) \dot{u}_i + \Delta t \left(1 - \frac{\gamma}{2\beta} \right) \ddot{u}_i \right) + K u_{i+1} = p_{i+1}
 \end{aligned} \tag{7.49}$$

Rewriting Equation 7.49 in terms of the displacement, velocity and acceleration gives

$$\begin{aligned}
 & u_{i+1} \left(\frac{M}{\beta \Delta t^2} + \frac{C\gamma}{\beta \Delta t} + K \right) + u_i \left(-\frac{M}{\beta \Delta t^2} - \frac{C\gamma}{\beta \Delta t} \right) \\
 & + \dot{u}_i \left(-\frac{M}{\beta \Delta t} + C \left(1 - \frac{\gamma}{\beta} \right) \right) + \ddot{u}_i \left(-M \left(\frac{1}{2\beta} - 1 \right) + C \Delta t \left(1 - \frac{\gamma}{2\beta} \right) \right) = p_{i+1}
 \end{aligned} \tag{7.50}$$

which can be written in the form of

$$A_0 u_{i+1} = A_1 u_i + A_2 \dot{u}_i + A_3 \ddot{u}_i + p_i \tag{7.51}$$

where

$$A_0 = \left(\frac{M}{\beta \Delta t^2} + \frac{C\gamma}{\beta \Delta t} + K \right) \tag{7.52}$$

$$A_1 = \left(-\frac{M}{\beta \Delta t^2} - \frac{C\gamma}{\beta \Delta t} \right) \tag{7.53}$$

$$A_2 = \left(-\frac{M}{\beta \Delta t} + C \left(\frac{\gamma}{\beta} - 1 \right) \right) \tag{7.54}$$

$$A_3 = \left(-M \left(\frac{1}{2\beta} - 1 \right) + C \Delta t \left(1 - \frac{\gamma}{2\beta} \right) \right) \tag{7.55}$$

The displacement at time $i + 1$ is

$$u_{i+1} = [A_0]^{-1} [A_1 u_i + A_2 \dot{u}_i + A_3 \ddot{u}_i + p_i] \tag{7.56}$$

and the acceleration can also be obtained from the equation of motion 7.46

$$\ddot{u}_{i+1} = [M]^{-1} [p_{i+1} - C \dot{u}_{i+1} - K u_{i+1}] \tag{7.57}$$

Special cases of the Newmark- β method arise for specific values of γ and β . For $\gamma = 1/2$ and $\beta = 1/4$, the Newmark method is identical to the constant average acceleration. For $\gamma = 1/2$ and $\beta = 1/6$, the Newmark method is identical to the linear acceleration. Finally, for $\gamma = 1/2$ and $\beta = 0$ the Newmark method is reduced to the central difference method. For $\gamma = 1/2$ the Newmark method is at least second-order accurate. It is first order accurate for all other values of γ [83]. If the residual nonlinear forces are not negligible, then Equation 7.46 must be solved using the Newton-Raphson method.

Newmark Method Stability

The Newmark's method is stable with the condition of Equation 7.58 [81],

$$\frac{\Delta t}{T_n} \leq \frac{1}{\pi\sqrt{2}} \frac{1}{\sqrt{\gamma - 2\beta}} \quad (7.58)$$

For $\gamma = \frac{1}{2}$ and $\beta = \frac{1}{4}$, (constant average acceleration method), the condition becomes

$$\frac{\Delta t}{T_n} < \infty \quad (7.59)$$

Equation 7.59 indicates that the constant average acceleration method is stable for any Δt . It is only accurate for small values of Δt . For $\gamma = \frac{1}{2}$ and $\beta = \frac{1}{6}$, the linear acceleration method is stable if

$$\frac{\Delta t}{T_n} \leq 0.551 \quad (7.60)$$

Computational Algorithm

The computational algorithm for the linear multiple degree-of-freedom Newmark Method for a system is shown in Box 7.3.2.

Box. 7.3.2: MDOF Linear Newmark Method

1. Initial Calculations

- (a) Solve $M\ddot{u}_0 + C\dot{u}_0 + Ku_0 = p_0$ for \ddot{u}_0 [Eq. 7.46]
- (b) Select Δt
- (c) Calculate A_1, A_2, A_3 from [Eq. 7.53, 7.54, 7.55]

2. Calculate for each time step, $i = 0, 1, 2, 3, \dots$

- (a) Obtain $u_{i+1} = \frac{A_1 u_i + A_2 \dot{u}_i + A_3 \ddot{u}_i + p_i}{A_0}$ [Eq. 7.56]
- (b) Obtain $\dot{u}_{i+1} = \frac{\gamma}{\beta \Delta t} (u_{i+1} - u_i) + (1 - \frac{\gamma}{\beta}) \dot{u}_i + \Delta t \left(1 - \frac{\gamma}{2\beta}\right) \ddot{u}_i$ [Eq. 7.48]
- (c) Obtain $\ddot{u}_{i+1} = \frac{1}{\beta \Delta t^2} (u_{i+1} - u_i) - \frac{1}{\beta \Delta t} \dot{u}_i - \left(\frac{1}{2\beta} - 1\right) \ddot{u}_i$ [Eq. 7.47]

3. Repeat for the next time step. Replace i by $i + 1$ **7.3.3 Numerical Methods Classifications**

The general classifications of numerical integration methods are: *explicit* and *implicit* [83]. For single step explicit methods, the displacements and velocities at t_{i+1} are determined in the closed form from the displacements, velocities and accelerations at t_i . Hence, for structural systems with linear elastic stiffness and damping, the discrete-time systems can be written as Equation 7.61.

$$\begin{bmatrix} u(t_{i+1}) \\ \dot{u}(t_{i+1}) \end{bmatrix} = A \begin{bmatrix} u(t_i) \\ \dot{u}(t_i) \end{bmatrix} + B f^{ext}(t_i) \quad (7.61)$$

where A is a $2n \times 2n$ discrete time dynamics matrix that depends on $M, C, K, \Delta t$, and the time step. However, the implicit methods are a solution of a set of linear algebraic equations at each time step [83].

Based on the equations shown, the solution in Newmark method is implicit, and the CDM is explicit. In the CDM no iterative procedure is required because all the constitutive variables are available from computations at previous time steps [84].

7.4 Time-stepping methods for Nonlinear Systems

The implementation of nonlinear systems in the Equations of motion is simply done by using internal forces rather than the stiffness multiplied by the displacement. Similar to the amended equation of motion for nonlinearity (Equation 7.13), this modification is applied to the time integration schemes.

$$M\ddot{u} + C\dot{u} + f(s) = p(t) \quad (7.62)$$

The modifications to the Nonlinear Newmark- β Method and the Central Difference Method are presented in the following sections.

7.4.1 Nonlinear Newmark- β Method

The equations of the Newmark- β method were derived in section 7.3.2. The acceleration, velocity and displacements equations do not change; however the equations of motion 7.62 is implemented, where the stiffness matrix multiplied by the displacements is replaced by the internal forces. The iteration scheme that will be used is the Newton-Raphson method, for static analysis of a nonlinear system. For the equations of motion written in the form of Equation 7.63, only A_0 changes since the stiffness matrix is not incorporated. The modified A_0 is shown in Equation 7.64.

$$A_0 u_{i+1} = A_1 u_i + A_2 u_{i-1} + p_i - f_{Si} \quad (7.63)$$

$$A_0 = \left(\frac{M}{\beta \Delta t^2} + \frac{C\gamma}{\beta \Delta t} \right) \quad (7.64)$$

It should be noted that this method determines the solution at time $(i+1)$ from the equilibrium condition at time $(i+1)$. The resisting force $(f_S)_{(i+1)}$ is an implicit function of the unknown $u_{(i+1)}$, therefore an iteration method is required [81].

Newton Raphson Iteration Scheme

An iterative procedure is used such that u^{j+1} can be found as an improved estimate from u^j . Expanding the resisting force $f_S^{(j+1)}$ in Taylor series about the known estimate u^j gives

$$f_S^{(j+1)} = F_S^j = \left. \frac{\partial f_S}{\partial u} \right|_{u^j} (u^{(j+1)} - u^{(j)}) + \frac{1}{2} \left. \frac{\partial^2 f_S}{\partial u^2} \right|_{u^j} (u^{(j+1)} - u^{(j)})^2 + \dots \quad (7.65)$$

If u^j is close to the solution then change $\Delta u^j = u^{(j+1)} - u^j$ will be small and the second higher order terms are neglected, leading to Equation 7.66

$$f_S^{j+1} = f_S^j + K_T^j \Delta u^j = 0 \quad (7.66)$$

$$K_T^j \Delta u^j = p - f_S^j = R^j \quad (7.67)$$

where K_T is the tangent stiffness at u^j . Solving 7.67 gives a new estimate of the displacement

$$u^{(j+1)} = u^{(j)} + \Delta u^{(j)} \quad (7.68)$$

The additional displacement $\Delta u^{(j+1)}$ due to the residual force is calculated from

$$K_T^{(j+1)} \Delta u^{(j+1)} = R^{(j+1)} \quad (7.69)$$

The new displacement is

$$u^{(j+2)} = u^{(j+1)} + \Delta u^{(j+1)} \quad (7.70)$$

The new value of $R^{(j+2)}$ is continued until convergence is achieved.

Computational Algorithm

The new computational algorithm for the nonlinear Newmark- β method is presented in Box 7.4.1.

Box. 7.4.1: MDOF Nonlinear Newmark method with Newton Raphson iteration

1. Initial Calculations
 - (a) Solve $M\ddot{u}_0 + C\dot{u}_0 + f(s)_0 = p_0$ for \ddot{u}_0 Eq. [7.46]
 - (b) Select Δt
 - (c) Calculate A_1, A_2, A_3 from [Eq.7.53,7.54,7.55]
2. Calculate for each time step, $i = 0, 1, 2, 3, \dots$
 - (a) initialize $j = 1, u_{i+1}^j = u_i, (f_s)_{i+1}^j = (f_s)_i$ and $(K_T)_{i+1}^j = (K_T)_i$
 - (b) $\hat{p}_i = A_1 u_i + A_2 \dot{u}_i + A_3 \ddot{u}_i + p_i$
3. For each Newton Raphson iteration, $j = 1, 2, \dots$
 - (a) Calculate residual force vector \hat{R}_{i+1}^j
 - (b) check if convergence is obtained. if convergence criteria is not met then continue to step 3c, otherwise go to step 4
 - (c) $(\hat{K}_T)_{i+1}^j = (K_T)_{i+1}^j + A_1$
 - (d) $\Delta u_{i+1}^{j+1} = \hat{R}_{i+1}^j / (\hat{K}_T)_{i+1}^j$
 - (e) $u_{i+1}^{j+1} = u_{i+1}^j + \Delta u_{i+1}^{j+1}$
Replace j by $j + 1$, and repeat steps 3a to 3e.
4. Calculate velocity and acceleration
 - (a) Obtain \dot{u}_{i+1} from [Eq. 7.48]
 - (b) Obtain \ddot{u}_{i+1} from [Eq. 7.47]
5. Repeat for the next time step i . Replace i by $i + 1$

7.4.2 Nonlinear Central Difference Method

Rewriting the equations of motion from Equation 7.73 to incorporate the inelastic behaviour gives

$$M\ddot{u}_i + C\dot{u}_i + (f_s)_i = P_i \quad (7.71)$$

$$\ddot{u}_i = [M]^{-1}(P_i - C\dot{u}_i - (f_s)_i) \quad (7.72)$$

$$M \left[\frac{u_{i+1} - 2u_i + u_{i-1}}{(\Delta t)^2} \right] + C \left[\frac{u_{i+1} - u_{i-1}}{2\Delta t} \right] + f_{Si} = p_i \quad (7.73)$$

so

$$A_0 u_{i+1} = A_1 u_i + A_2 u_{i-1} + p_i - f_{S_i} \quad (7.74)$$

where

$$A_0 = \left[\frac{M}{(\Delta t)^2} + \frac{C}{2\Delta t} \right] \quad (7.75)$$

$$A_1 = \left[\frac{M}{(\Delta t)^2} - \frac{C}{2\Delta t} \right] \quad (7.76)$$

$$A_2 = - \left[\frac{2M}{(\Delta t)^2} \right] \quad (7.77)$$

The difference between the linear and nonlinear CDM is in Equation 7.77, where the stiffness matrix K is no longer a part of the equation. The advantage is that K is no longer needed to be inverted in every iteration. Since the method will be applied to a MDOF system of high rise structures, this will significantly reduce computational cost as opposed to using the Newmark- β method. Another advantage is that $f_{(S_i)}$ is calculated explicitly, making the method one of the simplest in comparison to other MDOF procedures for analysis. The computational algorithm is therefore amended respectively. A disadvantage of using the CDM is that the time step must be really small. Considering that the mass and damping matrix are diagonalised, having a small time step is not so disadvantageous since the computational cost is quite low, and there is no stiffness matrix inversion. A special case of the dynamic problem can result in convergence of solution of a static problem. In other words, a static problem can be presented as a special case of dynamic problem. For representing the static case using the dynamic model, $Ku = F_{int}$. The mass matrix, and damping matrix of Equation 7.19 are presented in the following sections.

7.4.3 Summary of Methods

The method chosen for the nonlinear dynamic analysis is based on a comparison of the methods, shown in Table 7.1. Assuming a cantilever beam, with span of 1m, and 0.15m cross-section, the calculated critical time step for the Central Average Acceleration Method, Δt can be any number, however it must be small for

Table 7.1: Summary of advantages and disadvantages

	Newmark- β	Central Differences
Numerical method	Implicit	Explicit
critical Δt	Stable with large Δt	Stable at small Δt
Nonlinearity adaptation	Requires iteration scheme such as the Newton Raphson method Requires inverting the stiffness matrix in every iteration	No iteration scheme required does not require inverting the stiffness matrix

obtaining desired accuracy, and for the CDM should be at least $\Delta t = 1.6 \times 10^{-4} = 0.00016$.

7.5 Dynamic Formulation and Application in AEM

Now that the elastic and inelastic dynamic equations are formulated, they will be applied in the context of AEM to analyse structural systems subject to dynamic loading. The mass and damping matrix are formulated in the following sections. Application of the dynamic analysis to earthquake loading and extreme wind loading is presented in the following chapters.

7.5.1 Determination of Mass Matrix

The mass matrix for a single element is a 3×3 matrix, since each element has 3 degrees-of-freedom. The mass matrix is a diagonal matrix, with the diagonal elements shown in Equation 7.78. The element mass and inertia are assumed lumped at the element centre. The mass matrices must comply with the following conditions [85]: (1) symmetry: $(M^e)^T = M^e$; (2) conservation; and (3) positivity: the matrix should have diagonally positive elements.

$$M^e = \text{diag} \left\{ \begin{matrix} M_1 \\ M_2 \\ M_\alpha \end{matrix} \right\} = \text{diag} \left\{ \begin{matrix} m/2 \\ m/2 \\ \alpha m l^2 \end{matrix} \right\} \quad (7.78)$$

where, $[M_1]$ and $[M_2]$ are the element mass in the x direction and the y-direction respectively, and $[M_3]$ is the mass due to the rotation direction, m is the total mass of the element, α is a small value and l is the length of the element. In the computational algorithm, the mass matrix is:

1. localized: mass matrix of each element is formed separately
2. transformed from local to global coordinates: $M_g = T^t M T$
3. assembled into global matrix with all elements and degrees-of-freedom

7.5.2 Determination of Damping Matrix

The process by which vibration diminishes in amplitude is damping [81]. The Rayleigh Damping is a proportional damping model that expresses the damping as a linear combination of mass and stiffness, shown as Equation 7.79.

$$\mathbf{C} = a\mathbf{M} + b\mathbf{K} \quad (7.79)$$

where a and b are damping parameters, $[\mathbf{C}]$ is the damping matrix, $[\mathbf{M}]$ is the mass matrix, and $[\mathbf{K}]$ is the stiffness matrix.

a and b calculation

For linear problems the natural frequencies ω_i and the modes of vibration ϕ_i can be obtained. The damping ratio for the i^{th} mode of a system is

$$\xi_i = \frac{a}{2\omega_i} + \frac{b\omega_i}{2} \quad (7.80)$$

where, ξ_i is the damping ratio, and ω_i is the natural frequency. For every ω_i there is a corresponding ξ_i . Two values of ξ_i can be set to solve the two equations with two unknowns a and b using Equation 7.80. Once a and b are calculated the damping matrix \mathbf{C} can be calculated.

It is evident that with an increasing ω_i , then ξ_i will get bigger. However this is not significant since the larger ω_i are resulted from higher degrees of modal shapes which are considered insignificant. For simplicity of the dynamic analysis using the Gaussian AEM, b is chosen as zero. So the damping matrix is calculated

as $C = aM$.

7.5.3 Implementing dynamics and nonlinearity in MATLAB code

Implementing the nonlinear time stepping schemes into the dynamic code is presented. The nonlinearity in the model comes from the spring material nonlinearity and is determined by whether the material is elastic or elasto-plastic, which is related to the softening model yield criteria. Including the softening model along with the Central Difference method allows to generate a code with both linear and nonlinear behaviour. A few modifications are required to be done to the return mapping softening algorithm for implementing the CDM. Firstly, the stiffness matrix is not needed to be updated with every iteration, since the dynamic model does not require the stiffness matrix, rather only the internal forces need to be calculated. Therefore, the stiffness matrix is not needed to be calculated in every iteration. Secondly, since the CDM is an explicit method the Newton Raphson iteration scheme is not needed. Considering that there is no stiffness matrix update needed or inversion, and no Newton Raphson scheme, this leads to a computationally low cost algorithm.

The computational algorithm for a nonlinear dynamic code with AEM is explained for each time step. At the first time step an initial displacement velocity and acceleration are calculated from an initial guess ($u = 0$). Then the Gaussian AEM with softening material behaviour begins. There is a loop for every element. For each element, the stresses and strains for each spring are calculated from the displacement calculated using the CDM. Based on the calculated stresses and strains the yield criteria for each spring is examined. The yield criteria determines whether the springs are elastic, elasto-plastic or failed, and then the corresponding internal forces are calculated. For failed springs, the internal force is set to be zero. The internal forces for each springs are assembled to the global force vector to be used in the next time step iteration. At the next time step the internal forces are updated, as well as all other external forces for that time step, and the new displacement, velocity and acceleration are calculated using the CDM. Then the Gaussian AEM algorithm begins again. This process is repeated until the

time required is reached. The computational algorithm is displayed in Box 7.5.3.

Box. 7.5.1: Nonlinear CDM with Gaussian AEM

1. Initial Calculations
 - (a) Obtain Mass and Damping matrix of system
 - (b) $\ddot{u}_i = [M]^{-1}(P_i - C\dot{u}_i - (f_s)_i)$ Eq.[7.72]
 - (c) Solve $u_{-1} = u_0 - \Delta t(\dot{u}_0) + \frac{(\Delta t)^2}{2}\ddot{u}_0$ [Eq. 7.40]
 - (d) Calculate A_0, A_1 and A_2 [Eq. 7.75, 7.76, 7.77]
 - (e) select appropriate Δt
2. Calculate for each time step, $i = 0, 1, 2, 3, \dots$
 - (a) $u_{i+1} = [A]^{-1}[A_1u_i + A_2u_{i-1} + p_i - f_{s_i}]$ Eq.[7.74]
 - (b) $\dot{u}_i = \frac{u_{i+1} - u_{i-1}}{2\Delta t}$ and $\ddot{u}_i = \frac{u_{i+1} - 2u_i + u_{i-1}}{(\Delta t)^2}$ Eq. [7.30]
 - (c) Begin Gaussian AEM loop
 - Loop through every element and then spring to calculate the new stresses and strains from u_{i+1} , using return mapping algorithm and softening yield criteria.
 - Update internal force vector f_{s_i} .
3. Repeat from 2 for the next time step. Replace i by $i + 1$

7.6 Dynamic Analysis for Verification

This section presents some implementation of the dynamic model to simple structures. Analysis of structures undergoing free vibration with and without damping are presented to ensure that the model behaves as expected. A large displacement analysis of a frame is then presented, where no element separation is allowed.

7.6.1 Free Vibration

Free vibration is the motion of a structure without an external forces or dynamic excitation [81]. The vibration is initiated by an initial disturbance to the structure. This phenomenon is verified in the AEM algorithm presented. Consider a cantilever beam with a load applied at the free end at time step 500 ($\Delta t = 0.00005$, time = 0.025 sec, iteration 500 out of 10,000). The free vibration of the undamped and damped system are presented as follows.

Undamped system

For an undamped system the expected behaviour of the beam after a disturbance is shown in Figure 7.14. The equations of motion governing the undamped system are presented in Equation 7.81, with initial conditions in Equation 7.82.

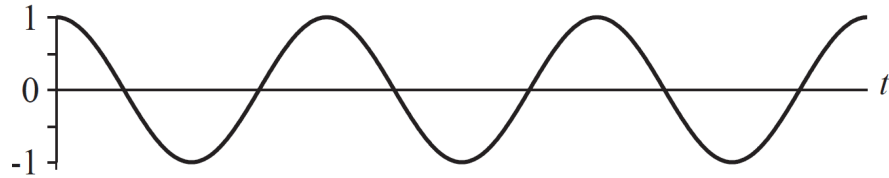


Figure 7.14: Free vibration of undamped system [81]

$$M\ddot{u} + Ku = 0 \tag{7.81}$$

$$u = u(0) \quad \dot{u} = \dot{u}(0) \tag{7.82}$$

Figure 7.15 shows the displacement, velocity and acceleration of the point at which the load is applied. Figure 7.15a is the displacement, velocity and acceleration of the free end of the system during the first 0.2 seconds. As can be seen before the perturbation was presented in the 500th iteration, the displacement, velocity and acceleration is zero. From Figure 7.15b the graphs show that the system is vibrating freely with no damping occurring. The results show good accordance with the expected result from Figure 7.14.

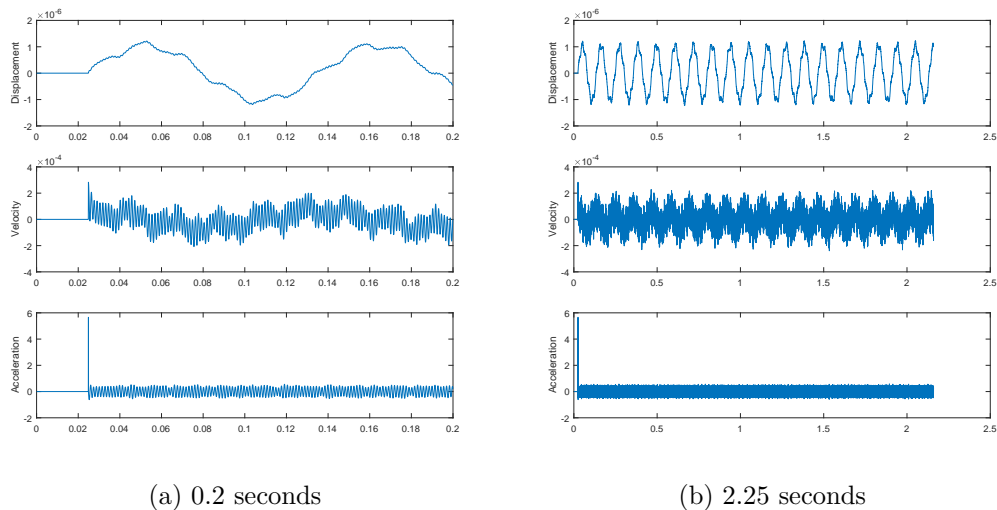


Figure 7.15: Free vibration of point at which load is applied

Damped system

The free vibration of a damped system is shown in Figure 7.16, where the vibration eventually "damps" out due to the damping coefficient in the system. Similar to the example in the undamped system, a cantilever beam is disturbed at the 500th time step, and the displacement, velocity and acceleration are shown in Figure 7.17. It is evident that leaving the system to react to the disturbed force eventually leads to a static solution.

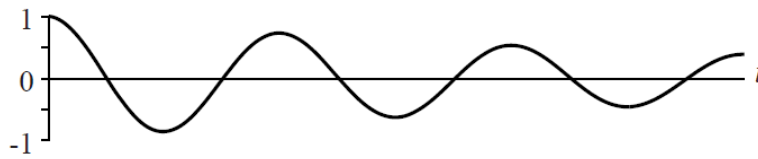


Figure 7.16: Free vibration of damped system [81]

$$M\ddot{u} + C\dot{u} + Ku = 0 \quad (7.83)$$

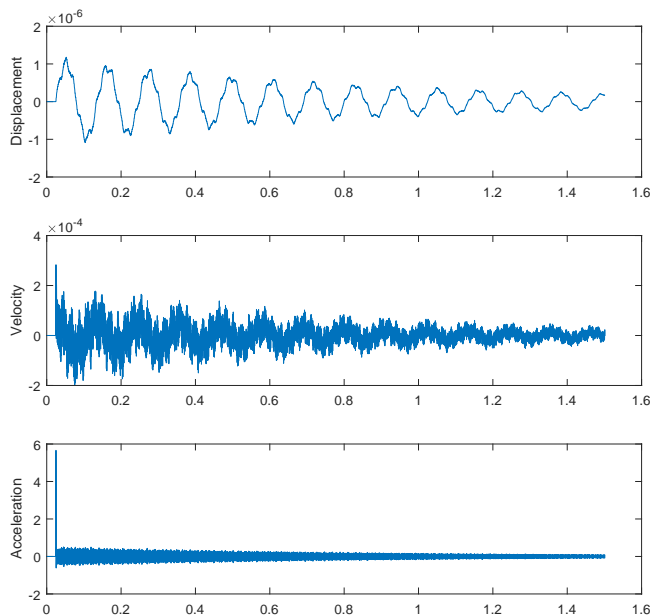


Figure 7.17: Displacement, velocity and acceleration of damped cantilever system at free end

7.7 Analysis Results

Different types of loading scenarios are implemented on beams and frames in this section to demonstrate the dynamic behaviour of a multiple degree-of-freedom system. Considering a cantilever beam with 1m span and $0.15 \times 0.15\text{m}$ cross-section. The material properties are similar to the beam shown from Table 5.1. Different loading conditions are applied to the beam as shown below.

Point load increasing with time

Figure 7.18a displays the force-displacement diagram of the free end of the beam, where the load is applied. Figure 7.18b shows the displacement, velocity and acceleration of the point at which the load is applied, with respect to time. The Figure shows that the displacement, velocity and acceleration damp out to eventually a static solution. Figure 7.19 is the deflection of the beam at different time steps. It is clear that the deflection is oscillating between the positive and negative y direction, which is expected in the dynamic behaviour.

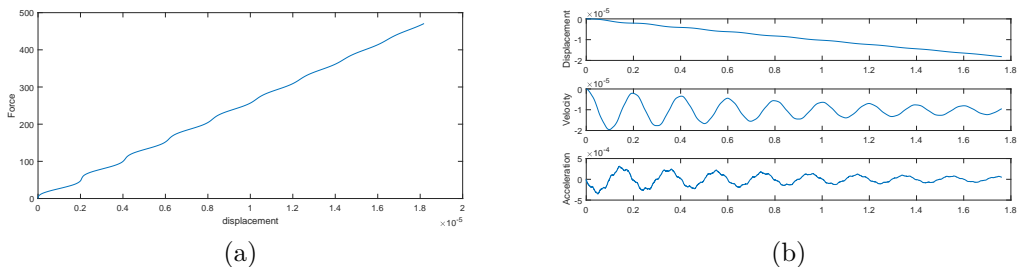


Figure 7.18: displacement, velocity and acceleration at free end

Figure 7.19 shows the behaviour of the beam deflection at different time steps.

Point load on cantilever beam with no damping

The acceleration velocity and displacement of the cantilever beam with no damping is shown in Figure 7.20. The results show that velocity and acceleration are clearly undamped. The displacement increases with time (in the negative direction) because the load is incrementally increasing.

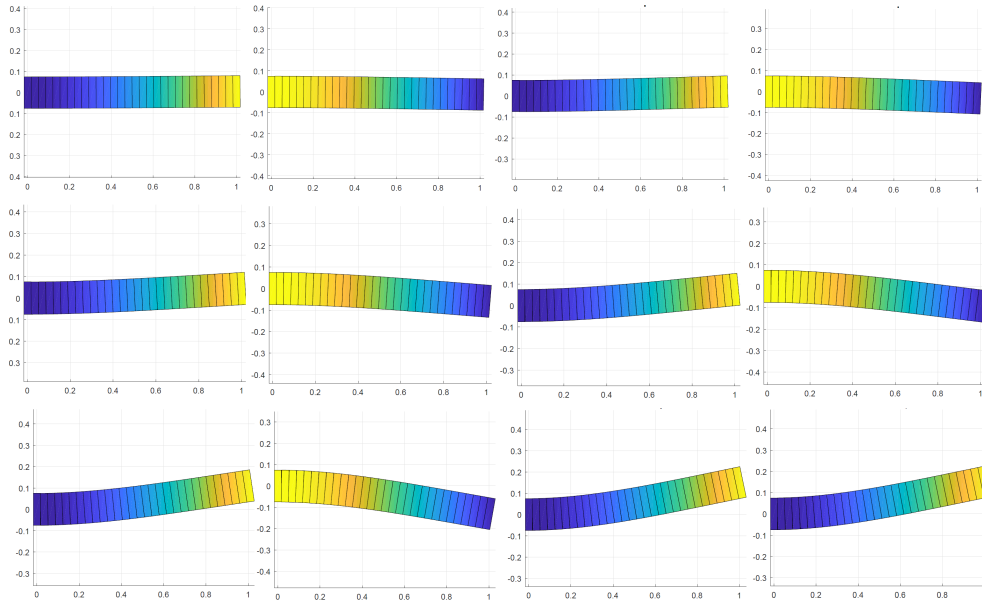


Figure 7.19: Beam Deflection of cantilever beam at different time steps

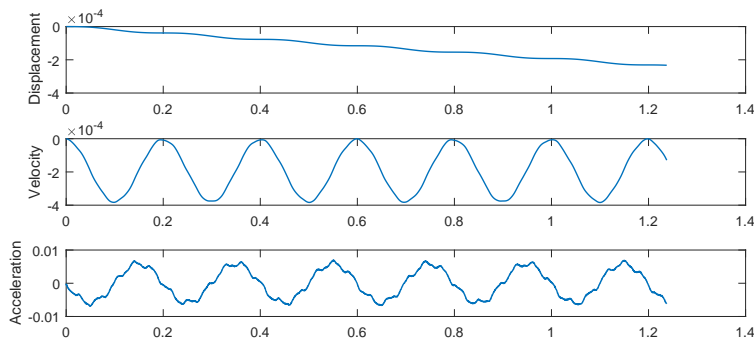


Figure 7.20: Displacement, velocity and acceleration of free free end of cantilever beam for undamped system

Point load increasing with time applied sinusoidally

The cantilever beam is subject to an incrementally increasing sinusoidal load, shown in Equation 7.84. Figure 7.21 is the force displacement diagram of the free end of the cantilever beam, subjected to the loading. Figure 7.22 shows the displacement, velocity and acceleration versus the time. The sinusoidal behaviour is clearly shown.

$$F_{ext} = F(t) \times \sin(\omega_n t) \tag{7.84}$$

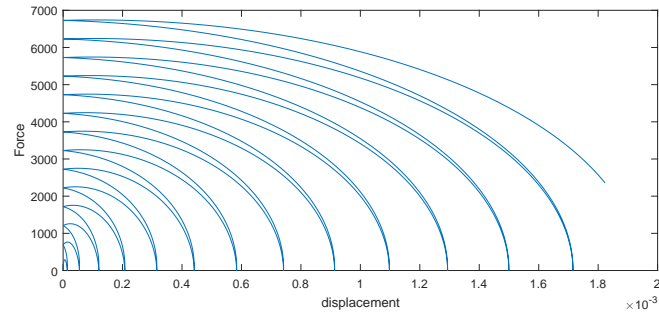


Figure 7.21: Force-displacement diagram for sin load

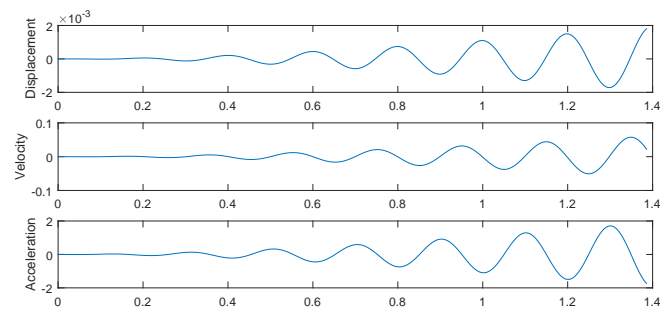


Figure 7.22: Displacement, velocity and acceleration at free end for cantilever beam with sin load

Large displacement Analysis

The dynamic analysis is applied to a multi-storey frame. In this example no failure (element separation) between elements is considered. So if the structure is subjected to large loads then unrealistic large displacements are expected. The deflection of a column frame subject to a large load that results in large displacement is presented. The frame has material properties of steel and is loaded at the top left point in the x-direction with an incrementally increasing load. The softening material model is used and the structure is analysed dynamically using the nonlinear CDM. The structure undergoes permanent deformation since the load is very large plastic deformation was found in most elements. The unfactored deflection of the frame is shown in Figure 7.23. As can be seen from the deflection figures, at time 1.8 seconds, the frame already had a deflection of approximately 6m at the top roof, which is unrealistic. The large deformation of the structure is well presented.

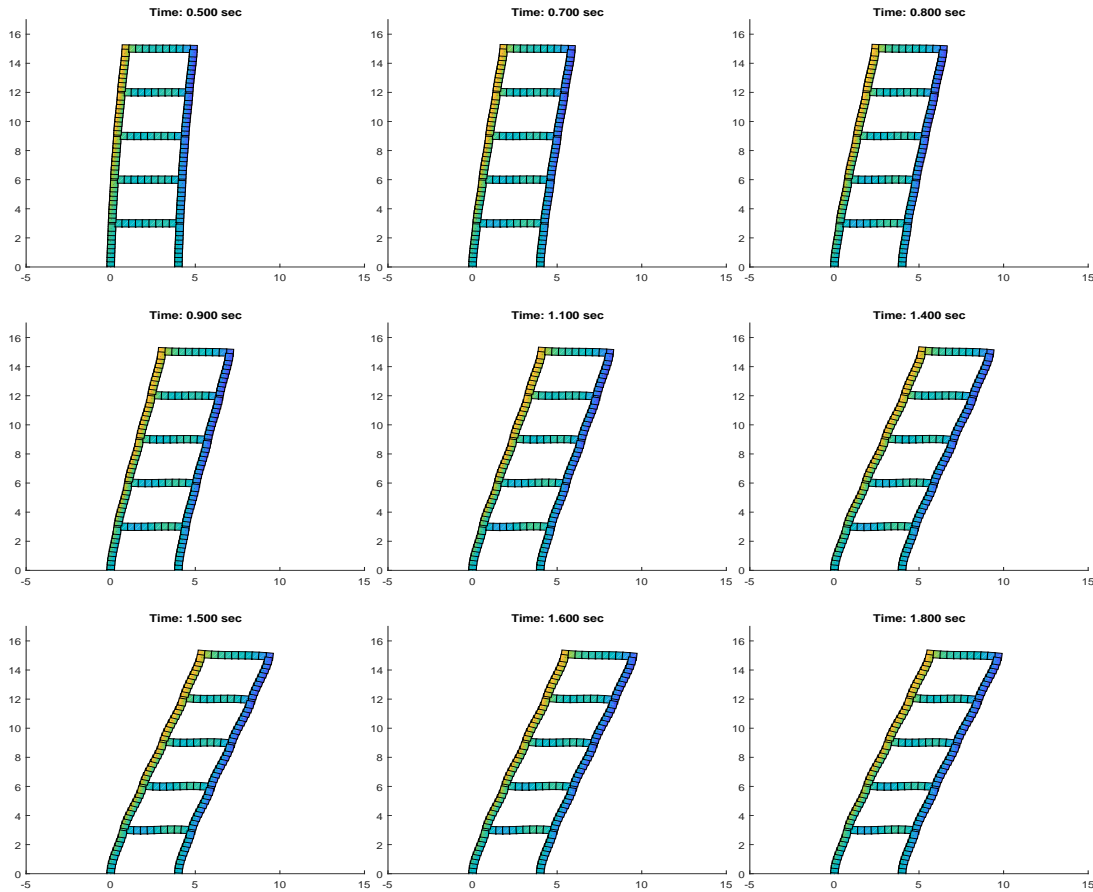


Figure 7.23: Large displacement for tall frame with no collapse

7.8 Conclusion

In this chapter a damage material model was presented for modelling softening material behaviour. The return mapping algorithm was formulated based on the 1D Hardening plasticity model. Material damage was represented as a material that experiences a softening behaviour. The return-mapping algorithm successfully modelled the behaviour, however it caused problems when springs exceeded the failed strain point. If a spring exceeds the failure limit then it would be considered totally detached from the system. In order to represent a failed spring, the stiffness of the spring is set as zero, rather than deleting the spring from the whole system. The problem is that zeros in the stiffness matrix cause the stiffness matrix to become singular, and cannot be inverted.

The use of a dynamic time integrator solved the problem of singularity in the stiffness matrix from the softening material behaviour. The Central Difference

Method was chosen as the most suitable integrator, rather than the Newmark- β Method. The CDM is explicit so does not require an iterative procedure to solve the dynamic equations. Although using the time step size required for the CDM is quite small, the advantages still outweigh this disadvantage. For simplicity, the damping matrix was chosen to be calculated using only the mass matrix. So the damping matrix is diagonal.

Some analysis of structures were presented such as the free vibration of a damped and undamped cantilever beam, analysis of cantilever beam with a sinusoidal load, and a large displacement analysis of a frame.

Since the damage material model and the failure of elements has been established in the Gaussian-AEM model the analysis of progressive collapse of structures can be presented. The collapse of frames subject to earthquake and wind loads are presented in the following chapters.

Chapter 8

Structures subject to Earthquake loads

In this chapter, dynamic analysis of frames subject to earthquakes is presented. The purpose is to analyse simple frame structures and their reaction to recorded time-acceleration data of earthquakes that had occurred. Modern building codes have strict requirements on the design of buildings to resist earthquakes. This chapter will entail an introduction to how earthquakes occur and how they are measured. From the given data of previous earthquakes, the ground acceleration is applied to the frames and the response of the structures is analysed using the nonlinear dynamic Gaussian AEM. The modification to the AEM algorithm is presented along with some examples.

8.1 Introduction

An earthquake is considered as one of the most destructive natural disasters [86]. Buildings have partially or totally collapsed during earthquakes [87] such as the ones in Valparaiso, Chile in 1985 [88]; Mexico City in 1985 [89],[90]; Luzon, Philippines in 1990 [91]; Guam in 1993 [92] ; Northridge, Calif. in 1994 [93]; Kocaeli, Turkey in 1999 [94]; Chi-Chi, Taiwan in 1999 [95]; and Bhuj, India in 2001 [96].

Several of the structural collapses occurred in buildings that were designed with accordance to modern and current seismic design codes [87]. Some of the

Table 8.1: Some of the Deadliest Earthquakes [97]

Date	Location	Deaths	Magnitude
July 27, 1976	China, Tangshan	655,000 (estimated)	7.5
June 20, 1990	Iran	50,000	7.7
Dec. 26, 2004	Sumatra, Indonesia	227,898	9.1
Oct. 8, 2005	Pakistan	85,000	7.6
May 12, 2008	Sichuan, China	87,586	7.9
Jan. 12, 2010	Haiti	222,570	7

deadliest earthquakes are displayed in Table 8.1, where the magnitude, the number of deaths the location and year are shown. The data shows that there is a significantly huge death toll as a circumstance to those earthquakes. For this reason, building design codes take into account the effect of earthquakes so that the structures can resist the natural occurrence in case it was to happen.

8.1.1 How do earthquakes occur?

An earthquake is the shaking and vibration of the earth's crust due to movement of the earth's plates (plate tectonics) [98]. When tectonic plates do not move smoothly against one another, a pressure build up occurs. When the pressure is released, an earthquake occurs. The point at which the pressure is released is called the focus. The point on the Earth's surface above the focus is called the epicentre. The energy of the earthquake is released in seismic waves that spread out from the focus. The most severe damage occurs closest to the epicentre. These terms are better displayed in Figure 8.1.

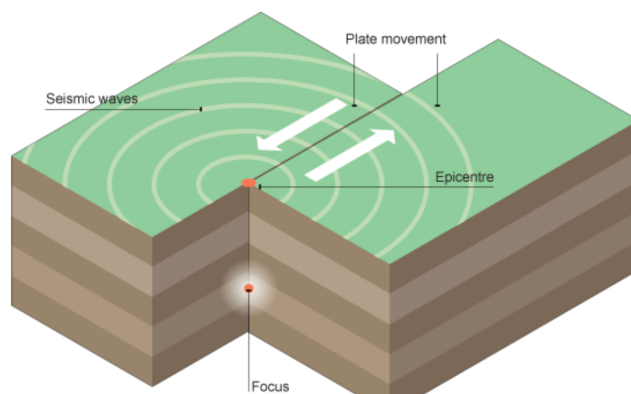


Figure 8.1: Focus, epicentre and seismic waves demonstration [99]

Understanding the earthquakes that may occur in regional areas is an impor-

tant factor in structural design of buildings. Every area has its own "scale" based on previous occurrences of earthquakes in that region. Structural design codes attribute an earthquake load factor as well as a region code. Therefore, analysing whether a structure will fail under seismic loading is very important in design of structure.

8.1.2 Seismic Scales

Two common measures are used to characterise ground motion: acceleration, and intensity. The acceleration is usually measured by seismometers that work during intensive shaking near an earthquake. An example of the data obtained from a seismograph is shown in Figure 8.2. This data is from the Indonesia earthquake that occurred in 2004. Seismic hazards of areas estimate how probable an area is likely to experience a certain acceleration at a given time [100]. Intensity is a descriptive way of presenting earthquakes, and the Modified Mercalli intensity (MMI) scale is used, which uses Roman scales to present the intensity, where I is generally unfelt and XII is total destruction [100]. Table 8.2 shows the difference between the Mercalli and Richter scales in how they are measured, calculated and scaled. Table 8.3 lists the intensity of the scale and what each number could represent.

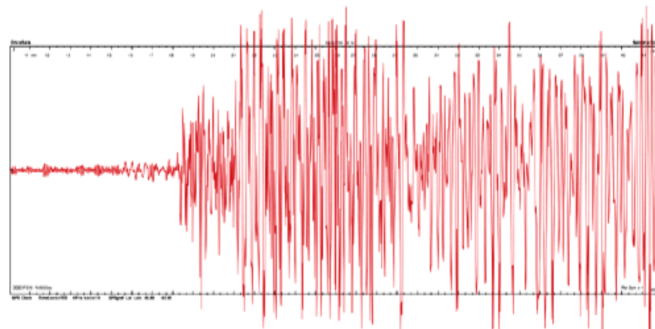


Figure 8.2: Seismogram of Sumatra, Indonesia 2004 earthquake [101]

8.1.3 Structural Damage

Figure 8.3b displays a building that collapsed in the Kobe, Japan 1995 earthquake. The death toll for that earthquake was 5,100 people [103]. The earthquake had a magnitude of 7.2, and a duration of 20 seconds. Since 1981, many of the

Table 8.2: Methods of measuring earthquakes [102]

	Mercalli Scale	Richter Scale
Measures	Effects caused by earthquake	Energy released by earthquake
Measuring Tool	Observation	Seismograph
Calculation	Quantified from observation of effect on earths surface, human, objects and man-made structures	Base-10 logarithmic scale obtained by calculating logarithm of the amplitude of waves.
Scale	I (not felt) to XII (total destruction)	From 2.0 to 10.0+. A 3.0 earthquake is 10 times stronger than a 2.0 one.
Consistency	Varies depending on distance from epicentre	Varies at different distances from the epicentre, but one value is given for the earthquake as a whole.

structures built had been designed to strict seismic codes. Newly built high rise structures were generally undamaged. Figure 8.3a shows a woman walking in Kobe the day after the earthquake. Figure 8.3b shows a satellite image of Sumatra Indonesia in 2004 before and after the earthquake with magnitude 9.1 took place.



(a) Structural collapse during the 1985 Mexico City earthquake

(b) Kobe, Japan 1995 earthquake [104]

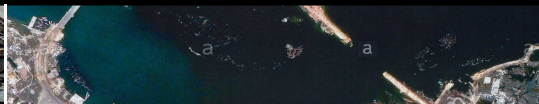
Table 8.3: Mercalli scale & Richter scale [102]

Mercalli	Richter	Witness Observations
I	1.0 to 2.0	Felt by very few people; barely noticeable.
II	2.0 to 3.0	Felt by a few people, especially on upper floors.
III	3.0 to 4.0	Noticeable indoors, especially on upper floors, but may not be recognized as an earthquake.
IV	4	Felt by many indoors, few outdoors. May feel like heavy truck passing by.
V	4.0 to 5.0	Felt by almost everyone, some people awakened. Small objects moved. Trees and poles may shake.
VI	5.0 to 6.0	Felt by everyone. Difficult to stand. Some heavy furniture moved, some plaster falls. Chimneys may be slightly damaged.
VII	6	Slight to moderate damage in well built, ordinary structures. Considerable damage to poorly built structures. Some walls may fall.
VIII	6.0 to 7.0	Little damage in specially built structures. Considerable damage to ordinary buildings, severe damage to poorly built structures. Some walls collapse.
IX	7	Considerable damage to specially built structures, buildings shifted off foundations. Ground cracked noticeably. Wholesale destruction. Landslides.
X	7.0 to 8.0	Most masonry and frame structures and their foundations destroyed. Ground badly cracked. Landslides. Wholesale destruction.
XI	8	Total damage. Few, if any, structures standing. Bridges destroyed. Wide cracks in ground. Waves seen on ground.
XII	8.0 or greater	Total damage. Waves seen on ground. Objects thrown up into air.



(a) 1964, Japan [105]

(b) 1998 Turkey, Adana [106]



(a) Woman walking in Kobe the day after the earthquake [107]

(b) A satellite image of Sumatra, Indonesia, before and after [108]

8.2 Earthquake Implementation in AEM

Although the damage to structures from earthquakes are quite severe, modelling the effect of a past earthquake on a linear elastic structure is straightforward. Recalling the equation of motion, there will be an extra external load applied to the structure which represents the earthquake effect. The data needed is the acceleration of the ground motion. The force equation due to the earthquake is shown in Equation 8.1.

$$F_Q(t) = -M\mathbf{d}(\ddot{u}_Q(t)) \quad (8.1)$$

where $F_Q(t)$ is the earthquake force vector at time step t , M is the diagonal mass matrix, \mathbf{d} is the earthquake input vector, and $\ddot{u}_Q(t)$ is the ground acceleration of the earthquake at time step t . To represent ground motion in the x-direction, the x-degrees of freedom in the vector contain the value of the acceleration. It is similar for the y-degrees of freedom if there was ground motion in the y-direction. The gravity effect is also included to the equation of motion by Equation 8.2.

$$F_g = M(\ddot{u}_g) \quad (8.2)$$

where, F_g is the gravity force vector, and \ddot{u}_g is $-9.81m/s^2$ at every y degree-of-freedom. The equation of motion at every time step is therefore shown as Equation 8.3 for a nonlinear case. Representing a linear dynamic case is having $F_{int} = Ku$.

$$M\ddot{u} + C\dot{u} + F_{int} = F_{ext}(t) + F_g + F_Q(t) \quad (8.3)$$

8.2.1 Earthquake Data

The acceleration used for the earthquake load applied to the following examples is based on the 1940 El Centro Earthquake. The acceleration time-history plot is shown in Figure 8.3. The time history for the Kobe 1995 earthquake is shown in Figure 8.4. The El Centro data was recorded for 50 seconds, while the Kobe data was recorded for 140 seconds. From the two graphs it can be seen that the Kobe earthquake was more powerful since it had a maximum acceleration of almost $8 \times 10^4 m/sec$ while, the El Centro earthquake had a maximum acceleration of $3.5 \times 10^4 m/sec$. The data is collected from reference [109]. There are several more

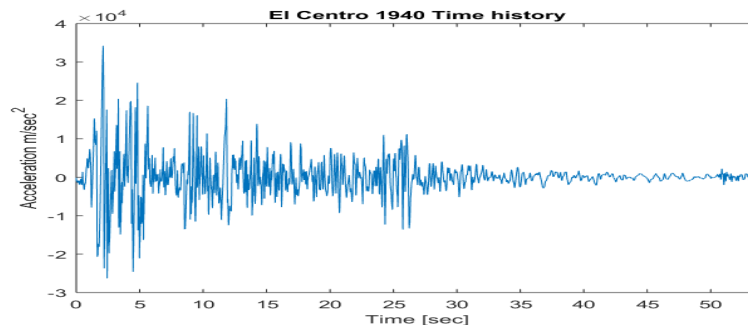


Figure 8.3: El Centro 1940 time history acceleration graph

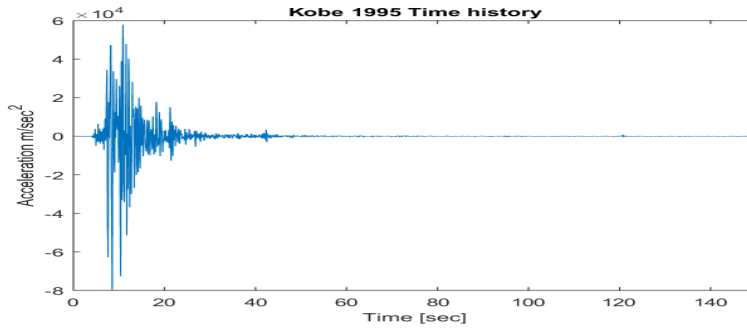


Figure 8.4: Kobe, Japan 1995 time history acceleration graph

earthquake data that are available, however for the purpose of demonstration only the El Centro and Kobe earthquakes are considered. In the following sections the implementation of earthquake data to the Applied Element code is presented for analysis of 2D frames.

8.2.2 Frame Implementation

2D frames with different loads, heights and floors are analysed using the Gaussian AEM in this section. As mentioned in previous chapters, the code is written in MATLAB. The frame nodes and connectivities are generated in ANSYS Mechanical APDL. ANSYS exports a data file containing the number of nodes, the table of connectivities and the degrees of freedom. MATLAB is used to read the exported data files from ANSYS to create the frame and begin the analysis of the frame using the Gaussian springs based AEM.

8.3 Applications

Some of the applications of the frame analysis to model the progressive collapse behaviour of structures are presented in this section. Different frame dimensions are considered and subject to the Kobe earthquake. There is no contact considered between elements.

8.3.1 1x1 Frame

The frame shown in Figure 8.5 is analysed for the point load applied at the midspan of the roof level shown, as well as with base excitation due to earthquake

loading, and inclusion of gravity effect. The properties of the materials are shown in Table 8.4. The ends at the boundary are fixed in the three degrees of freedom that are considered: horizontal direction, vertical direction and rotation. Figure 8.6 is the displacement, velocity and acceleration of the point at the midspan, before any failure in the frame occurs. Figure 8.7 is the displacement, velocity and acceleration . Figure 8.8 displays the deflection of the frame in the first millisecond. The deflection is factored so it can be seen. However, in reality the deflection cannot be seen and this is shown in the unscaled deflections presented in Figures 8.8a - 8.8c. Figure 8.9 presents the progressive collapse of the frame at different time steps until collapse occurs. As expected the frame first fails at the bottom right column near the boundary and later fails from the applied load that was at the midspan.

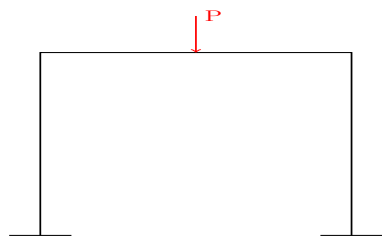


Figure 8.5: Frame with point load

Parameters	Value	Units
Modulus of Elasticity E	200,000	[MPa]
Shear Modulus of Elasticity G	76,923	[MPa]
Yield Stress	250	[MPa]
Beam span	3	[m]
Column span	5	[m]
cross-section width	0.15	[m]
cross-section thickness	0.15	[m]
Applied Load	1000	[N]

Table 8.4: Section Properties

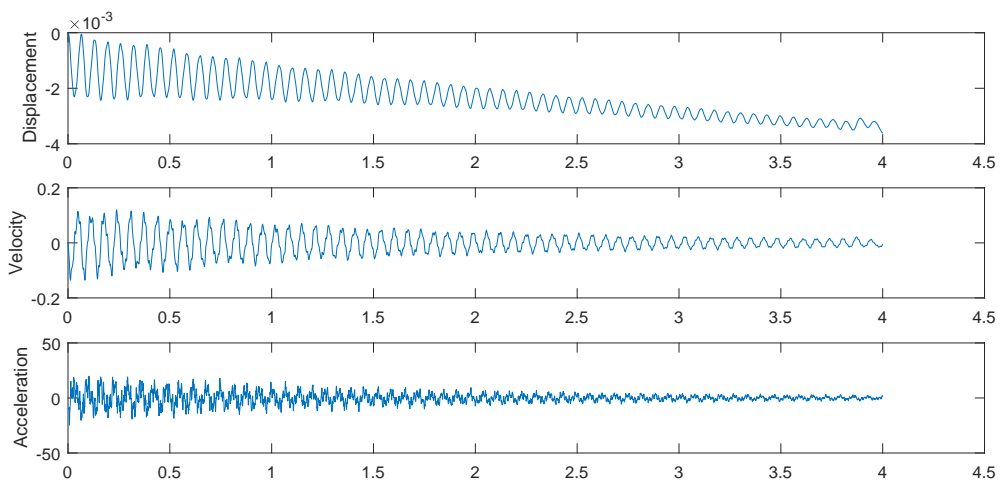


Figure 8.6: Acceleration, velocity and displacement vs. time at midspan before failure occurs

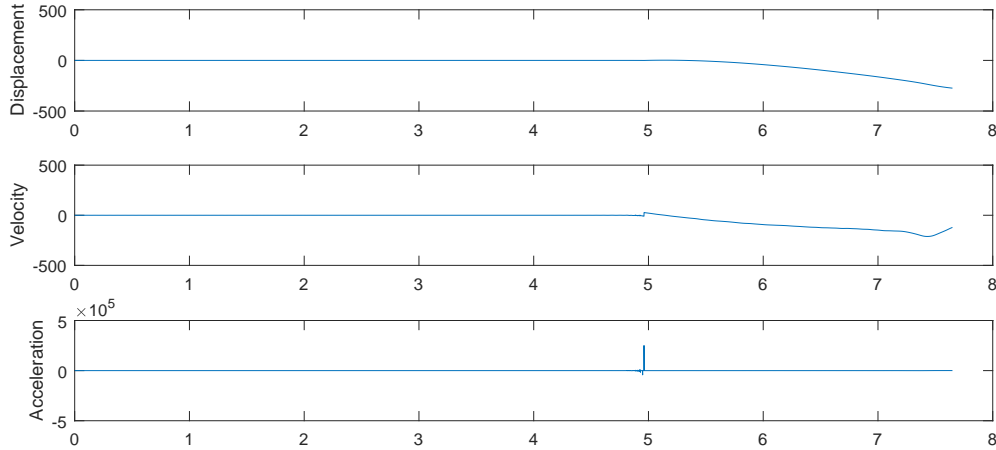


Figure 8.7: Displacement, velocity and acceleration after failure at midspan

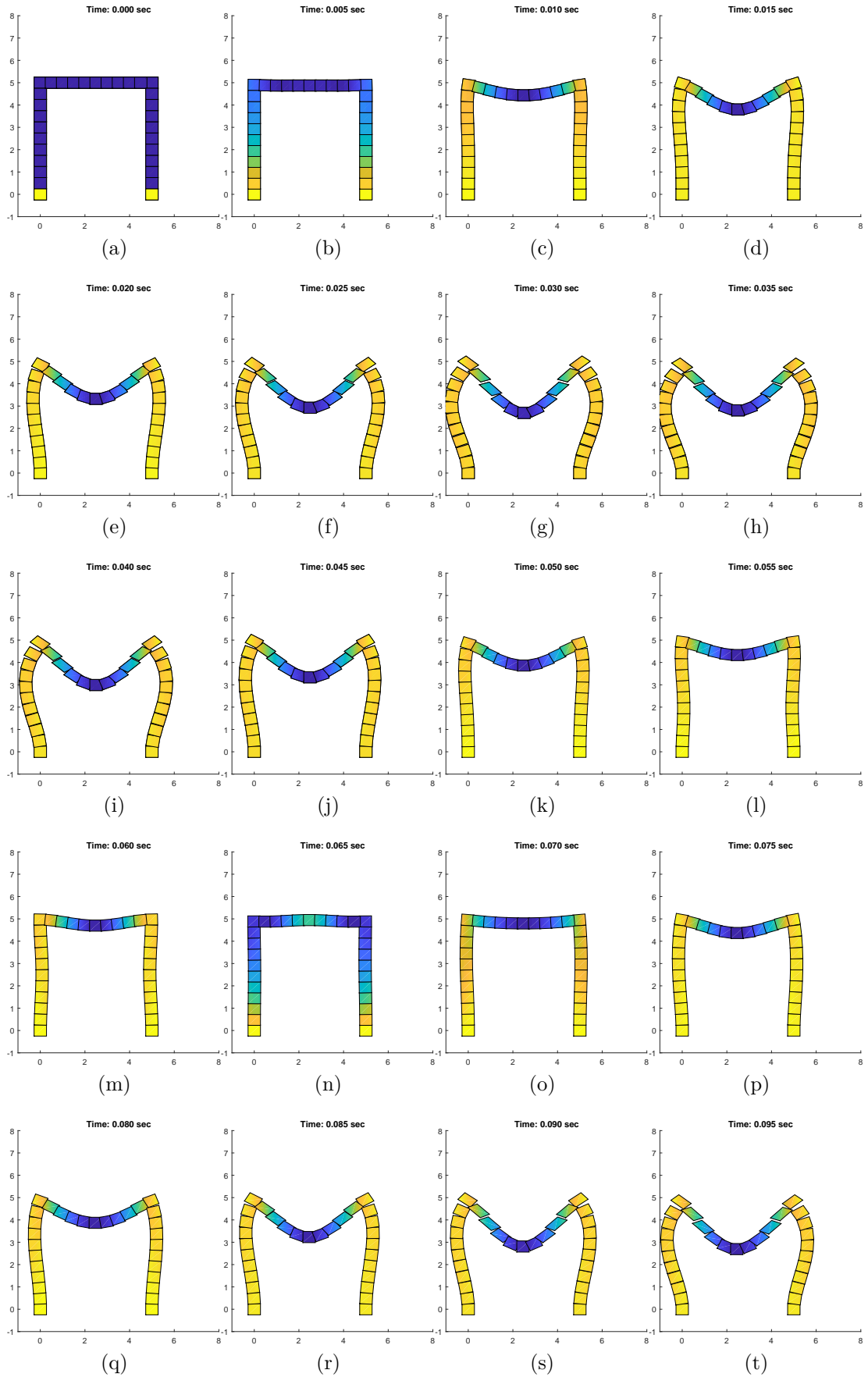


Figure 8.8: Factored frame deflection in first 0.1 second under earthquake Kobe load

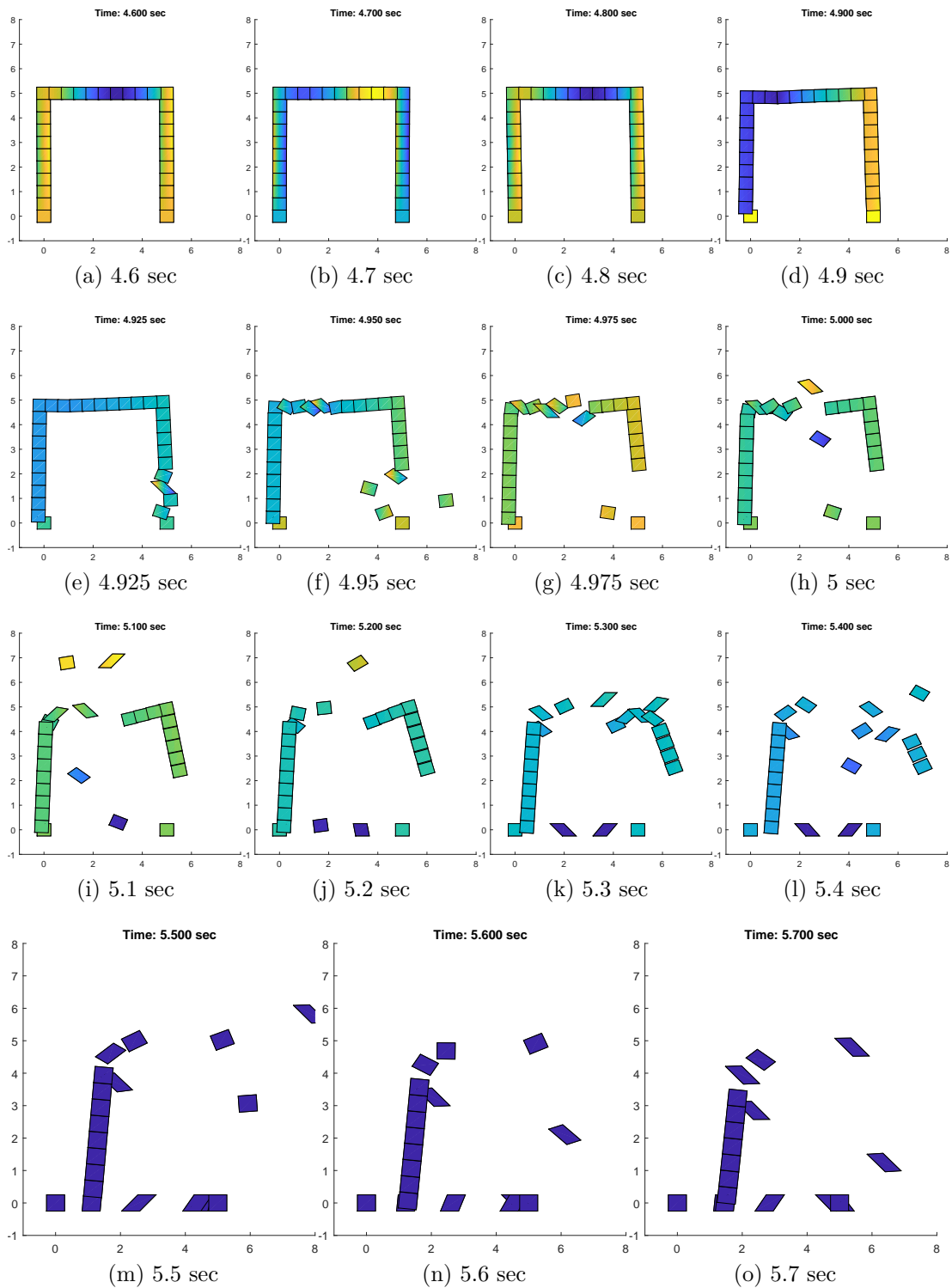


Figure 8.9: Progressive collapse of 1x1 frame with earthquake Kobe loading and loading applied at midspan

8.3.2 3x8 Frame

A frame with 8 floors and 3 bays is presented. The applied load on the frame is the El Centro earthquake, and a fixed incremental load applied in the positive x-direction along the first floor of the frame. Gravity is included. The results are shown in Figures 8.10 and 8.11. It can be seen that the structure fails due to the external load first, and the remainder of the building progressively collapses.

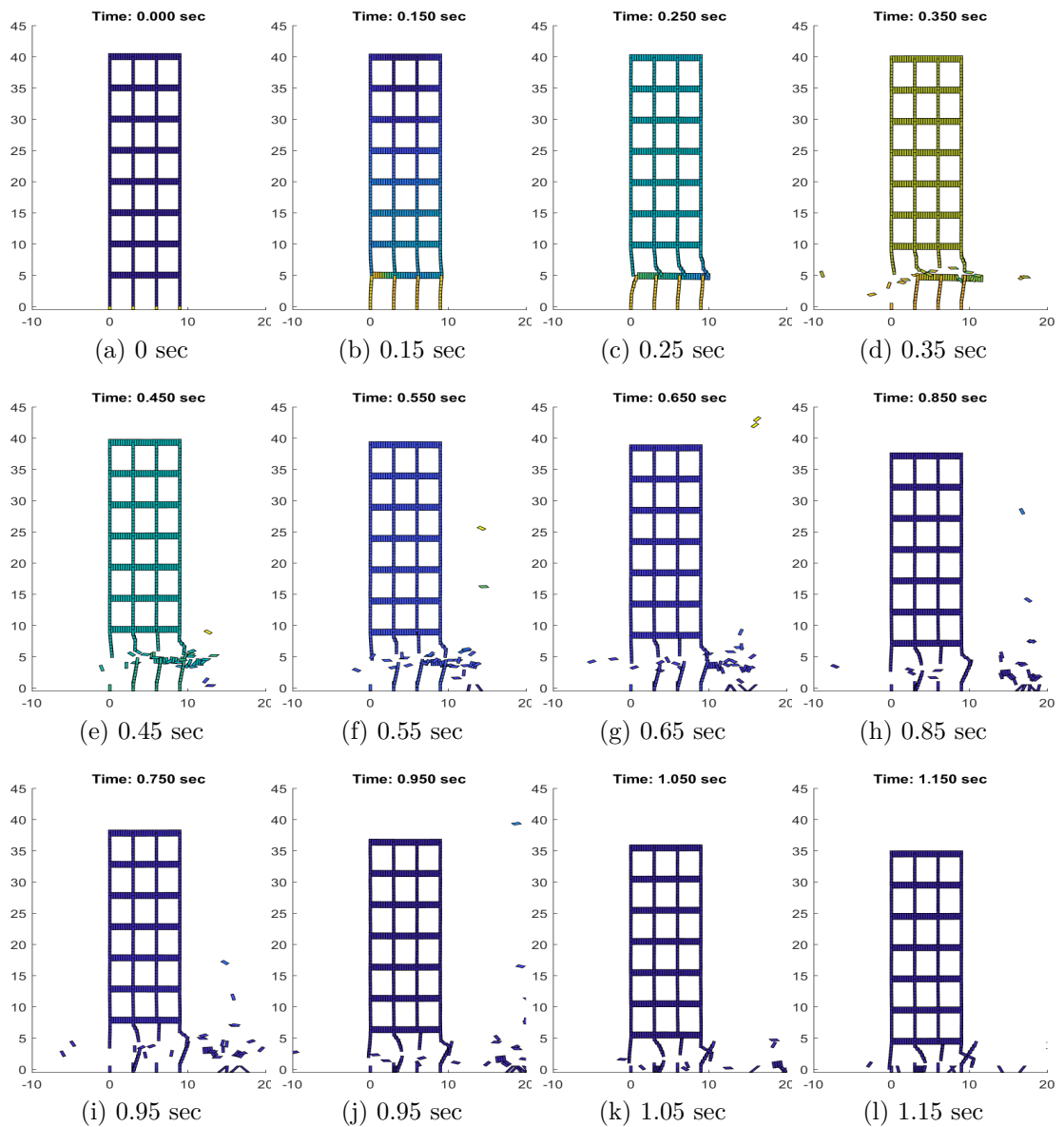


Figure 8.10: Progressive collapse of 3x8 frame with earthquake loading and load applied at midspan

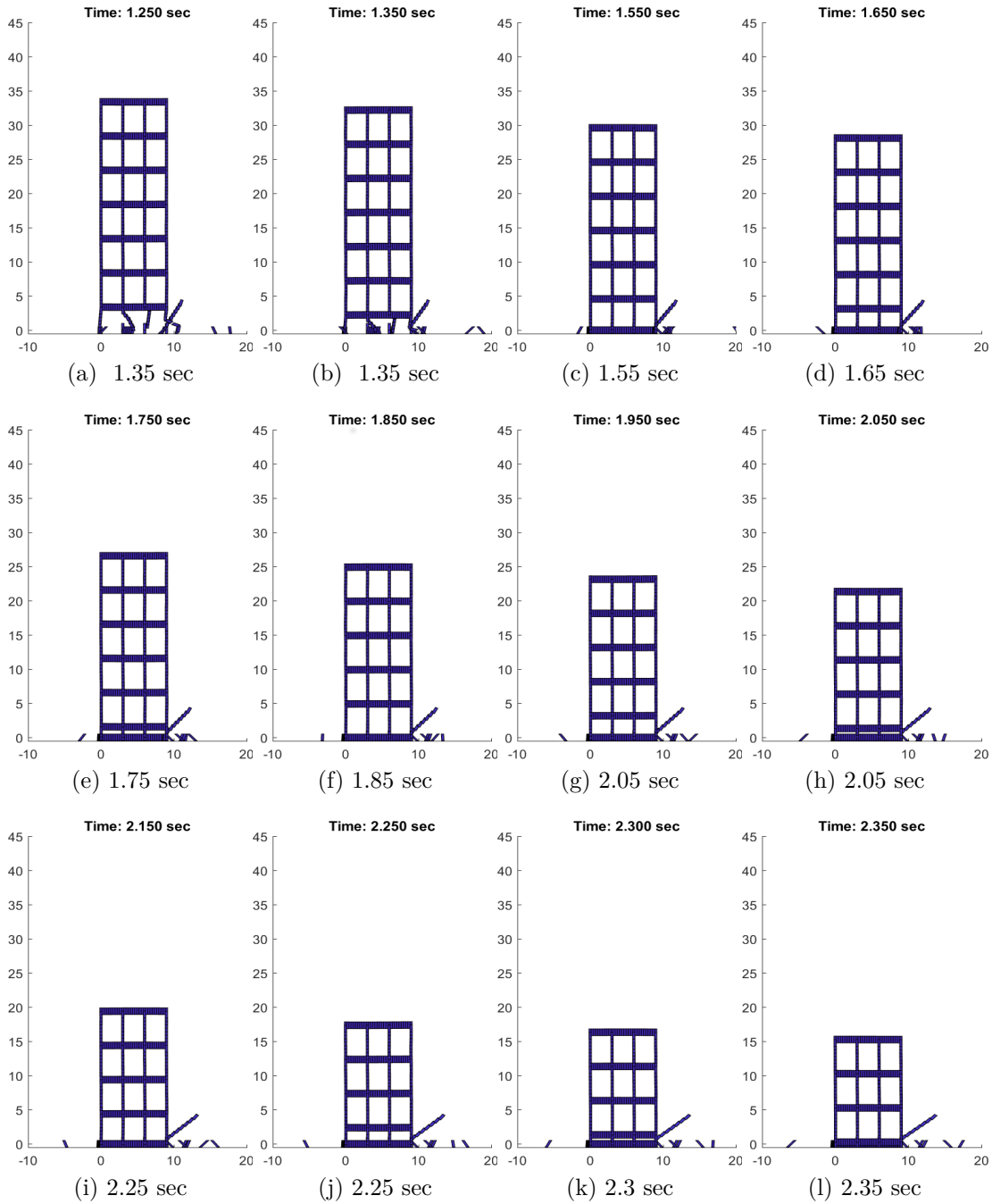


Figure 8.11: Progressive collapse of 3x8 frame with earthquake loading and loading applied at midspan (continued)

8.3.3 Multi-storey frame

The next application is a multi-storey frame, shown in Figure 8.12, subject to the El Centro earthquake. The failure begins at the bottom left frame shown in Figure 8.12c at 0.85 seconds.

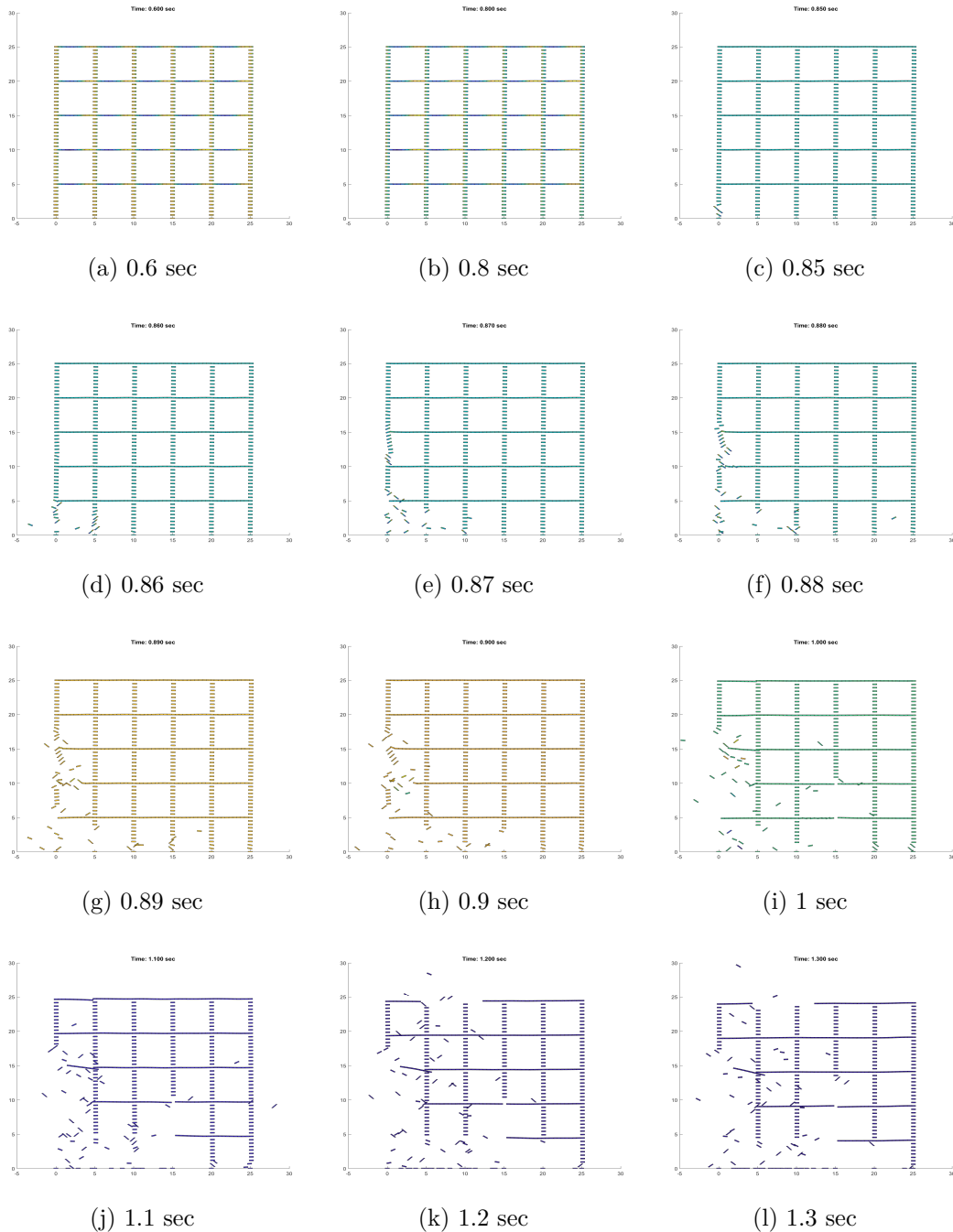


Figure 8.12: Analysis of multi-storey steel frame subject to El Centro Earthquake

8.3.4 2x8 Frame

Figure 8.13 depicts the progressive collapse of a 2x8 frame subject to the El Centro Earthquake as well as a point load in the positive y direction applied on the left wall at the first floor.

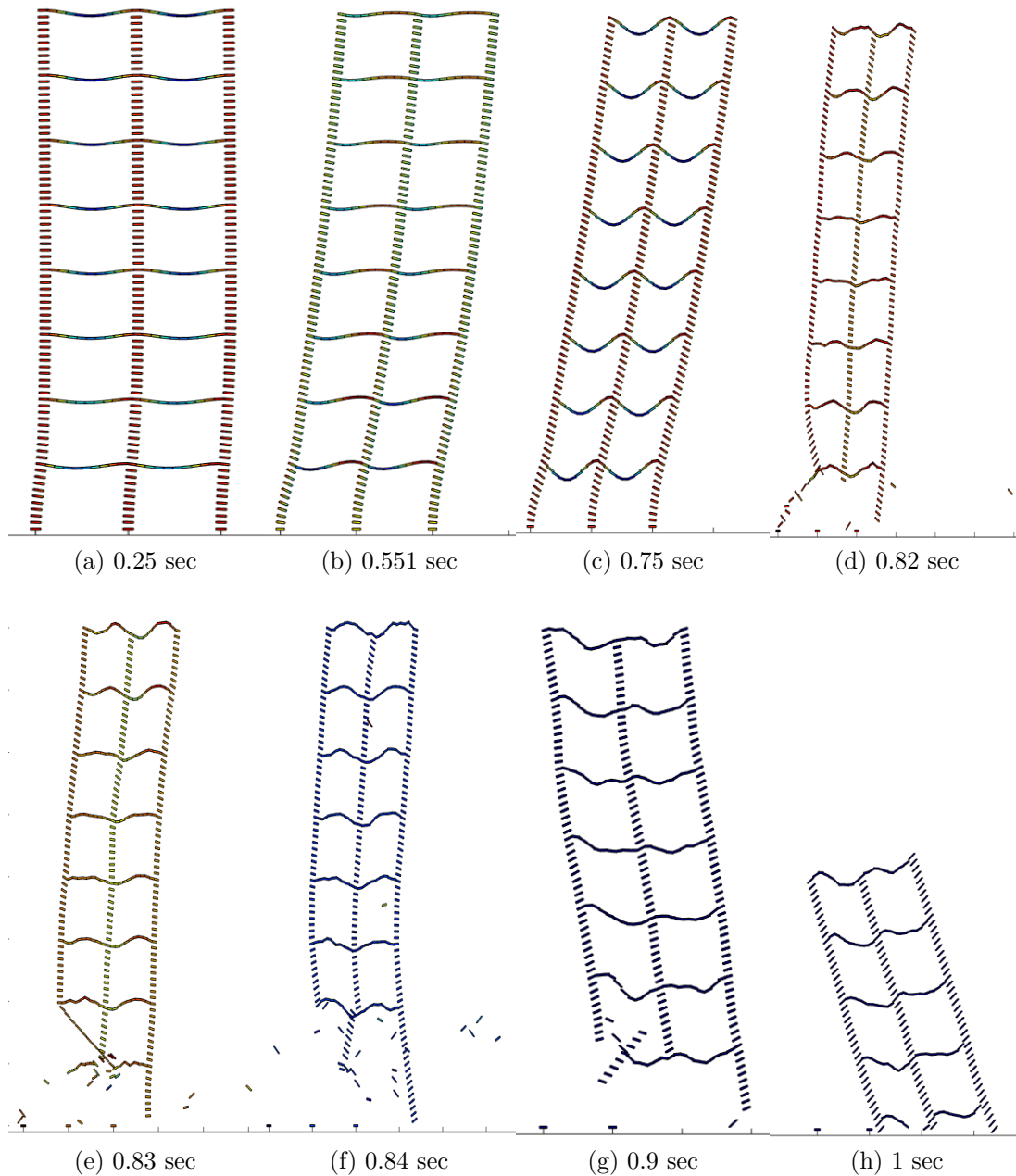


Figure 8.13: Time history of a high rise frame undergoing seismic loading and point load at in positive x-direction at first floor

8.3.5 High rise frame - 15 floors

Figure 8.14 shows the progressive collapse behaviour of a frame with 15 floors. The figure does not show the total collapse of the frame, rather just until where major elements of the frame have failed. The total collapse of the structure can be seen if the simulation is run for longer. From the collapse it can be seen that first the structure undergo serious oscillations and finally collapses near the boundary.

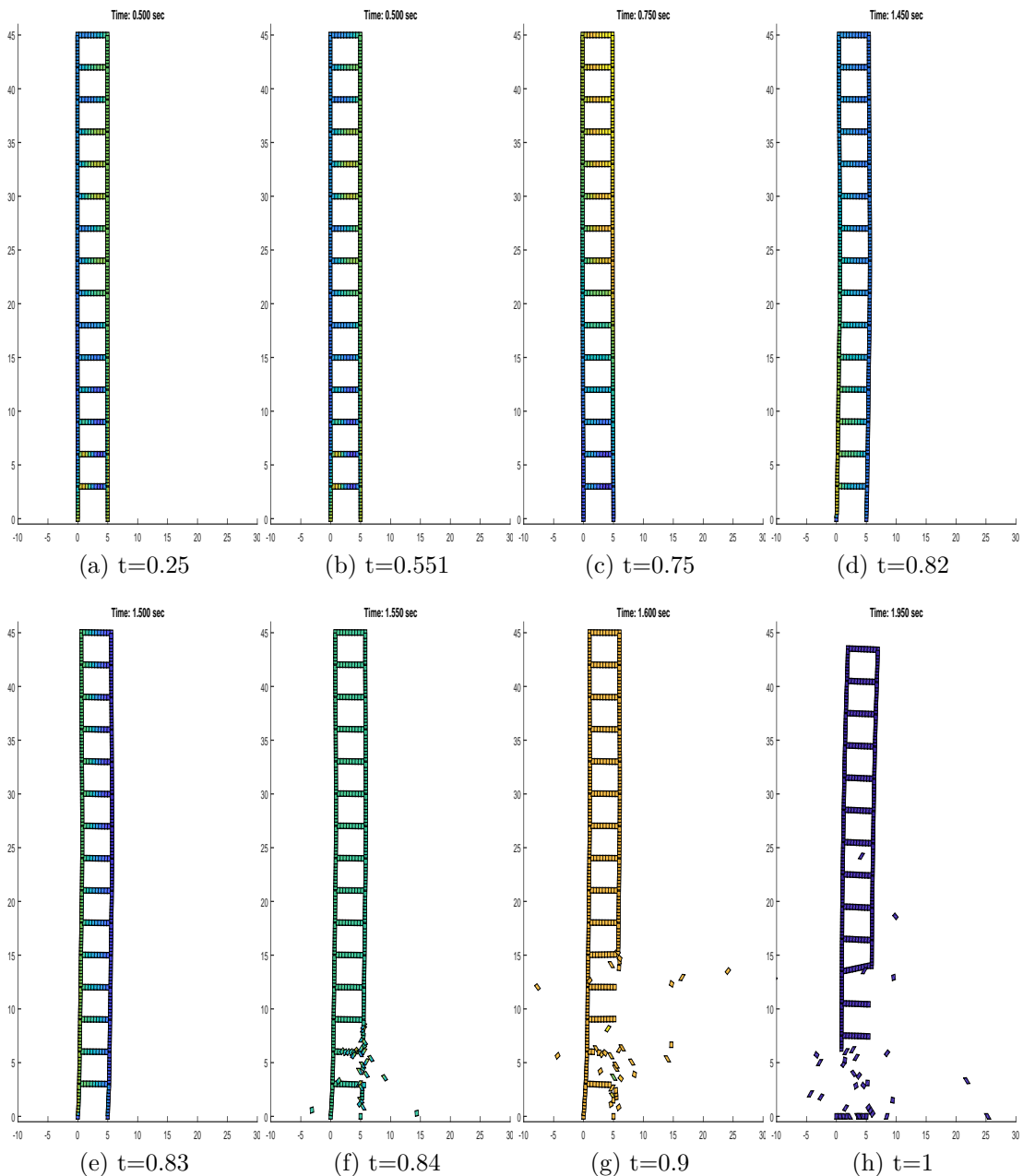


Figure 8.14: Time history of a high rise frame undergoing seismic loading and point load at in positive x-direction at first floor

8.4 Conclusion

The progressive collapse of different structures subject to earthquakes were successfully analysed in this chapter. The analysis was performed using the Gaussian springs based AEM for nonlinear dynamic behaviour. The implementation of earthquake loading to the structure was quite simple, given that the time history data from an earthquake is presented. From the acceleration at every time step, the force is calculated, and applied as an external force on all degrees of freedom of the structure.

Different materials can be used to model the frames as well as reinforced concrete. Although some of the figures presented did not show total collapse of the structure, this is just due to the run time of the analysis. Future improvements would entail including contact between elements, and contact between the elements and the ground. When contact between elements is included, effect of failing neighbouring structures can be analysed.

Chapter 9

Structures Subject to Extreme Wind Loads

In this chapter, the Gaussian spring based AEM is used to analyse structures subject to different weather conditions such as mean wind speeds, 3 second gusts and extreme conditions. Firstly, the weather condition is analysed in FLUENT to simulate the forces around the structure resulting from the applied wind load. The forces generated are then input into the Matlab code where the Gaussian spring based AEM is used to model the behaviour of structures due to the applied wind loads, and if the structure will experience collapse or not.

A brief introduction to the collapse of structures that occurred in the past due to wind loads is presented. Then the CFD model is built and explained. And finally, the structure is analysed in the MATLAB code to check for possible collapse of the structure. The purpose of this analysis is to present an application of wind loads to the structure that can be quite realistic, due to the wind being analysed on FLUENT first, rather than being applied as constant external forces.

9.1 Collapse of Structures due to Wind loads

In structural design codes, wind is usually represented by a speed profile. Its features and effects depend on the velocity of the wind, the geometry of the building and the protection from surrounding obstacles [110]. In slender structures, wind is one of the main load actions to be considered [110]. The environment has a

great influence on a building and accurate analysis of the wind conditions should be experimentally produced using wind tunnel tests [111]. Low structures also undergo significant influences from wind, depending on the geometry plan and and the locations of the structures columns, the wind can create torsional forces in the frame.

There has been several recorded structural damages due to wind storms in the last 50 years. This is better presented in Figure 9.1, which shows the number of natural disasters since the 1950's - 2004 [112]. As can be seen, a large percentage of structural damage is due to wind storms rather than floods or earthquakes. Typhoon Mirielle in September 1991 caused 6 billion dollars of damage. There was 8 billion dollars in damages from 10 typhoons in Japan 2004, 28 billion dollars in economic losses along with 2,541 deaths in August 2005, from Hurricane Katrina [113]. This is why it is important to analyse structural behaviour under extreme weather conditions.

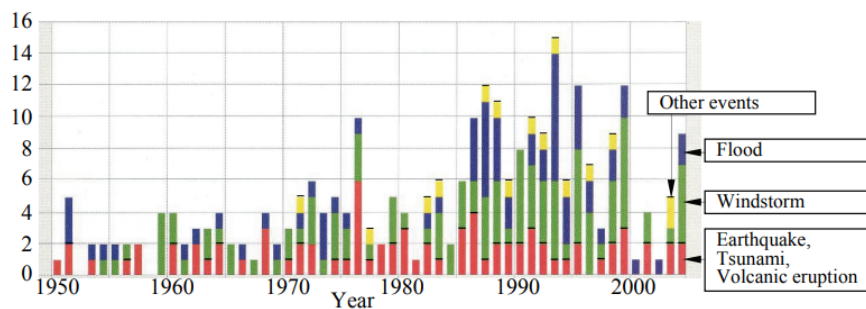


Figure 9.1: Devastating natural disasters. Red: Earthquake, Tsunami, Volcanic eruption. Blue: Flood. Green: wind-storm. Yellow: other events. [112]

Firstly a relationship between the mean wind speed and 3 second gust is explained. Table 9.1 displays the equivalence of different wind conditions with their corresponding damage associated. The damage does not only depend on the wind speed but also on the quality of the structure, so the table phenomena is not precise [113]. From the table it can be deduced that damage to structures starts to occur 40 m/s gusts, and extreme damage starts with 45 m/s mean speed, or 70 m/s gusts. Therefore, these values will be used for analysis in the following sections.

Table 9.1: Wind induced phenomena [113]

Wind speed		Phenomena/Damage
10 min mean	3s gust	
5 m/s	7- 10 m/s	- Vortex resonance/fatigue damage of truss members
10-15 m/s	15-20 m/s	- Handrail vibration/wind-induced noise - Vortex resonance of steel chimneys - Vibration perception in flexible high-rise buildings
20 m/s	30 m/s	- Seasickness and discomfort in high-rise buildings - Damage to garage shutters - Falling down of pedestrians
25 m/s	40 m/s	- Damage to roof tiles - Damage to window panes due to wind-borne debris
30 m/s	45 m/s	- Collapse of RC block fences - Damage to steel sheet roofing - Overall roof lift-off - Collapse of wooden houses - Falling down of gravestones
35 m/s	50 m/s	- Damage to window panes due to wind pressure of high-rise buildings - Blow over of heavy tombstones
40 m/s	60m/s	- Damage to cladding of high-rise buildings - Limit of allowable distortion of external sealing compounds
45 m/s	70 m/s	- Main frame stresses in high-rise buildings exceed elastic Limit

Damage to structures

Damage to structures due to recent typhoons are presented in this section. Figure 9.2 shows the damage to a soccer stadium in Korea, 2002. Figure 9.3 displays the damage to wind energy facilities due to Typhoon Maemi in 2003.

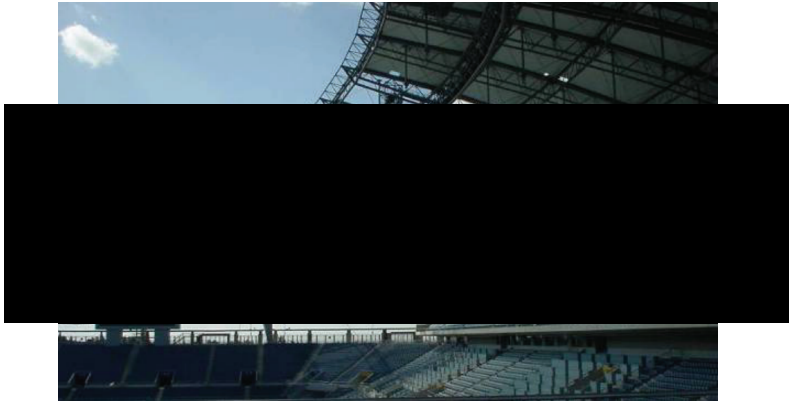


Figure 9.2: Damage to soccer stadium in Korea due to Typhoon Rusa, 2002 [113]



Figure 9.3: Damage to wind energy facilities in Miyakojima island due to Typhoon Maemi, 2003 [114]



■ : Broken windows

Figure 9.4: Broken windows in residential building in Korea, due to Typhoon Maemi [113]

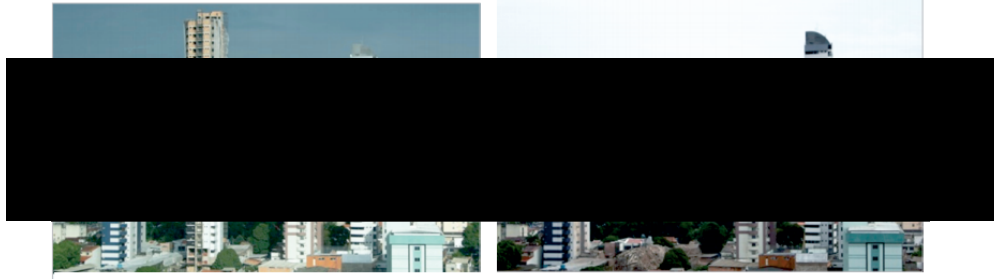


Figure 9.5: Collapse of building under construction undergoing intense winds [115]

9.2 Using CFD for turbulent wind analysis

Using computational fluid dynamics (CFD) for wind analysis is a fast and efficient way to determine the wind behaviour without needing to conduct expensive wind tunnel tests. There are some limitations on wind tunnel tests, such as tools scarcity, since big tunnels are required for urban models investigations and the scarcity in the number of measurement points in models [116]. The advantage of using CFD over wind tunnel tests is that the simulation gives a quantitative and qualitative wind flow representation of the whole volume rather than specific measurement points.

Several validation processes have been developed to improve and verify the accuracy of the CFD models in comparison to the wind tunnel tests. The FLUENT software is used for the CFD simulations [116].

In this project, FLUENT is used to model the wind behaviour and the forces exerted on the structure. The gust wind is modelled in FLUENT for 3 seconds. A general model and set up for the CFD model is presented and later the wind speeds will be changes to simulate the different conditions. From FLUENT we can obtain the force on each wall at every iteration. This is a kind of mean average force.

To implement the wind load in the AEM Matlab code, the force on each wall at each time step is applied on all the wall nodes. So the force obtained from the first time step is just one value for the whole wall. This value is applied to every node in that wall, and similarly for the roof, etc. At every next time step a new force is applied and the value is obtained from Ansys. This will be better explained with an example.

Figure 9.6 shows an overview of how the processes will work. The geometry can be created in Ansys mechanical, and in parallel the forces due to the wind loads is obtained from FLUENT. Then the data files are exported to be read in the Matlab code for the frame to be analysed.

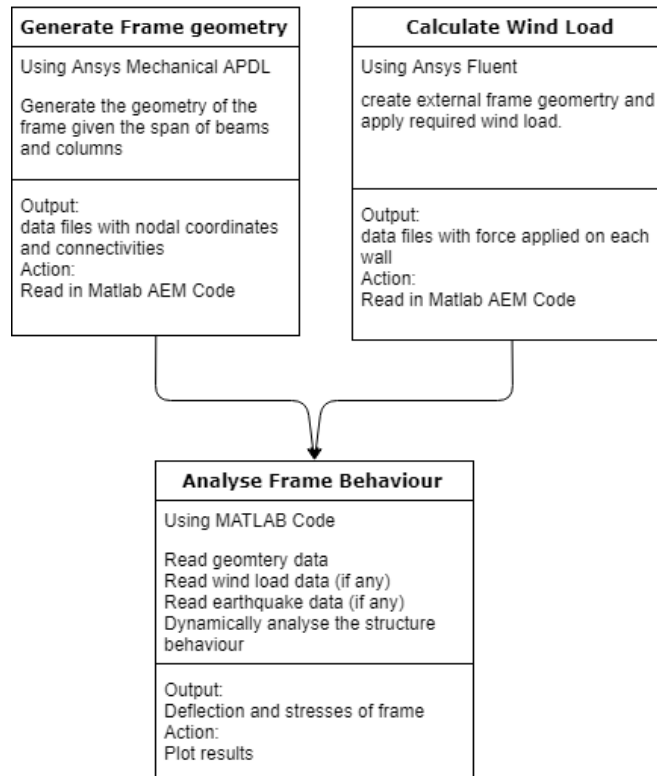


Figure 9.6: Flow chart for procedure

9.2.1 Solution Model

There are two major groups of turbulence models: RANS models (Reynolds-averaged Navier-Stokes models) and LES models (Large Eddy Simulation Models). Among the RANS models are the standard $k - \epsilon$ model and its variations, as well as the Reynolds Stress Model (RSM). However, it has been known that the $k - \epsilon$ model is not appropriate for modelling airflow around buildings [117]. The RSM methods give better results for the flow around buildings. On the other hand, LES are more appropriate for analysis of wind around buildings because they solve the largest eddy and simulate only the smallest eddies [116]. However, LES methods require immense computational power, very fine meshing and long calculation time. Most common CFD software do not offer full LES models in

three dimensions.

Case study validation test Reiter [116] performed a validation analysis of wind around a single building, around a group of buildings and a dense urban environment, to select the right turbulence model and other parameters. The results of the validation test were compared to a wind tunnel test published by Wiren [118]. The structure is 12m high and 18m wide. The configuration of the system is shown in Figure 9.7; where $L = 80\text{m}$ wide. Important factors that affect the simulation are:

- The blocking ratio should not exceed 3% (the ratio between the vertical surfaces of the building exposed to the wind and the surface from the air inlet surface).
- The minimum length of the simulation field is $5 \cdot \min(L, 2H)$ upstream of the building and $8 \cdot \min(L, 2H)$ downstream. (L is length of building and H is height).
- When wind speed is low, thermal effects can influence the air movements

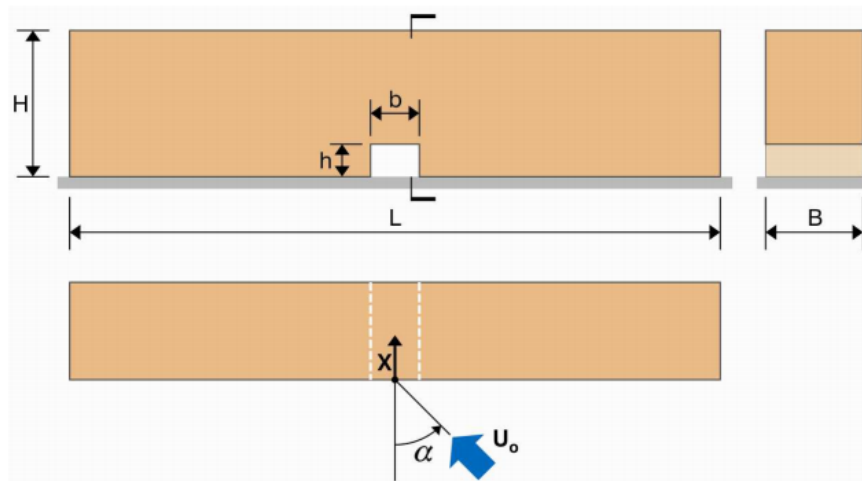


Figure 9.7: Configuration of the simulation for flow past a single building [116]

The wind profile that was used in the CFD model is equal to the one of the wind tunnel test, and had a profile of $U = 10(z/2)^{0.125}$; where U is the wind speed, z is the height at which the wind speed is calculate, and the turbulence intensity is 14%. One of the simplest descriptors of atmospheric turbulence is the turbulence intensity [113]. It is the ratio of the standard deviation of a wind speed σ component to the mean wind speed U ; σ/U .

For the simulation, 1,384,836 cells were used for the mesh. Figure 9.8 shows the results from the CFD models in comparison to Wiren wind tunnel test results. The CFD models that were considered are based on the realizable 2nd order, $k - \epsilon$ 2nd order and the RSM 2nd order models. The findings are as follows.

The standard $k - \epsilon$ shows that the maximum discomfort intensity is the the first third of the passage; which is similar to the wind tunnel test results, however, the position of maximum discomfort is not simulated correctly. The realizable $k - \epsilon$ model improves the estimation of the location of the discomfort estimation; however still underestimates the location of the maximum discomfort. The Reynolds stress model gives the most accurate results, since it identifies the critical area correctly and the value of the maximum wind discomfort [116].

Therefore, the Reynolds stress model will be used for analysis in the scope of this thesis, since it is the most accurate for a building type configuration.

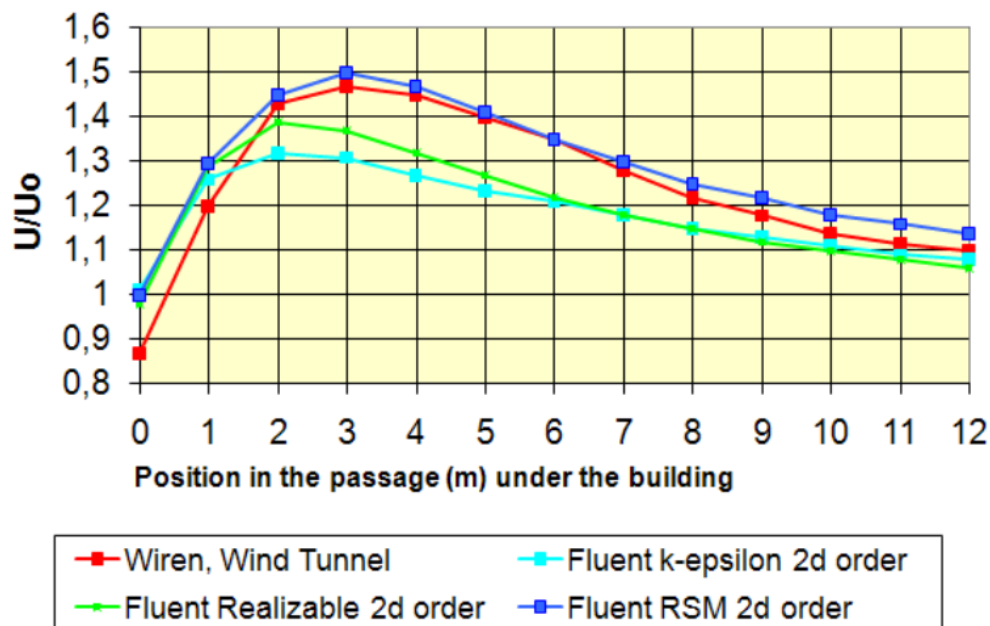


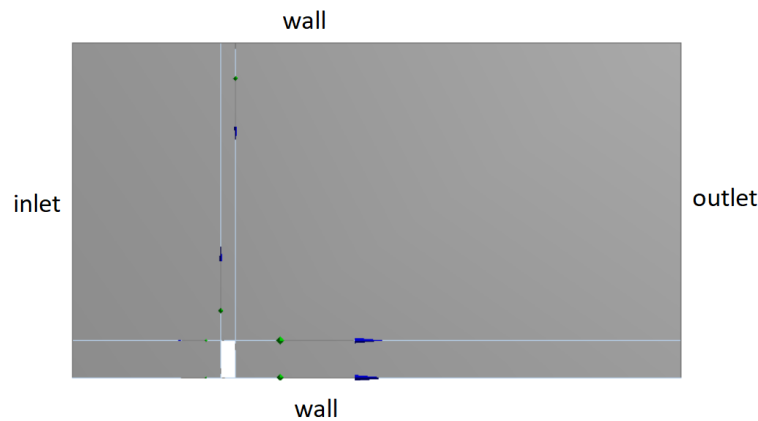
Figure 9.8: Comparison of results from FLUENT and from the wind tunnel test [116]

9.2.2 CFD Model

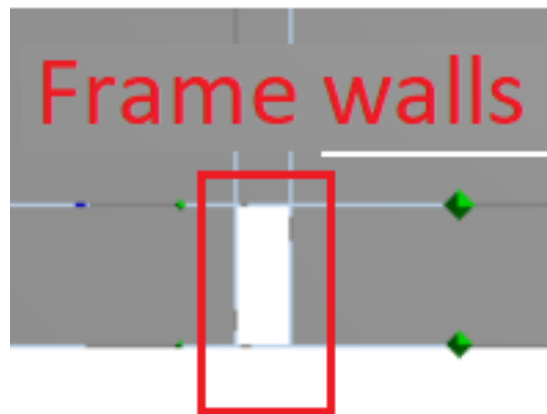
Problem Definition

Considering a frame of 10 metres height and 4 metres width, and a wind speed of 40 m/s running for 3 seconds. The frame is shown in Figure 9.9a, along with

the external surface boundary. The surfaces are labelled to show the inlet, outlet and the walls. The frame walls are highlighted in Figure 9.9b. The wind is applied from the inlet with the required velocity. The structure of the frame is the empty space in the figure, where the walls have the material properties of steel or concrete, as desired. The no-slip conditions are applied on the frame wall. Since turbulence is expected, the unsteady state flow is selected for the analysis.



(a) Geometry of frame in Boundary



(b) Denotation of Frame walls in CFD Model

Figure 9.9: Boundary conditions

Mesh

The mesh refinement is very important to produce good quality precision [116]. It is recommended that the mesh is refined at the pedestrian level and locations where strong wind gradients are expected. The mesh for the surface is generated by using equally sized quadratic elements since the flow is aligned with the

geometry, and the geometry is not complex. The mesh is displayed in Figure 9.10.

The mesh can be better generated for a more efficient mesh. For instance, there could be finer mesh refinement around the structural body and more dense closer to the boundary walls and the outlet. However, a face mesh with equally sized elements was used for simplicity and demonstration purposes. The mesh is showed to have good results for capturing the air flow around the structure and is therefore selected for all models in this chapter.

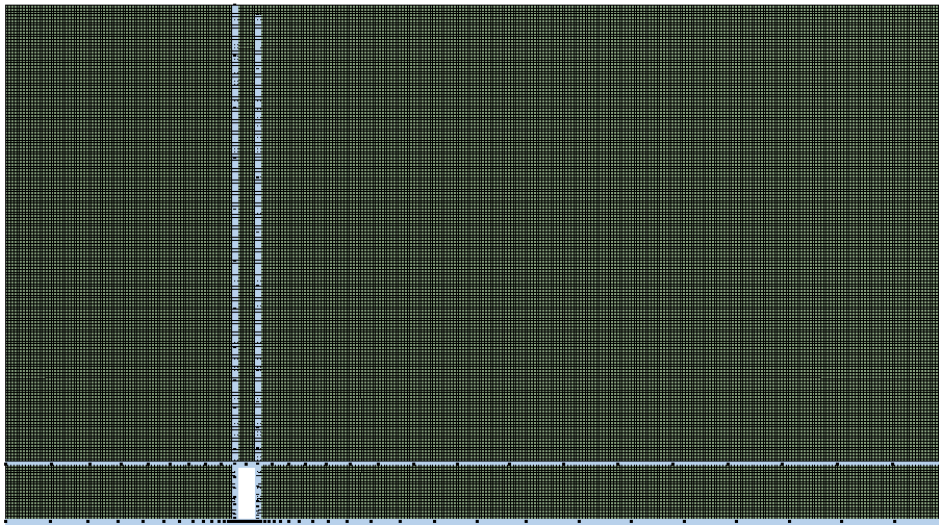


Figure 9.10: Mesh for flow around structure

Time step size

To run for three seconds, the time step size is 0.01 seconds, with a total number of 300 time steps. From the CFD model the output required is the force applied on each wall, in the x and y direction. The output will result in an average force along each wall for every iteration. So there will not be a different value for the force at each node along a wall.

Also, it is important to mention that the walls of the building are rigid and will not deflect due to the applied wind load. Therefore, when the forces are being applied in the AEM code, they are the forces that were applied to the undeformed shape. In other words, if a node "a" was to move due to the wind load, the load applied in later iterations is the load applied at that specific time step with the

original configuration of the node.

The solution model used for modelling the 3 second gust is the 'Reynolds stress model', with a coupled pressure-velocity scheme and Second Order Upwind for the turbulent kinetic energy and the turbulent dissipation rate.

9.2.3 40 m/s 3 second gust wind

Applying a wind speed of 40m/s in the x-direction from the inlet wall, the results are displayed as follows.

CFD Results

Figure 9.11 shows the contours of velocity, vorticity, dynamic pressure and turbulence kinetic energy for the 10x4 m frame. The residuals are shown in Figure 9.12. The residuals show that the flow is unsteady, and resemblant to turbulent flow. The force on each wall is shown in Figure 9.13. The forces are an average value at each iteration on each wall. These values are input into the AEM Gaussian code where the frame will be analysed due to the forces.

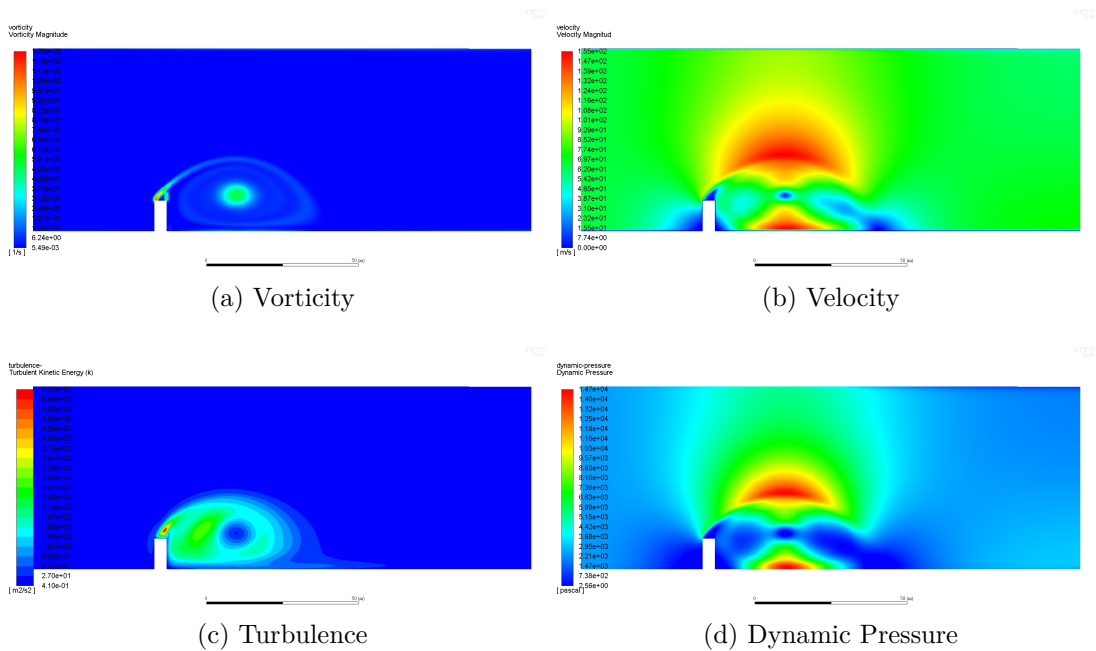


Figure 9.11: Vorticity, velocity, dynamic pressure and turbulence kinetic energy for flow past building with 40 m/s wind speed

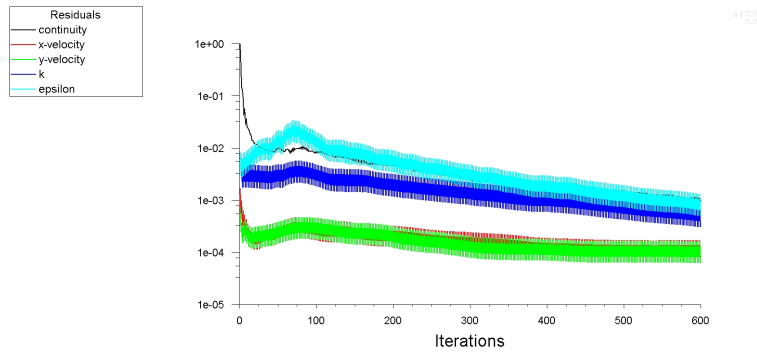


Figure 9.12: Residuals for turbulent flow

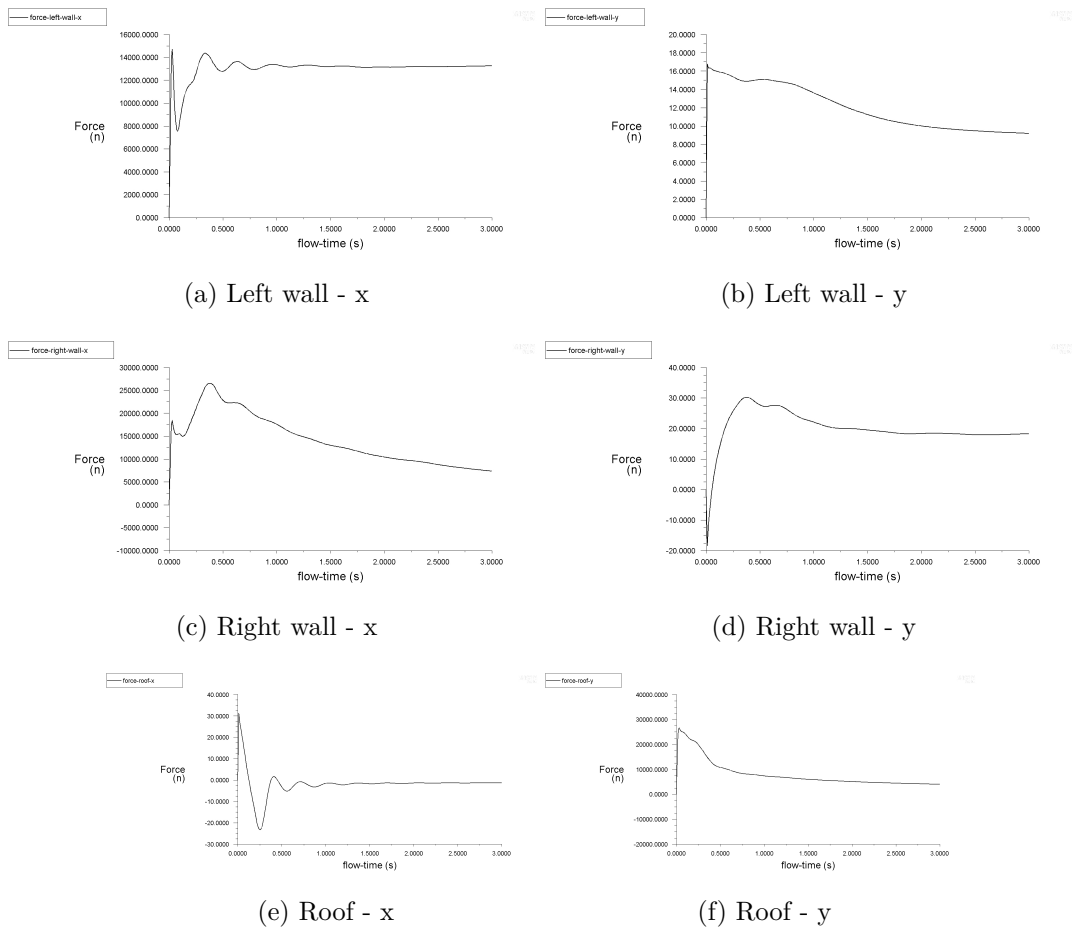


Figure 9.13: Forces on each wall in x and y directions due to 40 m/s wind speed

Analysis of structure in AEM

The forces in the x and y directions on each wall is applied to the frame in AEM. Figure 9.14 displays the displacement velocity and acceleration for a point on the left wall for the duration of the three seconds gust. The frame deflection is shown in Figure 9.15. The deflection is multiplied by 10^3 so the deflection may

be seen. There was no collapse in the structure reported. The analysis therefore shows that a frame of dimensions $10m \times 4m$ can with steel material properties can withstand a 3 second gust of 40 m/s. The most significant forces on the structure are the forces on the left wall in the x-direction, and the roof in the y-direction. Table 9.2 is the maximum average force applied on each wall.

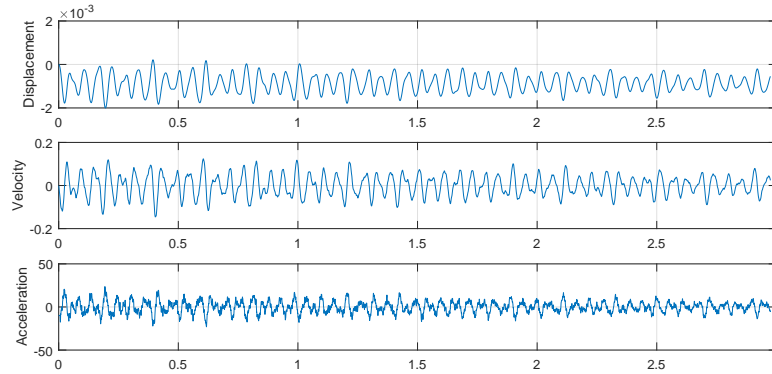


Figure 9.14: Displacement, velocity and acceleration of a single point of the frame due to the wind load of 40 m/s

Table 9.2: Maximum Average force applied on each wall of the frame

Wind speed 40 m/s	
Location	Maximum force [N]
Left wall -x	14,700.0
Left wall - y	16.8
Right wall - x	30.2
Roof - x	31.5
Roof - y	26,400.0

9.2.4 70 m/s 3 second gust wind

An extreme wind load of 70 m/s for the three second gust is applied on the same frame structure. Figure 9.16 depicts the forces on the left and right wall in the x and y direction. It can be seen that the results lead to an eventual steady state solution where the forces remain constant. In Figure 9.17 the contours of velocity, turbulence and vorticity are presented. The deflection of the frame at several seconds are shown in Figure 9.18. From the deflection it can be seen that the structure starts to collapse at 0.35 seconds near the right boundary nearest to the ground. Eventually there is a total collapse of the frame.

9.2. USING CFD FOR TURBULENT WIND ANALYSIS

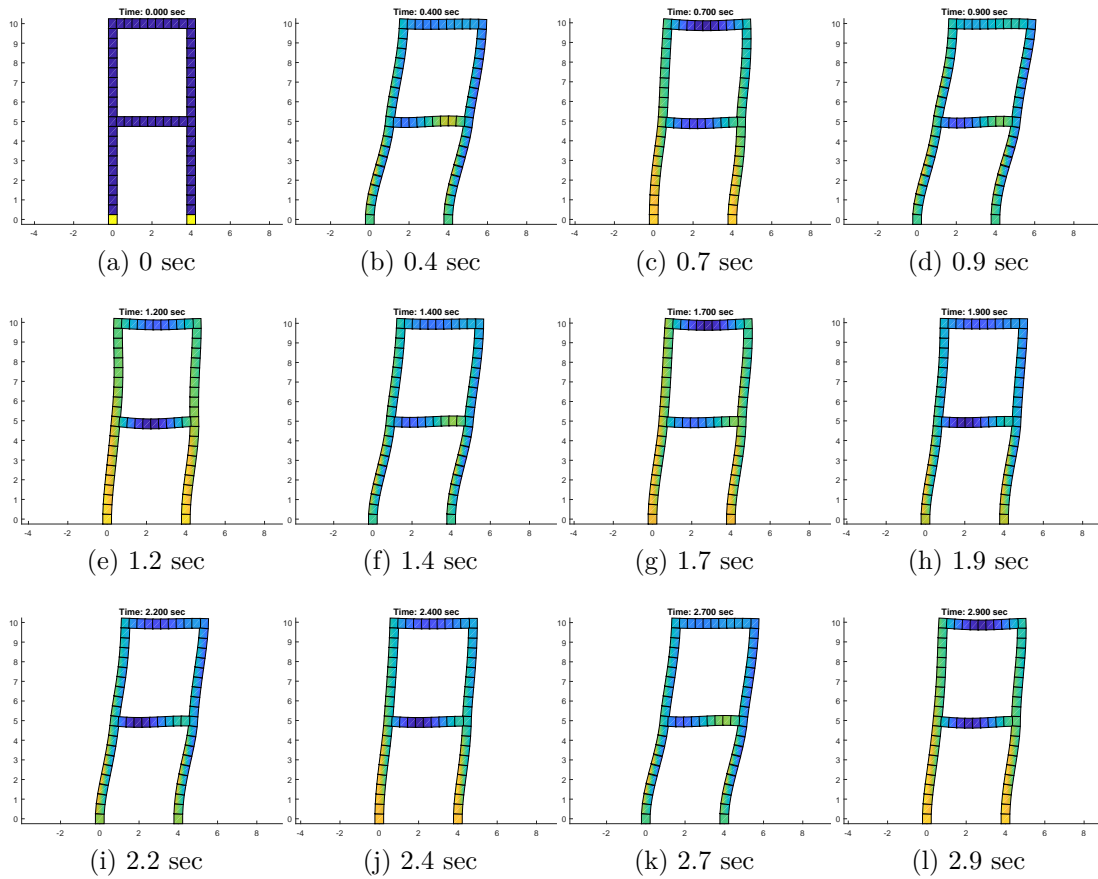


Figure 9.15: Frame displacement factored by 10^3 for 3 sec gust 40 m/s wind speed

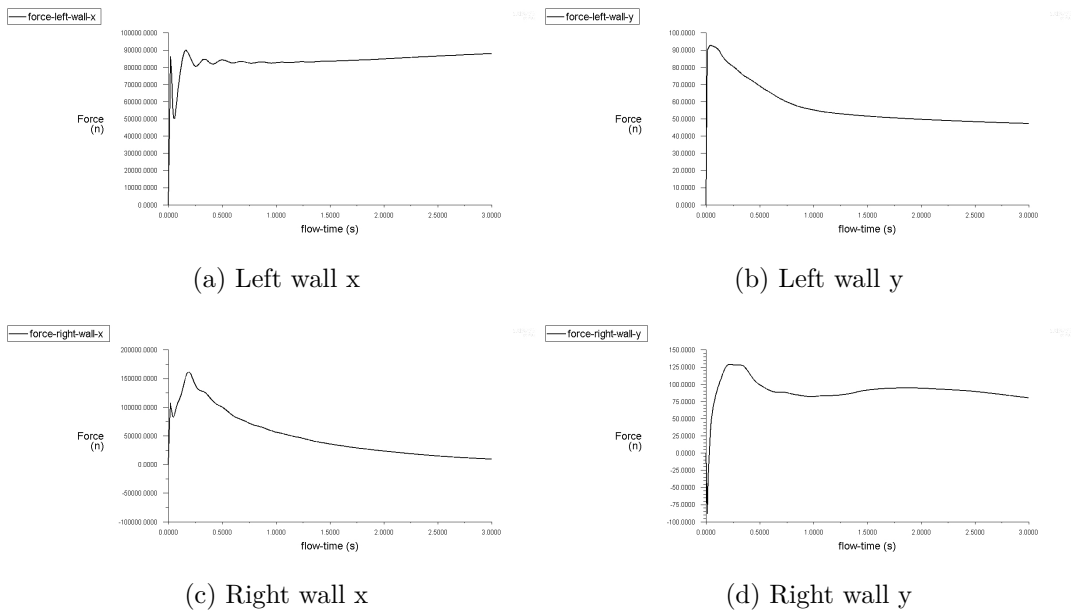


Figure 9.16: Forces on left and right wall due to 70 m/s wind speed

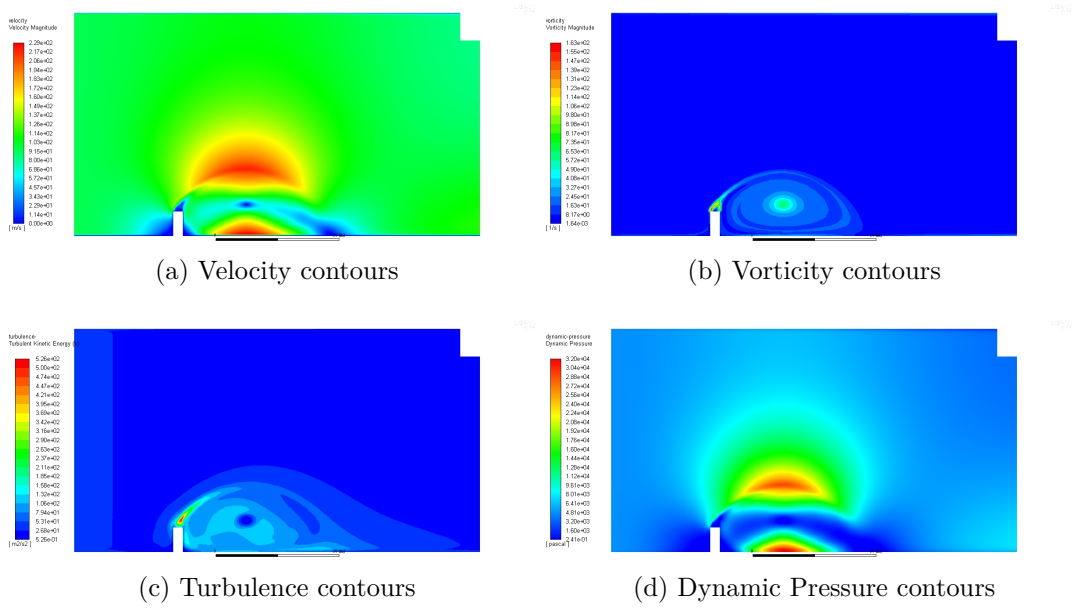


Figure 9.17: Contours due to the 70 m/s wind speed, 3 second gust

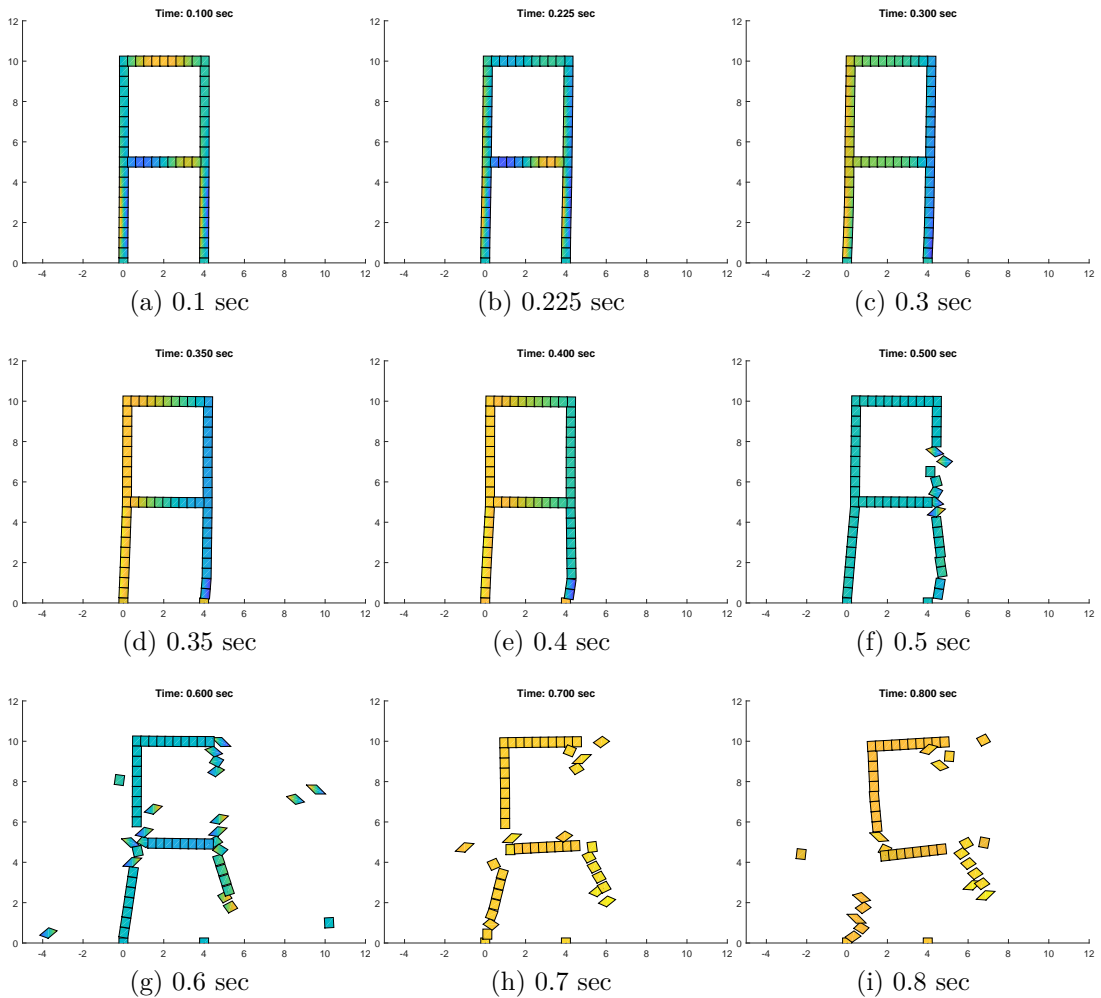


Figure 9.18: Collapse of frame subject to 70 m/s wind speed

9.3 Loads from surrounding structures

It is also important to consider the change in the wind effect due to surrounding structures. An analysis done by Aly showed that the existence of short buildings in the upstream wind increases the turbulence in the region [119]. Since the scope of this thesis only covers 2D analysis, only 2D CFD models are examined.

Analysing the structure in the middle after a 40 m/s 3 second gust. The geometry model is shown in Figure 9.19 for three adjacent buildings. Figure 9.20 represents the surface mesh around the buildings. A standard mesh with equal sized elements was used, for simplicity. Figure 9.21 shows the forces on all the

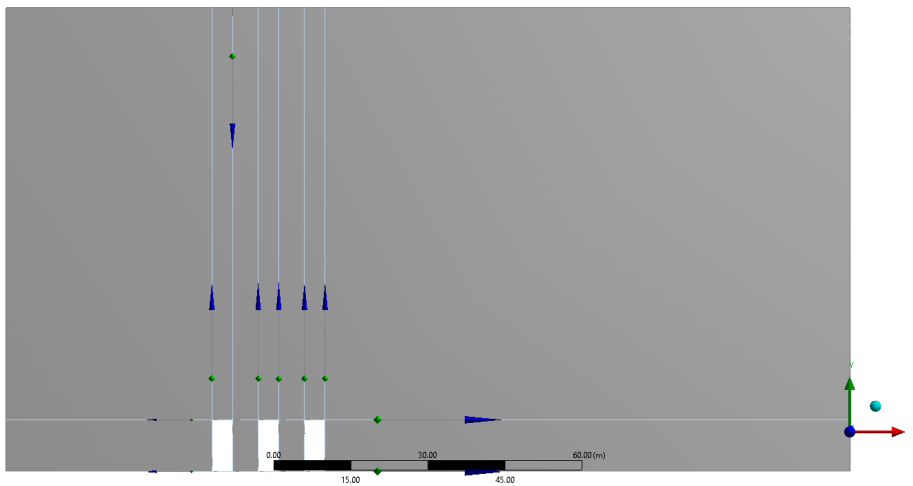


Figure 9.19: Geometry model for three adjacent buildings

building walls for the third structure.

Figure 9.22 shows the vorticity, velocity, turbulence kinetic energy and the dynamic pressure contours.

Figure 9.24 shows the deflection of the frame subject to the 3 second gust wind speed of 40 m/s while being affected by neighbouring structures.

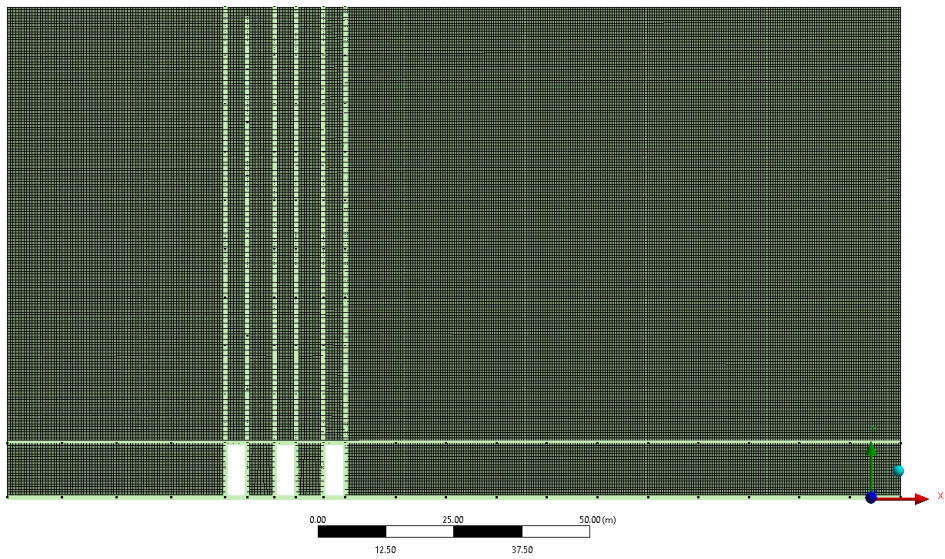


Figure 9.20: Mesh for three adjacent buildings

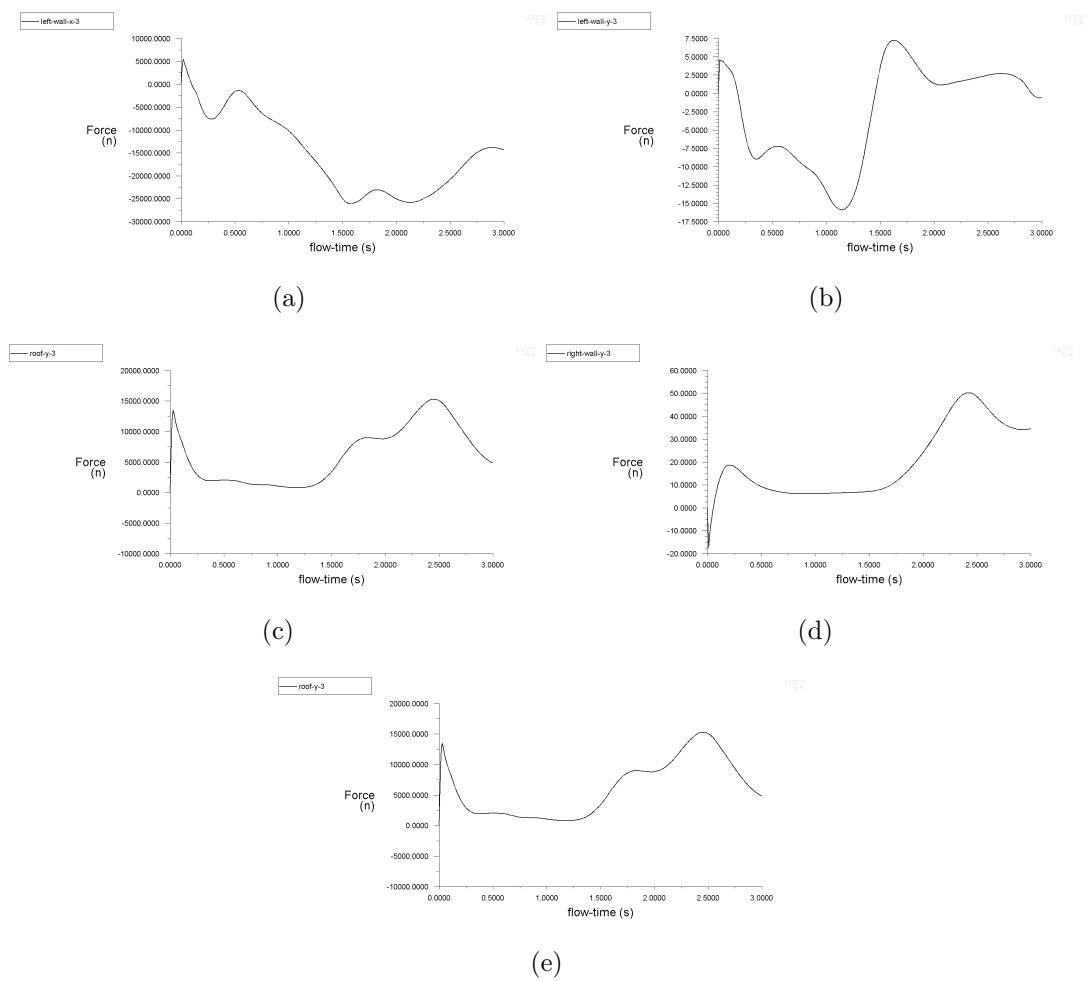


Figure 9.21: Forces on all the walls for the third building with 3 second gust wind 40m/s

9.3. LOADS FROM SURROUNDING STRUCTURES

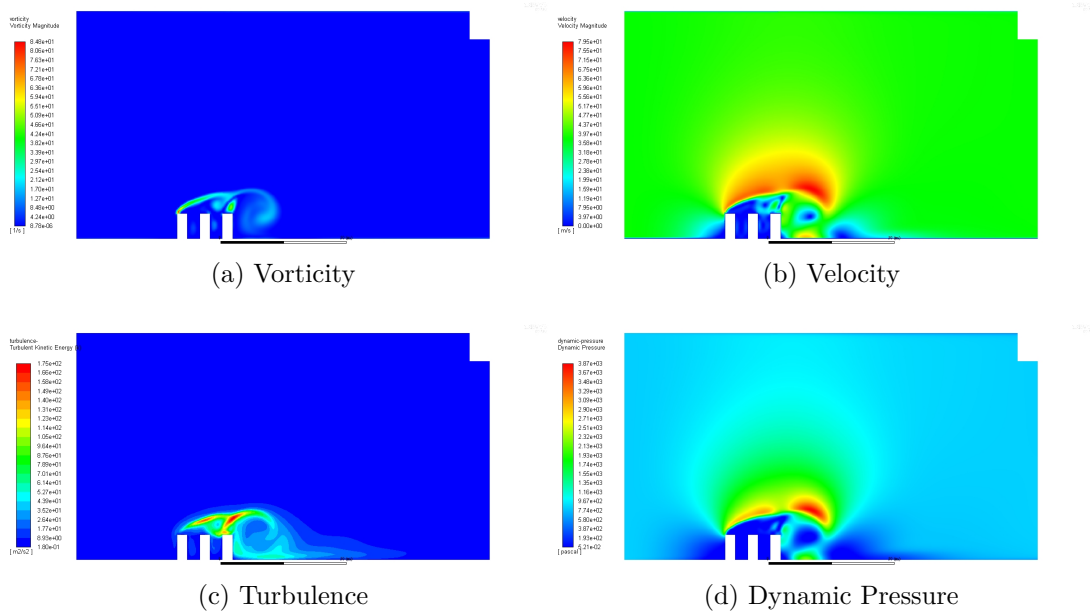


Figure 9.22: Vorticity, velocity, turbulence and dynamic pressure contours of three adjacent buildings with 40 m/s wind speed

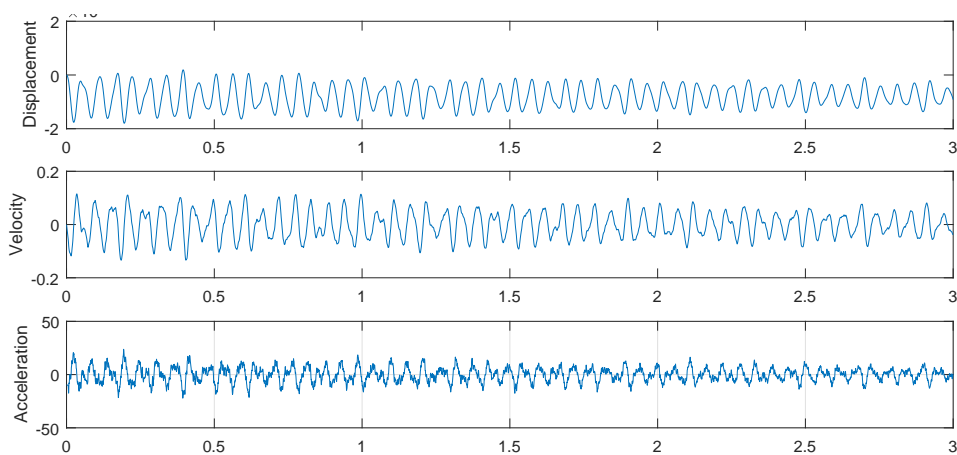


Figure 9.23: Displacement velocity and acceleration for the third building at 40 m/s 3 second gust

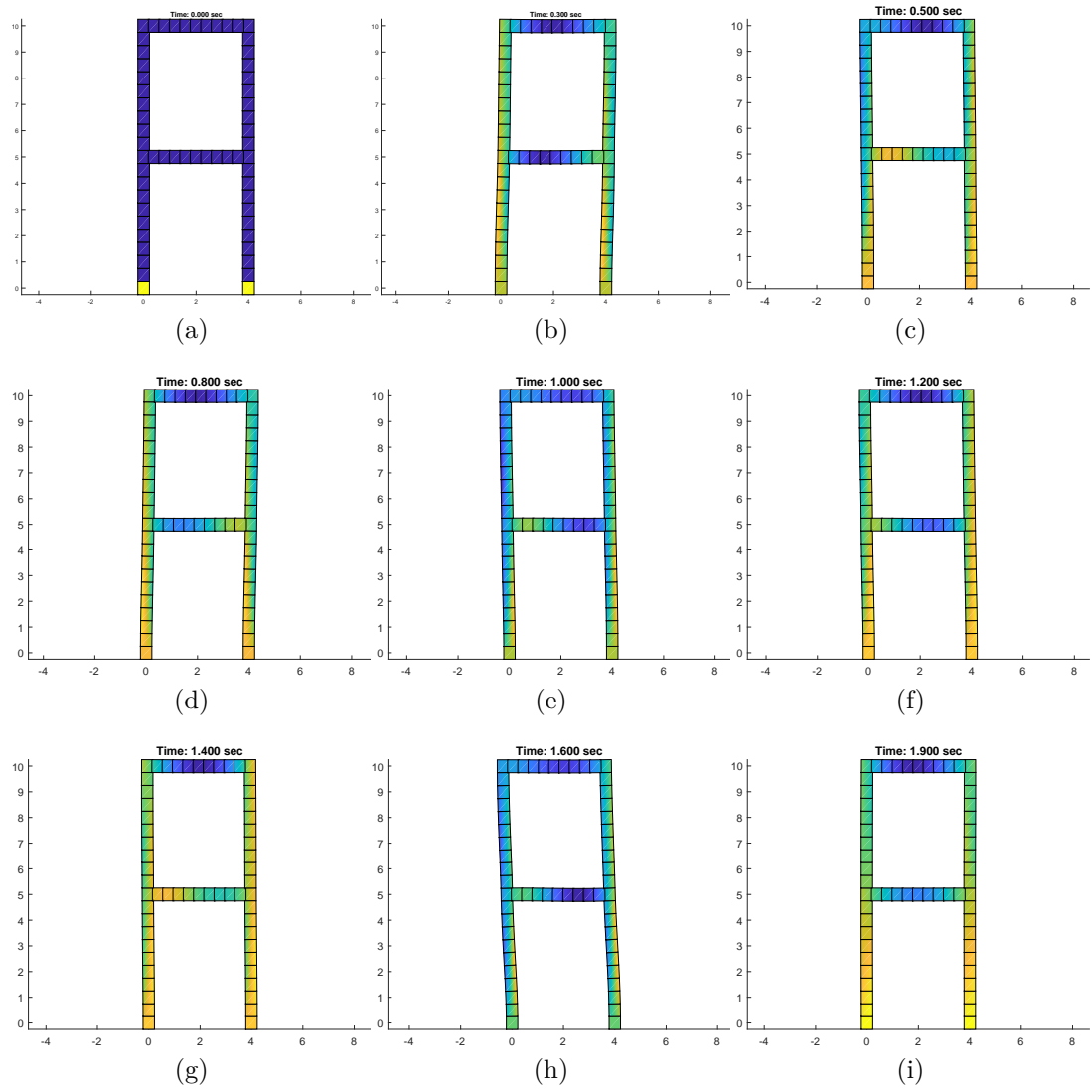


Figure 9.24: Frame deflection subject to 40 m/s wind; effect of neighbouring buildings

9.4 Conclusion

The analysis of structures subject to wind loading conditions was performed in this chapter. The wind analysis is performed in FLUENT, where there is a velocity inlet that presents the desired wind speed for analysis. The structure undergoes the wind analysis for 3 seconds to replicate the 3 second gust. At each time step an average force from each wall is recorded. The forces are then applied to the frame in the MATLAB code, to perform the deflection analysis of the structure using the Gaussian springs based AEM.

The purpose of using FLUENT to emulate the wind behaviour is to obtain relatively realistic wind loads from 3 second gust behaviours, and not to analyse how the wind should behave. Also it is simply used to demonstrate different applications of loads to be included in the AEM analysis.

Although only 3 second gusts were used to analyse the structures, longer periods of time can easily be modelled. The same models will be used, except they will be run for longer. It was simply for demonstration purposes and the scope of this thesis that 3 second wind gusts are chosen for analysing structures under extreme weather conditions.

It is also important to mention that the FLUENT and Matlab code are not directly coupled, because during the Ansys analysis, it is expected that the structure should deform after being subject to the extreme wind. However, this is not the case. In Ansys the walls are completely rigid, and the forces obtained are based on the original configuration of the frame, not its deformed shape.

The results from this chapter showed successful modelling of the collapse of structures subject to extreme wind loading.

Part IV

Conclusions

Chapter 10

Concluding Remarks

10.1 Conclusions

Based on a comprehensive review of computational methods used for modelling the progressive collapse of structures, the AEM is deemed to be one of the simplest schemes with acceptable accuracy.

The AEM is implemented as a discretisation of structural elements into rectangular rigid bodies that are connected along the edges of the elements with pairs of shear and normal springs. The material behaviour of the structural elements are modelled through the springs stiffness. Various advantages arise from the use of springs between elements. Firstly, when a spring exceeds a specific yield strain and is considered to have failed then the spring can be easily removed from the system to represent the discontinuity between elements. Another advantage is the capability of defining unique material properties to specific springs at specific locations. This grants a straightforward implementation of multiple materials within the same element, such as modelling reinforced concrete. The AEM also exhibits a good advantage in adequately modelling both the continuum and discrete elements behaviour. Before any element separation occurs the structural system behaves as a continuum, while as springs start to fail and elements detach, discrete element behaviour is considered.

The deflection and internal stresses of several structural beams are assessed using the conventional AEM and it is evident that the computational efficiency of the method is inadequate since a sizable amount of elements and springs per

element is required to achieve a specific level of accuracy.

In this thesis, a modification to the AEM has been presented, where the number of springs between elements is optimised using the Gaussian quadrature to locate the optimal location of springs. The findings of the application of the Gaussian AEM to simple structures for linear and nonlinear material behaviour are presented in the following section.

10.1.1 Linear and Nonlinear Gaussian AEM

As mentioned earlier, the Gaussian AEM utilises Gaussian quadrature weights and locations for defining spring locations across a pair of rigid elements.

Linear Gaussian AEM

In the linear elastic case structural beams were subject to a point load. The expected normal stress along a rectangular beam cross-section is a linear line with a value of zero at the neutral axis. Using the Gaussian springs it was found that exactly 2 gaussian springs were needed to significantly improve the analysis and reduce the computational cost. This simple change showed that using the Gaussian AEM significantly less springs were required for attaining an acceptable level of accuracy.

Nonlinear Gaussian AEM

Nonlinear material behaviour was then implemented in the analysis. The material nonlinearity was represented by a 1D Hardening plasticity algorithm. Based on the yield criteria springs were classified as elastic or elasto-plastic and the corresponding spring stiffness were calculated. A cantilever beam was analysed using the Gaussian AEM and the FEM solution from ANSYS, and the results showed good accuracy.

In the case of a rectangular cross-section undergoing elasto-plasticity, the stress along the cross-section is expected to experience plasticity at the top and bottom fibres of the cross-section and elasticity along the middle of the cross-section. Hence, the stress along the cross-section is split into three parts (plastic-elastic-plastic). 10 Gaussian springs were used to appropriately capture the tran-

sition between the plastic and elastic regions along the rectangular cross-section. The Newton Raphson iteration scheme was implemented in the Gaussian AEM with rate dependent Hardening plasticity. Remarkably a quadratic convergence in the analysis was observed.

Adaptive Gaussian AEM

Since each part of the elasto-plastic material behaviour can be represented linearly, 2 Gaussian springs are enough to explicitly represent each region. The exact number of springs needed to represent the stresses along a cross-section is known, an adaptive technique was formulated to exploit this, where only 6 springs were required for the nOnlinear analysis. The adaptive scheme is as follows. At each load increment, the first NR iteration has an initial number of 10 Gaussian springs. After the first iteration the strain and stress of each spring is computed from the deflection obtained. Based on the yield criteria, springs are classified as elastic or elasto-plastic. If all the springs between a pair of elements were elastic, then the number of springs were changed from the initial 10 springs to 2 Gaussian springs. However, if the springs were found to be elasto-plastic, then the number of springs between an element was changed to 6. The exact location at which the stress changes from elasto-plastic to linear is calculated by obtaining the intersection of the two lines. Those intersection points were referred to as transition points. For the remaining NR iterations, the new springs configuration is used. At the next load increment the initial number of springs is returned to 10 and the process is repeated again. Using the transition springs and the adaptive technique significantly reduced the computational cost since the number of springs in the whole system was reduced at each time step. Since the linear and nonlinear material behaviour was successfully modelled using the Gaussian AEM and the springs distribution was optimised, modelling the material damage was then considered.

The novel use of the Gaussian springs shows a phenomenal revelation since the size of the model significantly decreases, and therefore optimising the number of springs required per element. Only 2 Gaussian springs are required for linear elements, and 6 Gaussian springs for nonlinear elements.

10.1.2 Modelling Damage Fragmentation and Progressive Collapse in AEM

In this thesis, damage was considered as a type of softening material behaviour. A return mapping algorithm for the softening material behaviour was developed to predict and correct the stress based on a strain increment. First, the strain softening algorithm was verified to show that the return mapping behaviour works correctly then it was implemented to the Gaussian AEM code.

Since the material model was produced, fracture was then considered. If a spring exceeds its failed limit, then the spring stiffness is set to zero so as to "remove" the failed spring from the system. The problem is that having failed springs in the system results in having zeros in the global stiffness matrix. This resulted in no convergence in the NR due to the singularity of the stiffness matrix. Also, the eigen values for the system are negative after the failed point is surpassed. A solution to these problems is using a dynamic model for analysis.

Different time-stepping methods were compared for finding the most appropriate method for use in modelling the damage and progressive collapse of structures. The Newmark-Beta method, the linear acceleration method and the Central difference method were compared. The CDM was chosen as the most appropriate method for this scope since it is explicit, and no iterative procedure is required because all the constitutive variables are available from computations at previous time steps. The drawback is the requirement of a small increment of time step. However, the damping matrix and mass matrix were diagonal, and the stiffness matrix did not need to be inverted at every time step since there was no NR iteration required, so ultimately even though the number of total time steps is larger, the overall computational cost is still considered smaller.

Since the softening model can represent both linear and nonlinear material properties, then implementing the softening model to the CDM allowed to produce a code with both linear and nonlinear material behaviour. A modification to the algorithm was required however, since the dynamic model did not require the calculation of the stiffness matrix in every iteration, rather only the internal forces were needed. Secondly, since the CDM was used no NR iteration scheme

was needed for nonlinear analysis.

The damage and fragmentation model was then used for application of frames subject to earthquake loads, and to extreme wind gusts. The progressive collapse of each of those structures due to the earthquake loads, and sometimes including external horizontal loads to simulate effect of nearby objects or impact, were analysed, and the progressive collapse of the structures were clearly represented.

Frames were then subject to 3 second wind gust loads. The 3 second wind was first simulated using CFD in ANSYS Fluent. The analysis for different wind speeds and different structures was performed. After the analysis was complete, the forces that were generated on the walls were exported to the MATLAB code, where the structure would then be analysed for the external forces. The progressive collapse of the structures was successfully shown in the cases that the wind speed was very large.

10.2 Concluding Remarks

Based on the findings in this thesis, the following final remarks can be made:

1. The efficiency and the accuracy of the AEM is successfully improved by using the Gaussian distribution for optimising the springs locations.
2. Only 2 linear Gaussian springs, and 6 nonlinear Gaussian springs are needed between a pair of elements.
3. An adaptive springs procedure is implemented to distribute element springs based on current state of material behaviour (elastic or elasto-plastic) for an overall reduced computational cost.
4. A softening return mapping algorithm is developed for representing damage in materials .
5. A time integrating technique is required when elements in structures exceed their failed limits and separation occurs. The element separation causes stiffness matrix singularity.
6. The progressive collapse of structures is successfully modelled using the Gaussian-AEM and softening material behaviour, with implementation to structures subject to earthquakes and extreme wind loads.

10.3 Recommendations for further research

- **Include contact between elements.** Including the contact between elements can give more realistic results when the collapse occurs, and especially if effect of collapse of surrounding structures are considered.
- **Implementation to 3D AEM.** The Gaussian AEM should be expended to application of 3D elements, this can allow 3D models of frames to be analysed for collapse.
- **Flow past buildings in 3D.** Based on the extreme wind application chapter, it is interesting to model the effect of wind due to surrounding structures from all directions.

Part V

References

Bibliography

- [1] Natural Catastrophes - Our World in Data. Sept. 15, 2018. URL: <https://ourworldindata.org/natural-catastrophes> (visited on 09/15/2018).
- [2] Eisuke Ikuta et al. “Measurement of the human body damage caused by collapsed building”. In: 13th World Conference on Earthquake Engineering. 2004.
- [3] John L Gross and William McGuire. “Progressive collapse resistant design”. In: Journal of Structural engineering 109.1 (1983), pp. 1–15.
- [4] Xinzheng Lu, Xuchuan Lin, and Lieping Ye. “Simulation of Structural Collapse with Coupled Finite Element-Discrete Element Method”. In: Computational Structural Engineering. Ed. by Yong Yuan, Junzhi Cui, and Herbert A. Mang. Dordrecht: Springer Netherlands, 2009, pp. 127–135.
- [5] XZ Lu et al. “Numerical simulation for the progressive collapse of concrete building due to earthquake”. In: Proc. the 14th World Conference on Earthquake Engineering. October. 2008, pp. 12–17.
- [6] Kimiro Meguro and Hatem Tagel-Din. “Applied Element Method for Structural Analysis”. In: Doboku Gakkai Ronbunshu 2000.647 (2000), pp. 31–45.
- [7] Uwe Starossek. Progressive collapse of structures. Vol. 153. Thomas telford London, 2009.
- [8] J Rätty. “Limiting the extent of localised failure according to SFS-EN 1991-1-7”. In: Diplomityö, Aalto Yliopisto, Espoo (2010).
- [9] SM Marjanishvili. “Progressive analysis procedure for progressive collapse”. In: Journal of Performance of Constructed Facilities 18.2 (2004), pp. 79–85.

- [10] Edgar V Leyendecker and Bruce Ellingwood. Design methods for reducing the risk of progressive collapse in buildings. Vol. 98. US Department of Commerce, National Bureau of Standards, 1977.
- [11] Kyaw Myo Lynn and Daigoro Isobe. “Structural collapse analysis of framed structures under impact loads using ASI-Gauss finite element method”. In: *International journal of impact engineering* 34.9 (2007), pp. 1500–1516.
- [12] Hajime Okamura and Kohichi Maekawa. “Nonlinear analysis and constitutive models of reinforced concrete”. In: *Gihodo, Tokyo* 10 (1991).
- [13] JJ Jiang. “Nonlinear Finite Element Analysis of RC Structure”. In: *Shanxi Science and Technology Press, Xian* (1994).
- [14] Georgios Michaloudis et al. “Modelling structural failure with finite element analysis of controlled demolition of buildings by explosives using LS-DYNA”. In: *High Performance Computing in Science and Engineering’09*. Springer, 2010, pp. 539–551.
- [15] Peter A Cundall. “A computer model for simulating progressive, large scale movement in blocky rock systems”. In: *Symp. ISRM, Nancy, France, Proc. Vol. 2*. 1971, pp. 129–136.
- [16] Nian Qi and Jihong Ye. “Nonlinear dynamic analysis of space frame structures by discrete element method”. In: *Applied Mechanics and Materials*. Vol. 638. Trans Tech Publ. 2014, pp. 1716–1719.
- [17] Enrico Masoero et al. “Progressive collapse mechanisms of brittle and ductile framed structures”. In: *Journal of engineering mechanics* 136.8 (2010), pp. 987–995.
- [18] E Masoero et al. “DEM simulations of the progressive collapse of framed structures”. In: *12th International Conference on Fracture. NRCanCAN-MET*. 2009.
- [19] A Munjiza, DRJ Owen, and N Bicanic. “A combined finite-discrete element method in transient dynamics of fracturing solids”. In: *Engineering computations* 12.2 (1995), pp. 145–174.

-
- [20] Eric Perkins and John R Williams. “Generalized spatial binning of bodies of different sizes”. In: *Discrete element methods: Numerical modeling of discontinua*. 2002, pp. 52–55.
- [21] E Rougier, A Munjiza, and NWM John. “Numerical comparison of some explicit time integration schemes used in DEM, FEM/DEM and molecular dynamics”. In: *International journal for numerical methods in engineering* 61.6 (2004), pp. 856–879.
- [22] John R Williams, Eric Perkins, and Ben Cook. “A contact algorithm for partitioning N arbitrary sized objects”. In: *Engineering Computations* 21.2/3/4 (2004), pp. 235–248.
- [23] Andrews Munjiza and KRF Andrews. “NBS contact detection algorithm for bodies of similar size”. In: *International Journal for Numerical Methods in Engineering* 43.1 (1998), pp. 131–149.
- [24] A Munjiza, DRJ Owen, and AJL Crook. “Energy and momentum preserving contact algorithm for general 2D and 3D contact problems.” In: (2014).
- [25] A Munjiza, KRF Andrews, and JR White. “Discretized contact solution for combined finitediscrete method”. In: (2014).
- [26] A Munjiza and KRF Andrews. “Penalty function method for combined finite–discrete element systems comprising large number of separate bodies”. In: *International Journal for Numerical Methods in Engineering* 49.11 (2000), pp. 1377–1396.
- [27] A Munjiza, T Bangash, and NWM John. “The combined finite–discrete element method for structural failure and collapse”. In: *Engineering Fracture Mechanics* 71.4-6 (2004), pp. 469–483.
- [28] Antonio A Munjiza. *The combined finite-discrete element method*. John Wiley & Sons, 2004.
- [29] Antonio Munjiza, KRF Andrews, and JK White. “Combined single and smeared crack model in combined finite-discrete element analysis”. In: *International Journal for Numerical Methods in Engineering* 44.1 (1999), pp. 41–57.

- [30] A Munjiza and KRF Andrews. “Penalty function method for combined finite–discrete element systems comprising large number of separate bodies”. In: *International Journal for Numerical Methods in Engineering* 49.11 (2000), pp. 1377–1396.
- [31] Antonio A Munjiza, Earl E Knight, and Esteban Rougier. *Computational mechanics of discontinua*. John Wiley & Sons, 2011.
- [32] Xinzheng Lu et al. “Numerical simulation for the progressive collapse of concrete building due to earthquake”. In: *a a 2* (2008), p. 2.
- [33] T Bangash and A Munjiza. “A computationally efficient beam element for FEM/DEM simulations of structural failure and collapse”. In: *Discrete Element Methods: Numerical Modeling of Discontinua*. 2002, pp. 133–137. DOI: [https://doi.org/10.1061/40647\(259\)24](https://doi.org/10.1061/40647(259)24).
- [34] Nikolina Zivaljic, Hrvoje Smoljanovic, and Zeljana Nikolic. “A combined finite-discrete element model for RC structures under dynamic loading”. In: *Engineering Computations* 30.7 (Oct. 2013), pp. 982–1010. DOI: 10.1108/ec-03-2012-0066.
- [35] Hrvoje Smoljanovi, Nikolina ivalji, and eljana Nikoli. “A combined finite-discrete element analysis of dry stone masonry structures”. In: *Engineering Structures* 52 (July 2013), pp. 89–100. DOI: 10.1016/j.engstruct.2013.02.010.
- [36] Ye Jihong and Qi Nian. “Combination of DEM/FEM for Progressive Collapse Simulation of Domes Under Earthquake Action”. In: *International Journal of Steel Structures* 18.1 (2018), pp. 305–316.
- [37] A. Munjiza et al. “Fracture and fragmentation of thin shells using the combined finite-discrete element method”. In: *International Journal for Numerical Methods in Engineering* 95.6 (June 2013), pp. 478–498. DOI: 10.1002/nme.4511.
- [38] Kimiro Meguro and Motohiko Hakuno. “Fracture analyses of concrete structures by the modified distinct element method”. In: *Doboku Gakkai Ronbunshu* 1989.410 (1989), pp. 113–124.

-
- [39] Motohiko Hakuno and Kimiro Meguro. “Simulation of concrete-frame collapse due to dynamic loading”. In: *Journal of engineering mechanics* 119.9 (1993), pp. 1709–1723.
- [40] Kimiro Meguro and Motohiko Hakuno. “Application of the extended distinct element method for collapse simulation of a doubledeck bridge”. In: *Doboku Gakkai Ronbunshu* 1994.483 (1994), pp. 17–27.
- [41] Limin Sun et al. “Application of extended distinct element method with lattice model to collapse analysis of RC bridges”. In: *Earthquake engineering & structural dynamics* 32.8 (2003), pp. 1217–1236.
- [42] Atsushi ITOH, Junichiro NIWA, and Tada-aki TANABE. “Non-linear dynamic analysis of reinforced concrete piers based on lattice model”. In: *Doboku Gakkai Ronbunshu* 2001.676 (2001), pp. 27–39.
- [43] Tadahiko Kawai. “New element models in discrete structural analysis”. In: *Journal of the Society of Naval Architects of Japan* 1977.141 (1977), pp. 174–180.
- [44] T Kawai. “Discrete Limit Analysis of Reinforced Concrete Structures Using Rigid Bodies-Spring Models”. In: *The finite element method in the 1990s*. Springer, 1991, pp. 182–191.
- [45] Tadahiko Kawai. “Some consideration on the finite element method”. In: *International Journal for Numerical Methods in Engineering* 16.1 (1980), pp. 81–120.
- [46] Tadahiko Kawai and Yutaka Toi. “A discrete method of limit analysis and its application to plastic stability problems of structural members”. In: *Engineering Structures* 5.1 (1983), pp. 38–44.
- [47] Yutaka Toi. “Shifted integration technique in one-dimensional plastic collapse analysis using linear and cubic finite elements”. In: *International Journal for Numerical Methods in Engineering* 31.8 (1991), pp. 1537–1552.
- [48] E A. Tingatinga, H Kawakami, and S M. Shrestha. “Three-Dimensional Seismic Collapse Analysis of Wooden Houses Using Rigid Body-Spring Method”. In: 2 (Sept. 2008), pp. 116–123.

- [49] Yutaka Toi and Daigoro Isobe. “Adaptively shifted integration technique for finite element collapse analysis of framed structures”. In: *International Journal for Numerical Methods in Engineering* 36.14 (1993), pp. 2323–2339.
- [50] Daigoro Isobe. *Progressive Collapse Analysis of Structures: Numerical Codes and Applications*. Butterworth-Heinemann, 2017.
- [51] N Katahira et al. “Development of macro-model seismic collapse simulator for framed structures using ASI-Gauss technique”. In: *Proceedings of 14th WCEE (CD)*. Beijing: The 14th WVEE Organizing Committee (2008).
- [52] M. Papadrakakis et al. *A Dynamic Finite Element Code for Analyzing Collapse Behaviours of Framed Structures Under Seismic Loads*.
- [53] Kimiro Meguro and Hatem Tagel-Din. “A new efficient technique for fracture analysis of structures”. In: *Bulletin of Earthquake Resistant Structure Research Center, IIS, Univ. of Tokyo* 30 (1997), pp. 103–116.
- [54] Kimiro Meguro and Hatem Tagel-Din. “A new simplified and efficient technique for fracture behavior analysis of concrete structures”. In: *Proceedings of the Third International Conference on Fracture Mechanics of Concrete and Concrete Structures (FRAMCOS-3)*. Vol. 2. 1998, pp. 911–920.
- [55] Huda Helmy, Hamed Salem, and Sherif Mourad. “Computer-Aided Assessment of Progressive Collapse of Reinforced Concrete Structures according to GSA Code”. In: *Journal of Performance of Constructed Facilities* 27.5 (Oct. 2013), pp. 529–539. DOI: 10.1061/(asce)cf.1943-5509.0000350.
- [56] Nabil A. Rahman, Ayman Elfouly, and Michael Booth. “Alternate Path Progressive Collapse Analysis of Steel Stud Bearing Wall Structures”. In: *Structures Congress 2011*. American Society of Civil Engineers, Apr. 2011. DOI: 10.1061/41171(401)247.
- [57] Marin Lupoae and Carmen Bucur. “Building demolition - positive aspect of progressive collapse”. In: 4 (Jan. 2009), p. 10.

- [58] Said Elkholy, Hatem Tagel-Din, and Kimiro Meguro. “Structural failure simulation due to fire by applied element method”. In: JCOSAR2003, the Fifth Japan Conference on Structural Safety and Reliability, Tokyo, Japan. 2003.
- [59] K Worakanchana and K Meguro. “Voronoi Applied Element Method For Structural Analysis: Theory And Application For Linear And Non-Linear Materials”. In: The 14th World Conference on Earthquake Engineering October. 2008, pp. 12–17.
- [60] Nam-Ho Kim. Introduction to nonlinear finite element analysis. Springer Science & Business Media, 2014.
- [61] Junuthula Narasimha Reddy. Theory and analysis of elastic plates and shells. CRC press, 2006.
- [62] Detailed Explanation of the Finite Element Method (FEM). Sept. 10, 2018. URL: <https://www.comsol.com/multiphysics/finite-element-method> (visited on 09/10/2018).
- [63] Antonio Munjiza, Esteban Rougier, and Earl Knight. Large Strain Finite Element Method: A Practical Course. Nov. 2014. ISBN: 978-1-118-40530-7.
- [64] K Liu and W Liu. “Application of discrete element method for continuum dynamic problems”. In: Archive of Applied Mechanics 76.3-4 (2006), pp. 229–243.
- [65] Prashidha Kharel’s Blog: Formulating the Applied Element Method: Linear 2D (Part I). Aug. 29, 2018. URL: <http://blog.prashidha.com/2014/03/formulating-applied-element-method.html> (visited on 09/05/2018).
- [66] Kimiro Meguro and H Sayed Tagel-Din. “Applied element method used for large displacement structural analysis”. In: Journal of Natural Disaster Science 24.1 (2002), pp. 25–34.
- [67] A Okabe et al. Spatial tessellations: concepts and applications of Voronoi tessellations. 2000.

- [68] Eduardo A de Souza Neto, Djordje Peric, and David RJ Owen. Computational methods for plasticity: theory and applications. John Wiley & Sons, 2011.
- [69] Kenneth Runesson et al. “Constitutive modeling of engineering materials-theory and computation”. In: Volume I General Concepts and Inelasticity (2006).
- [70] JC Simo and TJR Hughes. Computational Inelasticity, Interdisciplinary Applied Mathematics 7. 1998.
- [71] Louie L Yaw. “Nonlinear static 1D plasticity various forms of isotropic hardening”. In: Walla Walla University 25 (2012).
- [72] Dr Ulrich Hoppe. “Computational Plasticity”. In: Lecture Notes, Ruhr University Bochum (2010).
- [73] Djordje Peric. “Computational Plasticity”. In: Lecture Notes, Swansea University (2013).
- [74] Rade Vignjevic et al. “Modelling of strain softening materials based on equivalent damage force”. In: Computer Methods in Applied Mechanics and Engineering 335 (June 2018), pp. 52–68. DOI: 10.1016/j.cma.2018.01.049.
- [75] Zdenk P. Baant, Ted B. Belytschko, and Ta-Peng Chang. “Continuum Theory for Strain-Softening”. In: Journal of Engineering Mechanics 110.12 (Dec. 1984), pp. 1666–1692. DOI: 10.1061/(asce)0733-9399(1984)110:12(1666).
- [76] Rodney Hill. “Acceleration waves in solids”. In: Journal of the Mechanics and Physics of Solids 10.1 (1962), pp. 1–16.
- [77] Jean Mandel. “Conditions de stabilité et postulat de Drucker”. In: Rheology and Soil Mechanics/Rhéologie et Mécanique des Sols. Springer, 1966, pp. 58–68.

- [78] AH Marchertas, RF Kulak, and YC Pan. “Performance of blunt crack approach within a general purpose code”. In: *Nonlinear Numerical Analysis of Reinforced Concrete*, ed., LE Schwer, Am. Soc. of Mech. Engrs., New York (1982), pp. 107–123.
- [79] Clifford Truesdell and Walter Noll. “The non-linear field theories of mechanics”. In: *The non-linear field theories of mechanics*. Springer, 2004, pp. 1–579.
- [80] Jacques Hadamard. *Lecons Sur Un Propagation Des Ondes*. 1903.
- [81] Anil K Chopra. *Dynamics of structures: Theory and applications*. 2001.
- [82] Nathan M Newmark. “A method of computation for structural dynamics”. In: *Journal of the engineering mechanics division* 85.3 (1959), pp. 67–94.
- [83] Henri Gavin. “Numerical integration for structural dynamics”. In: ().
- [84] Georg GroSSeholz, Delfim Soares, and Otto Estorff. “A stabilized central difference scheme for dynamic analysis”. In: *International Journal for Numerical Methods in Engineering* 102.11 (2015), pp. 1750–1760.
- [85] Mass Matrix Construction Overview. Online. URL: <https://www.colorado.edu/engineering/CAS/courses.d/MFEMD.d/MFEMD.Ch16.d/MFEMD.Ch16.pdf>.
- [86] Ronald Hamburger and Andrew Whittaker. “Design of steel structures for blast-related progressive collapse resistance”. In: 44 (Mar. 2004), pp. 41–53.
- [87] Roberto Villaverde. “Methods to Assess the Seismic Collapse Capacity of Building Structures: State of the Art”. In: *Journal of Structural Engineering* 133.1 (Jan. 2007), pp. 57–66. DOI: 10.1061/(asce)0733-9445(2007)133:1(57).
- [88] Earthquake Engineering Research Institute. *Learning from Earthquakes Program*, Loring A Wyllie, and Bruce A Bolt. The chile earthquake of March 3, 1985. The Institute, 1986.

- [89] Roberto Villa Verde. “Explanation for the numerous upper floor collapses during the 1985 Mexico city earthquake”. In: *Earthquake Engineering & Structural Dynamics* 20.3 (1991), pp. 223–241. DOI: 10.1002/eqe.4290200303.
- [90] J. Osteraas and H. Krawinkler. “The Mexico Earthquake of September 19, 1985 Behavior of Steel Buildings”. In: *Earthquake Spectra* 5.1 (Feb. 1989), pp. 51–88. DOI: 10.1193/1.1585511.
- [91] Anshel J Schiff. “Earthquake spectra. Philippines Earthquake reconnaissance report”. In: *Earthquake spectra* 7 (1991), pp. 1–141.
- [92] Craig D Comartin. *Guam earthquake of August 8, 1993*. Earthquake Engineering Research Institute, 1993.
- [93] John F Hall, WT Holmes, and P Somers. “Northridge earthquake, January 17, 1994”. In: *Preliminary reconnaissance report* (1994).
- [94] Alex K Tang. *Izmit (Kocaeli), Turkey, Earthquake of August 17, 1999 Including Duzce Earthquake of November 12, 1999: Lifeline Performance*. Vol. 17. ASCE Publications, 2000.
- [95] Joseph Uzarski and Christopher Arnold. *Chi-Chi, Taiwan, earthquake of September 21, 1999: reconnaissance report*. Vol. 17. Earthquake Engineering Research Institute, 2001.
- [96] JV Hengesh et al. “Bhuj, india earthquake of january 26, 2001-reconnaissance report”. In: (2002).
- [97] *Deadliest Earthquakes in History*. July 23, 2018. URL: <https://www.livescience.com/6932-deadliest-earthquakes-history.html> (visited on 07/23/2018).
- [98] Seth Stein and Michael Wysession. *An introduction to seismology, earthquakes, and earth structure*. John Wiley & Sons, 2009.
- [99] BBC - GCSE Bitesize: Causes. Aug. 10, 2015. URL: http://www.bbc.co.uk/schools/gcsebitesize/geography/natural_hazards/earthquakes_rev1.shtml (visited on 07/23/2018).

- [100] Michael Wysession Seth Stein. An Introduction to Seismology, Earthquakes and Earth Structure. John Wiley and Sons Ltd, Sept. 1, 2002. 512 pp. ISBN: 0865420785. URL: https://www.ebook.de/de/product/3770366/seth_stein_michael_wysession_an_introduction_to_seismology_earthquakes_and_earth_structure.html.
- [101] Sumatra, Indonesia, Dec. 26, 2004. July 23, 2018. URL: <http://geosurvey.ohiodnr.gov/beyond-border-region-quake-events/sumatra-indonesia-dec-26-2004> (visited on 07/23/2018).
- [102] Harry O Wood and Frank Neumann. "Modified Mercalli intensity scale of 1931". In: Bulletin of the Seismological Society of America 21.4 (1931), pp. 277–283.
- [103] Kobe Earthquake. Feb. 16, 2012. URL: <http://www.vibrationdata.com/earthquakes/kobe.htm> (visited on 07/23/2018).
- [104] The Editors of Encyclopaedia Britannica, ed. Kbe earthquake of 1995. Encyclopædia Britannica, inc., Apr. 2017. URL: <https://www.britannica.com/event/Kobe-earthquake-of-1995>.
- [105] Dr. Amit Srivastava, Chaitanya Goyal, and Akash Jain. Review of Causes of foundation failures and their possible preventive and remedial measures. Jan. 2012.
- [106] Structural engineering aspects of the June 27, 1998 AdanaCeyhan (Turkey) earthquake - ScienceDirect. July 24, 2018. URL: <https://www.sciencedirect.com/science/article/pii/S0141029600000468> (visited on 07/24/2018).
- [107] January 17 in the Ring of Fire | Multimedia | teleSUR English. July 23, 2018. URL: <https://www.telesurtv.net/english/multimedia/January-17-in-the-Ring-of-Fire-20150117-0022.html> (visited on 07/23/2018).
- [108] Alamy Limited. A satellite image of Sumatra, Indonesia, before and after the Stock Photo: 103996337 - Alamy. July 23, 2018. URL: <https://www.alamy.com/stock-photo-a-satellite-image-of-sumatra-indonesia-before-and-after-the-devasting-103996337.html> (visited on 07/23/2018).

- [109] Jacob C. Earthquake Database. Feb. 16, 2017. URL: <http://web.iitd.ac.in/~matsagar/EqDataBase.htm> (visited on 07/24/2018).
- [110] Svend Ole Hansen Claes Dyrbye. Wind Loads on Structures. John Wiley & Sons, 1997. ISBN: 0 471 95651 1.
- [111] Lorenzo Rosa et al. “Wind-induced dynamics and loads in a prismatic slender building: A modal approach based on unsteady pressure measurements”. In: 107-108 (Aug. 2012), pp. 118–130.
- [112] Munich Reinsurance. Topics Geo annual review: Natural catastrophes 2004. 2004.
- [113] Yukio Tamura. “Wind-induced damage to buildings and disaster risk reduction”. In: Proceedings of the APCWE-VII, Taipei, Taiwan (2009).
- [114] Kangpyo Cho et al. “Typhoon (Maemi) attack and its damage in Southern Korea celebrating Thanksgiving festival of Chusok”. In: Sixth Asia-Pacific Conference on Wind Engineering. 2005.
- [115] Edificio Real Class - Construtora Real. Aug. 14, 2018. URL: <http://compradordeimovel.no.comunidades.net/edificio-real-class-construtora-real> (visited on 08/14/2018).
- [116] Sigrid Reiter. “Validation process for CFD simulations of wind around buildings”. In: Proceedings of the European Built Environment CAE Conference. Londres. 2008, p. 18.
- [117] Shuzo Murakami. “Overview of turbulence models applied in CWE--1997”. In: Journal of Wind Engineering and Industrial Aerodynamics 74 (1998), pp. 1–24.
- [118] BG Wiren. “A wind tunnel study of wind velocities in passages between and through buildings”. In: Proceedings of the 4th International Conference on Wind Effects on Buildings and Structures,(Heathrow 1975). 1975, pp. 465–475.
- [119] Aly Mousaad Aly. “The role of turbulence on the response of buildings to extreme wind”. In: ()).